

Fast imaging in non-standard  
X-ray computed tomography  
geometries

Thomas De Schryver



Fast imaging in non-standard X-ray computed tomography geometries Thomas De Schryver



UNIVERSITEIT  
GENT

2017



# Fast imaging in non-standard X-ray computed tomography geometries

---

ir. Thomas De Schryver

Proefschrift ingediend tot het behalen van de graad van  
Doctor in de wetenschappen:  
fysica  
Academiejaar 2016-2017





Universiteit Gent  
Faculteit Wetenschappen  
Vakgroep Fysica en Sterrenkunde

Examencommissie : Prof. Dr. Dirk Poelman (voorzitter)  
Prof. Dr. ir. Matthieu Boone (secretaris)  
Prof. Dr. Luc Van Hoorebeke (promotor)  
Dr. Alessandro Mirone  
Prof. Dr. Jan Sijbers  
Prof. Dr. ir. Stefaan Vandenberghe  
Dr. ir. Jan Aelterman

Universiteit Gent  
Faculteit Wetenschappen  
Vakgroep Fysica en Sterrenkunde  
Proeftuinstraat 86, B-9000 Gent, België

Proefschrift ingediend tot het behalen van de graad van  
Doctor in de wetenschappen:  
fysica  
Academiejaar 2016-2017



© Thomas De Schryver, 2017

Alle rechten voorbehouden. Niets uit deze uitgave mag worden vermenigvuldigd en/of openbaar gemaakt door middel van druk, fotokopie, microfilm, elektronisch of op welke andere wijze ook, zonder voorafgaande schriftelijke toestemming van de auteur.

---

All rights reserved. No part of this publication may be reproduced in any form by print, photo print, microfilm or any other means without the author's written consent.



# Acknowledgements

True to my ‘deadline mentality’, there have been some late hours involved in composing the following 200 or so pages. To be fair about one third of the contents did not touch paper before 12 o’clock in the evening, which had the perverse effect of keeping me away from my beloved little family. During the scarce conversations I still had with my spouse during that time, often the same questions kept on popping up: “And, have you finished writing?” To which last week, I was finally able to reply: “Almost, … but I still have to write the most difficult paragraph. The paragraph I am sure of at least more than seven people in the audience of my public defence will read.” In any case, forgetting to acknowledge somebody’s contribution to my dissertation is just one of the mistakes in life I do not want to make. Particularly, because I genuinely belief this work was not an individual endeavour. So if your name is not mentioned throughout the remainder of this section, and you feel entitled to a ‘thank you’, I probably did forget to mention you, and I should thank you anyway for reading the very first paragraph of my dissertation. Strengthened by this little piece of built-in insurance, I guess not much can go wrong. So, here we go!

First of all, Luc, thank you for hiring me and giving me this (second) chance. Your integrity, kindness and passion for physics were a true inspiration to work hard. I also solemnly swear to annoy my wife with your contagious, frivolous sense of humour, which I mastered very well during the last four years. I am buying a quad-copter drone as we speak, and I will always point out to my children that somebody forgot to switch off the ventilators next to the E17-highway in ‘Beervelde’. Manu, thank you for rekindling the engineer inside of me and showing me how fun it is to program hardware. I am looking forward to working with you once more at XRE, and getting my daily dose of trivia during a ‘coffee brigade 2.0’ excursion. Matthieu, you might have been right about Facebook, but what I actually meant is that Snapchat stock will drop to zero in the near future. Anyway, if and when you are planning to go on a conference trip to Australia for one week again, sign me up! Memorable is the word, although I will be arranging the lodging next time. And always remember, I tend to show my affection to people by gently bullying them. Amélie, I am sorry for recommending you to wear sandals during ‘de dodentocht’. That was clearly bad advice, and luckily the blisters

healed nicely just in time before you had to put on your high heel wedding shoes. Channelling your admirable sense of duty into a PhD is certain to bring forward great things. Marjolein, I know I am leaving my work in good hands, and looking at the way you document your research, I guess that dissertation is going to write itself. Frederic, our (not so) junior addition to the team, I would have wanted to stick around a bit longer to see what you are up to, because now I have the feeling I will be missing out on some cool stuff. Last but not least, Jelle, I know we had our differences in the early days, but I am glad this is all in the past. Moreover, I think we can be proud of what we achieved when looking back at our developments in the TomFood project. I also want to thank our Geology-connection, in particular Veerle, for your energetic leadership and ever positive attitude. Wesley and Tom, for the memorable trip to SLS, a.k.a. the ‘how to make a boring 24h experiment fun’-trip. Tim, thank you for regularly inviting me to go and see a KAA Gent match. If you’re ever lonely in the stands, you have my number. And, thank you Jeroen, ‘fracture-guy’, for helping me crush stuff during in-situ scanning. Always happy to help you think out new pick-up lines for your next ‘Sziget’-festival. From WoodLab, thank you Jan for the fascinating CT discussions and bringing so much enthusiasm and passion to the table. Let’s one day bring this enthusiasm to a pub table in one of the many hip new establishments popping up in our neighbourhood. I also want to thank Philippe, Roland and Patrick, for always being ready to take in my workshop tickets and frankly keeping things running at the INW. Finally, in the category of ex-colleagues, I want to thank the BioMMeda-group, in particular Prof. Patrick Segers for understanding the choices I made back in the day. You should know that 50 percent of the time I still think I could have made the ‘better’ choice. Although, looking at the end result, I guess it does not matter any more.

From old to new, thank you Denis, Marijn, Bert, Sofie, Bruno, and joining us soon, Manu. I think it is safe to say that I have never been so excited about a job in my life. Working with you guys feels very familiar and rewarding, and building CT scanners might just become my full time hobby.

The research described in this dissertation would not have taken place without the financial support of the Agency for Innovation by Science and Technology in Flanders (IWT, SBO project 120033 “TomFood”). In particular, I want to thank Dr. Pieter Verboven and Prof. Bart Nicolai for bringing together the heterogeneous, though very complimentary specialities of several research groups all across Flanders, with the unified goal of improving and implementing X-ray CT as an imaging tool in food industry. So, thank you, Jan De Block, Sofie De Man and Barabara Duquenne from ILVO, Johan Claeys, Maria Christaki and Sofie Morren from the Thomas More Lab4Food, Bart Nicolai, Pieter Verboven and Mattias Van Dael from Mebios at KU Leuven, and thank you Vincent Van Nieuwenhove, Eline Janssens and Jan Sijbers from UAntwerp, for the interesting scientific discussions.

Before going over to the more personal acknowledgements, I once again want to express my great appreciation for the interest the members of the jury, Prof. Dirk

Poelman, Prof. Luc Vanhoorebeke, Prof. Matthieu Boone, Dr. Alessandro Mirone, Prof. Jan Sijbers, Prof. Stefaan Vandenberghe and Dr. Jan Aelterman, have shown in my work, and the constructive dialogue brought forward by their valuable input.

Dear friends, you know who you are, my beloved football mates from ‘MVC Het Plan’, ‘Plooiers9000’, ‘the Happy Friends Association’, ‘de bende’. I look forward to celebrating life with you guys for many years to come. I also want to make clear that I have a real job now, and that you are technically no longer my bosses, as I am no longer being paid through your taxes.

Birgit and Dirk, you know I am not a complicated man, as we say in Dutch ‘de liefde van de man gaat door de maag’. But it is so much more than the delicious Sunday meals and the relaxing holidays. You and the whole family are one of the reasons why I love Floor so much. Know that I feel loved and at home in the ‘Visserij’.

My beloved brothers and sisters, I frequently think about how certain of my personality traits can be traced back to one or several of yours, the boy with five mothers and four fathers. It is scary and at the same time very reassuring to know how much we are alike. A piece of us got missing in 2008, and I for one still think about Dorothée daily, if not for the briefest moment, still wondering ‘why’. However, I find comfort in the fact that in the end it brought us all closer together. So, when you are telling somebody about your little brother’s PhD, please add ‘... and I helped him do it!’

This especially holds for the guests of honour to this occasion, my father and mother Jan and Marie-Thérèse De Schryver - De Pauw. How did you do it? How did you bring up eight kids? What is your secret? This mystery certainly put things in perspective, in the sense that writing a PhD dissertation is probably and literally equivalent to your casual family walk in the park. So, this work is for you! But you will have to share it, ...

... share it, with the subjects of the paragraph I am sure of at least more than seven people in the audience of my public defence will read. Floor and Otto-Jan, I could try and say how much you contributed to this thesis, but I would probably just end up thanking you for keeping me alive and healthy the last couple of months. I could try, but the acknowledgements might just turn into a love letter. I could try, ... but let me just finish by repeating that completing this PhD with you is and will probably be the fourth happiest moment in my life, right behind the birthdays of our two children (wink) and the day I met you.

Gent, 2017  
Thomas De Schryver



# Nederlandse samenvatting

## –Summary in Dutch–

X-stralen tomografie werd oorspronkelijk ontwikkeld als een medische beeldvormingstechniek, maar kende al sinds de uitvinding van de eerste X-stralen CT-scanner door Hounsfield een brede waaier aan toepassingen buiten dit gebied in verschillende onderzoeks- en industrietakken, met als doel het niet-destructief visualiseren van de interne structuren in een object. Samen met zijn partners in het SBO<sup>1</sup> TomFood project heeft het ‘Centrum for X-stralen tomografie van de Universiteit Gent’ (UGCT) kunnen onderkennen dat het niet-destructieve karakter van X-stralen CT een belangrijke, toegevoegde en innovatieve waarde in de voedingsmiddelenindustrie kan hebben. Hierbij wordt specifiek aandacht besteed aan CT als enerzijds een onderzoekstool, voor het verbeteren van de kwaliteit van voeding en de productieprocessen ervan, maar anderzijds als een middel om de kwaliteit van voedingsmiddelen op te volgen, bij voorkeur aan een transportband met een hoge doorvoersnelheid.

Om de haalbaarheid van een dergelijke transportbandtoepassing van X-stralen CT voor kwaliteitscontrole te bepalen, wordt er in dit werk een alternatieve CT-geometrie voorgesteld. Met een vaststaande X-stralen bron en detector, brengt deze zogenaamde ‘transportbandgeometrie’ een object in beeld door voor dit object een gecombineerde translatie- en rotatiebeweging te beschouwen, langs en respectievelijk rond twee loodrecht op elkaar staande assen. Een theoretische analyse toont aan dat een transportbandgeometrie met dit traject in staat is om acquisities te genereren die voldoen aan de Tuy-Smith voorwaarde en dus exacte CT-reconstructies kunnen opleveren. De voorgestelde geometrie kan ook zonder meer ingebouwd worden in een bestaande transportbandconfiguratie, maar hierbij is het vooral belangrijk dat de doorvoersnelheid gerespecteerd wordt en dat het uiteindelijk ontwerp dan ook afgesteld wordt op deze doorvoersnelheid. Het CT-beeldvormingsproces moet dus snel verlopen, doch voldoende beeldkwaliteit voorzien om een accurate kwaliteitscontrole van een product toe te laten. De beeldkwaliteit wordt in dit werk gekwantificeerd door de grootte van de kleinst detecteerbare details in een beeld vast te leggen door middel van Fourier gebaseerde resolutiecriteria, namelijk via ‘Fourier-schil-correlatie’ en de ‘spectrale signaalruis-verhouding’. De ontwerpsparameters voor een toestel gebaseerd op de trans-

---

<sup>1</sup>Strategisch Basis onderzoek

portbandgeometrie, vooral met betrekking tot diens afmetingen en snelheid waar mee deze beelden produceert, kunnen vastgelegd worden door de detailgrootte uit te zetten in functie van de doorvoersnelheid. Finaal blijkt uit deze analyse dat kwaliteitscontrole met X-stralen CT op een transportband weldeegelijk mogelijk is aan een respectabele resolutie en doorvoersnelheid, afhankelijk van welke producten er precies in beeld worden gebracht.

De afweging tussen beeldkwaliteit en doorvoersnelheid werd uiteindelijk toegepast op echte data afkomstig van een demonstratieopstelling die het gedrag van een transportbandgeometrie nabootst, maar in eerste instantie werden voor de transportbandgeometrie echter gesimuleerde beelden geproduceerd. Hiervoor werd een eerste orde model voor X-stralen radiografie geïmplementeerd op een grafische rekeneenheid (GPU), met bijzondere aandacht voor de fysische betrekkingen die het poly-chromatische en ruisachtige karakter van een radiografie beschrijven. Door deze ‘*radiografie simulator*’ vervolgens te combineren met een flexibele en intuïtieve manier om aan alle CT scanner componenten een arbitraire oriëntatie toe te kennen, wordt het ook mogelijk om volledige CT acquisities te simuleren in arbitraire en ongebruikelijke geometrieën, zoals de transportbandgeometrie.

Deze arbitraire geometrieën werden tevens opgenomen in een Python-reconstructiemodule, die een GPU-implementatie van de iteratieve ‘*Ordered Subset*’ (OS) reconstructietechniek voorziet, via een nauwe koppeling met CUDA C-code. Deze iteratieve aanpak is vooral interessant, omdat deze het toelaat een nauwkeuriger model van de voorwaartse projectie en/of extra a priori informatie over het in-beeld-gebrachte object in rekening te brengen tijdens de iteraties. In dit werk werden de projectie en terug-projectie operatoren van de OS-techniek aangepast, opdat reconstructies overweg zouden kunnen met lokale, niet-rigide vervormingen in een object, die zouden kunnen plaatsvinden gedurende de CT-acquisitie ervan. Deze vervormingen kunnen afgeleid worden door strategisch gekozen acquisities op elkaar te registreren, waarvoor verschillende algoritmen ter beschikking zijn. De ‘*Demons*’, ‘*optical phase flow*’ en ‘*B-spline*’ registratiemethodes werden in deze thesis bestudeerd en geëvalueerd in de context van enerzijds de CT acquisitie van een dynamische in-situ compressie van een aluminiumschuim en anderzijds de in-situ rijs van brooddeeg aan een gecontroleerde temperatuur. De B-spline methode leverde over de gehele lijn de meest consistente en robuuste resultaten, zelfs bij grote vervormingen. Dit is dan ook de methode bij uitstek om vervormingsvelden af te schatten, die dan op hun beurt kunnen opgenomen worden in het reconstructieproces. Uit de aluminiumschuim- en brooddeegapplicaties is verder gebleken dat deze combinatie weldeegelijk de aanwezige bewegingsartefacten kan reduceren en in sommige gevallen zelfs volledig kan elimineren. Het succes van deze registratieaanpak opent ook nieuwe deuren naar een doorgedreven integratie van de X-stralen CT-beeldvormingstechniek met een geavanceerde numerieke modellering van de dynamische processen, die via de techniek in beeld worden gebracht. Met deze aanpak kan X-stralen CT verheven worden van een

techniek die louter de attenuatie van een object visualiseert, tot een volledige 3D in-situ materiaal karakterisatie van het object.

De rode draad doorheen dit werk, die ook terug te vinden is de hierboven vermelde ontwikkelingen, is **snelle beeldvorming met ongebruikelijke X-stralen CT geometrieën protocollen** met als doel:

- X-stralen CT te gebruiken voor niet-destructieve kwaliteitscontrole op een transportband (*'in-line CT'*).
- het verbeteren van de visualisatie van dynamische processen, die betrekking hebben op lokale en niet-rigide structurele wijzigingen binnenin het bemeten object(*'4D-CT'*).



# English summary

Ever since Hounsfield invented his '*EMI-scanner*', X-ray computed tomography has been taken out of its medical context as a way to non-destructively image the interior of objects in a wide variety of research and industry branches. Together with its partners in the TomFood project, the '*Ghent University Centre for X-ray Tomography* (UGCT) recognised that the non-destructive character of X-ray CT can create an added and innovative value in the food industry. Specifically, CT could be used as an inspection and engineering tool, with the goal of controlling and improving the quality of both food products and their production processes, preferably in an in-line setting.

As a cornerstone to the work presented here, and the TomFood project as whole, the feasibility of applying X-ray CT to an in-line production setting as a quality inspection tool was studied by introducing an alternative CT geometry. In this so-called '*conveyor belt CT geometry*', the sample's trajectory combines a translation and a partial rotation about an axis that is perpendicular the translation axis, as it passes in between a fixed X-ray source and detector. Through a theoretical analysis, it can be shown that this trajectory produces Tuy-Smith compliant acquisitions, that lead to exact CT reconstructions. By following this design, the conveyor belt geometry would be amendable to a direct implementation into an existing conveyor belt configuration, but more importantly the design has to be tuned towards maintaining the production line's throughput. In other words, the imaging process has to be fast, while still producing images that are good enough to be useful in a product quality assessment. To find the ideal design parameters for the conveyor belt geometry, a methodology was devised which quantifies the CT image quality in terms of a minimally detectable feature size, as determined by Fourier Shell Correlation and Spectral Signal to Noise Ratio resolution metrics. By setting out these feature sizes as a function of the inspection device's throughput, it can be concluded that in-line CT is indeed possible at a respectable resolution and throughput, depending on the type of sample that is being imaged.

Before testing the design methodology discussed above on real life data produced by a hardware mock up, it was first applied to a series of simulated conveyor belt CT datasets. Thus, as an important prerequisite to the feasibility study, an accurate and fast radiography simulation tool had to be developed. For this, an established first order physics model for X-ray radiographs, including their polychromatic and noise laden nature, was implemented on a '*Graphical Processing*

*Unit*' (GPU), and was supplemented with a flexible and intuitive way to define arbitrary configurations of the CT scanner components. As a result, CT acquisitions can now be simulated in arbitrary, non-standard geometries, such as the conveyor belt geometry.

These arbitrary geometries were also included in a Python-CUDA reconstruction tool, that provides a GPU based implementation of the Ordered Subset iterative reconstruction algorithm. This iterative approach is particularly interesting because it allows for improved versions of the forward projection model and a priori information on the imaged object to be incorporated in the iterative loop. In this work, the projection and back projection steps in the Ordered Subset reconstruction tool were altered, to account for an object that is locally and non-rigidly deforming during a CT acquisition. These deformations can be inferred through an algorithm that registers strategically chosen reference acquisitions, which can for example be given by the short scan sub-acquisitions of a standard single rotation cone beam scan. Several registration algorithms were evaluated, namely the Demons, optical phase flow and B-spline methods, by looking at their performance on CT data acquired from an in-situ aluminium foam compression experiment and the in-situ heating of a leavening dough sample. The B-spline method provided the most consistent and robust results up to very large deformations, making it the preferred method to estimate deformation fields. As demonstrated throughout the applications for this topic, the motion blurring artefacts can effectively be eliminated by incorporating these deformation fields into the iterative reconstruction algorithm. The effectiveness of this registration approach, also opens up the new prospect of combining X-ray CT imaging and a thorough numerical modelling of an imaged dynamic process, not specifically limited to mechanical deformations, with the final goal of elevating the X-ray CT technique from a way to image an object's attenuation to a 3D in-situ material characterisation.

Bringing together all of the above, the unifying premise of this work is **fast CT imaging using non-standard geometries and protocols**, with the goal of

- bringing X-ray CT to an in-line setting as a non-destructive quality inspection tool, i.e. in-line CT, and
- improving the visualisation of dynamic processes, specifically pertaining to local and non-rigid structural changes of an imaged object, i.e. 4D-CT.

# Table of Contents

<b>Acknowledgements</b>	<b>i</b>
<b>Nederlandse samenvatting –Summary in Dutch–</b>	<b>v</b>
<b>English summary</b>	<b>ix</b>
<b>List of Figures</b>	<b>xv</b>
<b>List of Tables</b>	<b>xix</b>
<b>List of Acronyms</b>	<b>xxi</b>
<b>List of Symbols</b>	<b>xxv</b>
<b>List of Publications</b>	<b>xxix</b>
<b>1 Introduction</b>	<b>1-1</b>
1.1 Main contributions . . . . .	1-3
1.2 Outline . . . . .	1-4
References . . . . .	1-6
<b>2 X-ray CT imaging &amp; simulation</b>	<b>2-1</b>
2.1 The X-ray CT imaging process . . . . .	2-2
2.1.1 Acquisition . . . . .	2-2
2.1.2 Reconstruction . . . . .	2-5
2.1.3 Visualisation & Analysis . . . . .	2-14
2.2 UGCT scanner systems . . . . .	2-16
2.2.1 HECTOR - The High energy scanner . . . . .	2-16
2.2.2 EMCT - A gantry based CT scanner . . . . .	2-17
2.2.3 Medusa - A multi detector system . . . . .	2-18
2.3 Simulating X-ray radiographs . . . . .	2-20
2.3.1 Radiography/CT simulation in literature . . . . .	2-20
2.3.2 First order modelling of the acquisition physics . . . . .	2-21
2.3.3 Secondary effects in radiographic image formation . . . . .	2-28
2.3.4 GPU acceleration . . . . .	2-34

2.4	Describing a cone beam CT geometry . . . . .	2-35
2.4.1	Global versus component reference frames . . . . .	2-35
2.4.2	Rigid motion - Rotation & Translation . . . . .	2-36
2.4.3	Affine motion - Scaling & Shear . . . . .	2-38
2.4.4	Defining CT trajectories . . . . .	2-40
2.5	An example: simulated CT scans of fruit . . . . .	2-40
2.5.1	A fruit phantom . . . . .	2-40
2.5.2	Testing the simulator . . . . .	2-41
2.6	Conclusion . . . . .	2-44
	References . . . . .	2-45
<b>3</b>	<b>CT Reconstruction algorithms</b>	<b>3-1</b>
3.1	Analytic reconstruction . . . . .	3-2
3.1.1	2D CT . . . . .	3-2
3.1.2	3D CT . . . . .	3-8
3.2	Iterative reconstruction . . . . .	3-13
3.2.1	CT as an algebraic system of equations . . . . .	3-13
3.2.2	Iterative inversion strategies . . . . .	3-14
3.2.3	A GPU accelerated SART implementation . . . . .	3-19
3.2.4	Handling large CT reconstruction volumes . . . . .	3-23
3.2.5	A Python-CUDA iterative CT reconstruction tool . . . . .	3-27
3.2.6	An example: iterative helical CT reconstruction . . . . .	3-29
3.3	An outlook to more advanced iterative algorithms . . . . .	3-34
3.4	Conclusion: analytic or iterative? . . . . .	3-36
	References . . . . .	3-37
<b>4</b>	<b>Simulation and mock up validation of an alternative in-line CT geometry</b>	<b>4-1</b>
4.1	Introduction: from 2D to 3D . . . . .	4-2
4.2	The conveyor belt CT acquisition . . . . .	4-4
4.2.1	Geometry . . . . .	4-4
4.2.2	Throughput . . . . .	4-9
4.2.3	Detector & X-ray tube settings . . . . .	4-11
4.3	A simulated & hardware mock up conveyor belt . . . . .	4-12
4.3.1	Real life & simulated acquisitions . . . . .	4-12
4.3.2	Comparing the simulations to the mock-up data . . . . .	4-15
4.4	Reconstruction quality & throughput . . . . .	4-18
4.4.1	Spectral resolution metrics . . . . .	4-18
4.4.2	Image quality as a function of throughput . . . . .	4-22
4.5	Towards a simulation based design . . . . .	4-24
4.6	Conclusion . . . . .	4-25
	References . . . . .	4-27

---

<b>5 Imaging dynamic processes with CT</b>	<b>5-1</b>
5.1 In-situ process control . . . . .	5-2
5.1.1 Temperature control . . . . .	5-3
5.1.2 Tensile & compression stage . . . . .	5-7
5.2 Tracking 3D deformation with CT . . . . .	5-8
5.2.1 Registration of 3D images . . . . .	5-8
5.2.2 Optical intensity flow . . . . .	5-12
5.2.3 Optical phase flow . . . . .	5-17
5.2.4 B-spline registration . . . . .	5-24
5.3 Motion corrected iterative reconstruction . . . . .	5-25
5.3.1 Recap - The SART algorithm . . . . .	5-25
5.3.2 Motion corrected SART . . . . .	5-27
5.4 Applications . . . . .	5-30
5.4.1 Registration in $\mu$ CT applications . . . . .	5-30
5.4.2 Rigid registration of a moving tree stem . . . . .	5-31
5.4.3 In-situ compression of aluminium foams . . . . .	5-33
5.4.4 In-situ leavening of dough . . . . .	5-44
5.5 An outlook to in-situ 3D characterisation of micro structured materials . . . . .	5-51
5.6 Conclusion . . . . .	5-54
References . . . . .	5-56
<b>6 Conclusion &amp; Outlook</b>	<b>6-1</b>
<b>A Machine specifications</b>	<b>A-1</b>
<b>B Registration parameters</b>	<b>B-1</b>



# List of Figures

1.1 Food and drink industry is still the largest manufacturing sector in the EU . . . . .	1-2
2.1 The essential components of an X-ray cone beam CT setup. . . . .	2-2
2.2 The principle of photon generation and detection in a lab-based X-ray CT setup. . . . .	2-4
2.3 Interaction mechanisms between atomic electrons and X-ray photons	2-5
2.4 Energy dependency of the mass attenuation coefficient per interaction mechanism. . . . .	2-6
2.5 Energy dependency of the detection efficiency and tube spectrum .	2-6
2.6 Reconstruction of the linear attenuation coefficient to a voxelised grid. . . . .	2-7
2.7 Geometrical unsharpness caused by a finite X-ray spot size . . . . .	2-8
2.8 Radon transform of a sphere. . . . .	2-10
2.9 Tuy-Smith condition in a fan beam CT geometry. . . . .	2-11
2.10 Cone beam artefacts in helical and circular cone beam CT. . . . .	2-11
2.11 Beam hardening shift, towards higher energies, of the X-ray spectrum. . . . .	2-12
2.12 Beam hardening causes cupping. . . . .	2-12
2.13 Motion blurring due to sample tilt. . . . .	2-13
2.14 3D rendering of an apple dataset and a frontal virtual cross section through it. . . . .	2-15
2.15 Analysis of the pore size distribution in pharmaceutical pill . . . . .	2-15
2.16 The Environmental CT scanner (ECMT). . . . .	2-17
2.17 The multi detector Medusa system. . . . .	2-19
2.18 Clever binning of an X-ray tube emission spectrum. . . . .	2-23
2.19 The concept of ray tracing in 2D. . . . .	2-25
2.20 Characterisation of a detector response as a function of X-ray energy	2-26
2.21 X-ray scattering in an apple, visualised through line profiles. . . . .	2-29
2.22 The principle of phase contrast. . . . .	2-31
2.23 Heeling in a directional X-ray source. . . . .	2-33
2.24 Theoretical peak performances of CPUs and GPUs . . . . .	2-35
2.25 Reference frames in a cone beam projective geometry. . . . .	2-36
2.26 Realigning a volume's affine reference frame with the global orthogonal frame. . . . .	2-40

2.27	Procedure for constructing a digital apple phantom . . . . .	2-41
2.28	Comparison between a real and simulated radiograph. . . . .	2-42
2.29	Comparison between SNR-profiles from simulated and real radio-graphs. . . . .	2-43
2.30	Comparison between the reconstruction of a simulated and a real CT dataset. . . . .	2-43
2.31	Simulated radiographs in arbitrary geometrical configurations. . .	2-44
3.1	Parallel beam geometry. . . . .	3-2
3.2	The Fourier slice theorem in two dimensions. . . . .	3-4
3.3	Ramp filter in the Fourier domain with adjustable modulation of high frequency components. . . . .	3-6
3.4	Fan beam geometry with a flat detector. . . . .	3-7
3.5	Circular cone beam geometry with a flat detector. . . . .	3-9
3.6	Tam-Danielsson window and PI-lines in helical cone beam CT. .	3-11
3.7	$\kappa$ -lines & planes on a flat detector in a helical CT geometry. . .	3-12
3.8	Basic concept of iterative CT reconstruction. . . . .	3-15
3.9	Kaczmarz algorithm in 2D with and without noise. . . . .	3-16
3.10	Effect of the projection access pattern on SART based CT reconstructions. . . . .	3-18
3.11	Joseph's method for an equidistant sample of $\mu$ -values on a ray. .	3-21
3.12	Calculating intersection weights through pixel based splatting on a cubic voxel. . . . .	3-21
3.13	Multi GPU implementation of an iterative CT reconstruction scheme.	3-24
3.14	A multi resolution framework to reconstruct large CT volumes on a single GPU. . . . .	3-25
3.15	Copy and compute queues to handle large volume iterative CT reconstructions through chunk swapping. . . . .	3-27
3.16	Speed of the chunk swapping technique as a function of the subset size. . . . .	3-28
3.17	Analytical and iterative reconstructions of a helical CT acquisition, imaging a set of tree drilling cores. . . . .	3-33
4.1	Several commercially available in-line CT solutions. . . . .	4-3
4.2	Schematic top view of the conveyor belt geometry. . . . .	4-5
4.3	Conditions leading to a complete conveyor belt trajectory. . . . .	4-5
4.4	Trajectories of the top and bottom ROI points throughout their conveyor belt movement. . . . .	4-7
4.5	Angular range covered by the points in a rectangular region containing the ROI. . . . .	4-8
4.6	SNR as a function of the X-ray tube's high voltage. . . . .	4-12
4.7	Conveyor belt add-on module installed on the Medusa system. .	4-14
4.8	Comparison between projections acquired with the mock-up conveyor belt and their simulated counterparts. . . . .	4-16

---

4.9	Comparison between simulated and mock-up reconstruction of the Elstar apple. . . . .	4-17
4.10	Radial power spectra for the noise only and data reconstructions. .	4-19
4.11	The Spectral Signal-to-Noise Ratio (SSNR) of a volume reconstructed with a varying number of projections. . . . .	4-20
4.12	Fourier shell correlation curves (FSC) of a volume reconstructed with a varying number of projections. . . . .	4-22
4.13	Detectable feature sizes as a function of the throughput. . . . .	4-24
5.1	UGCT's home made cooling stage. . . . .	5-4
5.2	Cooling stage electronics and controlinterface. . . . .	5-6
5.3	Examples of some applications with the cooling stage. . . . .	5-7
5.4	The Deben CT5000-TEC stage installed on the EMCT & an example of a load-displacement curve. . . . .	5-8
5.5	General formulation of deformation. . . . .	5-10
5.6	Image registration flow chart. . . . .	5-13
5.7	A 1D wavelet analysis with a cascading filter bank. . . . .	5-18
5.8	Aliasing region in the frequency responses of the db7 wavelet filters.	5-19
5.9	Artistic impression of a 2D-DWT high pass filter spectrum's amplitude. . . . .	5-20
5.10	A 1D dual-tree complex wavelet transform filter bank. . . . .	5-21
5.11	Idealised spectrum from one of the six bands of 2D DT-CWT. .	5-22
5.12	Real part of the six complex wavelet bands of DT-CWT. . . . .	5-22
5.13	1D cubic B-splines on an 11 point control grid. . . . .	5-25
5.14	Reconstructions of single rotation circular scan of a beech. . . . .	5-32
5.15	Motion corrected reconstructions of a multi rotation acquisition by using rigid registration before averaging. . . . .	5-33
5.16	An aluminium foam in its uncompressed state, and how it is placed on the bottom plate of the Deben compression stage. . . . .	5-34
5.17	Reconstruction of the first rotation in a dynamic acquisition of an in-situ aluminium foam compression. . . . .	5-35
5.18	Scoring curves for Demons, phase flow and B-spline registration for the dynamic aluminium foam acquisition. . . . .	5-37
5.19	Difference images, comparing the different registration approaches at varying degrees of displacement. . . . .	5-38
5.20	An inverted deformation field caused by a phase wrap in the fine scale levels of the phase flow registration pyramid. . . . .	5-40
5.21	Three cases showing the impact of a motion corrected reconstructions of compressed aluminium foam. . . . .	5-41
5.22	Motion corrected reconstruction of a single rotation acquisition by registering the short scan sub-acquisitions. . . . .	5-44
5.23	Multiple iterations in a motion corrected reconstruction of a single rotation acquisition. . . . .	5-45
5.24	Modification to the temperature control stage, which allows it to heat up a dough sample. . . . .	5-47

5.25	Reconstruction of the last rotation in the in-situ dough leavening acquisition. . . . .	5-48
5.26	Scoring curves for Demons, phase flow and B-spline registration for the leavening dough acquisition. . . . .	5-48
5.27	Difference images comparing the B-spline results to the original (unregistered) images at various dough leavening stages. . . . .	5-49
5.28	Three cases showing the impact of a motion corrected reconstructions of a leavening dough. . . . .	5-50
5.29	Motion corrected leavening dough reconstructions of cases two and three with an equal amount of volume updates. . . . .	5-50
5.30	von Mises stress distribution in a compressed aluminium foam. . .	5-52
5.31	Example of a tetrahedral finite element mesh of an aluminium foam.	5-54

# List of Tables

2.1	Overview of some existing X-ray radiography/CT simulation tools.	2-22
2.2	Settings for the base line scan, used to construct a digital fruit phantom. . . . .	2-42
3.1	Overview on a selected number of existing CT reconstruction tools.	3-30
3.2	Scan settings of the helical tree-ring analysis dataset. . . . .	3-32
4.1	Overview of the geometrical parameters of the conveyor belt mock-up. . . . .	4-14
4.2	Overview of the scans performed with the mock-up and the simulated scans. . . . .	4-15
5.2	Imaging parameters for circular cone beam scans of a beech tree, using one or several rotations. . . . .	5-32
5.3	Settings for the dynamic acquisition of an in-situ compression of aluminium foam. . . . .	5-36
5.4	Settings for three single rotation acquisitions of an in-situ compression of aluminium foam. . . . .	5-42
5.5	Settings for a dynamic acquisition with in-situ temperature control of a bread dough sample. . . . .	5-46
A.1	Workstation specifications. . . . .	A-1
B.1	Registration parameters for calculating the aluminium foam registration scores. . . . .	B-2
B.2	Registration parameters for calculating the leavening dough registration scores. . . . .	B-2



# List of Acronyms

## A

ADC	Analog to Digital Converter
ADU	Analog to Digital Unit
ART	Algebraic Reconstruction Technique
ASTRA	All Scales Tomographic Reconstruction Antwerp

## C

CCD	Charge Coupled Device
CG	Conjugate Gradient optimisation method
Cph CT	The Copenhagen CT reconstruction tool
CPU	Central Processing Unit
CS	Compressed/Compressive Sensing
( $\mu$ )CT	(micro) Computed Tomography
CUDA	(NVIDIA) Compute Unified Device Architecture

## D

DT-CWT	Dual Tree Complex Wavelet Transform
DVC	Digital Volume Correlation
DWT	Discrete Wavelet Transform

## E

EMCT	Environmental Computed Tomography system
ESRF	Electron Synchrotron Radiation Facility

## F

FBP	Filtered Back Projection
FDK	Feldkamp David Kress reconstruction algorithm
FEM	Finite Element Model/Modelling
FFD	Free Form Deformation
FOV	Field of View
FSC	Fourier Shell Correlation

<b>G</b>	GPU	Graphical Processing Unit
<b>H</b>	HECTOR	High Energy Computed Tomography scanner Optimised for Research
<b>I</b>	ILVO	Flemish Institute for Agriculture and Fisheries Research
	ITK	Imaging Toolkit
<b>J</b>	JIMA	Japanese Inspection Instruments Manufactures' Association pattern
	JIT	Just In Time compilation
<b>M</b>	MR(I)	Magnetic Resonance (Imaging)
	MTF	Modulation Transfer Function
	MVF	Motion Vector Field
<b>N</b>	NCC	Normalised Cross Correlation
<b>O</b>	ODD	Object Detector Distance
	OS	Ordered Subset reconstruction technique
<b>P</b>	PEEK	Poly Ether Ether Ketone
	PET	Positron Emission Tomography
	PID	Proportional Integral Differential process control
	PICCS	Prior Image Constrained Compressed Sensing
	PProGRess	Pore-scale Processes in Geomaterials Research group
	PV	Principal Value
	PyHST	The ESRF Python High Speed Tomography toolbox
<b>R</b>	RAM	Random Access Memory
	RAS	Random Access Scheme
	RMSE	Root Mean Square Error
	ROI	Region Of Interest
	RP	Radiation Physics research group

**S**

SART	Simultaneous Algebraic Reconstruction Technique
SBO	Strategisch Basisonderzoek (in Dutch)
(A)SGD	(Adaptive) Stochastic Gradient Descent
SPECT	Single-Photon Emission Computed Tomography
SIMD	Single Instruction Multiple Data
SIRT	Simultaneous Iterative Reconstruction Technique
SOD	Source Object Distance
(S)SNR	(Spectral) Signal to Noise Ratio
SSD	Sum of Square Differences
STP	Steepest Descent optimisation method

**T**

TEC	Thermo-Electric Cooling element
TDW	Tam Danielsson Window
TIE	Transport of Intensity Equation
TIGRE	Tomographic Iterative GPU-based Reconstruction
TV	Total Variation minimisation

**U**

UGCT	Ghent University Centre for X-ray Tomography
------	--

**V**

VOI	Volume Of Interest
VTK	Visualisation Toolkit

**W**

WDS	Weighted Distance Scheme
-----	--------------------------

**X**

XMI	X-ray Microspectroscopy and Imaging research group
-----	--



# List of Symbols

Consistent throughout this work, unless redefined locally

$j$	Pixel index
$\mu$	Linear attenuation coefficient
$I_0$	Incoming X-ray Flux
$p_j$	Ray sum measured by pixel $j$
SDD	Source Detector Distance
SOD	Source Object Distance
ODD	Object Detector Distance
$p_d$	Detector pixel pitch
$p_v$	Volume voxel pitch
$p_s$	X-ray spot size
$M$	Magnification factor
$\mathcal{R}$	Radon transform
$\vec{x}$	Point in space $[x, y, z]^T$
$Q_{eff}$	Detector quantum efficiency
$D_{eff}$	Effective energy deposit, fraction of the photon energy deposited in the detector
$P_t$	Tube power
$t_{exp}$	Detector exposure time
$\vec{O}_s$	Source point
$\vec{O}_d$	Detector centre
$\vec{O}_v$	Reconstruction volume centre
$\lambda$	Relaxation factor
$\mathcal{H}$	Hilbert transform in the frequency domain
$k_H$	Hilbert transform in the spatial domain
$N_p$	Number of projections
$\mathbf{A}$	Affine transform
$\mathbf{I}$	Identity transform

**Chapter 2****2.1**

$\vec{\theta}$	A Radon plane's unit normal
$r$	A Radon plane's distance to the origin
$\gamma$	Half cone beam opening angle

**2.3**

$E$	X-ray photon energy
$\Delta E_i$	Width of energy bin $i$
$N_{o,j,i}$	Number of photons emitted by the source in the direction of pixel $j$ in energy bin $i$
$T_{j,i}$	Fraction of the photons transmitted through the object in the direction of pixel $j$ in energy bin $i$
$N_{e^-}$	Number of electrons hitting the source target
$\vec{d}_j$	Unit normal from source point to centre of pixel $j$
$\kappa$	Gain factor for conversion between energy deposit and ADUs
$E_{d,j}$	Energy deposited in pixel $j$
$\mathcal{N}$	Normal distribution
$\Omega_j$	Solid angle of pixel $j$
$\delta$	Refractive index decrement
$\vec{n}(\vec{x}, \lambda)$	Complex refractive index
$\lambda$	Wavelength
$\vec{k}$	Wavevector
$T_\delta$	Ray sum of $\delta$
$T_\mu$	Ray sum of $\mu$
$\nabla_\perp$	Gradient measured in plane perpendicular to a ray
$l_c$	Lateral coherence length

**2.4**

$s, d, v$	Indices referring to the source, detector and volume respectively
$\alpha, \beta, \gamma$	Rotation angles about the x, y and z axes respectively
$X, Y, Z$	Global frame coordinates (capital)
$x, y, z$	Local frame coordinates (small caps) e.g. $x_{d,v}$ : detector coordinate in local volume frame
$R$	Rotation transform
$Sc$	Scaling transform
$Sh$	Shear transform
$S$	Combined scaling and shearing transform

---

## Chapter 3

### 3.1

$\theta$	Angular position
$r$	Coordinate parallel to the detector, local to the object
$r'$	Coordinate parallel to the detector, local to the detector
$F$	Fourier transform of $\mu$
$P_\theta$	Projected attenuation at position $\theta$
$\mathcal{G}$	Ram-Lak filter in the frequency domain
$M_t$	Off-centre magnification in fan beam, cone beam and helical
$z_p$	Helical pitch
$\psi$	$\kappa$ -plane coordinate

### 3.2

$T$	Linear projection operator
$\hat{p}_j$	Estimated ray sum collected by pixel $j$
$c_j$	Correction image to be back projected
$t_{jm}$	Intersection length between ray $j$ and voxel $m$
$\hat{t}_{jm}$	Back projection weight of pixel $j$ in voxel $m$
$T_j$	Total volume intersection length of ray $j$
$S$	Oversampling factor in Joseph's method
$\delta_{jj_p}$	Dirac delta

## Chapter 4

$H$	Horizontal travel conveyor distance
$L$	Detector length
$\Theta$	Rotation angle
$W$	Detector run out
$D_{ROI}$	ROI diameter
$D_s$	Sample diameter
$\alpha$	Half source opening angle
$I_{av}$	Intensity averaged along detector span
$SDD_{ref}$	Reference SDD
$I_{ref}$	Intensity measured at $SDD_{ref}$ in the detector centre
$N_s$	Number of samples imaged simultaneously
$T_{eff}$	Effective throughput
$M_s$	Spot demagnification
$M_o$	Object magnification (equal to $M$ )
$\sigma_p^2$	Estimated pixel variance
$n_o$	Number of open beam images per data frame
$\beta$	Number of photons per ADU
$F_d$	Fourier power spectrum of the data reconstruction
$F_n$	Fourier power spectrum of the noise reconstruction

## Chapter 5

$\mathcal{M}$	Coordinate mapping
$\vec{x}_{f/m}$	Fixed/moving coordinates
$\mu_{f/m}$	Attenuation distribution in the fixed/moving state
$\vec{u}$	Displacement vector
$\tau_{f/m}$	Fixed/moving time instance
$\tau_R$	Time of reconstructed state
$\mathcal{C}$	Cost function or metric for deformation estimation
$\vec{w}$	Motion model parameter vector
$\nabla_{\vec{x}}$	Gradient operator
$\theta_d$	Phase of the wavelet coefficients in subband $d$ of a DT-CWT
$\psi$	Wavelet function
$\phi$	Scaling function
$\mathcal{B}_{n_x,k}$	Basis spline of degree $k$ centred at $n_x$
$w^c$	Relative weight of a projections within a set
$w^a$	Aperture weighting of a rays within one projection
$\chi$	Score of a registration algorithm a.f.o. the deformation's progression
$n_v$	Number of voxels
$\epsilon_{ij}$	Strain tensor
$\sigma_{ij}$	Stress tensor
$E$	Young's elasticity modulus
$\nu$	Poisson's ratio

# List of Publications

## **Publications directly related to sections or chapters in this dissertation**

### **Sections 2.3 & 2.4**

Dhaene, Jelle, Elin Pauwels, Thomas De Schryver, Amélie De Muynck, Manuel Dierick, and Luc Van Hoorebeke. 2015. "A Realistic Projection Simulator for Laboratory Based X-ray micro-CT." Nuclear Instruments & Methods in Physics Research Section B-beam Interactions with Materials and Atoms 342:170-178.

### **Chapter 4**

De Schryver, Thomas, Jelle Dhaene, Manuel Dierick, Matthieu Boone, Eline Janssens, Jan Sijbers, Mattias van Dael, Pieter Verboven, Bart Nicolai, and Luc Van Hoorebeke. 2016. "In-line NDT with X-ray CT Combining Sample Rotation and Translation." NDT & E International 84:89-98.

### **Section 5.1.1**

De Schryver, Thomas, Marijn Boone, Tim De Kock, Barbara Duquenne, Maria Christaki, Bert Masschaele, Manuel Dierick, Matthieu Boone, and Luc Van Hoorebeke. 2016. "A Compact Low Cost Cooling Stage for Lab Based X-ray micro-CT Setups." In AIP Conference Proceedings, ed. MD DeJonge, DJ Paterson, and CG Ryan. Vol. 1696. Melville, NY, USA: American Institute of Physics (AIP).

### **Section 5.4.3**

De Schryver, Thomas, Jeroen Van Stappen, Marijn Boone, Matthieu Boone, Manuel Dierick, Veerle, Cnudde, and Luc Van Hoorebeke. 2017. "4D visualisation of in-situ aluminium foam compression with lab-based motion compensated X-ray micro-CT." In iCT2017 Conference Proceedings. Leuven, Belgium.

### **Others**

1. Wanzhao, Li, Jan Van den Bulcke, Thomas De Schryver, Joris Van Acker. 2016. "Investigating water transport in MDF and OSB using a gantry-based X-ray CT scanning system", Wood Science & Technology, 50(6):1197-1211

- 
2. Bultreys, Tom, Marijn Boone, Matthieu Boone, Thomas De Schryver, Bert Masschaele, Luc Van Hoorebeke, and Veerle Cnudde. 2016. "Fast Laboratory-based Micro-Computed Tomography for Pore-scale Research: Illustrative Experiments and Perspectives on the Future." *Advances in Water Resources*. 95:341-351
  3. Oliveira, Vanda, Jan Van den Bulcke, Joris Van Acker, Thomas De Schryver, and Helena Pereira. 2016. "Cork Structural Discontinuities Studied with X-ray Micromicrography." *Holzforschung*. 70(1):87-94
  4. Duquenne, Barbara, Bjorn Vergauwen, Claude Capdepon, Marijn A. Boone, Thomas De Schryver, Luc Van Hoorebeke, Stephanie Van Weyenberg, Paul Stevens, and Jan De Block. 2016. "Stabilising frozen dairy mousses by low molecular weight gelatin peptides." *Food Hydrocolloids*, 60:317-323
  5. De Kock, Tim, Marijn Boone, Thomas De Schryver, Jeroen Van Stappen, Hannelore Derluyn, Bert Masschaele, Geert De Schutter, and Veerle Cnudde. 2015. "A Pore-scale Study of Fracture Dynamics in Rock Using X-ray micro-CT Under Ambient Freeze-thaw Cycling." *Environmental Science & Technology* 49(5):2867-2874.
  6. Peeters, Geert, Charlotte Debbaut, Pieter Cornillie, Thomas De Schryver, Diethard Monbaliu, Wim Laleman, and Patrick Segers. 2015. "A Multilevel Modeling Framework to Study Hepatic Perfusion Characteristics in Case of Liver Cirrhosis." *Journal of Biomechanical Engineering-transactions of the ASME* 137 (5).
  7. Bultreys, Tom, Marijn Boone, Matthieu Boone, Thomas De Schryver, Bert Masschaele, Denis Van Loo, Luc Van Hoorebeke, and Veerle Cnudde. 2015. "Real-time Visualization of Haines Jumps in Sandstone with Laboratory-based Microcomputed Tomography." *Water Resources Research* 51(10):8668-8676.
  8. Herremans, Els, Pieter Verboven, Maarten LATM Hertog, Dennis Cantre, Mattias van Dael, Thomas De Schryver, Luc Van Hoorebeke, and Bart M Nicolaï. 2015. "Spatial Development of Transport Structures in Apple (*Malus x Domestica* Borkh.) Fruit." *Frontiers in Plant Science* 6.
  9. De Boever, Wesley, Ana Diaz, Hannelore Derluyn, Tim De Kock, Jeroen Van Stappen, Jan Dewanckele, Tom Bultreys, Matthieu Boone, Thomas De Schryver, Eirik TB Skjonsfjell , Mirko Holler, Dag W Breiby, and Veerle Cnudde. 2015. "Characterization of Composition and Structure of Clay Minerals in Sandstone with Ptychographic X-ray Nanotomography." *Applied Clay Science* 118:258-264.
  10. Billiet, Thomas, Elien Gevaert, Thomas De Schryver, Maria Cornelissen, and Peter Dubrule. 2014. "The 3D Printing of Gelatin Methacrylamide Cell-laden Tissue-engineered Constructs with High Cell Viability." *Biomaterials* 35:49-62.





# 1

## Introduction

Ever since Röntgen discovered X-rays in 1895, they have been used extensively to image the interior of objects without physically cutting them open, i.e. in a non-destructive way. Particularly in medicine, long before the advent of ultrasound and magnetic resonance (MR) imaging, X-ray radiographs have been used to image the interior of the human body to non-invasively infer a diagnosis for internal afflictions. Indeed, 2D radiography could be seen as the first real medical imaging technique but it was not until Hounsfield invented his EMI-scanner in 1972 that a 3D image of the human body could be visualised through the process of '*computed tomography*' (CT). While X-ray CT is commonly placed in a medical context, it is widely applied in a great variety of research branches and also for non-destructive testing and evaluation in industry. The challenges posed by this diversification have led to a continuous development and improvement of the X-ray CT technique at an ever increasing pace, in both laboratory and synchrotron facilities, with a strong focus on improving the spatial resolution. Nowadays, state of the art lab-based facilities are able to produce CT images at the micron scale, i.e. perform a micro-CT scan ( $\mu$ CT), on a routine basis in a matter of minutes, or even at the sub-micron scale (nano-CT) in the moderate time of approximately one hour.

One of the facilities, focussing on laboratory based X-ray  $\mu$ CT imaging, is the '*Ghent University Centre for X-ray Tomography (UGCT)*'. UGCT was founded in 2006 as a collaborative effort between the Radiation Physics (RP) group from

the Department of Physics and Astronomy, and the SGIG<sup>1</sup> group at the Department of Geology. Later in 2009, the UGCT was joined by the laboratory for Wood Technology (Woodlab) at the Department of Forest and Water Management. The work presented here is performed at the RP group, whose goal is to provide the best  $\mu$ CT images for any application, made possible through its expertise on every step of the imaging work flow and its underlying physics, from scanner design and acquisition protocols to CT reconstruction and image analysis.

As an expert in and advocate of X-ray CT, UGCT had the opportunity to participate in the SBO TomFood project, collaborating with the KULeuven based MeBios and Lab4Food groups, VisionLab from the University of Antwerp and the Flemish Institute for Agricultural and Fisheries research (ILVO). The TomFood project recognised the value and novelty of X-ray CT as an inspection and engineering tool in the food industry, a sector which up to this day is still the largest manufacturing sector in the EU, see Figure 1.1. A strong focus was put on the characterisation of the micro-structural properties of food, how they are influenced by production and storage processes, and how they impact quality, in particular for fruit and vegetables, and dairy and farinaceous products. In fact, quality improvement and control are the pillars in TomFood, which also motivate the application of X-ray CT to an in-line production setting as one of the most important milestones of the project.

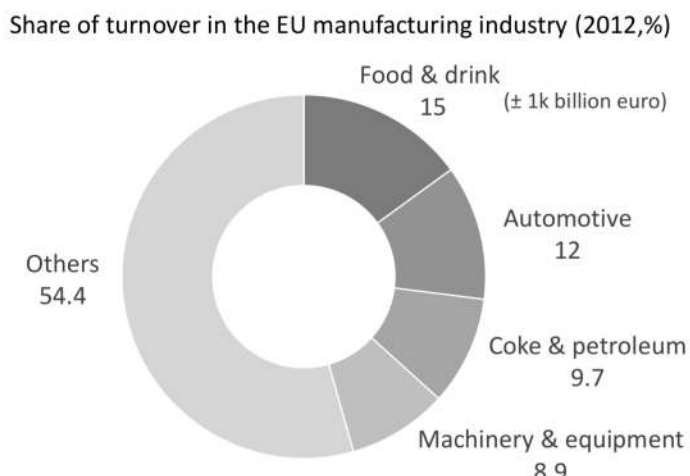


*Figure 1.1: According to the annual report with ‘Data & Trends of the European Food and Drink Industry’, the food and drink industry is still the largest manufacturing sector in the EU [1].*

A significant portion of the work presented here has led to a better understanding on how feasible in-line quality inspection with X-ray CT, so-called ‘*in-line*

<sup>1</sup>nowadays the Pore-scale Processes in Geomaterials Research group (PProGRess)

*CT*', really is within the conditions put forward by a production setting. In particular, the imaging process itself should not constitute a bottle neck and should be able to keep up with the nominal throughput in a production chain. Therefore, the imaging process needs to be fast, which leads to a degradation of image quality. In other words, investigating the feasibility of in-line CT is essentially equivalent to balancing out the trade-off between image quality and scanning speed.

A similar trade-off occurs when X-ray CT is used to image an object which is undergoing a dynamic process, causing its absorption characteristics, normally assumed to be fixed, to change during the course of an acquisition. Fortunately, X-ray  $\mu$ CT has matured to the point where it is now possible to image dynamic processes within micro-structures in 3D with a sufficient temporal resolution to follow the micro-structural changes caused by these processes through time, commonly referred to as '*4D-CT*'.

The premise of this work is **fast CT imaging using non-standard geometries and protocols**, with the goal of

- bringing X-ray CT to an in-line setting as a non-destructive quality inspection tool, i.e. in-line CT, and
- improving the visualisation of dynamic processes, specifically pertaining to local and non-rigid structural changes of an imaged object, i.e. 4D-CT.

The challenges presented by in-line and 4D-CT are tackled by exploiting the tight synergy between the acquisition level, where alternative CT geometries and protocols are explored, and the reconstruction level, where information on a sample's deformation will be inferred through local, non-rigid registration to be incorporated in the CT reconstruction algorithm. The applications presented here are non-standard in the sense that they would be considered difficult if not impossible to be properly imaged in a normal circular CT geometry.

## 1.1 Main contributions

The main contributions of the author to the field of X-ray CT in general, and in-line and 4D-CT in particular, are:

- a GPU<sup>2</sup>-accelerated implementation of a first order X-ray attenuation model, enabling the fast simulation of X-ray radiographs,

---

<sup>2</sup>Graphical Processing Unit

- a flexible and intuitive parametrisation for the geometrical configuration of X-ray CT scanner components, allowing X-ray CT acquisitions to be simulated on arbitrary, non-standard trajectories.
- the development of a GPU reconstruction tool, based on a combination of Python and CUDA, which can handle the reconstruction of CT data acquired in the aforementioned arbitrary geometries, with SIRT<sup>3</sup>, SART<sup>4</sup> and more generally OS<sup>5</sup>.
- a strategy to reconstruct large CT volumes on a GPU, by asynchronously balancing out copying and computation GPU work loads.
- a framework to assess the quality of CT reconstructions by using Fourier based resolution metrics, such as the SSNR<sup>6</sup> and FSC<sup>7</sup>.
- an implementation of this framework to an in-line CT conveyor belt geometry, that combines a sample rotation and a lateral translation, in both a simulated and hardware mock-up form.
- establishing the feasibility of in-line CT with the proposed conveyor belt geometry.
- the development of an in-situ temperature control stage.
- a thorough case study evaluation of several local, non-rigid registration algorithms, namely the Demons, B-spline and optical phase flow approaches.
- a simple GPU accelerated motion corrected version of the SART.
- new CT protocols, that can tolerate a significant degree of sample motion, given the aforementioned motion correction approach.

## 1.2 Outline

Chapter 2 introduces the basics of X-ray CT with a particular focus on the acquisition process. For this process, a first order model, including the polychromatic and noisy nature of X-ray radiography, is presented, working towards its implementation on a GPU architecture. The resulting GPU-accelerated ‘*radiography simulator*’ is calibrated to accurately reflect the properties of the X-ray tubes and detectors on the UGCT scanner systems, several of which are discussed in this

---

<sup>3</sup>Simultaneous Iterative Reconstruction Technique

<sup>4</sup>Simultaneous Algebraic Reconstruction Technique

<sup>5</sup>Ordered Subsets

<sup>6</sup>Spectral Signal to Noise Ratio

<sup>7</sup>Fourier Shell Correlation

chapter. In a next step, the simulator is supplemented with a flexible and intuitive description of the geometrical configuration of X-ray CT scanner components. Through this geometrical description, the simulator can produce X-ray CT data on arbitrary, non-standard trajectories, such as the in-line CT geometry presented throughout chapter 4.

Chapter 3 gives an overview on some common CT reconstruction algorithms by classifying them under the analytic and iterative categories. For the latter type, a reconstruction tool was implemented on the GPU by combining Python code with CUDA C. Apart from the fact that this tool can handle the reconstruction of CT data acquired in arbitrary geometries, chapter 3 also explains how it is able to accommodate very large reconstruction volumes by balancing out GPU copying and calculation operations. The usefulness of the resulting '*chunk swapping*' approach is also illustrated through the challenging example of iterative reconstruction on a helical dataset. Chapter 3 closes by underlining the flexibility of iterative CT reconstruction towards adopting advanced forward projection models, and a priori information on the imaged object. A short outlook and overview explains how these advanced models and the a priori information can be placed in a more general framework of regularised optimisation.

In chapter 4, the radiography simulator and the Python-CUDA reconstruction tool are combined in the study of an in-line X-ray CT inspection device, the so-called '*conveyor belt*' CT device. Through a theoretical analysis it can be shown that a sample's trajectory in this device, which combines a translation with a partial rotation of the sample about an axis perpendicular to the translation axis, is able to produce acquisitions, that lead to exact CT reconstructions. Also in this chapter, the FSC and SSNR resolution metrics are introduced as a way to evaluate a CT image's quality, specifically as a function of the CT acquisition and conveyor belt design parameters. As a result, the scan duration and the conveyor belt device dimensions can be tuned towards an optimised trade-off between inspection throughput and image quality. This trade-off was investigated on both simulated and real life data, coming from a hardware mock-up, that was realised as an extension to one of UGCT's scanner systems.

The fifth and final chapter discusses how X-ray CT can be used to image dynamic processes, which change a sample's structure or more generally its attenuation properties during the course of an acquisition. To explore and improve this 4D-CT imaging of dynamic processes, the UGCT acquired and developed several devices to control or initiate these processes. Chapter 5 discusses a uniaxial tensile-compression stage and a temperature control stage, which are used for the in-situ compression of an aluminium foam and for heating a leavening bread dough

sample in the applications section. In both of these cases, the dynamics of the processes lead to an excessive deformation of the sample during the acquisition, which results in motion blurring artefacts at the reconstruction level. In order to track this deformation, which is local and non-rigid in nature, three registration approaches, namely the Demons, B-spline and optical phase flow methods, are discussed and evaluated on the dough and aluminium foam acquisitions. Most importantly, this chapter explains how the deformation fields, inferred through registration, can be incorporated in a SART algorithm to produce motion corrected reconstructions. Finally, the chapter closes with an outlook to how X-ray CT imaging and a thorough modelling of the imaged dynamic process, can benefit from each other, with the final goal of elevating the X-ray CT technique from a way to image a object's attenuation to a 3D in-situ material characterisation.

## References

- [1] Food & Drink Europe. *DATA & TRENDS EUROPEAN FOOD AND DRINK INDUSTRY*. <http://www.fooddrinkeurope.eu/>.

# 2

## X-ray CT imaging & simulation

This chapter describes how X-rays and their interaction with matter can be used to image the interior of an object, going from a single 2D radiographic projection to a full 3D tomographic, digital representation of the object, by following the three step process of acquisition, reconstruction and visualisation (and/or analysis). After a short look into several of UGCT's CT systems, the remainder of this chapter focusses on the acquisition and specifically those physical aspects of the imaging process most relevant to the realistic and efficient simulation of X-ray radiographs. With a view to in-line CT as a cornerstone to this work, a realistic radiography simulator, which

- models the X-ray physics in a fast and accurate (to first order) way,
- allows for an intuitive and flexible description of the CT geometry, and
- runs on a Graphical Processing Unit (GPU),

was developed to both optimise existing CT setups and protocols, and explore how novel CT geometries and the underlying acquisition physics impact the image quality, in a cost effective way. Indeed, building a hardware setup versatile enough to mimic the quasi infinite combinations of CT geometries and tube-detector assemblies is not tractable.

## 2.1 The X-ray CT imaging process

### 2.1.1 Acquisition

#### Cone beam CT

The essential components of a CT setup are schematically depicted in Figure 2.1(a), next to the real life high energy CT system, ‘HECTOR’, built at the UGCT (Figure 2.1(b)). From a small focal spot, micron sized in the case of  $\mu$ CT, an X-ray tube emits a broadband spectrum of X-rays in all directions. Most of these X-rays are stopped in a collimator, giving the beam a conical shape directed towards the flat panel detector. This type of CT setup is thus referred to as a ‘*cone beam CT*’ setup, although generally, the cone illuminates the entire detector surface, such that the convex hull of the relevant X-rays, i.e. the ones that strike the detector, is actually pyramidal in shape. Only the X-rays emitted within the solid angle spanned by this cone are relevant to the formation of a radiograph, which essentially registers the shadow cast by an object placed within the X-ray cone.

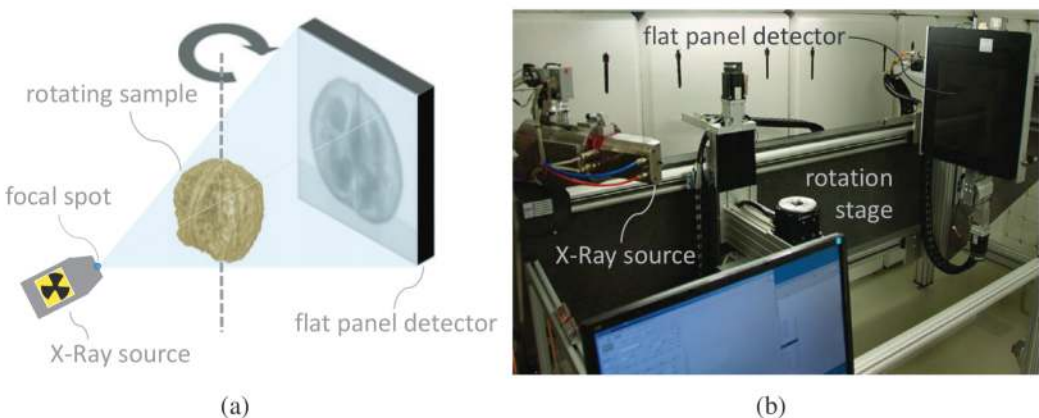


*Figure 2.1: The essential components of an X-ray cone beam CT setup in the schematic (a) can also be recognised in a real setup (b). Here UGCT’s High Energy CT scanner Optimised for Research (HECTOR) is shown [1].*

A single point of view radiograph represents a 2D projection of the object, measuring how strongly this object attenuates the X-rays passing through it. On such a 2D projection all of the object’s internal features are superimposed, making it impossible to unambiguously separate one feature from the other. To compute a digital slice, i.e. a tomogram, through an object and locate its internal features in 3D, a series of radiographs, taken from different directions, needs to be measured through a CT acquisition. In other words, a CT acquisition is formed by a series of radiographs, taken from an object performing a relative motion with respect to the source-detector assembly. In most cases this relative motion is circular, i.e. either the object (cfr. figure 2.1) or the source-detector assembly (the gantry) rotates around a fixed axis near the object’s centre, leading to a so called

circular cone beam CT acquisition. The circular motion is often combined with a (simultaneous) translation, resulting in ‘circle + line’ trajectories and helical CT, a common protocol for medical CT scanners. These compound trajectories are primarily conceived to optimise the sampling directions towards an exact reconstruction of the object (as explained in section 2.1.2), but can also be used to tailor the setup towards an implementation in an in-line conveyor belt environment (see chapter 4).

### From electrons to X-rays and back again

A detailed account on the working principles and technical aspects of the different types of lab based X-ray tubes and flat panel detectors can be found in [2, 3]. In short, X-ray tubes accelerate electrons by means of a high voltage a high voltage between a cathode filament and an anode target in a vacuum cavity. As these electrons rapidly decelerate during their collision with the target material, they emit bremsstrahlung X-ray photons and occasionally knock out electrons from the anode material, followed by the emission of characteristic X-rays as the excited anode atoms relax to their ground state. After passing through the imaged object and hitting the detector, the X-ray photons are essentially converted back to electrons. More precisely, electron-hole pairs are formed, either directly, e.g. in a CdTe based photodiode, or indirectly through an intermediate conversion of the X-ray photons to visible light photons in a scintillation material (e.g. Gadox or CsI), which can subsequently be converted to an electrical signal by conventional (amorphous) silicon photodiodes or CCD sensor. A pixelated flat panel detector is formed when these sensors are configured into a 2D array, making it possible to acquire a digital radiograph.

### Lambert-Beer law

The attenuation measured by a radiograph can physically be described through the Lambert-Beer law, which in its monochromatic form, i.e. for a single X-ray photon energy, is given by

$$I_d = I_0 e^{-\mu d}. \quad (2.1)$$

This law states that an incoming X-ray flux ( $I_0$ ) exponentially decays to a transmitted flux ( $I_d$ ) as it propagates through a material, in this case over a distance  $d$ . The exponential factor  $\mu$ , known as the linear attenuation coefficient, is proportional to the probability for an X-ray photon to interact with the propagation medium, commonly expressed per unit of length ( $\text{cm}^{-1}$ ). Since electrons are involved in all of the relevant interactions which stop X-ray photons from penetrating a material (see Figure 2.3), the linear attenuation coefficient indirectly relates to the electron density, which in turn depends on the physical material density and its chemical

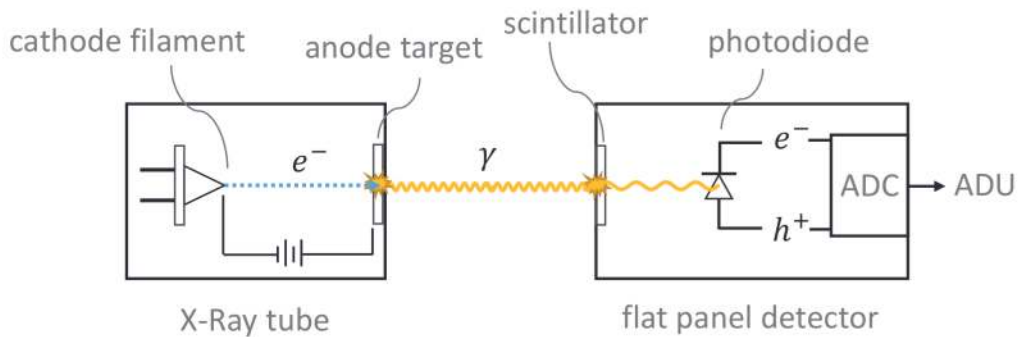


*Figure 2.2: The principle of photon generation and detection in a lab-based X-ray CT setup. An X-ray tube accelerates electrons towards a collision with a target material, where they produce a spectrum of bremsstrahlung and characteristic X-ray photons. These photons are converted to an analog electrical signal by a (flat panel) detector containing an array of photodiodes or a CCD sensor, either directly or through an intermediate scintillation. Finally, the analog signal is converted to a digital one by the analog-to-digital converter (ADC).*

composition. As a result the linear attenuation coefficient may vary significantly for a given material at different densities, unless it is normalised by the material's density to give the mass attenuation coefficient ( $\text{cm}^2/\text{g}$ )

$$\frac{\mu}{\rho} = \frac{\tau}{\rho} + \frac{\sigma}{\rho} + \frac{\sigma_r}{\rho} + \frac{\pi}{\rho} \quad (2.2)$$

This expression for the mass attenuation coefficient also reflects the additive contribution of the individual interaction mechanisms, listed in order of importance with respect to the X-ray energy range relevant to lab-based CT:

- the photoelectric effect ( $\tau$ ),
- Compton scattering ( $\sigma$ ),
- Rayleigh scattering ( $\sigma_r$ ), and
- pair production ( $\pi$ ),

where pair production is generally negligible in the context of lab-based X-ray  $\mu$ CT. It is important to recognise that all of these interactions strongly depend on the energy of the incident photons (see Figure 2.4), which leads to a more general polychromatic form of the Lambert-Beer law

$$I_j = \int_0^{E_{\max}} I_0(E) Q_{\text{eff}}(E) \exp \left[ - \int_{t_0}^{t_j} \mu(\vec{l}(t), E) dt \right] dE \quad (2.3)$$

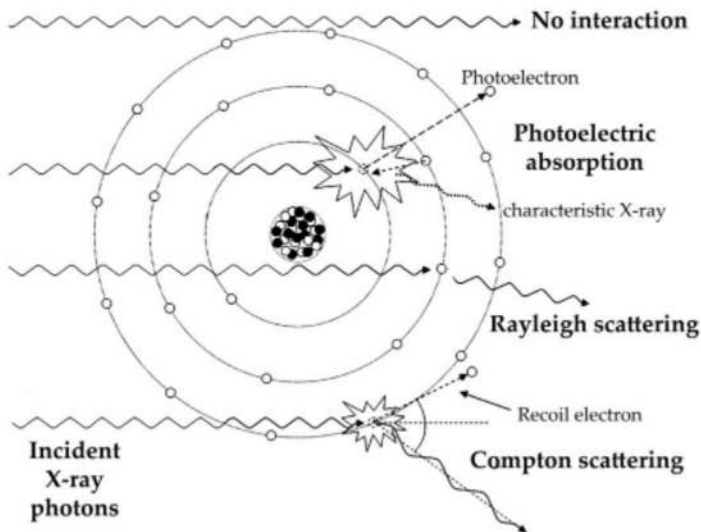


Figure 2.3: Schematic representation of the interaction mechanisms between atomic electrons and an incident X-ray photon [4].

Next to the local fluctuations of the attenuation coefficient along the integration path  $l$ , in most cases a straight line, equation (2.3) also incorporates the polychromatic nature of the imaging process through an energy dependency of  $\mu$ , the incident photon flux, which reflects the source's photon emission spectrum (see equation 2.10), and the detection efficiency ( $Q_{\text{eff}}$ ). Indeed, an ideal X-ray detector which linearly converts all of the energy carried by the X-ray photons crossing the detection plane to a usable signal does not exist, and also in a lab-based CT setup the X-ray sources produce incident spectra ( $I_0(E)$ ) with a large bandwidth (see Figure 2.5), up to a maximal energy ( $E_{\max}$ ) determined by its high voltage. Apart from the schematic overview in Figure 2.3, it is not the goal here to provide a detailed description of the interaction physics, for which the reader is referred to [4–6].

## 2.1.2 Reconstruction

The computational process which converts a series of 2D radiographs to a 3D digital distribution of an object's linear attenuation coefficient, is called a reconstruction. This section introduces the Tuy-Smith condition as a minimal mathematical requirement for an accurate reconstruction, and describes how the Lambert-Beer law links the radiographic measurements to the linear attenuation. The algorithms facilitating these reconstructions, traditionally classified as analytical or iterative, are described in a separate chapter (see chapter 3).

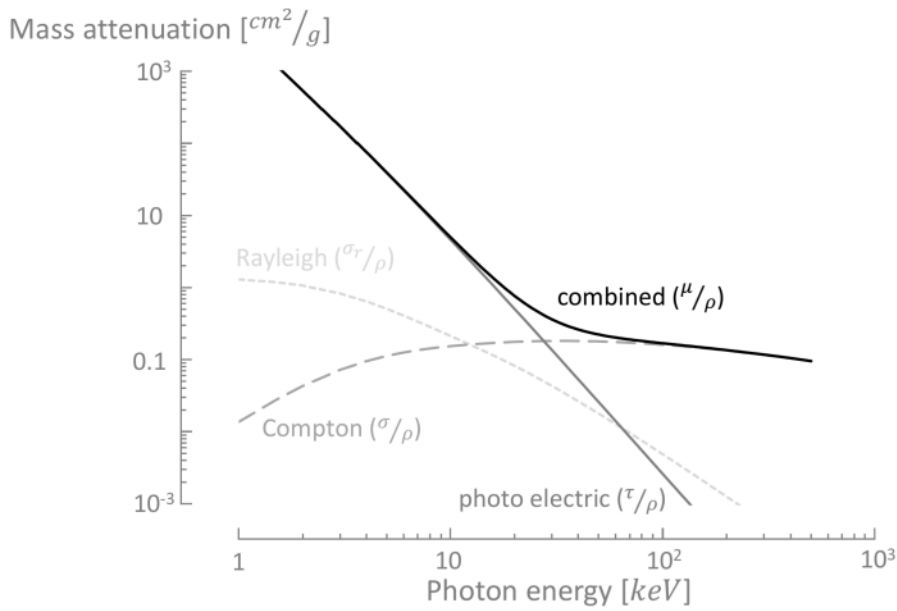


Figure 2.4: Energy dependency of the mass attenuation coefficient for soft tissue according to [7], decomposed according to the different electron-photon interaction mechanisms.

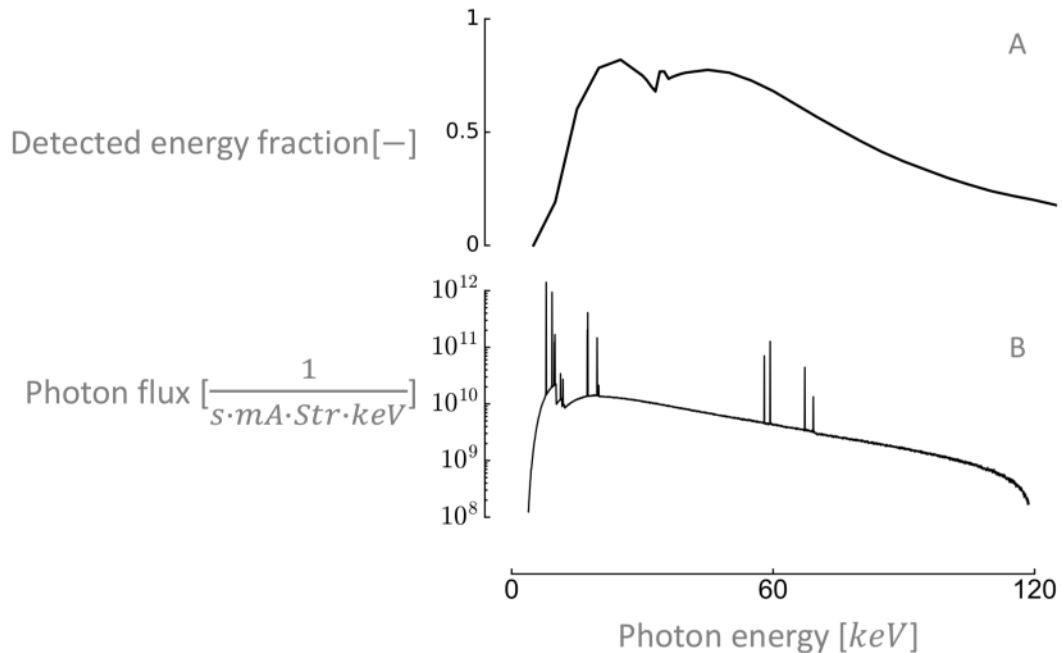
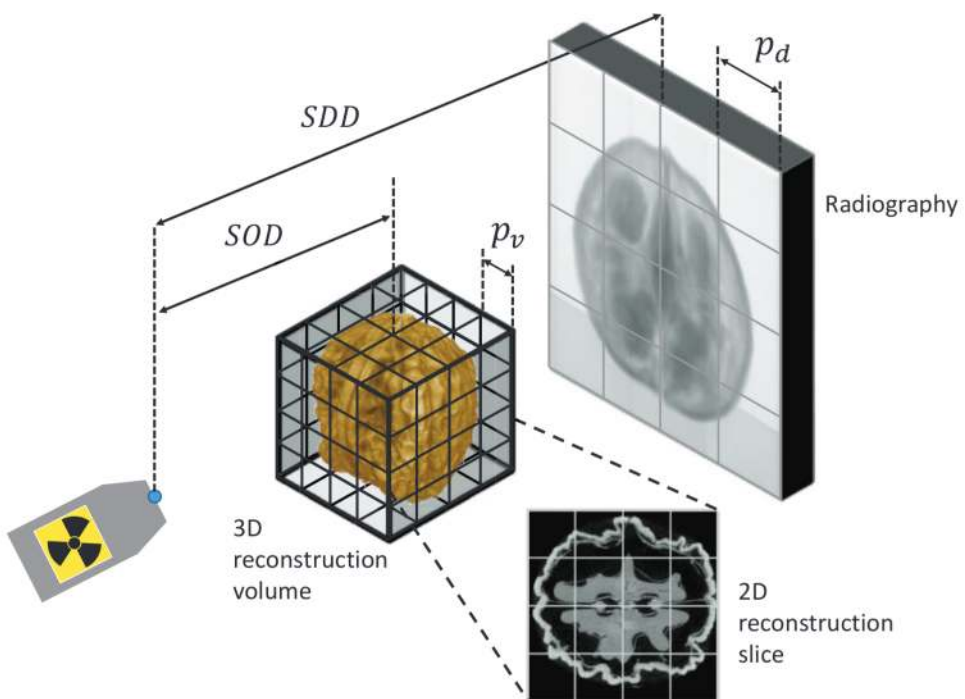


Figure 2.5: Lab-based CT imaging is polychromatic in nature as can be seen on these graphs for (A) the photon energy impinging on a flat panel detector, which will eventually be detected, multiplied with the detector's quantum efficiency, and (B) a typical spectrum produced by a lab-based X-ray tube.

## From pixels to voxels

In order to obtain a digital representation of the 3D attenuation distribution, it is generally assumed that the object is contained within a rectangular prism, which in turn can be subdivided into a regularly stacked grid of smaller rectangular prisms, called voxels (see Figure 2.6). Most of the time, these voxels are considered to be cubes with a side length  $p_v$ , which in principle can be chosen freely. Though a sensible choice, is to match the voxel's projection onto the detector plane with respect to the X-ray source point, to the detector's pixel size  $p_d$  following a geometrical magnification ( $M$ )

$$p_d = p_v \frac{SDD}{SOD} = p_v M \quad (2.4)$$



*Figure 2.6: The radiographs are used to reconstruct the linear attenuation coefficient into a digitised grid of voxels, with pitch  $p_v$  following a geometrical demagnification of the detector pixel size  $p_d$ . (SDD : Source Detector Distance, SOD: Source Object Distance)*

where SDD is the Source Detector Distance, and SOD the Source Object Distance. For typical magnification factors ranging between 10 and 100, a detector pixel size of  $100 \mu\text{m}$  leads to a voxel size in the micron range. As the voxel size shrinks down to the range of the X-ray tube's spot size  $p_s$ , it becomes important to consider the fact that  $p_s$  is indeed finite, and can thus influence the spatial resolving power. By taking into account a finite  $p_s$ , a better estimate for the voxel size can be derived, also on a geometrical basis,

$$p_v = \frac{p_d}{M} + (1 - \frac{1}{M})p_s. \quad (2.5)$$

As illustrated in Figure 2.7, the finite spot size causes a geometrical unsharpness around the edges of a feature projected in a radiograph. Furthermore, the spot size forms an intrinsic limit to the spatial resolution of lab-based cone beam CT, specifically at high magnifications, according to equation (2.5). The spot size depends on the type of X-ray tube, going from  $\pm 5 \mu\text{m}$  in directional tubes down to  $\pm 400 \text{ nm}$  in some transmission tubes [1, 8], and is intrinsically determined by how good the electrons can be focussed onto the target, and through which extent these electrons get scattered in the lateral direction. In practice however, the spot size is limited by the minimal area required for an adequate dissipation of the heat deposited in the target by the electrons hitting it. The smallest X-ray spots can thus only be attained for low X-ray fluxes, resulting in longer measuring times to obtain comparable image statistics.

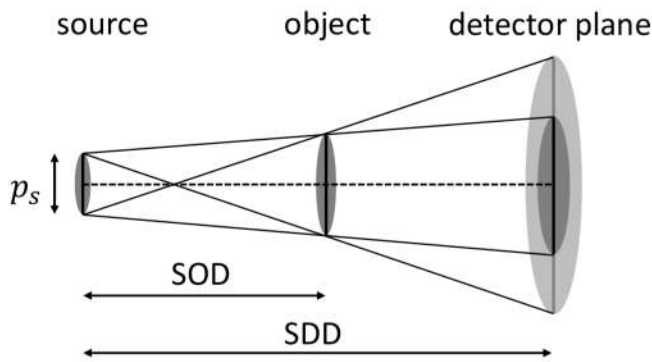


Figure 2.7: Geometrical unsharpness caused by a finite X-ray spot size  $p_s$

As a final note on the voxel size, it is important to note that (2.5) is only a geometrical estimate for an X-ray CT system's spatial resolving power and is often (wrongly) reported as a measure for resolution. First of all, (2.5) does not take into account the detector's point spread function, whose width is generally about 1.8 times the size of  $p_d$ , but for each individual detector is best determined by measuring its Modulation Transfer Function (MTF). Furthermore, resolution is actually measured in line pairs per mm, such that  $1/(2 p_v)$  might be considered a good estimate for it. In section 4.4.1, some alternative methods to calculate a fair estimate for the resolving power and resolution will be introduced.

### Radiographs measure line integrals

A standard reconstruction is based upon the inversion of the Lambert-Beer law, which in its monochromatic, ideal form can be rewritten as follows (cfr. equa-

tion (2.3))

$$p_j = -\ln \left[ \frac{I_j}{I_{0,j}} \right] = \int_{s_{0,j}}^{s_{p,j}} \mu(\mathbf{l}_j(s)) ds \quad (2.6)$$

representing the line integral of the linear attenuation coefficient along the ray path that connects the X-ray source point ( $\vec{x}_{s,j} = \mathbf{l}_j(s_{0,j})$ ) to the centre of detector pixel  $j$  ( $\vec{x}_j = \mathbf{l}_j(s_{p,j})$ ) for a particular orientation of the object. Here, the index  $j$  runs over all of the pixels in the complete series of radiographs each representing an individual measurement. Most importantly, equation 2.6 shows that the transmission values measured by the radiographs, or to be precise their negative logarithm, can be accurately modelled by line integrals through an object's linear attenuation function.

### The Tuy-Smith condition

Formulated in a more general way, a reconstruction is mathematically equivalent to inferring a spatially distributed quantity  $\mu(\vec{x})$  (where  $\vec{x} = [x, y, z]^T$ ) from a series of line integrals taken across this distribution. This, in turn, is very similar to inverting the Radon transform ( $\mathcal{R}$ ) of  $\mu(\vec{x})$ , defined by

$$\mathcal{R}\{\mu\}(\vec{\theta}, r) = \int \mu(\vec{x}) \delta(\vec{x} \cdot \vec{\theta} - r) d\vec{x} \quad (2.7)$$

which integrates  $\mu(\vec{x})$  across the plane with unit normal  $\vec{\theta}$  and distance  $r$  from the origin [9], see also Figure 2.8. An important prerequisite to the exact inversion of this transform is that for all of the  $(\vec{\theta}, r)$ -pairs a unique Radon value has to be defined. For a CT acquisition, this condition translates to the *Tuy-Smith condition* [10], which states that an object's attenuation function ( $\mu(\vec{x})$ ) can be reconstructed exactly only when each plane intersecting the object's support<sup>1</sup> contains at least one X-ray source point, or in other words each of these planes should intersect the source trajectory at least once, and of course be measured by the detector.

It is immediately clear that a circular source trajectory does not conform to the Tuy-Smith condition, as the attenuation value for any point situated in a plane parallel to the one containing the source trajectory, and thus not intersecting this trajectory, will according to the Tuy-Smith condition not be reconstructed exactly. Although adequate reconstructions can be obtained from a circular cone beam CT acquisition, the inaccuracies in the attenuation values caused by the violation of the Tuy-Smith condition, known as cone beam artefacts, do increase further away from the central plane containing the source trajectory. This central plane, where the cone is reduced to a fan, does not exhibit the cone beam artefact. With a fan

---

<sup>1</sup>The region where its attenuation coefficient is non-zero.

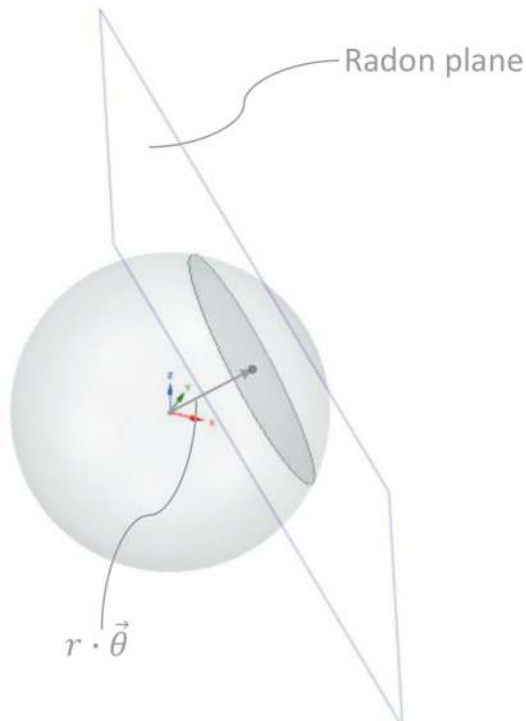


Figure 2.8: Radon transform of a sphere. In the Radon space of all  $(\vec{\theta}, r)$ -pairs, the plane integrals are stored at the points  $r \cdot \vec{\theta}$ .

beam CT acquisition the central plane can even be reconstructed exactly if the circular trajectory covers at least an angular range of

$$180^\circ + 2\gamma \quad (2.8)$$

where  $\gamma$  is half the opening angle of the X-ray fan spanning the object's circumference (see Figure 2.9). For off-centre planes, the cone beam artefact can be eliminated completely by considering other trajectories, as in helical and ‘circle+line’ CT (see Figure 2.10).

### Artefacts: Beam hardening & motion blurring

The Tuy-Smith condition is a geometrical requirement which leads to mathematically exact reconstructions in the light of equation (2.6), and as mentioned before, violating this condition leads to cone beam artefacts. In general, any discrepancy between the real imaging physics and geometry, and those assumed by equation (2.6) will lead to errors in the reconstruction, called artefacts. A survey on most of these artefacts and what causes them can be found in [13, 14]. In the context of this work it is interesting to consider the fact that the linear attenuation coefficient is actually a function of the X-ray energy (see Figure 2.5)

$$\mu \sim \mu(\vec{x}, E)$$

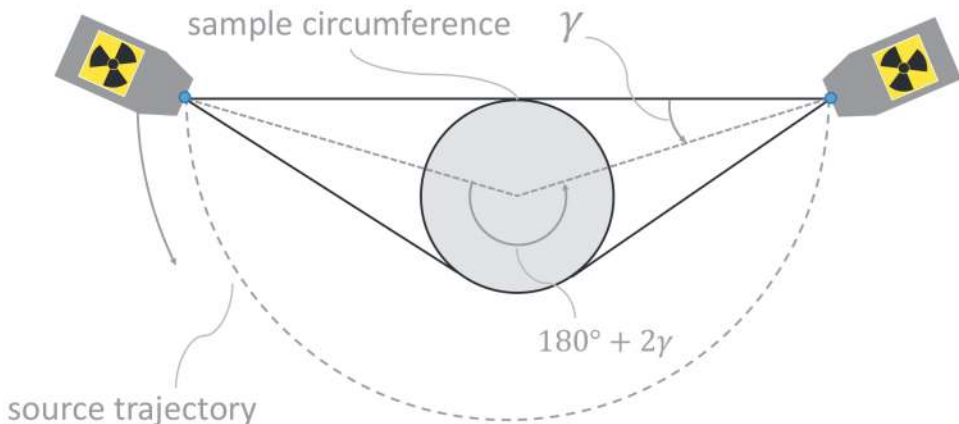


Figure 2.9: Tuy-Smith condition in a fan beam CT geometry.

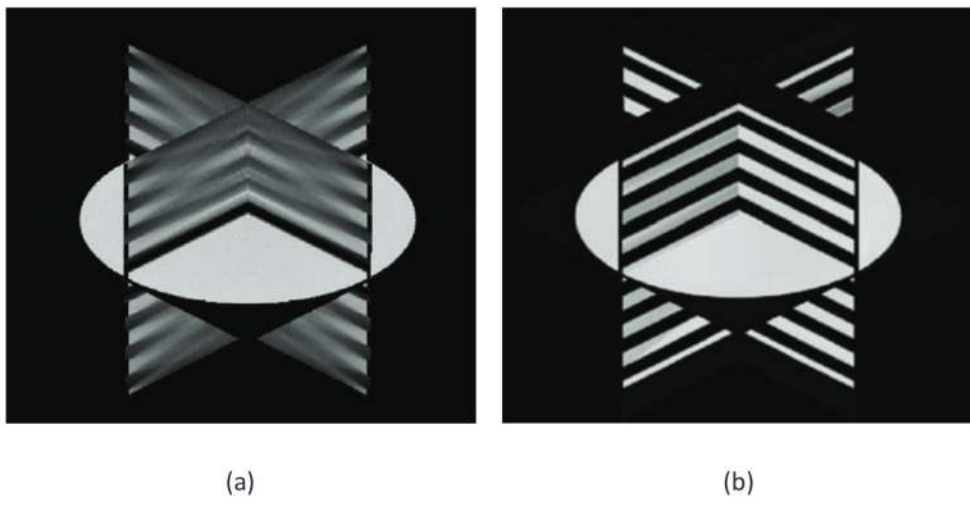
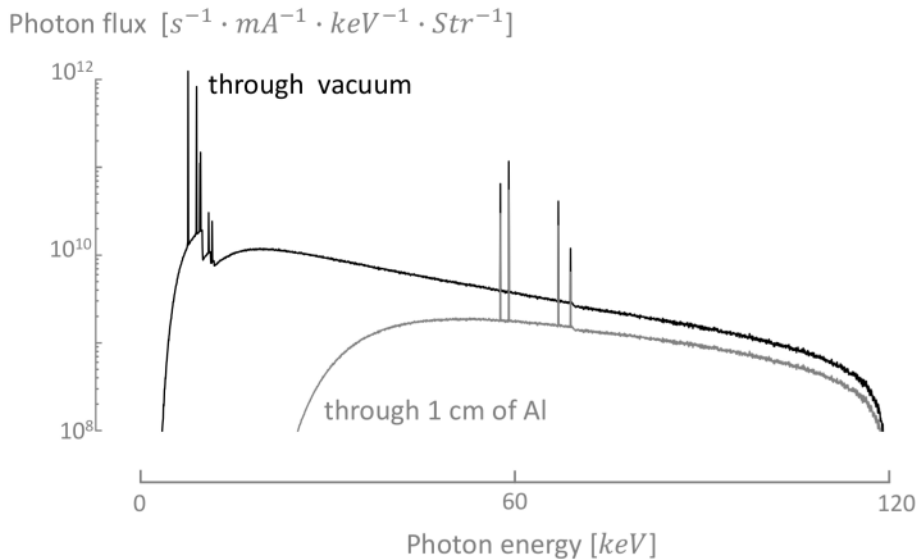


Figure 2.10: A cross-shaped vertical section through a simulated reconstruction of the Defrise phantom, illustrating (a) how the cone beam artefact distorts the reconstruction in a circular cone beam geometry, and (b) how they are eliminated in a helical cone beam geometry [11, 12].

causing the polychromatic tube spectrum to shift towards higher energies as it propagates through a sample, simply because X-ray photons with a higher energy are attenuated less (see Figure 2.11). As a result, an X-ray beam passing through a thick slab of material will on average measure a lower attenuation coefficient than those passing through a thin slab of the same material. This effect, called ‘beam hardening’, is most prominently expressed through the cupping artefact in a CT reconstruction, making the outer edges of a (homogeneous) samples appear brighter than its centre (Figure 2.12). Beam hardening is a clear illustration of how the energy dependencies in the imaging process can have a significant impact on a CT image. As such, with the pretence to construct a tool which can produce realistic

simulation of a CT scan, the polychromatic nature of the acquisition, as conveyed through the plots in Figure 2.5, needs to be modelled accurately (see section 2.3).



*Figure 2.11: The tube spectrum shifts towards higher energies, as the emitted X-rays propagate through a material, here a 1 cm slab of aluminum.*

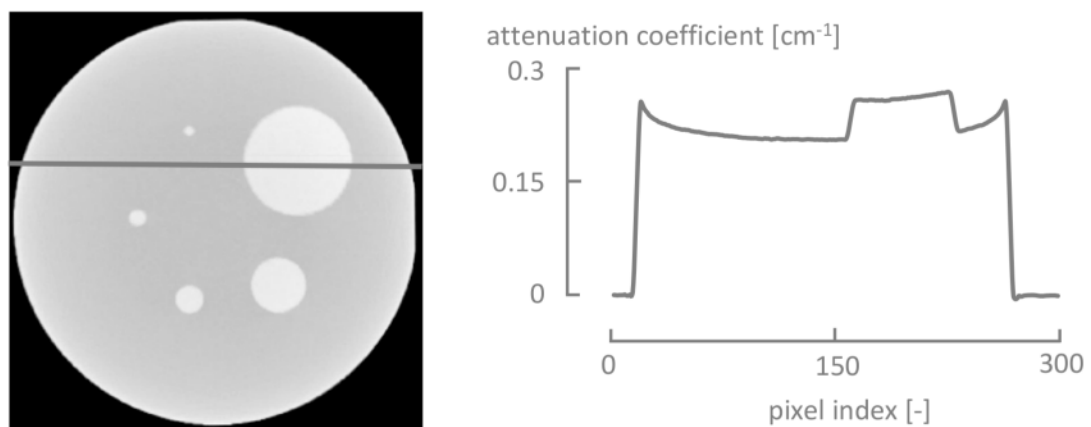


*Figure 2.12: The beam hardening process expresses itself through a brightening of the outer edges of a sample, here a simulated reconstruction (cfr. section 2.3) of a phantom for apple tissue with dense inclusions of varying size. This cupping artefact is clearly visible in both the CT reconstruction and a gray value profile across the line indicated on the reconstruction.*

Another source of artefacts is the temporal variation of the linear attenuation coefficient during a CT acquisition,

$$\mu \sim \mu(\vec{x}, E, t)$$

As a result, the gray values obtained through a standard reconstruction algorithm and/or scanning protocol will reflect the temporally averaged behaviour of the time varying linear attenuation, leading to blurred images. In general, this temporal variation in  $\mu$  can be caused by any change following a dynamic process within the sample, e.g. stress induced internal deformations, temperature related phase changes, imbibition of fluids in micro-pores etc. When the temporal change is attributed to a displacement or deformation of the sample, the resulting artefact is specifically referred to as a '*motion artefact*'. An example of a reconstruction of an apple rolling to its side is shown in Figure 2.13. The motion artefacts can be eliminated if the object's displacement is taken in to account during the reconstruction. Determining the correct displacement mode, going from global rigid to local non-rigid deformation, is however not straight forward. Chapter 5 explains how displacements can be registered and implemented in a reconstruction algorithm to rid the CT images of motion artefacts, but also as a diagnostic tool enabling 3D material characterisation.

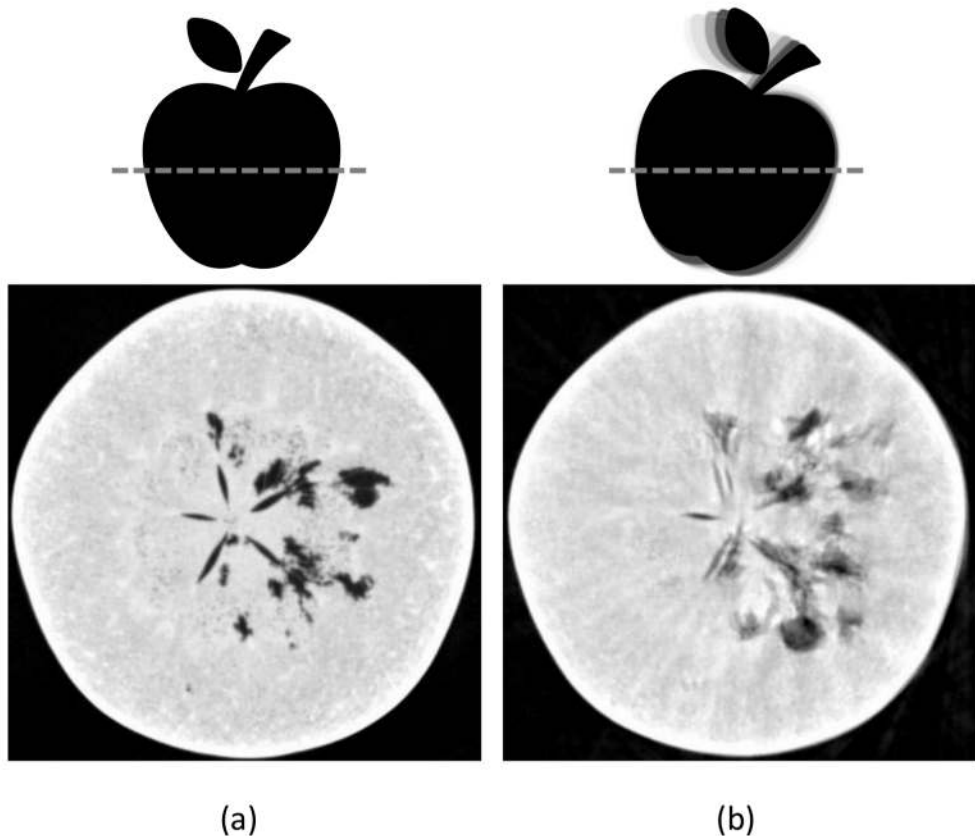


Figure 2.13: Vertical slice through a reconstruction of an apple (a) staying perfectly still, (b) performing a tilt of  $20^\circ$  during an acquisition. The reconstruction in (b) shows severe motion blurring artefacts. The tilt was artificially induced by moving the reconstruction grid, which is completely equivalent to a tilt of the apple.

### 2.1.3 Visualisation & Analysis

As a third and last step in the CT imaging chain the data produced by a reconstruction need to be interpreted. Often the 3D digital reconstruction volumes are stored as a stack of 2D images, each representing one slice perpendicular to the objects vertical axis (cfr. Figure 2.13). While these images are a first qualitative indication of how an object is built up internally, a true 3D visualisation has to be rendered through dedicated software tools. Next to commercial viewers (e.g. VG Studio and Avizo), there are many open source rendering alternatives such as VolView and 3D Slicer based on VTK [15] and Drishti [16]. A rendering with Drishti of the same apple as in Figure 2.13 is shown in Figure 2.14. The 3D renderings evidently require a human interpretation if any information on an object's structure is to be inferred from them, and still this only provides a qualitative evaluation.

The CT reconstructions also form a rich source of quantitative information on the internal structure of an object, that can be extracted in an automated way through dedicated analysis procedures, often starting with the segmentation of a structure or phase of interest. As an example, in Figure 2.15 the pores in a pharmaceutical pill are segmented and coloured according to their equivalent spherical diameter with the commercial Octopus Analysis software (InsideMatters, Ghent, Belgium). This is just one of many results attainable through proper image analysis, which in itself is a broad classification for all digital image manipulations and calculations involved in more than just visualisation. Despite its broad nature there are many open source initiatives which are actively maintained and bundle most of the established and bleeding edge image analysis algorithms, e.g. ITK [17], OpenCV [18], scikit-image [19] and Fiji [20].



Figure 2.14: Rendering of an apple dataset together with a virtual cross section in the frontal direction. The colouration is produced through a mapping of the original gray scale (attenuation) values to a set of colours chosen to mimic (i.e. not exactly represent) the apple's real colour. These images were rendered with Drishti [16].

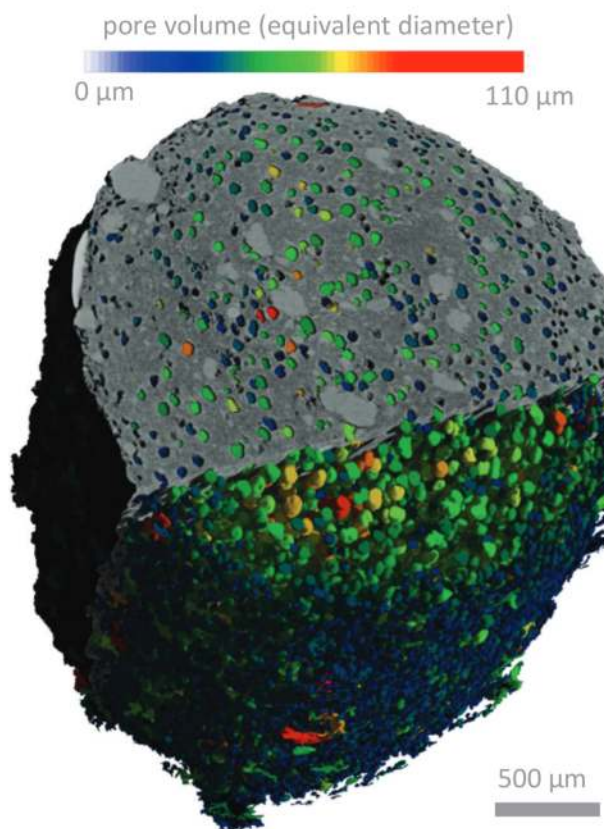


Figure 2.15: The pores in the matrix of a pharmaceutical pill (gray value rendering) are coloured according to their volume expressed in terms of equivalent diameter (courtesy of Matthieu N. Boone from [2]).

## 2.2 UGCT scanner systems

A first glimpse of one of the CT scanner systems built and commissioned at the UGCT was already shown in Figure 2.1(b), in this case the high energy HECTOR system. All of the scanners at the UGCT have a similar anatomy, containing at least one source and detector, and an actuation system to change the relative orientation of the sample with respect to the source and/or detector. The UGCT today manages up to 5 CT systems, one of which in close collaboration with the X-ray Micro-spectroscopy and Imaging (XMI) group of the Ghent University. However, the remainder of this section only discusses the specification of the three systems, most relevant to the work presented in this dissertation.

### 2.2.1 HECTOR - The High energy scanner

HECTOR, in full the *High Energy CT scanner Optimised for Research* (see Figure 2.1(b)) [1], was commissioned in 2012, with the specific goal of enabling qualitative CT acquisitions of large and highly attenuating objects. Not being restricted to these types of samples, HECTOR, due to its versatile tube settings and broad magnification range, up to now is responsible for almost all of the CT scans performed at the UGCT down to the 4  $\mu\text{m}$  mark, on a day to day basis.

#### X-ray source

A 240  $k\text{V}$  directional X-RAY WorX source is fixed on a granite stabilising block. This open-type tube, with a liquid-cooled target, is able to focus up to 280 W into a variable spot size, which is automatically regulated to prevent excessive heating and pitting damage to the target. At a target power of 10 W the focal spot size can be brought down to 4  $\mu\text{m}$ , which sets the intrinsic resolution limit to the CT images produced by this system.

#### Detector

The images in this system are produced by a 2048 by 2048 flat panel detector containing pixels with a 200  $\mu\text{m}$  pitch on a column-shaped CsI scintillator (PerkinElmer 1620 CN3 CS). With its variable gain and exposure time (between 266 ms and 2000 ms), both the very high tube fluxes, generated by the high tube power, and low fluxes, transmitted through large and highly attenuating objects, can be acquired within the detector's dynamic range.

#### Motion actuation

The detector stage is mounted on a magnification axis, which can set an SDD up to 1.8 m. In practice, the SDD is bounded towards mediating cone artefacts, i.e.

minimally 1 m, and excessively long measuring times, as the X-ray flux captured by the detector decreases quadratically with the SDD. Furthermore, the detector can be translated in-plane with its vertical and horizontal actuators to enable tiling and extended Field Of View (FOV) imaging.

The angular position of the sample can be set very accurately, with a positioning error well below  $3 \mu\text{m}$ , by the air-bearing rotation stage, which can support up to 80 kg. The sample stage can also be translated in the magnification and vertical direction, allowing for both circular and helical CT trajectories. Finally, to remotely and automatically centre a sample's Region Of Interest on the axis of rotation, an XY-Piezo stage was recently installed on the rotation stage.

### 2.2.2 EMCT - A gantry based CT scanner

In the Environmental CT system, or EMCT [8], the source and detector are mounted on a gantry. The gantry assembly rotates around the scanned object, very similar to a medical CT device, though in a horizontal plane (see Figure 2.16). With this setup, a sample can be imaged by continuously rotating around it, without risking that any of the external wires or tubes to external equipment could be caught up in the rotational movement. Although the EMCT's gantry rotates relatively slowly as compared to for instance HECTOR's rotation stage, the continuous scanning approach makes it possible to produce CT data for samples with a dynamically evolving internal structure, as result of undergoing an in-situ dynamic process. This is why the EMCT is the preferred system for the studies in this work, which are related to dynamic and fast imaging.



Figure 2.16: A top view on the gantry assembly of the Environmental CT scanner (EMCT), with an X-ray source on the left and a flat panel detector on the right.

### X-ray source

To facilitate a gantry based design, a compact 130 kV X-ray source was chosen (Hamamatsu L9181), which is of the closed, directional type. Again the tube power is regulated with respect to the focal spot size, going from a maximum of 39 W to 4 W at a lower bound focal spot size of 5  $\mu\text{m}$ . Nevertheless, JIMA pattern ([www.jima.jp](http://www.jima.jp)) line pairs below 4  $\mu\text{m}$  have been resolved with this tube.

### Detector

The detector, a Xineos1313 flat panel with a CsI scintillator, is installed at a fixed SOD from the source. 30 full frames of 1300 by 1300 pixels with a pitch of 100  $\mu\text{m}$ , can be acquired each second. When a two by two (hardware) binned frame or a ROI are read out, frame rates of 50 fps and 300 fps, respectively, can even be achieved.

### Motion actuation

Next to the fast detector, the dynamic imaging capabilities of the EMCT are made possible through the continuously rotating gantry, which also rotates relatively fast (12 seconds per rotation). While this is fast for a gantry based  $\mu\text{CT}$  system, the rotation speed does constitute a technical limitation to the temporal resolution for CT imaging with the EMCT. On the other hand, given the limited flux produced by the low power tube, the image quality can not be sustained at scan times much lower than this 12 seconds, during which an adequate SNR can barely be acquired.

A mechanical brace, holding the source and detector at a fixed SDD, is mounted on a linear magnification stage, which in turn is mounted on the rotating gantry. Contrary to the medical gantry based systems, the EMCT can thus set a variable magnification, making it a quite unique system. With a vertical translation axis, fixed to the stationary support, a sample, and its connections to peripheral equipment, can be transported upwards through a 19 cm bore hole in the gantry's granite stabilizing block, where it is introduced into the FOV.

### 2.2.3 Medusa - A multi detector system

The very first setup built at the UGCT [21] was refurbished in 2014 with a completely new, more accurate and more flexible actuation system. The system has evolved from a dual tube to a single transmission tube setup with multiple detectors, which can be automatically exchanged through a simple translational movement (see Figure 2.17). Depending on the attenuation properties and size of a sample, a particular detector can be chosen for CT imaging, down to a 1  $\mu\text{m}$  res-

olution. As explained in chapter 4, Medusa was also upgraded with an add-on module to emulate an in-line CT geometry fitting to an industrial setting.



*Figure 2.17: The Medusa system currently has three detectors mounted on a translation stage which can accurately align each detector on the optical axis of an open type transmission tube. The complete system is mounted on an actively damped and levelled table. Note that the Varian detector on the left is shielded in a led box, when the other detectors are used.*

## X-ray source

The X-rays in this system are produced with a transmission tube of the open type (Feinfocus FXE160.51), accelerating electrons through a high voltage of up to 160 kV. The electromagnetic lenses can efficiently focus the electrons into spots smaller than 2  $\mu\text{m}$ , although JIMA patterns of  $\pm 0.7 \mu\text{m}$  have been visualised using this tube. This lower limit is strongly affected by the target material and thickness [3], which can be changed from a diamond backed 5  $\mu\text{m}$  thick tungsten target to a diamond backed molybdenum one with four quadrants of varying thickness (i.e. 1  $\mu\text{m}$ , 3  $\mu\text{m}$ , 6  $\mu\text{m}$  and 8  $\mu\text{m}$ ). The high thermal conductivity of the diamond backing allows for a dissipation of up to 10 W of power in the tube's target.

## Detectors

On the Medusa system three detectors are mounted on a translation stage, which can accurately align each detector with the optical axis. For larger ( $\pm 1 \text{ cm}$ ) and denser samples, Medusa is equipped with two CsI flat panel detectors with a pixel pitch of 127  $\mu\text{m}$ , and an active pixel matrix of 1516 by 1900 and 1152 by 1152, respectively (Varian PaxScan 2520 and Varian PaxScan 1515). The latter is a part of an add-on module for in-line CT geometries and serves as a temporary substitute for the older Varian PaxScan, which was inherited from the original dual-tube

setup. As an upside to the newer Varian's smaller active area, it can be read out much faster, i.e. 28 fps as opposed to 7.5 fps. The smaller, less attenuating samples are imaged with a CCD Photonic Science VHR camera with a pixel pitch of 9  $\mu\text{m}$ , mounted on the right hand side of the translation stage, as viewed from the source (see Figure 2.17).

### Motion actuation

To guarantee a precise and vibrationless angular positioning of the sample, its rotation is carried out by an air-bearing stage, supported by a vertical axis, which can move the sample in and out of the FOV. Both this vertical axis, holding the rotation stage, and the detector translation stage are mounted on a magnification axis, as such the SDD and SOD can be adjusted separately, allowing for an X-ray propagation distance of up to 1.4 m. Additionally, a sample's centre of mass can be accurately aligned with the rotation axis by using the XY-Piezo positioning system installed on top of the rotation stage. Finally, the complete system is assembled on an actively damped and levelled table, to prevent external vibrations from distorting high resolution measurements.

## 2.3 Simulating X-ray radiographs

### 2.3.1 Radiography/CT simulation in literature

As mentioned in the introduction to this chapter, the GPU based realistic radiography simulator, which adopts the first order model described in the following section, was developed to optimise both existing CT setups and protocols, and explore how novel CT geometries and the underlying acquisition physics impact the image quality. Indeed, a radiography simulator can serve as a cost effective tool to study and validate conceptual designs for new CT geometries, before actually building a real life implementation for these geometries.

UGCT is not the only research group active in the field of X-ray radiography simulation. A non-exhaustive overview of several X-ray radiography and CT simulation codes is given in table 2.1. Unfortunately, while some of these tools could be a valuable substitute for the radiography simulator described in this work, most of them are either not freely available, no longer maintained or are tailored to a very specific application, e.g. breast mammography [22, 23] and CT metrology [24]. It should also be mentioned that ASTRA, also in table 2.1, is actually a CT reconstruction toolbox, which due to its readily accessible projection operator can in fact be used as a (monochromatic) X-ray radiography/CT simulator. Given the fact that a CPU implementation of the first order model described below was already available at the UGCT, it was an evident choice to reimplement this code in porting

it to a GPU. By doing this, UGCT can fully control the back-end implementation of, and the physics related features that are implemented in the radiography simulator. A thorough account on the details of this radiography simulator, dubbed ‘Arion’, can also be found in [25].

### 2.3.2 First order modelling of the acquisition physics

The energy dependency of the imaging process was briefly touched through equation (2.3). Discretizing the integrals in this equation with respect to the energy and spatial coordinate is the first step towards simulating a radiograph. The number of photons acquired by one of the detector pixels (index  $j$ ) can be modelled as follows (cfr. equation (2.3))

$$N_j = \sum_{i=0}^n N_{0,j,i} T_{j,i} Q_{\text{eff},i} = \sum_{i=0}^n N_{j,i} \quad (2.9)$$

where both the emitted ( $I_{0,i}$ ) and detected ( $I_{j,i}$ ) X-ray beam spectra were exchanged for the effective number of photons emitted by the source towards pixel  $j$  ( $N_{0,j,i}$ ), and those detected by it ( $N_{j,i}$ ). Indeed, both quantities are linearly proportional to one another, according to

$$N_{0,j,i} [\# \text{photons}] = N_{e^-} \cdot \Omega_j \cdot \Delta E_i \cdot I_{0,i} \left[ \frac{\#\text{photons per } e^-}{\text{keV} \cdot \text{Str}} \right] \quad (2.10)$$

given the solid angle of the pixel ( $\Omega_j$ ), the width of the discrete energy bin ( $\Delta E_i$ ) and the number of electrons hitting the target to produce X-rays ( $N_{e^-}$ ). equation (2.9) stipulates that the number of photons detected by a pixel can be calculated independently for each term representing one out of  $n$  energy bins, and that each term is composed out of three factors which reflect the polychromaticity of the X-ray tube spectrum ( $N_{0,j,i}$ ), the sample’s transmission properties ( $T_{j,i}$ ) and the detector’s quantum efficiency ( $Q_{\text{eff},i}$ ). In the following, these three contributions are discussed in an order which reflects the travelling direction of an X-ray photon, i.e. in an order relevant to the photon’s generation in the X-ray tube, its interaction with the sample and its detection with a flat panel detector, respectively.

#### X-ray emission spectra

The number of photons of a particular energy ( $E_i$ ) emitted by the X-ray tube target in a unit solid angle and per electron hitting the target, i.e. the **X-ray emission spectrum** ( $I_{0,i}$ ), is assumed to be known or calculated, e.g. through Monte Carlo simulations, which are commonly accepted as the most accurate method in resolving stochastic particle based radiation transport [34, 35]. Dhaene *et al.* [25] calculated the spectra using the BEAMnrc Monte Carlo code [36, 37], and devised a clever way to accurately approximate the emission spectra with a small number

**Table 2.1:** Overview of some existing X-ray radiography/CT simulation tools. The most important features of these tools are reported, i.e. whether they are implemented on a GPU, implement the polychromatic source, object and detector properties, implement noise and scattering, start from an underlying CAD or voxel based object volume model, are actively maintained, and are freely available.

of energy bins, leading to a significant reduction in the time needed to compute a result for equation (2.9). This binning technique singles out the characteristic peaks and the edges attributed to the tube's target and exit window materials (see Figure 2.18). The remaining continuum Bremsstrahlung spectrum can then be approximated by a small number of bins, which being interleaved with bins dedicated to describing the peaks and edges in the spectrum, do not necessarily have an equal width. As a result, the tube emission spectra are encoded at a series of irregularly spaced energies ( $E_i$ ) at the centres of  $\Delta E_i$ -wide bins, each containing  $I_{0,i} \times \Delta E_i$  photons of energy  $E_i$  emitted per unit of solid angle and per electron hitting the tube target. A notable difference between the spectra in Figure 2.5(b) and Figure 2.18, both pertaining to a similar tungsten target X-ray tube, is the presence of the characteristic peaks at  $\pm 18\text{ keV}$ , generated within the first tube's molybdenum aperture.

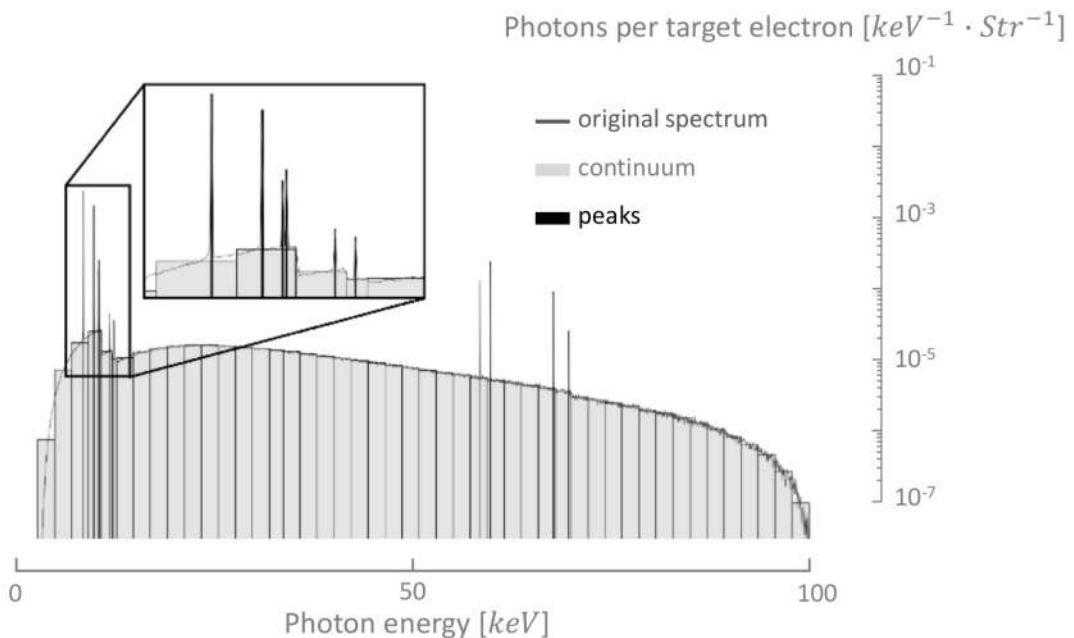


*Figure 2.18: After extracting the peaks and edges, characteristic to the tube's target material (tungsten in this case), the smooth continuum Bremsstrahlung spectrum can be approximated with a limited number of bins (Courtesy of Jelle Dhaene, adapted from [25]).*

## Ray tracing

One of the crucial assumptions made for the radiography simulator is that the X-rays do indeed behave like ‘rays’, connecting the focal source point to the centres of the detector pixels through straight paths. The probability for X-ray photons with an energy  $E_i$  to be transmitted through an object can be found by tracing this

ray as it passes through the object. Following Lambert-Beer's law, the **transmission factor** in equation (2.9) is given by

$$T_{j,i} = \exp \left( - \sum_{l=0}^L \mu(\vec{x}_l, E_i) \Delta t \right) \quad (2.11)$$

where the linear attenuation coefficient is sampled at equidistant position along the intersection of the ray  $j$  with the support of  $\mu(\vec{x})$ , where  $t_l \in [t_{in}, t_{out}]$ , as shown in Figure 2.19.

$$\vec{x}_l = \vec{O}_s + \vec{d}_j \cdot (t_l + t_{in}) \quad (2.12)$$

with

$$\begin{aligned} \vec{d}_j &= \frac{\vec{x}_j - \vec{O}_s}{\|\vec{x}_j - \vec{O}_s\|} \\ t_l &= l \cdot \Delta t \end{aligned}$$

This simple ray tracing approach is very efficient if  $\mu(\vec{x}_l, E_i)$  is parametrised and discretised in an appropriate way. Several options with a varying degree in accuracy and computational cost are thoroughly described in [11, 38], referred to as ‘splatting’ techniques in literature. However, the obvious and simplest choice, with the prospect of an efficient implementation on a GPU and compatibility with CT reconstructions, is to distribute  $\mu(\vec{x}_l, E_i)$  on a voxelised grid, cfr. section 2.1.2. Furthermore, the radiography simulator labels each voxel with an index to a look up table listing all of the materials contained within the object. In other words, the object is digitally represented by a phantom volume composed out of material labels. These labels link to their material’s energy dependent attenuation curve, as retrieved from the XCOM Photon Cross Sections Database ([www.nist.gov](http://www.nist.gov), cfr. Figure 2.4). Each time an X-ray intersects one of the voxels, the attenuation curve for the material contained within this voxel is interpolated at the current bin energy ( $E_i$ ). This approach economises the amount of memory necessary to store a digital phantom in CPU or GPU RAM, because the material labels can be encoded through fairly low bit depth unsigned integers, e.g. 8 bit unless the object is composed out of more than 256 different materials.

### The detector’s quantum & energy conversion efficiency

When an X-ray photon finally reaches the detector, its detection is subject to a series of events, each with a finite probability of actually occurring (cfr. Figure 2.2). Namely, whether or not the X-ray photon induces a scintillation, the resulting luminescence reaches the photodiode, and finally creates electron-hole pairs. It is quite difficult to model all of these effects even through Monte Carlo simulations.

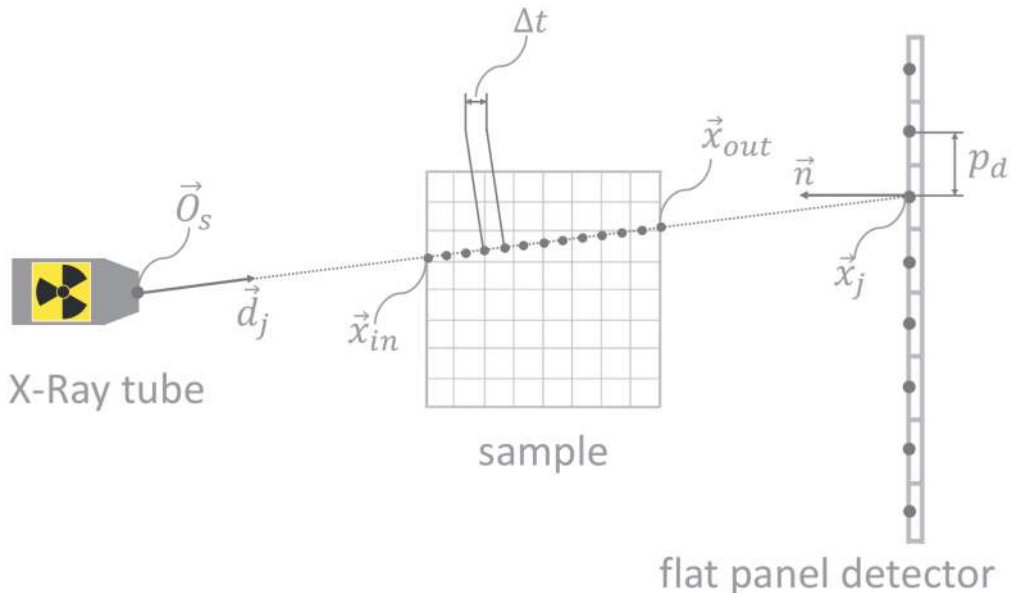


*Figure 2.19: 2D analog of a simple ray tracing technique. As the ray progresses from the X-ray tube’s focal spot to the centre of a detector pixel, the linear attenuation coefficients are sampled and accumulated at equidistant positions along the ray-object intersection.*

*The object’s attenuation distribution is encoded on a voxelised grid, similar to a CT reconstruction volume.*

This is why it is implicitly assumed here that a detector’s output is proportional to the X-ray energy deposited in the scintillator. In other words, not all of the conversion effects are considered, such that the energy deposit can be estimated through a Monte Carlo simulation, which approximates a detector as a layered structure composed out of an entrance window, a reflective foil, a scintillator and an a-Si photodiode [3, 25]. The detector response as a function of energy is then characterised by the probability for a photon to be detected, i.e. **the quantum efficiency** ( $Q_{\text{eff}}$ ), and how much of a detected X-ray photon’s energy is effectively deposited in the scintillator, i.e. **the effective energy deposit** ( $D_{\text{eff}}$ , see Figure 2.20). It is sufficient to consider the product of these quantities (cfr. Figure 2.5(a)) when only the average energy deposit in each pixel has to be calculated, while an accurate model for the noise distribution in a radiograph requires them to be treated separately, as described in the next paragraph.

## Noise

When addressing the noise in radiographic images an important distinction has to be made between unintended spatial variations in the image, e.g. when the pixels in a detector have slightly different responses to an identical input, and temporal variations in a detector’s output within each individual pixel. The radiography simulator neglects the noise contributions attributed to non-idealities of the detector,

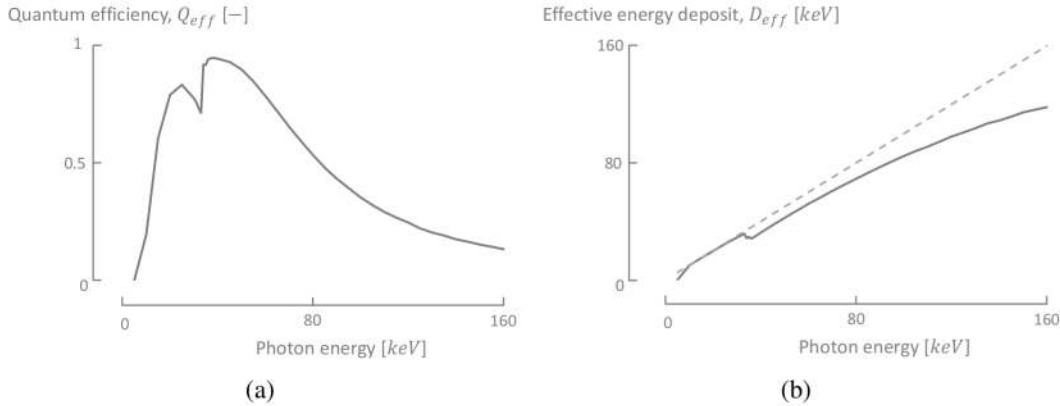


*Figure 2.20: The energy dependency of a detector response can be characterised through (a) a quantum efficiency, and (b) the mean energy a detected photon effectively deposits in the detector photodiodes.*

by assuming a uniform response across all of its pixels, for which the output is not subject to any electronic noise. The dominant noise component is caused by quantum fluctuations in the detected number of photons, which follows the Poisson distribution.

$$\mathcal{P}(k|N) = \frac{e^{-N} \cdot N^k}{k!} \quad (2.13)$$

In particular, this distribution holds for the photons counted in a pixel  $j$  for each individual energy bin  $i$ , leading to a variance of

$$\sigma_{j,i}^2 = N_{j,i} \quad (2.14)$$

on this count. If  $N_{j,i} > 20$ , which is almost always the case, the Poisson distribution can be accurately approximated by a Gaussian one

$$\mathcal{P}(k|N_{j,i}) \sim \mathcal{N}(k|N_{j,i}, \sqrt{N_{j,i}})$$

However, rather than a number of photons the flat panel detector's output is actually determined by the energy deposited in it. Luckily, following the effective energy deposit (cfr. Figure 2.20(b)), the energy detected in each bin ( $E_{d,i}$ ) is also proportional to the number of photons detected by each pixel on a per bin basis, which can be summed over  $i$  to obtain the integral energy deposit.

$$E_{d,j} = \sum_{i=0}^n E_{d,j,i} = \sum_{i=0}^n D_{\text{eff},i} \cdot N_{j,i} \quad (2.15)$$

A flat panel detector finally converts this energy deposit to an analog-to-digital unit (ADU,  $U_j$ ), through its photodiodes and ADC, which can to a first order be modelled as a linear process.

$$U_j = \kappa E_{d,j} \quad (2.16)$$

The gain factor  $\kappa$ , expressed in units of ADU per  $eV$ , incorporates the conversion from photon energy to electron charge, the amplification of this charge to a voltage, and finally the digitisation of this voltage to an ADU.  $\kappa$  serves as a calibration factor to tune the radiography simulations towards a particular detector and its gain settings. A good rule of thumb is that each ADU level can hold no more than one or two photons of approximately  $30\text{ keV}$ , which by design corresponds to the mean energy of the X-ray transmission spectra measured for most moderately absorbing samples (e.g. soft tissue in medical CT). By combining equations 2.14 to 2.16, the variance on the ADUs can be calculated through

$$\sigma_{u,j}^2 = \kappa^2 \sum_{i=0}^n D_{\text{eff},i}^2 \cdot N_{j,i} \quad (2.17)$$

where the individual energy bins are described by independent Gaussian distributions. As such, the ADUs in pixel  $j$  ( $u_j$ ) are distributed according to

$$\mathcal{P}(u_j) \sim \mathcal{N}(U_j, \sigma_{u,j}) \quad (2.18)$$

### The first order simulation model

To finalise the first order simulation model for X-ray radiographs, the number of electrons ( $N_{e^-}$ ) and the solid angle of a pixel ( $\Omega_j$ ), as introduced in equation (2.10), need to be defined. In the context of X-ray  $\mu$ -CT, the target electron load is commonly reported as the product of the tube wattage ( $P_t$ ) and the exposure time ( $t_{exp}$ ) at a certain tube high voltage ( $V_t$ ), rather than units of  $mAs$ , as in medical CT. The number of electrons hitting the tube target is then given by

$$N_{e^-} = \frac{P_t t_{exp}}{V_t e^-}$$

where  $e^-$  is the elementary charge. The solid angle of a pixel as viewed from the source can be approximated by (see Figure 2.19)

$$\Omega_j = -\frac{p_d^2}{\left\| \vec{x}_j - \vec{O}_s \right\|^2} \vec{d}_j \cdot \vec{n} \quad (2.19)$$

In summary, the equations throughout this section can be combined to yield a statistical estimate for the ADUs in pixel  $j$  by sampling the Gaussian distribution

$\mathcal{N}(U_j, \sigma_{u,j})$  for which

$$U_j = \kappa \cdot \sum_{i=0}^n D_{\text{eff},i} \cdot N_{j,i} \quad (2.20)$$

$$\sigma_{u,j}^2 = \kappa^2 \cdot \sum_{i=0}^n D_{\text{eff},i}^2 \cdot N_{j,i} \quad (2.21)$$

$$N_{j,i} = N_{e^-} \cdot \Omega_j \cdot \Delta E_i \cdot I_{0,i} \cdot Q_{\text{eff},i} \cdot \exp \left( - \sum_{l=0}^L \mu(\vec{x}_l, E_i) \Delta t \right) \quad (2.22)$$

### 2.3.3 Secondary effects in radiographic image formation

In the model described throughout the previous section some implicit assumptions have been made, aimed at bypassing secondary physical effects, which in reality are almost certainly present but do not have a significant or unmanageable quantitative impact on the simulated radiographs. The most relevant secondary effects, which are discussed in this section, relate to the fact that (1) X-rays do not necessarily follow straight paths, and (2) do not originate from a singular point in space. These effects were not incorporated in the radiography simulator, however in explaining their origin during the course of this section, some opportunities towards implementing them in future versions of the radiography simulator, are discussed.

#### Scattering

Through equation 2.2, it was established that the linear attenuation coefficient is determined by a combination of interactions between atomic electrons and the X-ray photons. Equation 2.22 states that the number of photons travelling along the path  $l$  exponentially decreases at a rate which is dictated by the total attenuation coefficient. However, only the photons undergoing a photo electric interaction actually disappear from  $l$  as they are absorbed, while the Compton and Rayleigh interactions force the photons to be scattered away from their straight ray paths. Although equation 2.22 reflects the correct attenuation behaviour, it does not treat scattered photons, which can still be registered on a completely different detector pixel (not  $j$ ). Photons can even undergo multiple scattering interactions, making them difficult to simulate, in particular when the photon's energy is not conserved, cfr. Compton interactions.

With the pretence of predicting the 3D distribution of radiation dose across an object, Freud *et al.* have recognised that scattering needs to be taken into account, and they have devised a first-order deterministic method to accurately account for the scattering contributions [27]. On the level of a radiograph however, the effects of scattering are averaged out and are expressed through a global low frequency

offset, with a footprint which disperses across the image as the scattered photons travel a longer distance from the object to the detector (Object Detector Distance, ODD). The scattering footprint can have a visible effect on a radiograph when the ODD is small enough (see Figure 2.21(a)), depending on the scattering properties of the object. A simple, although crude way of levelling out this offset, is to perform a deconvolution with a large, predetermined kernel, cfr. a Richardson-Lucy deconvolution [39] where the non-scattered direct signal can be modelled by Dirac or an estimate for the point spread function of the detector. For example, in Figure 2.21(b) a uniform kernel with a size roughly matching the extent of the projected object, was used. Despite its efficacy, this deconvolution approach is an ad hoc correction which needs to be visually assessed. As such, the inverse process of convolving a simulated radiograph with a broad kernel is by no means a good approach towards modelling a process like scattering, which is very object dependent. While the method described by Freud *et al.* is proficient in predicting scattering contributions, the overall low impact of scattering on a radiograph does not justify the added computational burden of implementing this method in the radiography simulator presented here.

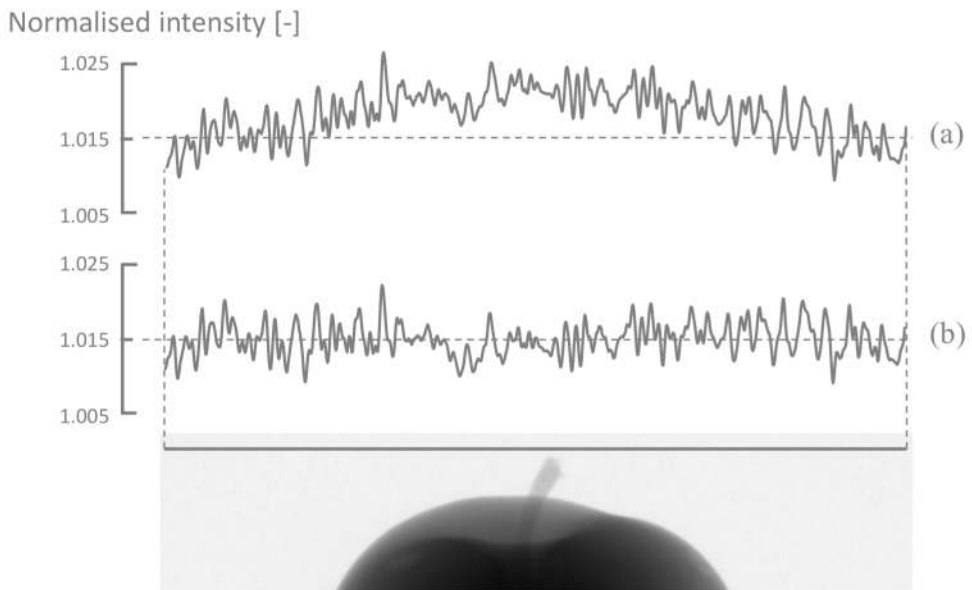


*Figure 2.21: X-ray scattering in an apple. At a small ODD ( $\pm 24$  cm) the contribution of the scattered X-rays can be visualised through the line profile indicated on a flat field normalised radiograph of the apple. The curved profile in (a) reveals a surplus intensity caused by scattered photons. (b) Using a broad uniform kernel, the profile can be flattened through a Richardson-Lucy deconvolution.*

### Phase contrast

Similar to scattering, X-rays can be put off their course by refracting at material inhomogeneities. While in essence the refraction process is rooted in a spatial variation of scattering properties at the atomic level, it is easier to understand through a wave interpretation and the ray optics derived from it. The interaction between an electromagnetic wave, with a wavelength  $\lambda$ , and its propagation medium can be described by the complex refractive index

$$n(\vec{x}, \lambda) = 1 - \delta(\vec{x}, \lambda) + i\beta(\vec{x}, \lambda)$$

where  $\delta$  is called the *refractive index decrement*, and  $\beta$  refers to the *extinction coefficient*. As a monochromatic plane wave  $u_0(x, y)$  (wavevector  $\vec{k} = (0, 0, k_z = 2\pi/\lambda)$ ) propagates through a medium in the  $z$ -direction according to,

$$\begin{aligned} u(\vec{x}) &= u_0 \cdot \exp\left(i \int k_z n dz\right) \\ &= u_0 \cdot \exp\left(ik_z \int dz\right) \cdot \exp\left(ik_z \int \delta(\vec{x}) dz\right) \cdot \exp\left(-k_z \int \beta(\vec{x}) dz\right) \end{aligned}$$

its phase front is transversely modulated through a phase factor containing the refractive index decrement, which only has an effect on the square modulus intensity ( $I(x, y) = |u(x, y)|^2$ ) when these phase fronts are allowed to propagate over a certain distance [2, 11]. Moreover, the wave field's amplitude decreases exponentially at a rate  $\beta$ , which corresponds to the Lambert-Beer law when looking at the intensity, with

$$\mu = 2 \cdot k_z \cdot \beta.$$

According to the ray optical approach it can be shown that the ray trajectories  $\vec{x}(s)$ , which are orthogonal to the wave fronts, should satisfy the following differential equation [40]

$$\frac{d^2}{ds^2} \vec{x}(s) - \frac{d}{ds} \left[ \delta(\vec{x}) \frac{d}{ds} \vec{x}(s) \right] = -\nabla \delta(\vec{x}) \quad (2.23)$$

This equation implies that straight ray paths are only possible in a homogeneous medium, wherein  $\delta(\vec{x}) \equiv \delta$  and  $d^2\vec{x}/ds^2 = 0$ . While this clearly illustrates how refraction is induced through spatial variation in  $\delta$ , it is more interesting to look at how the phase effects contribute to a radiograph. Figure 2.22 schematically depicts how refraction distorts the intensity profile of a high- $\delta$  object on a detector. In a radiograph, this distortion is expressed through an accentuation of the contrast around the object's edges, also known as *phase contrast edge enhancement*. In transmission based CT, phase contrast is sometimes classified as an artefact,

because the edge enhancement may lead to false conclusions on the material constitution at the edges of an object, or other features might be obscured by it [2, 41]. In most cases however, phase contrast is seen as a powerful new imaging modality, yielding information on the refractive index decrement and even subresolution scattering structures (dark field imaging), particularly when it is induced through gratings [42].

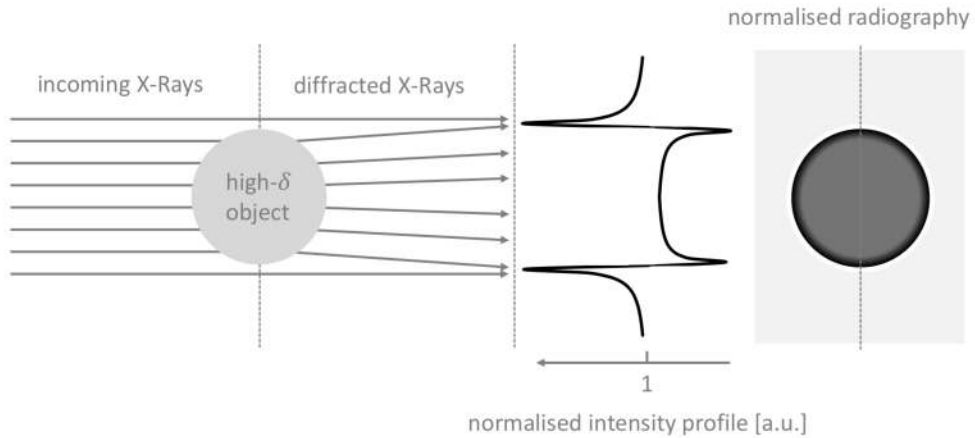


*Figure 2.22: The principle of phase contrast. The X-rays, refracted at the edges of an object, are registered on the detector as an enhancement of the object's contour (based on [43]).*

An accurate model for the phase contrast contribution can be derived by considering how the X-ray beam intensity is transported between the object and a detector. It can be shown that the beam intensity at a distance  $z = d$  from the exit plane situated at  $z = 0$  behind the object, can be approximated by the second-order *transport of intensity* (TIE) equation [2, 43, 44]

$$I_d(x, y) = \frac{I_0}{M^2} e^{-T_\mu} \left[ 1 - \frac{d}{M} \nabla_\perp^2 T_\delta + \frac{d}{M} \nabla_\perp T_\mu \cdot \nabla_\perp T_\delta \right] \quad (2.24)$$

with a magnification  $M$  and gradient operator  $\nabla_\perp$ , evaluated in the plane perpendicular to the propagation direction. The transmission thickness  $T$  along a ray path  $\vec{l}(t)$  through an object is given by

$$T_\delta = \int_{t_{in}}^{t_{out}} \delta(\vec{l}(t)) dt \quad (2.25)$$

$$T_\mu = \int_{t_{in}}^{t_{out}} \mu(\vec{l}(t)) dt$$

for the refractive index decrement and the attenuation coefficient, respectively. In many cases, even a first-order approximation is justified, since the second term in equation (2.24) is rather small.

$$I_d(x, y) \approx \frac{I_0}{M^2} e^{-T_\mu} \left[ 1 - \frac{d}{M} \nabla_{\perp}^2 T_\delta \right] \quad (2.26)$$

Equation (2.26) presents a simple opportunity towards the incorporation of phase contrast in the radiography simulator, by calculating the transverse Laplacian of the integrated refractive index decrement (equation (2.25)) for each pixel. However, to visualise phase contrast in a lab-based CT setup, both a high temporal and spatial coherence is required from the X-ray source. A high temporal coherence is attained through a small bandwidth X-ray spectrum, which is poorly satisfied for most lab-based sources. A high spatial coherence on the other hand, can be reached by increasing the ODD with respect to the spot size ( $p_s$ ), in order to improve the lateral coherence length

$$l_c = \frac{\lambda \cdot \text{ODD}}{p_s}$$

which represents the maximal distance between two correlated points in a complex wave front. This formula underlines the fact that a phase contrast profile needs to propagate over certain distance to be fully developed, which may lead to impractical measuring distances (e.g. up 200 metres at some synchrotron facilities), if the spot size becomes to large. With a view to industrial applications, where large spot sizes are common, the implementation of phase contrast models is not relevant to the radiography simulator.

### Finite spot size

Through Figure 2.7 it was already established that the X-ray source is not a singular point in space, and that its finite extent causes an inherent blurring of an object's projection in a radiograph. Especially when the magnified spot size is larger than the point spread function of the detector, which according to most detector MTFs is about 1.8 times the detector pixel size,

$$1.8 \cdot p_d \leq p_s \frac{\text{ODD}}{\text{SOD}}$$

the blurring effect can no longer be ignored, and has to be modelled to obtain a correctly simulated radiograph. A straight forward approach would to model a finite spot as a collection of discrete source points, each contributing to the radiograph according to their weight and relative intensity in the source spot's area. However, since the computational effort for this approach increases linearly with number of subdivision points, it is not particularly attractive. An other more efficient approach is to mimic the blurring effect through a convolution of the simulated radiograph with a blurring kernel, which serves a point response of the finite spot to a representative point in the object's volume. On geometrical grounds it

is clear that this blurring kernel can vary across the detector plane, and strongly depends on the shape of the source spot, which in turn depends on the type of X-ray source (directional or transmission) and its target load settings. Due to its lack in generic applicability, the kernel approach was not pursued any further as part of the radiography simulator, but can always be implemented as a post-processing measure.

## Heeling

Heeling is a secondary effect which specifically occurs when a directional X-ray source is used. It is also related to the finite size of a source spot, which extends not only across the surface of an X-ray target, but also towards the depth direction of the target bulk. Due to the directional target's inclination, some of the photons generated within the bulk of the target will have travelled a longer way towards the surface than others. As result, one side of the radiograph will be illuminated with a less intense and more beam hardened spectrum (see Figure 2.23(b)). Heeling is typically more persistent at the higher tube voltages, because high energy electrons can penetrate deeper into the anode as they are converted to X-ray photons [3]. The X-ray spot can also be dislocated by geometrical aberrations on the target surface, leading to an increased expression of heeling, e.g. when the electrons hit the inclined flanks of a small hole in the target as a result of thermal damage ('pitting').

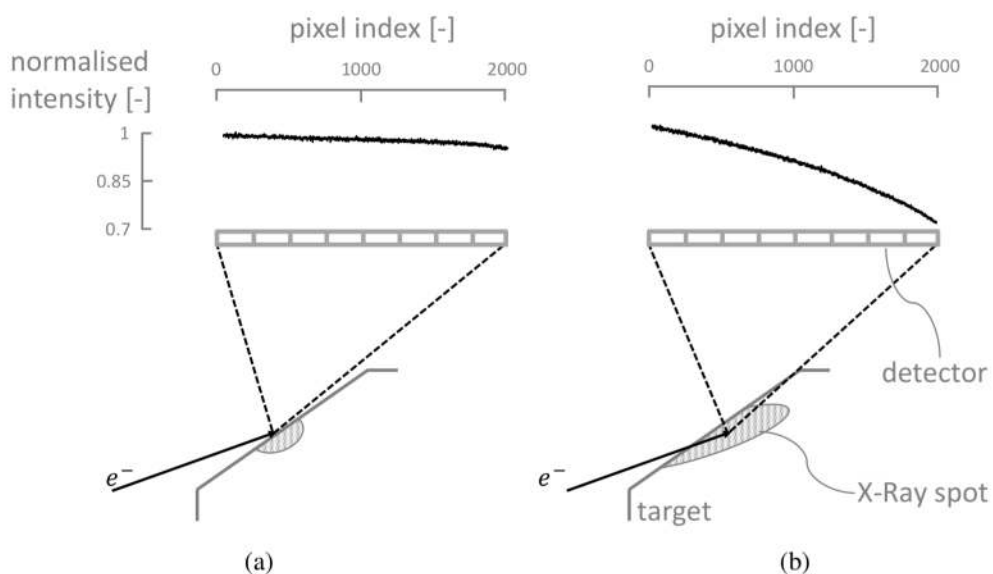


*Figure 2.23: Heeling in a directional X-ray source. As the epicentre of the X-ray generation shifts towards the bulk of the target anode from (a) to (b), heeling becomes more persistent in the non-uniform illumination of the detector. In this case, the heeling effect is induced by pitting damage (Heeling profiles courtesy of Amelie De Muynck).*

Although heel ing is complicated by its dependence on the tube high voltage and various causes like pitting, next to the target's inclination, it can be modelled by considering a virtual source with a gradually varying spectrum. This spectrum depends on the direction in which the photons are emitted from the inclined target, predominantly changing with respect to the angle about the axis of inclination (i.e. parallel to the plane in Figure 2.23). It is actually this lateral variation in the beam spectrum that produces artefacts similar to beamhardening, i.e. a sample volume is imaged with different spectra thus leading to different effective  $\mu$ -values. The lateral drop in the detected intensity on the other hand can easily be eliminated through normalisation.

### 2.3.4 GPU acceleration

The process of calculating a simulated X-ray radiograph is a typical example of a single instruction which is performed on multiple data elements (single instruction, multiple data, SIMD). In this case, a ray tracing operation is performed for each pixel element in and each position of the detector, across multiple energy bins. GPUs in particular excel at data-parallel processing by mapping this SIMD paradigm to a large set of concurrent threads, with the goal of optimising the ratio between arithmetic operations and memory access operations. As a result, GPUs are able to hide the data access latencies through a high arithmetic intensity, rather than using big data caches or complicated flow control, as is the case for CPUs [45]. GPUs also provide some more advanced caching schemes (texturing), which are optimised towards graphical applications, and allow for highly efficient one, two and three dimensional linear interpolation. Coincidentally, it is the high end 3D graphics in the gaming industry that boosted the success of the GPU, through its mass production. As a result, the scientific computing community now has access to an ever increasing performance at a very low cost (Figure 2.24).

The implementation of the radiography simulation case, which is obviously very SIMD and graphical in nature, on a GPU with texturing capabilities, has led to an order in magnitude speed-up of the calculation, going from  $\pm 20$  ms on a CPU to  $\pm 600$   $\mu$ s for a single 500 by 500 frame [25]. This brings the computation time for a simulation of multi-energy and multi-projection CT scans to a range suitable for large scale studies. Similar speed-ups can be achieved for CT reconstruction algorithms, as was already demonstrated by [11]. Some new developments, with respect to the implementation of iterative CT reconstruction schemes on the GPU, will be discussed in chapter 3.

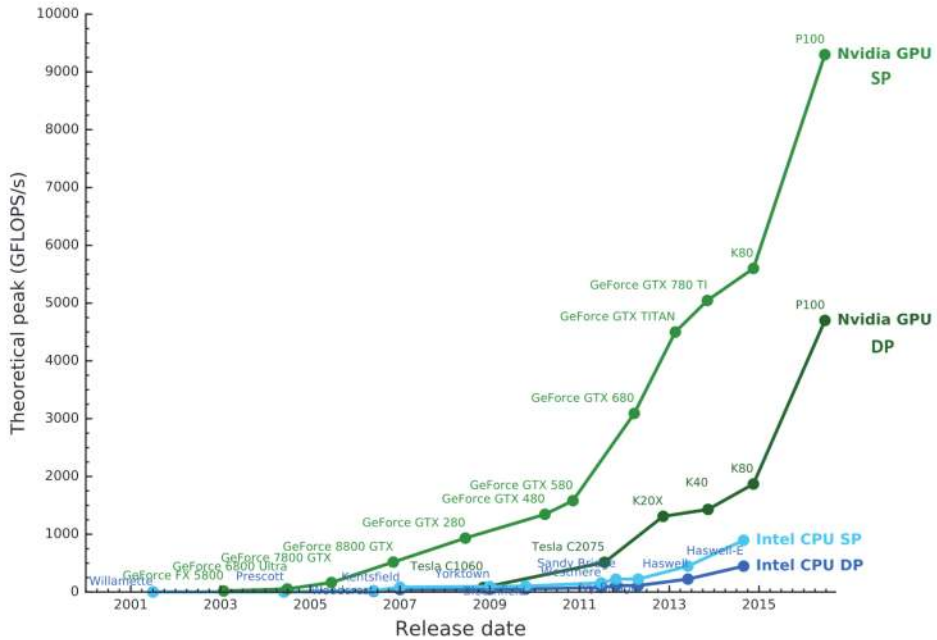


Figure 2.24: Comparison between the theoretical peak performances of GPUs versus CPUs. More and more, GPUs are vastly outperforming CPUs in terms of theoretical performance. Moreover, with the advent of the new Pascal architecture a leap in GPU performance has been achieved [46–48]. In this figure, SP and DP refer to Single and Double floating point operations, respectively.

## 2.4 Describing a cone beam CT geometry

### 2.4.1 Global versus component reference frames

A radiographic cone beam setup is a projective geometry composed out of three essential components, namely:

1. a source point,
2. a projected volume of interest (VOI),
3. and a flat panel detector.

To describe this geometry in a flexible way, and enable an arbitrary spatial configuration of the components, a local reference frame is attached to each one of them (see Figure 2.25). A parametrisation of this spatial configuration leads to 15 degrees of freedom, when only rigid transformations are considered, and when the source is effectively represented by a singular point. As explained, in the next sections this is a redundant representation, which allows users to intuitively define the orientations and locations of the components with respect to a global reference

frame of their choosing. On the other hand, to facilitate a GPU implementation which uses texture memory for efficient ray tracing interpolations, it is favourable to parametrise the rays in the projected volume's local frame. Using these native object coordinates, a rigid projective geometry can be described with only 9 degrees of freedom, and 15 degrees of freedom when global volume scaling and shears are accounted for (see sections 2.4.2 and 2.4.3).

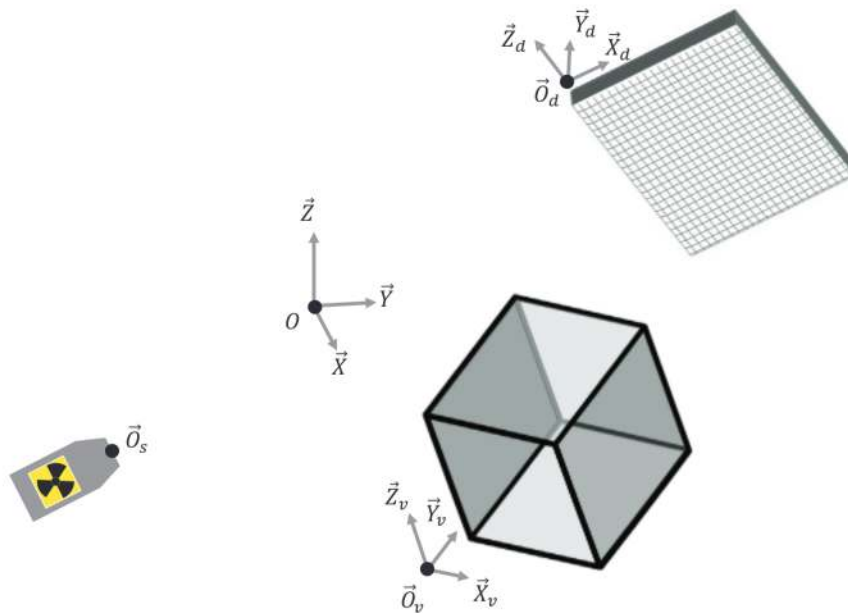


*Figure 2.25: Reference frames in a cone beam projective geometry. An arbitrary global reference frame is chosen to define the orientation and position of the local reference frames attached to the source point  $S = \{\vec{0}_s\}$ , the volume of interest  $V = \{\vec{0}_v, \vec{X}_v, \vec{Y}_v, \vec{Z}_v\}$ , and the flat panel detector  $D = \{\vec{0}_d, \vec{X}_d, \vec{Y}_d, \vec{Z}_d\}$ .*

## 2.4.2 Rigid motion - Rotation & Translation

First consider rigid motions, composed out of translations and rotations of the individual components. The most intuitive way of defining a scanner component's orientation is to define its rotational transform with respect to the origin of the global reference frame, followed by a translation to its final position in space. There are many ways to compose a rotation transform, 24 to be precise, but they are all defined by three rotation angles,  $\alpha$ ,  $\beta$  and  $\gamma$  ( $SO(3)$ ). Here, a definition is used which conforms to the CT nomenclature, where rotations about the  $Y$ -axis,  $X$ -axis and  $Z$ -axis are referred to as tilts, slants and skewes, respectively. It is also in this particular order that the components are rotated about the global axes

towards their final orientation, according to a set of so-called extrinsic Tait-Bryan angles [49, 50], which leads to the following 3D rotation transform

$$\mathbf{R}(\alpha, \beta, \gamma) = \mathbf{R}_Z(\gamma) \cdot \mathbf{R}_X(\alpha) \cdot \mathbf{R}_Y(\beta)$$

composed out of the three elemental rotations, e.g. about the  $Z$ -axis,

$$\mathbf{R}_Z(\gamma) = \begin{bmatrix} \cos \gamma & -\sin \gamma & 0 \\ \sin \gamma & \cos \gamma & 0 \\ 0 & 0 & 1 \end{bmatrix}$$

and similar matrices for the  $X$  and  $Y$ -axes. The final goal is to convert the coordinates of the detector pixels ( $\vec{x}_j$ ) and the source point ( $\vec{O}_s$ ), which together define a single ray (see equation (2.12)), from a representation in the detector frame

$$\vec{x}_j = x_{j,d} \cdot \vec{X}_d + z_{j,d} \cdot \vec{Z}_d$$

to representation in the volume's frame of reference

$$\vec{x}_j = x_{j,v} \cdot \vec{X}_v + y_{j,v} \cdot \vec{Y}_v + z_{j,v} \cdot \vec{Z}_v.$$

This can easily be achieved by first rotating the detector coordinates to the global frame, according to the prescribed detector angles, followed by a translation to its correct position.

$$\begin{bmatrix} X_j \\ Y_j \\ Z_j \end{bmatrix} = \mathbf{R}_d(\alpha_d, \beta_d, \gamma_d) \cdot \begin{bmatrix} x_{j,d} \\ 0 \\ z_{j,d} \end{bmatrix} + \vec{O}_d$$

Finally, a global coordinate transform is performed, which realigns the volume's position and orientation with the global coordinate axes. The result is a composite transform which links the local detector to the volume coordinates, expressed as

$$\begin{bmatrix} x_{j,v} \\ y_{j,v} \\ z_{j,v} \end{bmatrix} = \mathbf{R}_{d,v} \cdot \begin{bmatrix} x_{j,d} \\ 0 \\ z_{j,d} \end{bmatrix} + \vec{O}_{d,v} \quad (2.27)$$

where

$$\mathbf{R}_{d,v}(\alpha_{d,v}, \beta_{d,v}, \gamma_{d,v}) = \mathbf{R}_v^T \cdot \mathbf{R}_d \quad (2.28a)$$

$$\vec{O}_{d,v} = \mathbf{R}_v^T \cdot (\vec{O}_d - \vec{O}_v) \quad (2.28b)$$

$$\vec{O}_{s,v} = \mathbf{R}_v^T \cdot (\vec{O}_s - \vec{O}_v) \quad (2.28c)$$

The equations in (2.28) reveal how a rigid projective geometry can be parametrised by three rotation angles, combined with both the detector and source positions

with respect to the volume reference frame ( $\vec{O}_{d,v}$  and  $\vec{O}_{s,v}$ ), yielding 9 degrees of freedom in total. In summary, all of the ray tracing operations are handled in the volume's orthogonal reference frame, by transforming the native detector coordinates through an intermittent conversion to the global frame. This approach is very similar to the '*model-view*' principle introduced in OpenGL [51].

### 2.4.3 Affine motion - Scaling & Shear

The model-view transform is further complicated when a volume is subjected to a uniform stretch or shear. These modes of motion can be relevant in CT when an object is undergoing a global deformation during an acquisition. This normally leads to motion blurring artefacts in the reconstructions, unless the deformations are somehow estimated and properly compensated for [52–54]. While in some applications an object's deformation can be approximated by uniform stretches and/or shears, better results can be obtained through local, non-rigid descriptions of deformation, often based on registration techniques (see chapter 5) [55, 56]. Nonetheless, with a view to their application in CT reconstruction, uniform stretches and shears are a first order approach towards incorporating some notion of object deformation at a small computational overhead.

By including stretches and shears, 6 extra degrees of freedom will be introduced to the model-view transform. Indeed, the volume's reference frame is now affine, and has to undergo an orthogonalisation procedure (Gram-Schmidt) to be realigned with the global frame. Before this orthogonalisation, the affine frame can be translated to the global frame's origin, and can be rotated in such a way that its  $X_v$ -axis is parallel to the global frame's  $X$ -axis and its  $Y_v$ -axis lies within the global frame's  $XY$ -plane (Figure 2.26). When the affine frame is aligned in this way, the orthogonalisation can be described as a 2 step process, in which the three remaining  $\vec{Y}_v$  and  $\vec{Z}_v$ -components are eliminated, followed by a normalisation of the three volume frame axes. In terms of transformation matrices this can be written as

$$\mathbf{S}_v^{-1} = \mathbf{Sc}^{-1} \cdot \mathbf{Sh}^{-1} = \begin{bmatrix} 1/a_x & 0 & 0 \\ 0 & 1/a_y & 0 \\ 0 & 0 & 1/a_z \end{bmatrix} \cdot \begin{bmatrix} 1 & -\sigma_{xy} & -\sigma_{xz} \\ 0 & 1 & -\sigma_{yz} \\ 0 & 0 & 1 \end{bmatrix} \quad (2.29)$$

with

$$a_x = \langle \vec{X}, \vec{X}_v \rangle, \quad a_y = \langle \vec{Y}, \vec{Y}_v \rangle, \quad a_z = \langle \vec{Z}, \vec{Z}_v \rangle$$

$$\sigma_{xy} = \frac{\langle \vec{X}, \vec{Y}_v \rangle}{a_y}, \quad \sigma_{yz} = \frac{\langle \vec{Y}, \vec{Z}_v \rangle}{a_z}, \quad \sigma_{xz} = \frac{\langle \vec{X}, \vec{Z}_v \rangle}{a_z} - \sigma_{xy} \cdot \sigma_{yz}.$$

The scale-shear transform does not preserve orthogonality, and more importantly it changes the metric in the sense that distances are no longer the ones perceived in the original frame. For the ray tracing formula (2.11) this implies that for each individual ray the distance  $\Delta t$  should be scaled according to

$$\tilde{\Delta t} = \frac{\left\| \mathbf{R}_{d,v} \cdot (\vec{x}_j - \vec{O}_s) \right\|}{\left\| \mathbf{S}_v^{-1} \cdot \mathbf{R}_{d,v} \cdot (\vec{x}_j - \vec{O}_s) \right\|} \Delta t. \quad (2.31)$$

It is also important that the pixel solid angle ( $\Omega_j$ ) is evaluated before the orthogonalisation, in a frame where angles are preserved. In summary, the model-view previously described by (2.28) is extended towards a fully affine transform, and is now defined by

$$\begin{bmatrix} x_{j,v} \\ y_{j,v} \\ z_{j,v} \end{bmatrix} = \mathbf{A}_{d,v} \cdot \begin{bmatrix} x_{j,d} \\ 0 \\ z_{j,d} \end{bmatrix} + \vec{O}_{d,v} \quad (2.32)$$

with

$$\mathbf{A}_{d,v} = \mathbf{S}_v^{-1} \cdot \mathbf{R}_{d,v} \quad (2.33a)$$

$$\vec{O}_{d,v} = \mathbf{S}_v^{-1} \cdot \mathbf{R}_v^T \cdot (\vec{O}_d - \vec{O}_v) \quad (2.33b)$$

$$\vec{O}_{s,v} = \mathbf{S}_v^{-1} \cdot \mathbf{R}_v^T \cdot (\vec{O}_s - \vec{O}_v) \quad (2.33c)$$

keeping in mind the metric change attributed to the scales and shears. A projective geometry, including a geometrical distortion caused by scales and shears, can thus be parametrised with 15 degrees of freedom.

During the discussion above the scale and shear modes were mathematically factorised out of the complete affine transform. From the user's perspective, defining the shears and scales directly in this factorised form is not the most intuitive way to prescribe a sample's deformation. It is easier to look at the modes in their respective principal frames, where the scale and shear matrices effectively take on a form similar to the ones in (2.29). In other words, the user can provide frames in which the stretches and shears are operating in well defined directions, which means that their matrices are subjected to an orthogonal matrix transform of the form,

$$\hat{\mathbf{S}}'_v = \mathbf{R}^T \cdot \hat{\mathbf{S}}_v \cdot \mathbf{R}$$

rotating back and forward between the original volume frame and the principal frame, where  $\hat{\mathbf{S}}_v$  is diagonal or triangular for the scale or shear modes, respectively. The redundancy in this parametrisation allows user to intuitively prescribe each of the individual affine deformation modes for an object.

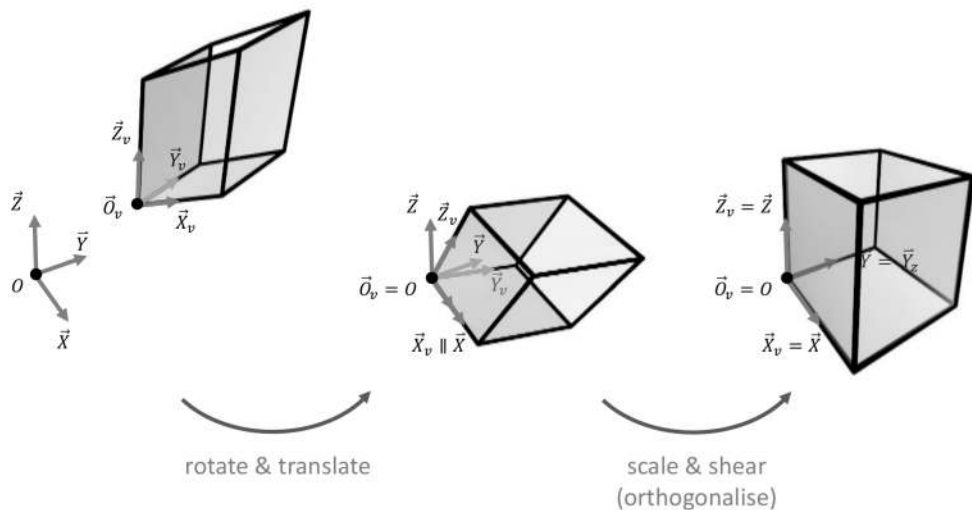


*Figure 2.26: Realigning a volume's affine reference frame with the global orthogonal frame. After aligning the XY-planes of both frames, such that  $\vec{X}_v \parallel \vec{X}$  and  $\vec{O}_v = O$ , the scales and shears can be eliminated through a Gram-Schmidt orthogonalisation.*

#### 2.4.4 Defining CT trajectories

A CT scan is essentially a large collection of radiographs, each acquired at a different relative orientation and/or position of the components in the cone beam setup. The sequence, which defines the component orientations, is called a CT trajectory, and links a 15 parameter entry to each radiograph in the CT scan. As mentioned before, the radiography simulator extracts the 15 parameter representation form a redundant parametrization of the projective configuration, where

- the source is defined by its position (3 parameters),
- the volume by its position, orientation, and scale and shear in their respective principal frames (18 parameters),
- and the detector by its position and orientation (6 parameters).

The radiography simulator also implements some standard trajectories, for which the component orientations and positions can be generated with just a few parameters, such that e.g. the source and detector travel along a helical or circular trajectory.

### 2.5 An example: simulated CT scans of fruit

#### 2.5.1 A fruit phantom

In the context of the TomFood project, the radiography simulator was used as a cost effective tool to evaluate alternative X-ray CT approaches for in-line quality

control on food products. Hence, in this section we demonstrate the capabilities of the radiography simulator, using a digital phantom of an Elstar apple. The same phantom will be used in the simulation based branch of the feasibility study on the in-line conveyor belt trajectory, discussed in chapter 4.

The digital phantom was based on a high quality X-ray micro-CT scan (voxel size  $64 \mu\text{m}$ ) of an Elstar apple. The 8-bit gray values in the reconstruction of this scan serve as a measure for the density of the apple tissue, which can be modelled as a soft tissue material when it comes to the mass attenuation coefficient (see Figure 2.4) [7]. In other words, each voxel in the digital phantom volume is set to contain soft tissue at a density which is linearly mapped to the gray values in the CT reconstruction of the high quality scan. In this mapping, air, with a density of  $1.2 \cdot 10^{-3} \text{ g/cm}^3$  [57], is represented by the lowest gray value, while the attenuation average taken across the bulk of the apple tissue  $\mu_{\text{bulk}} = 0.29 \text{ cm}^{-1}$ , is associated to the measured mass density of the apple tissue, i.e.  $\rho_{\text{apple}} = 0.84 \text{ g/cm}^3$ . To calculate the latter, the apple is weighed on a *mg*-scale, and the bulk tissue of the Elstar apple was digitally segmented (excluding the core air space) to obtain an accurate tissue volume estimate. In summary, the digital apple phantom is represented by a 3D regular grid of voxels each containing one out of 256 labels, referring to a soft tissue material with a linearly scaled density (see Figure 2.27).

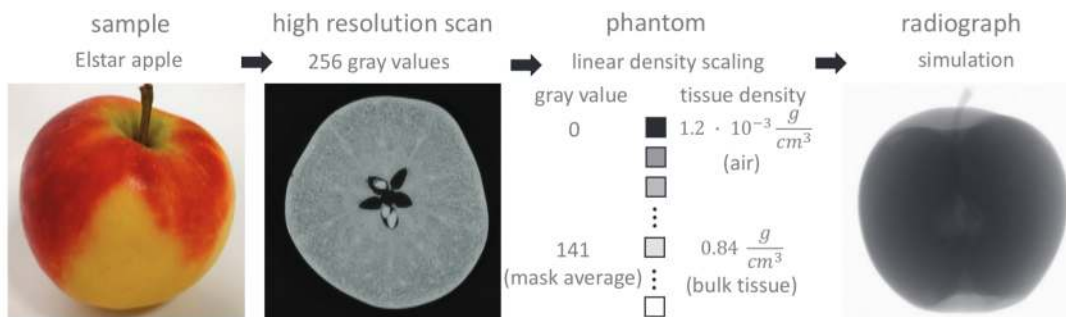


Figure 2.27: Procedure for constructing a digital apple phantom, as an input to the radiography simulator. The gray values from an X-ray  $\mu\text{CT}$  scan (voxel size  $64 \mu\text{m}$ ) of an Elstar apple are used to represent 256 apple tissue classes, which are modelled by a soft tissue mass attenuation curve and a density linearly scaled to their gray values.

## 2.5.2 Testing the simulator

### Real versus simulated

In Figure 2.28, a radiograph taken from the high quality acquisition, which forms the basis for the digital phantom, is compared to a simulated radiograph of the phantom at comparable tube and detector setting (see table 2.2). Both the radiographs and the selected line profile indicate a good agreement between the simula-

tions and the original base line scan. The small differences are caused by a slight misalignment of the phantom volume with respect to the real objects position. The output of the radiography simulator is also validated in chapter 4, where a similar comparison is made between the radiographs acquired in an in-line conveyor belt mock-up and its simulated counterpart.

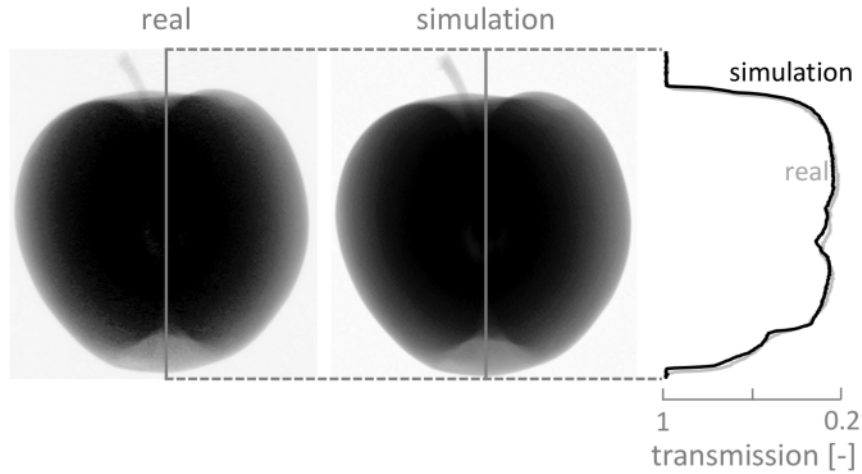


*Figure 2.28: Comparison between a real and simulated radiograph of the Elstar apple and its derived digital phantom, respectively. A good agreement is seen in both the radiographs and the indicated line profiles.*

*Table 2.2: Tube and detector settings for the circular cone beam scan, which forms the basis for the digital Elstar apple phantom.*

Tube	Feinfocus FXE160.51 with tungsten target		
Tube voltage	$(V_t)$	120	kV
Tube power	$(P_t)$	8	W
Detector	Varian PaxScan 1515DXT		
Exposure time	$(t_{exp})$	1668	ms
Detector size	$(W,H)$	(575,575)	-
Binned pixel size	$(P_d)$	254	$\mu\text{m}$
Binning	(-)	2 by 2	-
Geometry	Circular cone beam		
Source Detector Distance	$(\text{SDD})$	1030.2	mm
Source Object Distance	$(\text{SOD})$	520.1	mm
Number of projections	$(N_p)$	1400	-
Reconstruction	SART		
Voxel pitch	$(P_v)$	64	$\mu\text{m}$
Voxel grid	$(W,H,D)$	(512,512,376)	-
Iterations	(-)	1	-
Relaxation	(-)	0.5	-

It is also important to note that the radiography simulator adequately mimics the

noise behaviour of a real radiograph. An estimate for the Signal to Noise Ratio (SNR) can serve as a measure for the noise behaviour in the radiographs, and is calculated here by taking a moving average ( $\hat{\mu}$ ) and variance ( $\hat{\sigma}^2$ ) across a line profile. The SNR, expressed in  $dB$ , can be found with

$$\text{SNR} = 10 \cdot \log\left(\frac{\hat{\mu}^2}{\hat{\sigma}^2}\right) \quad (2.34)$$

as illustrated by Figure 2.29, for the line profile in Figure 2.28.

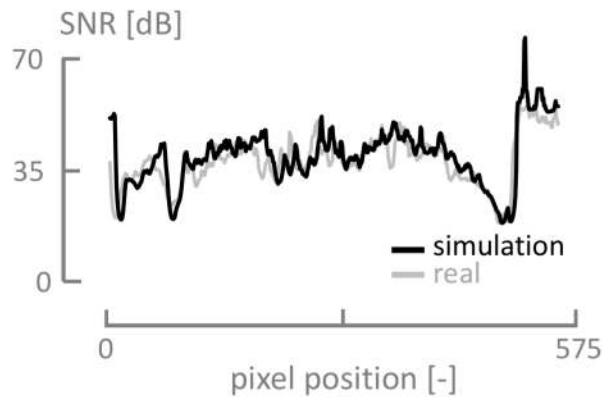


*Figure 2.29: A good agreement is found between the SNR-profiles in the simulated and real Elstar radiographs. The moving average and variance were evaluated with 9 pixel wide kernels.*

A final way to compare the simulations to the real data, is through their CT reconstructions, which prove to be nearly identical (see Figure 2.30). These results suggest that the methodology for constructing an apple phantom and calibrating its density, is valid and accurate.

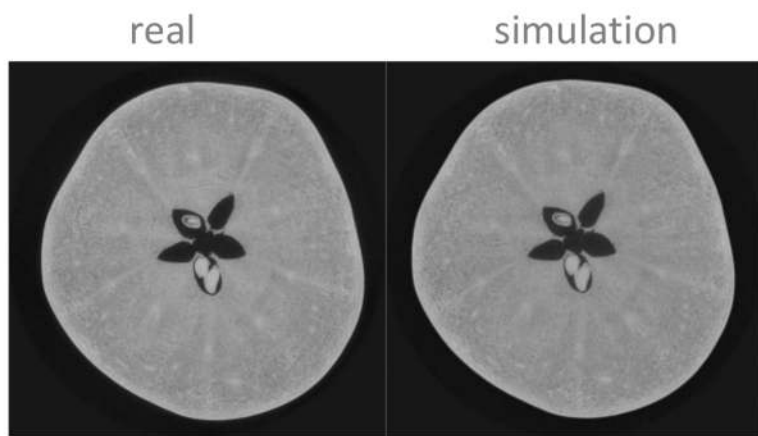


*Figure 2.30: Comparison between the reconstruction of a simulated and a real CT dataset, which prove to be nearly identical.*

## Arbitrary orientations

The same phantom can now be used to explore new geometrical configurations, for which real radiographs were or can not be acquired. The simulated radiographs of the rotated, compressed and sheared apple are depicted in Figure 2.31.

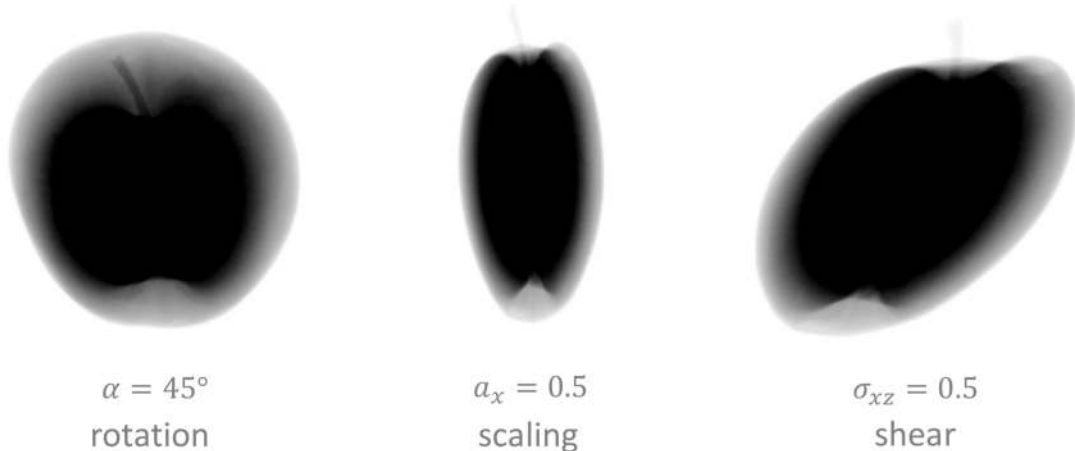


*Figure 2.31: Monochromatic simulations of radiographs taken in arbitrary geometrical configurations. From left to right, the apple is rotated about the X-axis, compressed in the X-direction and sheared parallel to the XY-plane.*

## 2.6 Conclusion

The essential steps of the X-ray CT imaging process, i.e. acquisition, reconstruction and analysis, have been touched in this chapter. A specific emphasis is put on the acquisition step, how its intricacies are translated to the hardware setups of the UGCT and how its physics can be modelled to a first order. Working towards the GPU-accelerated and realistic simulation of radiographs, a so-called ‘*radiography simulator*’ was developed [25]. The flexible and intuitive parametrisation of the geometrical configurations in which the radiographs are simulated, enable arbitrary trajectories to be defined for each of the components (source, object and detector). Moreover, the results of the radiography simulator prove to be valid and accurate, as demonstrated here through simulated radiographs of a carefully constructed digital fruit phantom. In summary, X-ray CT acquisitions in arbitrary, non-standard geometries can now be simulated, with a GPU-accelerated implementation of a first-order, polychromatic X-ray attenuation model.

## References

- [1] Be Masschaele, M Dierick, D Van Loo, M N Boone, L Brabant, E Pauwels, V Cnudde, and L Van Hoorebeke. *HECTOR: A 240kV micro-CT setup optimized for research*. Journal of Physics: Conference Series, 463(1):12012, 2013.
- [2] M N Boone. *New imaging modalities in high resolution X-ray tomography*. PhD thesis, Ghent University, 2013.
- [3] Jelle Vlassenbroeck. *Advances in laboratory-based X-ray microtomography*. PhD thesis, Ghent University, 2009.
- [4] J A Seibert and J M Boone. *X-ray imaging physics for nuclear medicine technologists. Part 2: X-ray interactions and image formation*. Journal of nuclear medicine technology, 33(1):3–18, 2005.
- [5] J A Seibert. *X-ray imaging physics for nuclear medicine technologists. Part 1: Basic principles of x-ray production*. Journal of nuclear medicine technology, 32(3):139–147, 2004.
- [6] J E Turner. *Atoms, Radiation, and Radiation Protection: Third Edition*. Wiley-VCH Verlag GmbH & Co. KGaA, 2007.
- [7] M J Berger and S M Seltzer. *XCOM Photon Cross Sections*, volume 3. Version, 1999.
- [8] M Dierick, D Van Loo, B Masschaele, J Van den Bulcke, J Van Acker, V Cnudde, and L Van Hoorebeke. *Recent micro-CT scanner developments at UGCT*. Nuclear Instruments and Methods in Physics Research Section B: Beam Interactions with Materials and Atoms, 324:35–40, 2014.
- [9] S R Deans. *Random and Abel Transforms*. In *Transforms and Applications Handbook*, Third Edition, Electrical Engineering Handbook. CRC Press, jan 2010.
- [10] B D Smith. *Image reconstruction from cone-beam projections: necessary and sufficient conditions and reconstruction methods*. IEEE transactions on medical imaging, 4(1):14–25, jan 1985.
- [11] Yoni De Witte. *Improved and practically feasible reconstruction methods for high resolution X-ray Tomography*. PhD thesis, Ghent University, 2010.
- [12] M Defrise, F Noo, and H Kudo. *A solution to the long-object problem in helical cone-beam tomography*. Physics in medicine and biology, 45(3):623–643, 2000.

- [13] J F Barrett and N Keat. *Artifacts in CT: Recognition and Avoidance*. Radio-Graphics, 24(6):1679–1691, 2004.
- [14] A Kak and M Slaney. *Principles of Computerized Tomographic Imaging*. Society for Industrial and Applied Mathematics, 2001.
- [15] W Schroeder, K Martin, and B Lorensen. *The visualization toolkit: an object-oriented approach to 3D graphics*. Kitware, 2006.
- [16] A Limaye. *Drishti: a volume exploration and presentation tool*. In Proc. SPIE, volume 8506, pages 85060X–85060X–9, 2012.
- [17] T S Yoo, Michael J Ackerman, W E Lorensen, W Schroeder, V Chalana, S Aylward, D Metaxas, and R Whitaker. *Engineering and Algorithm Design for an Image Processing API: A Technical Report on ITK - the Insight Toolkit*. Studies in Health Technology and Informatics, 85:586–592, 2002.
- [18] G Bradski. *The opencv library*. Doctor Dobbs Journal, 25(11):120–126, 2000.
- [19] S van der Walt, J L Schönberger, J Nunez-Iglesias, F Boulogne, Joshua D Warner, N Yager, E Gouillart, and T Yu. *scikit-image: image processing in Python*. PeerJ, 2:e453, 2014.
- [20] J Schindelin, I Arganda-Carreras, E Frise, V Kaynig, M Longair, T Pietzsch, S Preibisch, C Rueden, S Saalfeld, B Schmid, J-Y Tinevez, D J White, V Hartenstein, K Eliceiri, P Tomancak, and A Cardona. *Fiji: an open-source platform for biological-image analysis*. Nature Methods, 9(7):676–682, 2012.
- [21] B C Masschaele, J Vlassenbroeck, V Cnudde, M Dierick, P Jacobs, and L Van Hoorebeke. *UGCT: New X-ray radiography and tomography facility*. Nuclear Instruments and Methods in Physics Research Section A: Accelerators, Spectrometers, Detectors and Associated Equipment, 580(1):266–269, 2007.
- [22] K Bliznakova, Z Kolitsi, and N Pallikarakis. *Dual-energy mammography: simulation studies*. Physics in Medicine and Biology, 51(18):4497–4515, 2006.
- [23] K Bliznakova, R Speller, J Horrocks, P Liaparinos, Z Kolitsi, and N Pallikarakis. *Experimental validation of a radiographic simulation code using breast phantom for X-ray imaging*. Computers in Biology and Medicine, 40(2):208–214, 2010.

- [24] S Kasperl, J Hiller, and M Krumm. *Computed tomography metrology in industrial research & development*. International Symposium on NDT in Aerospace, pages 1–8, 2009.
- [25] J Dhaene, E Pauwels, T De Schryver, A De Muynck, Manuel Dierick, and L Van Hoorebeke. *A realistic projection simulator for laboratory based X-ray micro-CT*. Nuclear Instruments and Methods in Physics Research Section B: Beam Interactions with Materials and Atoms, 342:170–178, jan 2015.
- [26] P Duvauchelle, N Freud, V Kaftandjian, and D Babot. *Computer code to simulate X-ray imaging techniques*. Nuclear Instruments and Methods in Physics Research, Section B: Beam Interactions with Materials and Atoms, 170(1):245–258, 2000.
- [27] N Freud, P Duvauchelle, S A Pistruj-Maximean, J-M Létang, and D Babot. *Deterministic simulation of first-order scattering in virtual X-ray imaging*. Nuclear Instruments and Methods in Physics Research Section B: Beam Interactions with Materials and Atoms, 222(1-2):285–300, jul 2004.
- [28] N Freud, P Duvauchelle, J M Létang, and D Babot. *Fast and robust ray casting algorithms for virtual X-ray imaging*. Nuclear Instruments and Methods in Physics Research, Section B: Beam Interactions with Materials and Atoms, 248(1):175–180, 2006.
- [29] F Inanc. *Scattering and its role in radiography simulations*. NDT and E International, 35(8):581–593, 2002.
- [30] J Tabary, P Hugonnard, and F Mathy. *SINDBAD: a realistic multi-purpose and scalable X-ray simulation tool for NDT applications*. Int. Symp. on DIR and CT, Lyon, 2007.
- [31] F P Vidal and P F Villard. *Development and Validation of Real-time Simulation of X-ray Imaging with Respiratory Motion*. Computerized Medical Imaging and Graphics, 49:1–15, 2016.
- [32] W van Aarle, W J Palenstijn, J De Beenhouwer, T Altantzis, S Bals, K J Batenburg, and J Sijbers. *The ASTRA Toolbox: A platform for advanced algorithm development in electron tomography*. Ultramicroscopy, 157:35–47, 2015.
- [33] W van Aarle, W J Palenstijn, J Cant, E Janssens, F Bleichrodt, A Dabravolski, J De Beenhouwer, K J Batenburg, and J Sijbers. *Fast and Flexible X-ray Tomography Using the ASTRA Toolbox*. Optics Express, 24(22):25129–25147, 2016.

- [34] G Tirao, C Quintana, F Malano, and M Valente. *X-ray spectra by means of Monte Carlo simulations for imaging applications.* X-ray Spectrometry, 39(6):376–383, 2010.
- [35] E Acosta, X Llovet, E Coleoni, F Salvat, and J A Riveros. *Simulation of x-ray spectra generated by electron impact on solids.* X-ray Spectrometry, 28(2):121–127, 1999.
- [36] D W O Rogers, B A Faddegon, G X Ding, C.M. M Ma, J We, and T R Mackie. *BEAM: A Monte Carlo code to simulate radiotherapy treatment units.* Medical Physics, 22(5), 1995.
- [37] D W O Rogers, B Walters, and I Kawrakow. *BEAMnrc Users Manual.* Source, 509:1–260, 2011.
- [38] K Mueller. *Fast and accurate three-dimensional reconstruction from cone-beam projection data using algebraic methods.* PhD thesis, Ohio State University, 1998.
- [39] D a Fish, a M Brinicombe, E R Pike, and J G Walker. *Blind deconvolution by means of the Richardson-Lucy algorithm.* Journal of the Optical Society of America A, 12(1):58, 1995.
- [40] M Chabior. *Contributions to the characterization of grating-based x-ray phase-contrast imaging.* PhD thesis, Technical University of Dresden, 2011.
- [41] M N Boone, A Almeida, Y De Witte, M Dierick, Jean P Remon, C Vervaet, and L Van Hoorebeke. *Detection of very small density fluctuations in pharmaceutical samples by application of the Modified Bronnikov Algorithm on micro-CT data.* In MICROSCOPY AND MICROANALYSIS, volume 15, pages 386–387, 2009.
- [42] F Pfeiffer, T Weitkamp, O Bunk, and C David. *Phase retrieval and differential phase-contrast imaging with low-brilliance X-ray sources.* Nature Physics, 2(4):258–261, 2006.
- [43] A Peterzol, A Olivo, L Rigon, S Pani, and D Dreossi. *The effects of the imaging system on the validity limits of the ray-optical approach to phase contrast imaging.* Medical physics, 32(12):3617–3627, 2005.
- [44] P Cloetens. *Contribution to Phase Contrast Imaging, Reconstruction and Tomography with Hard Synchrotron Radiation.* PhD thesis, Vrije Universiteit Brussel, 1999.
- [45] NVIDIA. *Cuda C Programming Guide*, 2015.

- [46] Michael Galloy. *Performance comparison of CPUs and GPUs*. <https://github.com/mgalloy/cpu-vs-gpu>.
- [47] Nvidia. *List of Nvidia graphics processing units*. [https://en.wikipedia.org/wiki/List\\_of\\_Nvidia\\_graphics\\_processing\\_units](https://en.wikipedia.org/wiki/List_of_Nvidia_graphics_processing_units).
- [48] Intel. *List of Intel CPU microarchitectures*. [https://en.wikipedia.org/wiki/List\\_of\\_Intel\\_CPU\\_microarchitectures](https://en.wikipedia.org/wiki/List_of_Intel_CPU_microarchitectures).
- [49] Euler angles. [https://en.wikipedia.org/wiki/Euler\\_angles](https://en.wikipedia.org/wiki/Euler_angles).
- [50] Christoph Gohlke. *Homogeneous Transformation Matrices and Quaternions*. <http://www.lfd.uci.edu/~gohlke>.
- [51] OpenGL. <https://www.opengl.org>.
- [52] S Roux, L Desbat, A Koenig, and P Grangeat. *Exact reconstruction in 2D dynamic CT: compensation of time-dependent affine deformations*. Physics in Medicine and Biology, 49(11):2169, 2004.
- [53] Vincent Van Nieuwenhove, Jan De Beenhouwer, Thomas De Schryver, Luc Van Hoorebeke, and Jan Sijbers. *Affine deformation correction in cone beam Computed Tomography*. In Fully Three-Dimensional Image Reconstruction in Radiology and Nuclear Medicine, pages 182–185, Newport, Rhode Island, USA, 2015.
- [54] V Van Nieuwenhove, J De Beenhouwer, Thomas De Schryver, Luc Van Hoorebeke, and J Sijbers. *Data-Driven Affine Deformation Estimation and Correction in Cone Beam Computed Tomography*. IEEE TRANSACTIONS ON IMAGE PROCESSING, 26(3):1441–1451, 2017.
- [55] A a Isola, M Grass, and W J Niessen. *Fully automatic nonrigid registration-based local motion estimation for motion-corrected iterative cardiac CT reconstruction*. Medical physics, 37(3):1093–1109, 2010.
- [56] C P V Christoffersen, D Hansen, P Poulsen, and T S Sorensen. *Registration-based reconstruction of four-dimensional cone beam computed tomography*. IEEE Transactions on Medical Imaging, 32(11):2064–2077, 2013.
- [57] E W Lemmon, M O McLinden, and D G Friend. *Thermophysical properties of fluid systems*. NIST chemistry webbook, NIST standard reference database, 69, 2005.



# 3

## CT Reconstruction algorithms

The basic principles of CT reconstruction were already introduced in chapter 2. In short, the attenuation line integrals measured in each pixel of a radiography need to be inverted to the attenuation's spatial distribution, which is supported by a voxelised volume. The algorithms that implement this inversion, are traditionally classified as '*analytical*' or '*iterative*'. The iterative methods are historically the first to be used for CT reconstruction in the 1970s [1], but when large (512 by 512) voxel matrices were considered, their computational requirements soon became intractable for the computing power available at that time. Only with the advent of fast, Fourier based filtered-backprojection algorithms, CT reconstructions of larger voxel matrices became possible. As computing power nowadays is not an issue any more, the trend from iterative to analytical is reversing, in particular because the iterative reconstruction techniques are more flexible when it comes to implementing advanced X-ray physics models or specific a priori knowledge on the nature or behaviour of the imaged object [2].

As the gold standard approach to CT reconstruction, the relevant equations for the analytical techniques and their interpretation are briefly discussed in the next section. For the specifics on their implementation and derivations, the reader will be referred to the appropriate literature. The remainder and bulk of this chapter is dedicated to iterative reconstruction (section 3.2). As a part of this work, a hybrid Python-C GPU code was developed to facilitate the iterative reconstruction of CT datasets acquired along arbitrary trajectories. Central to this implementation is its GPU-acceleration and the ability to handle very large reconstruction volumes, not

limited by the GPU RAM's size.

## 3.1 Analytic reconstruction

### 3.1.1 2D CT

#### Parallel beam

The parallel beam configuration is the simplest and coincidentally the first geometry to which Cormack and Hounsfield tailored the concept of CT [1, 3, 4]. In this geometry a pencil X-ray beam and an opposing singular detector element are swept across a plane through the scanned object, sequentially acquiring the object's attenuation integrals along a series of parallel lines in a particular direction within that plane (Figure 3.1). When the source and detector rotate about a fixed point (the origin) within this plane, the resulting profile of the projected attenuation can be parametrised by the translation coordinate ( $r$ ) and an angle ( $\theta$ ), encoding the relative orientation of the object with respect to the source-detector assembly

$$P_\theta(r) = \int \int \mu(x, y) \cdot \delta(r - x \cos \theta - y \sin \theta) dx dy \quad (3.1)$$

equivalent to a 2D radon transform of  $\mu$  (cfr. equations 2.6 and 2.7) [5, 6].

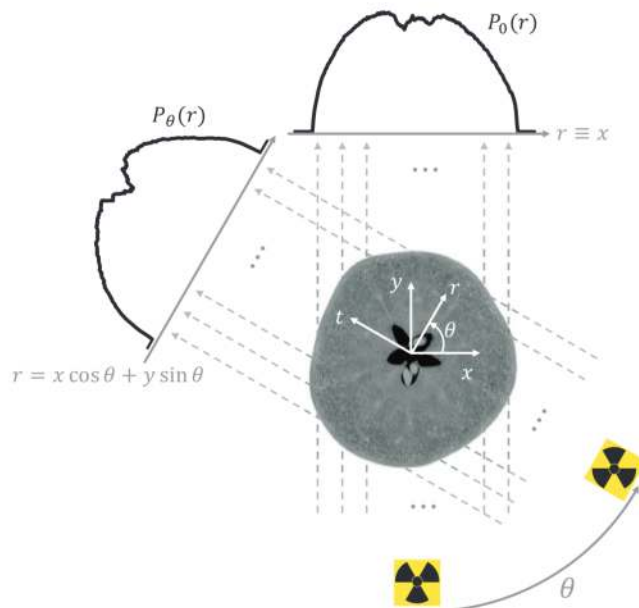


*Figure 3.1: Parallel beam geometry. In this geometry a pencil beam is swept across the object, parallel to the  $\theta$ -direction. In this way a profile of the projected attenuation can be measured.*

The Tuy-Smith condition, introduced in section 2.1.2, states that a mathematically exact reconstruction of the attenuation function  $\mu(x, y)$  can be obtained from the

measured line integrals, for all of the points in the support of  $\mu$  that are contained within the circular source trajectory. The key to inverting equation (3.1) towards an explicit expression for  $\mu(x, y)$ , lies in the ‘Fourier slice theorem’, which for the 2D case states that the 1D Fourier transform of a projection profile, acquired at an angle  $\theta$  is equal to the 2D Fourier transform of the  $\mu(x, y)$ -distribution, sampled along the line in Fourier space, which has the same angular orientation  $\theta$  with respect to the frequency axes  $(\xi, \eta)$ , as illustrated in Figure 3.2. In other words, by acquiring the projection profiles, the Fourier coefficients of  $\mu(x, y)$  are gradually sampled onto a cylindrical grid, which through an inverse Fourier transform can be converted back to  $\mu(x, y)$ . This inverse transform can be expressed in its cylindrical (frequency) coordinates  $(\rho, \theta)$ ,

$$\mu(x, y) = \int_0^{2\pi} \int_0^{\infty} F(\rho, \theta) e^{i2\pi\rho r} \rho d\rho d\theta \quad (3.2)$$

where  $F = \mathcal{F}_{(x,y)}[\mu(x, y)]$  is the 2D Fourier transform of  $\mu(x, y)$ , and  $r$  and  $\rho$  are defined through Figure 3.2. Moreover, there is an apparent symmetry for the parallel sampling strategy, between projections acquired at a  $180^\circ$  separation,

$$F(\rho, \theta + 180^\circ) = F(-\rho, \theta)$$

which further simplifies (3.2) to

$$\mu(x, y) = \int_0^{\pi} \left[ \int_{-\infty}^{\infty} F(\rho, \theta) |\rho| e^{i2\pi\rho r} d\rho \right] d\theta \quad (3.3)$$

This also means that  $\mu(x, y)$  can be reconstructed with data acquired during a rotation of only  $180^\circ$ , which again reflects the minimal requirements for a Tuy-Smith sufficient sampling. More importantly, equation (3.3) unveils a three step approach towards an exact reconstruction for a CT dataset acquired through parallel projections of the attenuation function:

1. The 1D Fourier transform of the projection profiles is calculated

$$S_\theta(\rho) = F(\rho, \theta) = \int_{-\infty}^{\infty} P_\theta(r) e^{-i2\pi\rho r} dr \quad (3.4)$$

2. A filtered version of these profiles is converted back to the spatial domain through an inverse Fourier transform

$$Q_\theta(r) = \int_{-\infty}^{\infty} S_\theta(\rho) |\rho| e^{i2\pi\rho r} d\rho \quad (3.5)$$

3. The filtered profiles are redistributed, i.e. back projected into the spatial domain according to

$$\mu(x, y) = \int_0^{\pi} Q_\theta(x \cos \theta + y \sin \theta) d\theta \quad (3.6)$$

This analytical procedure is, for obvious reasons, referred to as a ‘*filtered back projection*’ (FBP). Mathematically, the ramp filtering kernel  $\mathcal{G}(\rho) = |\rho|$  in equation (3.5) is introduced through the Jacobian of the coordinate change, going from Cartesian to polar coordinates in the Fourier domain. Intuitively, the kernel compensates for the fact that the sampling density is higher near the origin, and decreases according to the inverse of the distance to the origin. By reorganising equation (3.5) as follows,

$$Q_\theta(r) = \int_{-\infty}^{\infty} i2\pi\rho S_\theta(\rho) \frac{\mathcal{H}(\rho)}{2\pi} e^{i2\pi\rho r} d\rho \quad (3.7)$$

where the ‘*Hilbert filter*’ ( $\mathcal{H}$ ) is defined through,

$$\mathcal{H}(\rho) = \begin{cases} -i, & \rho > 0 \\ 0, & \rho = 0 \\ i, & \rho < 0 \end{cases}$$

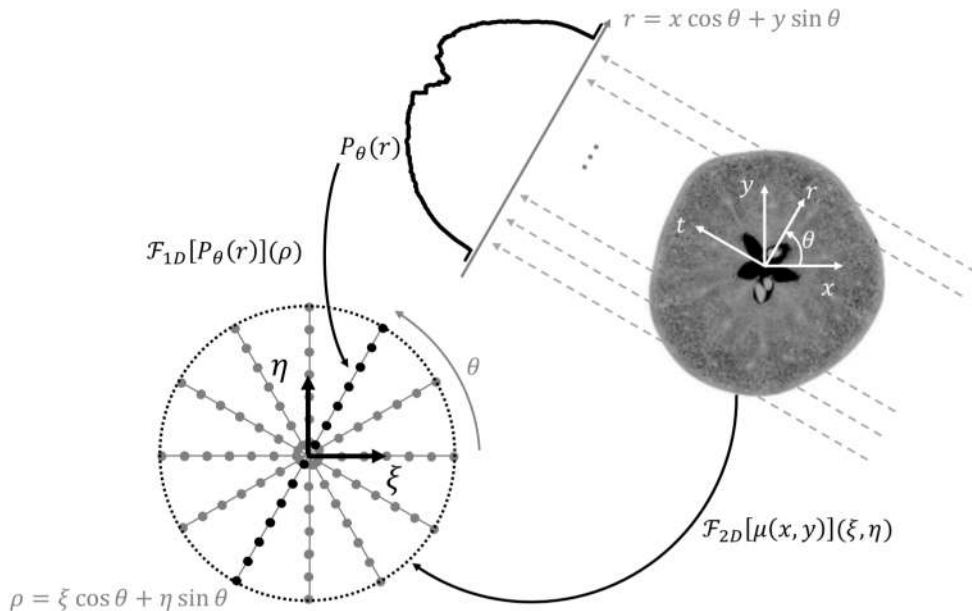


*Figure 3.2: The Fourier slice theorem in two dimensions. The 1D Fourier transform of parallel projections is equal to a slice in the 2D Fourier transform of the projected function, taken along the same direction.*

and considering that

$$\mathcal{F}_r [(\partial/\partial r) P_\theta(r)] (\rho) = i2\pi\rho S_\theta(\rho)$$

equation (3.7) can be interpreted as the Hilbert transform of the Radon transform’s derivative with respect to  $r$ . In the spatial domain this can also be expressed as

the principal value (PV) of a convolution between the Radon derivative and the tempered Hilbert distribution.

$$Q_\theta(r) = \text{PV} \left[ k_H(r') * \frac{\partial}{\partial r'} P_\theta(r') \right] (r) \quad (3.8)$$

with

$$k_H(r') = \frac{1}{\pi r'}.$$

This is a simplified version of the original inversion formula proposed by Grangeat, in his mathematical framework for cone beam 3D reconstruction [7]. A similar formula arises through Katsevich's work on helical CT trajectories, as discussed in section 3.1.2.

With a view to practical implementations of filtered back projection, it is important to note that the projection profiles are approximately band limited, in the sense that their highest frequency components are close to negligible. In the ideal case, there is no overlap between the periodic extensions of  $S_\theta(\rho)$ , and the integral in equation (3.5) can be restricted to the Nyquist sampling interval  $\rho \in [-\rho_{max}, \rho_{max}]$  with  $\rho_{max} = 1/(2p_d)$ . Here, we have implicitly taken into account the discrete nature of the sampling process, where the pixel positions in a finite detector of pixel width  $J$  are uniformly spaced, according to

$$r_j = jp_d \text{ with } j = -\lceil J/2 \rceil, \dots, \lfloor J/2 \rfloor$$

For the discretised versions of equation (3.4) to (3.6), the reader is referred to [6]. As a direct result of this discretisation, the ramp filter  $\mathcal{G}$  in (3.5) is also sampled, and truncated to a form known as the '*Ram-Lak*' filter. In other versions of the ramp filter, the higher frequency components are strategically down weighted, in order to suppress noise in the reconstructions. With the following practical implementation,

$$\mathcal{G}(\rho) = \begin{cases} |\rho| - 2p_d\alpha\rho^2 & \text{if } \rho > 1/(2p_d) \\ 0, & \text{otherwise} \end{cases}$$

the noise levels can be freely tuned by adjusting the parameter  $\alpha \in [0, 1]$  (see Figure 3.3).

### Fan beam

The fan beam geometry was already introduced through Figure 2.9, where the Tuy-Smith sufficiency of this geometry was established. The obvious difference with the parallel geometry is the oblique propagation of the rays, due to the finite

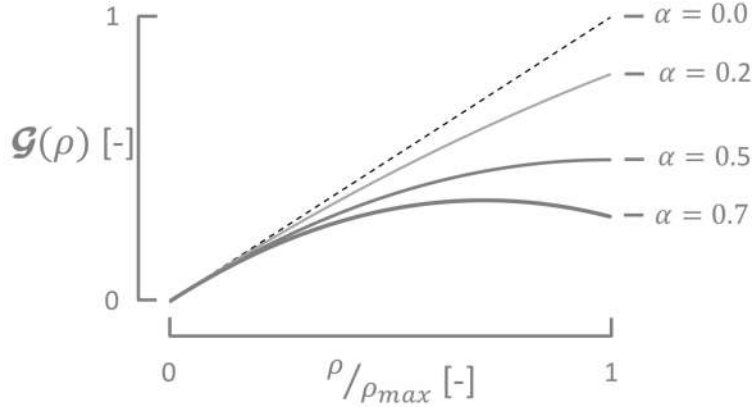


Figure 3.3: Ramp filter in the Fourier domain with adjustable modulation of high frequency components.

distance between the X-ray source point and the object centre (*SOD*). The fan based acquisition scheme forms the basis for the second generation of CT scanners [8], in which an attenuation profile of the object contained within the X-ray fan, can (almost) instantly be acquired across a multi-pixel line detector. Moreover, the lateral resolution of the projection profiles is boosted through a geometrical magnification (see Figure 3.4) with a factor

$$M = \frac{SDD}{SOD}.$$

When  $SOD \rightarrow \infty$ , there is no magnification and the fan geometry reverts back to a parallel one, revealing an intricate similarity between both. In fact, the fan beam reconstruction problem can easily be reformulated to a parallel reconstruction problem, by reordering the obliquely sampled rays into equivalent sets of parallel rays. The derivation of the fan beam FBP reconstruction formulae (3.9) is not within the scope of this work, but can be found in [5, 9, 10]. When a flat detector (Figure 3.4) is considered, the reconstruction formulae are given by

$$S_\theta(\rho) = \int_{-\infty}^{\infty} \frac{SDD}{\sqrt{SDD^2 + r'^2}} P_\theta(r') e^{-i2\pi\rho r'} dr' \quad (3.9a)$$

$$Q_\theta(r') = \int_{-\infty}^{\infty} S_\theta(\rho) |\rho| e^{i2\pi\rho r'} d\rho \quad (3.9b)$$

$$\mu(x, y) = \frac{1}{2} \int_0^{2\pi} \frac{M_t^2}{M^2} Q_\theta(M_t r) d\theta \quad (3.9c)$$

with

$$M_t = \frac{SDD}{SOD + t}$$

$$t = y \cos \theta - x \sin \theta$$

$$r = x \cos \theta + y \sin \theta$$

These equations are very similar to the ones for a parallel beam FBP reconstruction. In particular, the same three steps can be distinguished, where now pre- and post-weighting factors are introduced in to the Fourier transform and back projection steps, while the filtering step remains unchanged. Note, the magnification effect is reflected in the conversion between the local object and the detector coordinates (resp.  $r$  and  $r'$ ), i.e.  $r' = M_t r$ . For an exact reconstruction, the integration in (3.9c) can be restricted to an angular range of  $\pi + 2\gamma$  (cfr. equation (2.8)), leading to a so-called ‘short scan’. Only if the oversampled ray directions are correctly weighed with a ‘Parker filter’ [11], high frequency artefacts in the reconstructions, otherwise introduced by redundant data, can be avoided.

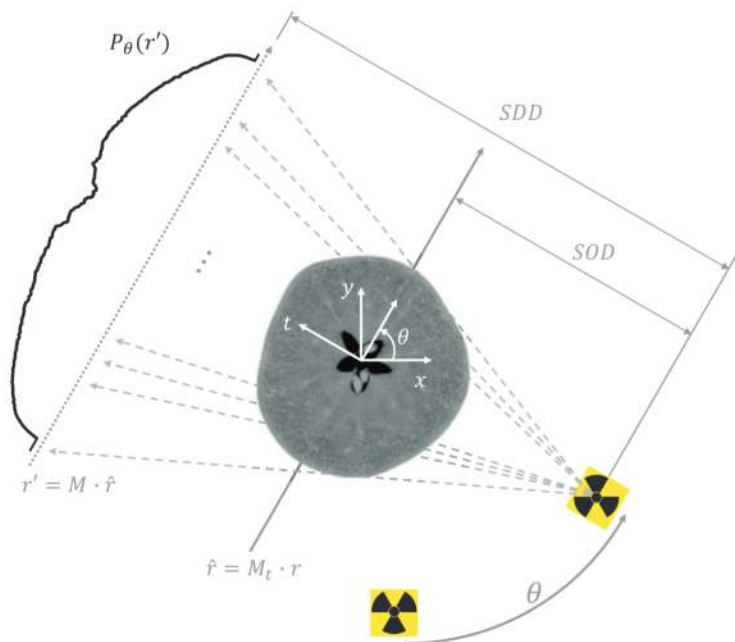


Figure 3.4: Fan beam geometry with a flat detector. The attenuation profile for an object contained within the X-ray fan, can (almost) instantly be acquired across a multi-pixel line detector. The source traces a circle with the origin at its centre.

### 3.1.2 3D CT

#### Cone beam CT

With the geometries described above it is theoretically possible to reconstruct a 3D attenuation distribution as a stack of individual 2D reconstructions. This is however a time consuming effort, which next to the rotational movement requires a vertical sweep, and in the case of the parallel geometry an extra horizontal sweep of the beam<sup>1</sup>. In the same way fan beam geometries eliminated the need for a horizontal pencil beam sweep, cone beams can suppress the vertical sweep. In other words, CT acquisition times were drastically reduced with the advent of the cone beam protocols, where the solid angle spanned by a large (flat) panel detector is uniformly illuminated by an X-ray source point. The contents of the cone formed by the detector surface and the source point is instantly projected within a single 2D radiograph. This opens up the perspective of sampling the entire Radon space in a very efficient way, and it was proven by Grangeat [7] that the Radon transform can be inverted through proper integration of its derivative. Again, the key to this inversion is the Fourier slice theorem, where in its 3D form the parallel lines are exchanged for a set of parallel planes defined by their mutual unit normal vector ( $\vec{\theta}$ ) and their distance  $r$  with respect to the origin. According to the Fourier slice theorem, the Fourier transform of  $\mathcal{R}\{\mu\}(\vec{\theta}, r)$  (cfr. equation (2.7)) with respect to  $r$ , forms a slice of  $\mu$ 's 3D Fourier transform in the  $\vec{\theta}$ -direction in frequency space ( $\vec{\xi} = [\xi, \eta, \zeta]$ ).

$$\mathcal{F}_r \left[ \mathcal{R}\{\mu\}(\vec{\theta}, r) \right] (\rho) = \mathcal{F}_{\vec{x}} [\mu(\vec{x})] (\vec{\theta} \cdot \rho) \quad (3.10)$$

The Tuy-Smith sufficiency condition determines whether this inversion will be exact, and as mentioned in section 2.1.2 this depends on the shape of the source trajectory.

#### Circular trajectories - the FDK algorithm

Except for the points enclosed within the source's 2D circular trajectory (cfr. parallel beam and fan beam CT), an exact reconstruction of a cone beam projected attenuation distribution can not be calculated from a CT dataset acquired in a cone beam circular geometry (see Figure 3.5). Indeed, any plane parallel to the one of the source trajectory (the centre plane), can by definition not contain the source and is thus not Tuy-Smith compliant. The most commonly adapted algorithm, which can still reconstruct off-centre planes with acceptable accuracy, was developed by Feldkamp, David and Kress (FDK) [10]. As a heuristic extension to fan beam reconstruction, FDK can exactly reconstruct the  $\mu$ -values in the centre plane.

---

<sup>1</sup>An exception are, for example, medical beamlines at synchrotrons, which can completely illuminate a small area detector.

Off-centre values, on the other hand, are subject to a vertical blurring, which deteriorates as the distance to the centre plane increases, i.e. a cone beam artefact arises (cfr. section 2.1.2). Despite this blurring, Rodet *et al.* have proven that any straight line integral through an FDK reconstructed volume is exact, even following lines parallel to the  $z$ -axis. They also provide a particularly handy parametrisation (3.11) for the FDK formulae [9, 10], from which the fan beam reconstruction equations (3.9) can be retrieved by setting  $z = 0$ .

$$S_\theta(\rho, z') = \int_{-\infty}^{\infty} \frac{SDD}{\sqrt{SDD^2 + r'^2 + z'^2}} P_\theta(r', z') e^{-i2\pi\rho r'} dr' \quad (3.11a)$$

$$Q_\theta(r', z') = \int_{-\infty}^{\infty} S_\theta(\rho, z') |\rho| e^{i2\pi\rho r'} d\rho \quad (3.11b)$$

$$\mu(x, y, z) = \frac{1}{2} \int_0^{2\pi} \frac{M_t^2}{M^2} Q_\theta(M_t r, M_t z) d\theta \quad (3.11c)$$

with

$$\begin{aligned} M_t &= \frac{SDD}{SOD + t} \\ t &= y \cos \theta - x \sin \theta \\ r &= x \cos \theta + y \sin \theta \end{aligned}$$

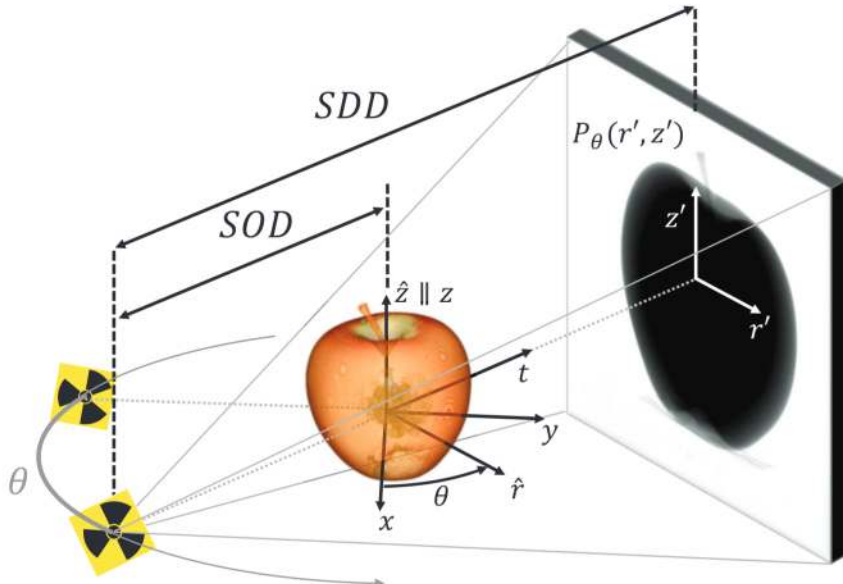


Figure 3.5: A circular cone beam geometry with a flat detector. A source spot casts a X-ray cone onto a flat panel detector, which acquires an entire 2D radiograph of the illuminated object. The source spot traces out a circle in the  $xy$ -plane with the origin at its centre.

### Helical trajectories - the Katsevich algorithm

Many Tuy-Smith compliant trajectories, which enable an exact reconstruction can be conceived, but with the prospect of a tractable practical realisation ‘*helical*’ trajectories [12] have taken the upper hand, next to less popular trajectories, e.g. ‘*circle+line*’ [13]. Conceptually, helical CT is quite simple and forms an elegant solution to a complete sampling of the Radon space, by letting the source point trace out a helical path in space relative to the scanned object, i.e.

$$\vec{O}_s(\theta) = \left[ SOD \cos \theta, SOD \sin \theta, z_p \frac{\theta}{2\pi} \right]^T,$$

where  $z_p$  represents the helical pitch (Figure 3.6). The helix can be spun out over multiple rotations ( $\theta > 2\pi$ ), encapsulating a cylindrical region of a large vertical extent. Moreover, it can be shown that all of the points within this cylindrical region can be reconstructed exactly. This is particularly easy to grasp for the points on any straight line that connects two (non-coinciding) points on the helical path, called a ‘*PI-line*’. From the following intuitive formulation of the Tuy-Smith sufficiency condition,

$\mu(\vec{x})$  can be reconstructed exactly in  $\vec{x}$  given any source trajectory,

1. that does not intersect  $\vec{x}$ , and
2. whose endpoints are collinear with  $\vec{x}$ .

it should be clear that all of the points on a PI-line can be reconstructed exactly if the source traverses the entire helical segment (a ‘*PI-segment*’) delineated by the PI-line’s endpoints ( $\vec{O}_s(\theta_t)$  and  $\vec{O}_s(\theta_b)$ )<sup>2</sup>. Furthermore, it can be shown that there is a unique PI-line intersecting each point  $\vec{x}$  contained within the cylinder encapsulated by the helix. Consequently, it is possible to exactly reconstruct the  $\mu$ -distribution supported by this cylinder, as long as the relevant PI-segments are covered. In short, if the PI-segment of  $\vec{x}$  is traversed by the source, its underlying  $\mu$ -value can be reconstructed.

As another somewhat trivial property, the PI-lines self-project the helical path onto the detector plane, when the source is positioned in one of the endpoints. If this is done for a series of consecutive PI-lines (see Figure 3.6(a)), the helical turns above and below the central source position are projected to a pair of lines crossing the detector. The area bounded by these lines is called a ‘*Tam-Danielsson window*’ (TDW) [14, 15], and contains the data relevant to reconstruction, in the sense that the remaining area outside of this window only measures redundant data. This is explained best through Figure 3.6(b), where the helical trajectory is considered to

---

<sup>2</sup>‘*t*’ as in ‘*top*’, ‘*b*’ as in ‘*bottom*’

be the result of a downward screw-like motion of the scanned object relative to a stationary source and detector. The rays in this figure represent one and the same PI-line, though depicted in two different rotational states of the object, i.e.  $\theta$  and  $\theta^* = \theta - \theta_t + \theta_b$ . In these states, the projections for all of the points on the rotated PI-line fall respectively onto the bottom and top boundaries of the TDW. Whereas in between, the PI-line's points are projected onto individual trajectories through and always falling inside of the TDW. In fact, following the reasoning above, these trajectories constitute the Tuy-Smith sufficient CT data.

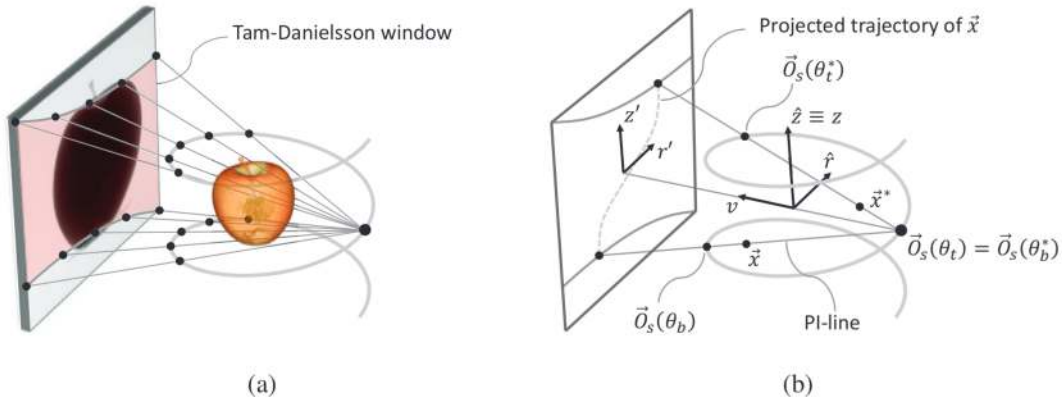


*Figure 3.6: Tam-Danielsson window (TDW) and PI-lines in helical cone beam CT. (a) The projections of the upper and lower segments on a helical path, with respect to a central source position, form the bounds to the TDW, which contains the non-redundant data necessary for an exact helical CT reconstruction. (b) The endpoints of a PI-line are always projected on the TDW boundaries. Other points are projected onto trajectories through and always falling inside of the TDW.*

A last important prerequisite to the reconstruction of helical CT data is the notion of so-called ‘ $\kappa$ -planes’ and their intersection with the detector plane, the ‘ $\kappa$ -lines’ (Figure 3.7). Each point  $\vec{x}$  can be associated to a unique  $\kappa$ -plane formed by the unique PI-line through  $\vec{x}$  and the source point on the helix halfway between the PI-line’s endpoints. For a given central source position ( $\theta$ ) all of the  $\kappa$ -planes are formed by the points  $\vec{O}_s(\theta), \vec{O}_s(\theta+\psi)$  and  $\vec{O}_s(\theta+2\psi)$  with  $\psi \in ]-\pi/2, \pi/2[$ , and the  $\kappa$ -lines can be expressed in local detector coordinates, as follows [6, 16, 17]

$$z'_\kappa(\theta, \psi) = z_p \cdot M \cdot \frac{\psi}{2\pi} \cdot \left( 1 + \frac{x'}{SDD \tan \psi} \right). \quad (3.12)$$

There are many algorithms to reconstruct helical CT data, in an either exact or approximate way [18, 19]. However, the concepts presented above, all relate to the FBP approach developed by Katsevich [20], as a specific case of his general inversion scheme for cone beam CT [21]. Following the parametrisation of Noo *et al.* [16, 17], Katsevich’s helical FBP reconstruction formulae are given by

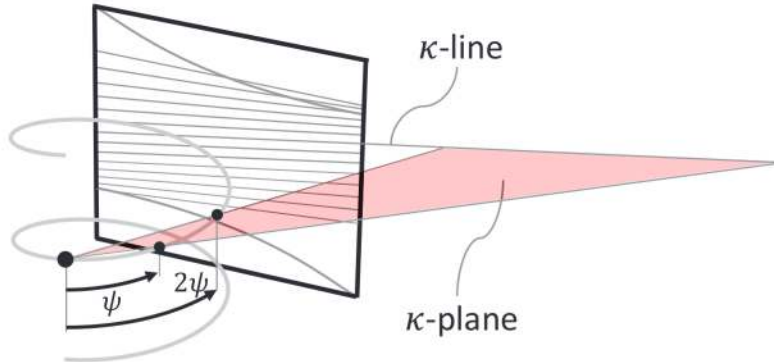


*Figure 3.7:  $\kappa$ -lines & planes on a flat detector in a helical CT geometry. A  $\kappa$ -plane is defined by a PI-line and the point on the helix half way between this PI-lines endpoints. A  $\kappa$ -line is formed by the intersection of a  $\kappa$ -plane with the detector plane. For a given detector position each point in the volume can be associated to a unique  $\kappa$ -line.*

$$P_\theta^D(r', z') = \left[ \frac{\partial}{\partial \theta} + \frac{r' + SDD^2}{SDD} \frac{\partial}{\partial r'} + \frac{r' z'}{SDD} \frac{\partial}{\partial z'} \right] P_\theta(r', z') \quad (3.13a)$$

$$Q_\theta(r', z'_\kappa) = \int_{-\infty}^{\infty} k_H(r' - r'') \frac{SDD}{\sqrt{SDD^2 + r''^2 + z''_\kappa^2}} P_\theta^D(r'', z'') dr'' \quad (3.13b)$$

$$\mu(x, y, z) = \frac{1}{2\pi} \int_{\theta_b(\vec{x})}^{\theta_t(\vec{x})} \frac{M_t}{SDD} Q_\theta(M_t r, M_t z^*) d\theta \quad (3.13c)$$

with

$$\begin{aligned} M_t &= \frac{SDD}{SOD + t} \\ t &= y \cos \theta - x \sin \theta \\ r &= x \cos \theta + y \sin \theta \\ z^* &= z - z_p \frac{\theta}{2\pi} \end{aligned}$$

The main difference between this algorithm and the FDK-algorithm for circular trajectories (equation (3.11)), is revealed in the filtering step, which is no longer performed in Fourier space. Indeed, the derivatives of the projection data is explicitly calculated and filtered with a Hilbert kernel similar to (3.8). Also, while the

pre-weighting factor is exactly the same as in the fan beam and FDK algorithms, the post-weighting factor in the back-projection step is notably different, assuring a fair weighting for all of the rays sampled while travelling the PI-segment of  $\vec{x}$ ,  $\theta \in [\theta_b(\vec{x}), \theta_t(\vec{x})]$ . Intuitively, the quadratic pre-weighting factor in the fan beam algorithm reflects the multiplicity in the circular sampling process, which is lifted by introducing a pitch ( $z_p > 0$ ). The filtering process in (3.13b) also involves a forward and backward resampling between the original detector coordinates  $(x', z')$  and the  $\kappa$ -lines  $(x', z'_\kappa)$ . In other words, the data is actually filtered along the  $\kappa$ -lines, and not across the original detector rows as is the case for fan beam and FDK reconstructions. For a specific implementation of the Katsevich algorithm, the reader is referred to [6, 16, 22].

## 3.2 Iterative reconstruction

### 3.2.1 CT as an algebraic system of equations

As a first step in the iterative reconstruction approach a forward model for the radiographic projection process needs to be formulated, such as the first order model introduced throughout section 2.3. In its monochromatic form for a single energy bin this first order model is based on the Lambert-Beer law, which directly explains the measured transmissions, cfr. equation (2.6). And with a view to reconstructing the  $\mu$ -distribution on a grid of voxels, as in Figure 2.19, the line integral in (2.6) can be discretised as follows

$$p_j = -\ln \left[ \frac{I_j}{I_{0,j}} \right] = \sum_{l=0}^L t_{jl} \cdot \mu_l. \quad (3.14)$$

True to the ray assumption, the weights  $t_{jl}$  can be interpreted as intersection lengths between rays  $j$  with voxels  $l$ . A set of algebraic equations can be composed by gathering the data sampled by each ray, which can subsequently be cast into a matrix form

$$\vec{p} = \mathbf{T} \vec{\mu}. \quad (3.15)$$

where  $\mathbf{T}$  represents a  $(J \times L)$  weight matrix, linking the  $J$  measurements to the  $L$  unknown attenuation values, i.e.

$$[\mathbf{T}]_{jl} = t_{jl} \text{ and } [\vec{\mu}]_l = \mu_l.$$

A reconstruction thus amounts to an inversion of the matrix equation (3.15). Unfortunately,  $\mathbf{T}$ , being a projection operator, is rarely invertible or even square for that matter, and (3.15) can only be inverted in a least square sense using the normal equations,

$$\vec{\mu} = (\mathbf{T}^T \mathbf{T})^{-1} \mathbf{T}^T \vec{p} = \mathbf{T}^\dagger \vec{p}$$

which minimises the least square norm  $\|\vec{p} - \mathbf{T}\vec{\mu}\|$ . Even the least squares approach is at the grace of a well conditioned Moore-Penrose inverse ( $\mathbf{T}^\dagger$ ), which is not the case for (3.15) describing a CT acquisition. Indeed, many measurements  $p_j$  stem from closely positioned and nearly parallel rays, leading to a poor linear independence of rows and columns in  $\mathbf{T}^T \mathbf{T}$ . In other words, if it exists, the Moore-Penrose inverse for the CT reconstruction problem is generally ill-conditioned, particularly when the data is dominated by inconsistencies with respect to equation (3.15), e.g. in the presence of noise.

However, it is not so much the ill-conditioned nature of (3.15), but rather its shear size, that complicates the inversion process. For example, a routine high resolution CT acquisition at the UGCT roughly consists out of 1000 cone beam projections on a 1000 by 1000 flat panel detector, i.e.  $10^9$  single pixel measurements. When these measurements are used to reconstructed a cubic grid of  $10^9$  voxels (1000 by 1000 by 1000), the system matrix quickly grows to contain  $10^{18}$  entries. Storing  $\mathbf{T}$  would thus require up to 4 exabytes of floating point values, and even calculating it would literally take ages. These technical challenges are addressed by the iterative inversion strategies and their GPU implementations, as explained in the next section. These techniques exploit the inherent sparse structure of  $\mathbf{T}$ , for efficient calculations of the matrix-vector product in (3.15), which do not require the system matrix in its explicit form.

### 3.2.2 Iterative inversion strategies

#### The iterative paradigm

The basic idea of any iterative reconstruction scheme (see Figure 3.8) is to calculate a simulated version the CT projection data ( $\vec{p}^{(0)}$ ), starting from an initial guess for the contents of the reconstruction volume ( $\vec{\mu}^{(0)}$ ). The difference between these simulations and the real radiographs ( $\vec{p}$ ) is subsequently redistributed across the volume in a back projection step. As such, a new updated version of the volume ( $\vec{\mu}^{(1)}$ ) is obtained, which can be plugged into the next iteration of this projection/back projection process. The above sequence is repeated over and over until the difference  $(\vec{p}^{(k)} - \vec{p})$  only marginally affects the next iterate  $\vec{\mu}^{(k)}$ , or in other words until  $\vec{\mu}^{(k)}$  converges to the fixed point ( $\vec{\mu}^*$ ) of the iterative scheme, which in the ideal case should be equal to the true distribution ( $\vec{\mu}^* \approx \vec{\mu}$ ).

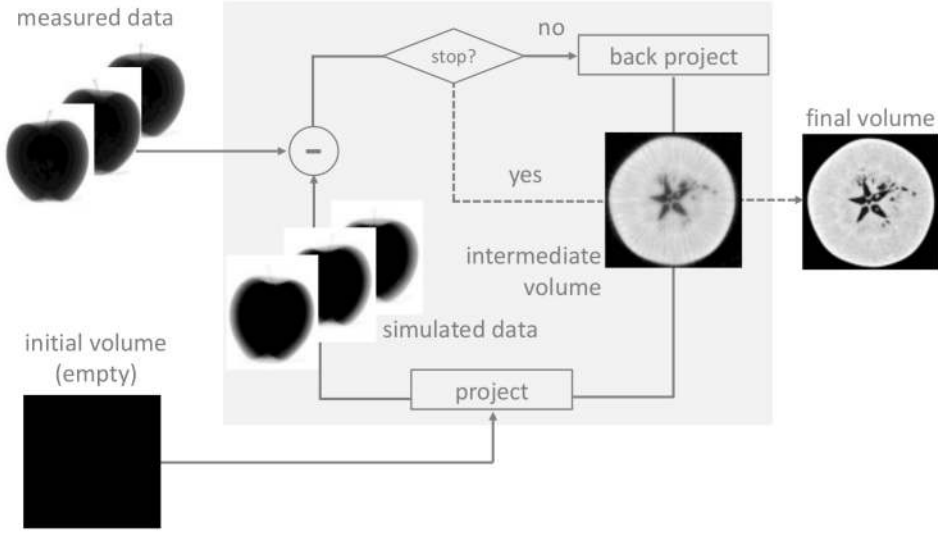


*Figure 3.8: Basic concept of iterative CT reconstruction. The simulated projections of an intermediate volume, which is often initialised as an empty volume, are compared to the measured data. The difference between the simulated and measured data is then back projected, leading to an update of the intermediate volume. By repeating this process the volume gradually converges to its final state (Based on [23]).*

### Kaczmarz & the algebraic reconstruction technique (ART)

The archetype of the iterative CT reconstruction algorithms, aimed at solving large systems of equations such as (3.15), was introduced by Kaczmarz [24, 25] long before the concept of X-ray CT was even conceived. To solve (3.15), Kaczmarz proposes an updating strategy in which an initial guess ( $\vec{\mu}^0$ ) is projected onto a  $(L-1)$ -dimensional hyperplane defined by one of the measurements, and its normal vector  $\vec{t}_0 = [t_{00}, t_{01}, \dots, t_{0L}]^T$  (equation (3.14)), to form a new estimate for the attenuation values ( $\vec{\mu}^{(1)}$ ). This process is repeated over and over, including the other measurement hyperplanes, leading to an update scheme ( $\vec{t}_0 = [t_{k0}, t_{k1}, \dots, t_{kL}]^T$ ) [5, 6, 24]

$$\vec{\mu}^{(k+1)} = \vec{\mu}^{(k)} + \frac{p_k - \vec{t}_k \cdot \vec{\mu}^{(k)}}{\vec{t}_k \cdot \vec{t}_k} \vec{t}_k \quad (3.16)$$

through which the intermediate attenuation values ( $\vec{\mu}^{(k)}$ ) gradually migrate towards a solution of (3.15) at the intersection of these hyperplanes. As mentioned before, this solution is rarely unique, and inconsistencies such as noise in the measurements only allow for an approximate solution, in the least squares sense, to be found. For example, in the ideal 2D case the Kaczmarz-algorithm retrieves the intersection between two oblique straight lines (Figure 3.9(a)). In the presence of noise however, measurements taken along the same ray vary statistically, spawning

a series of parallel lines in the  $(\mu_1, \mu_2)$ -plane, which do not intersect in a singular point (Figure 3.9(b)).

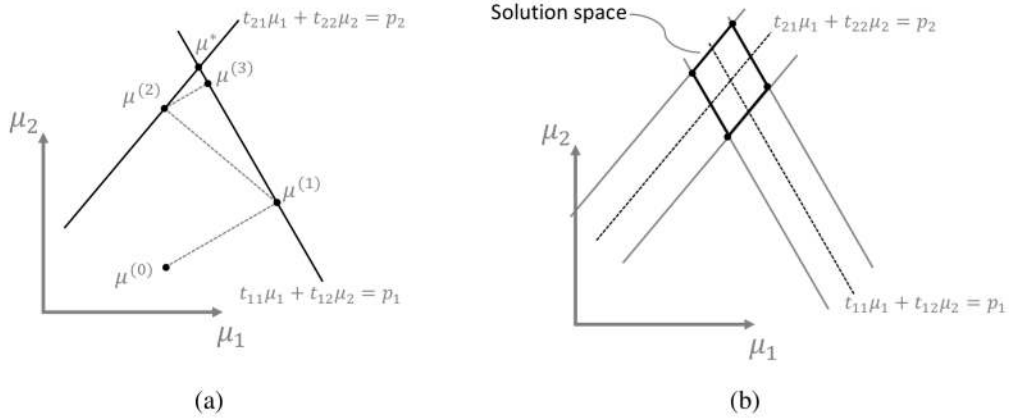


*Figure 3.9: Kaczmarz algorithm in 2D. (a) An iterative projection of the intermediate solution from one hyperplane (straight line in 2D) to another eventually converges to a unique intersection. (b) Noisy measurements along the same ray spawn a series of parallel lines in the  $(\mu_1, \mu_2)$ -plane. In this case there is no clear solution to (3.15).*

The Kaczmarz algorithm forms the blueprint for the algebraic reconstruction technique (ART), for which the update equation in a single voxel (index  $m$ ) is given by

$$\vec{\mu}_m^{(k+1)} = \vec{\mu}_m^{(k)} + \lambda \frac{p_j - \sum_{l=0}^L t_{jl} \cdot \mu_l^{(k)}}{\sum_{l=0}^L t_{jl}^2} t_{jm} \quad (3.17)$$

The only difference between (3.16) and (3.17) is the presence of a ‘*relaxation factor*’ ( $\lambda$ ), which dampens the contribution of each individual update. When  $\lambda$  is chosen to lie within  $]0, 1[$ , its overall effect is to smooth the higher frequencies, e.g. noise, in the intermediate solutions. While this results in a slower convergence rate, setting  $\lambda$  to an appropriately small value is also a necessary condition to make the ART algorithm converge in the first place [26]. During the iterations the index  $j$  is looped over all of the measurements, possibly revisiting several measurements more than once (when  $k > J$ ). For an optimally fast convergence, the order in which the index  $j$  is accessed, preferably produces a sequence of updates that provide complementary, orthogonal information towards the solution of the problem. Indeed, it is clear from Figure 3.9(a), that the intersection would be reached after only two iterations if the lines would be orthogonal to one another. The notion of orthogonality is a favourable trait found in popular approaches such as ‘*steepest descent*’ (STP) and ‘*conjugate gradient*’ (CG), which can also be used as iterative CT reconstruction schemes. In fact, most iterative CT reconstruction schemes,

including STP, CG and ART, can be unified through the generalised Landweber formula [26, 27]

$$\vec{\mu}^{(k+1)} = \vec{\mu}^{(k)} + \boldsymbol{\Lambda}^{(k)} \mathbf{B}^T \left( \vec{p} - \mathbf{T} \cdot \vec{\mu}^{(k)} \right) \quad (3.18a)$$

$$= \vec{\mu}^{(k)} + \boldsymbol{\Lambda}^{(k)} \mathbf{B}^T \vec{q}^{(k)} \quad (3.18b)$$

where  $\boldsymbol{\Lambda}$  is the generalisation of the relaxation factor  $\lambda$  to a diagonal matrix form, and  $\mathbf{B}$  represents a back projection operator which redistributes the projection errors ( $\vec{q}$ ) across the volume, e.g. in the case of ART

$$[\mathbf{B}]_{jm} = \frac{t_{jm}}{\sum_{l=0}^L t_{jl}^2} \quad \text{and} \quad [\boldsymbol{\Lambda}]_{jm} = \lambda \cdot \delta_{jm}.$$

### Accumulating updates - SART, SIRT and ordered subsets (OS)

While in ART only a single ray is taken into account for updating the volume at each iteration, most iterative CT reconstruction schemes tend to aggregate the contributions of multiple rays into one simultaneous update. When an update is accumulated across a collection of rays, i.e. a so-called ‘ordered subset’ (OS), the update scheme needs to be revised [28, 29].

$$\vec{\mu}_m^{(k+1)} = \vec{\mu}_m^{(k)} + \lambda \sum_{j \in \text{OS}} \frac{\left( p_j - \sum_{l=0}^L t_{jl} \cdot \mu_l^{(k)} \right)}{T_j} \cdot \hat{t}_{jm} \quad (3.19)$$

where the subset normalised back projection weights ( $\hat{t}_{jl}$ ) and the total length traced by ray  $j$  ( $T_j$ ) are given by

$$\begin{aligned} \hat{t}_{jm} &= \frac{t_{jm}}{\sum_{j \in \text{OS}} t_{jm}} \\ T_j &= \sum_{l=0}^L t_{jl} \end{aligned}$$

The ordered subsets generally contain all of the pixels within one or more projections, yielding the ‘*Simultaneous Algebraic Reconstruction Technique*’ (SART) [30] and the ‘*Simultaneous Iterative Reconstruction Technique*’ (SIRT) [31], when one projection or respectively all of the projection data is used to calculate the update. As such, it is clear that both SART and SIRT are special cases of the general OS reconstruction scheme [28], in which any number of projections can be incorporated in the update calculation.

### Accessing schemes

For SART in particular, the focus in updating is shifted from single pixel to whole projection updates, such that the optimal order for accessing the individual pixels essentially boils down to ordering the projections in a way that promotes convergence. It turns out that a simple sequential accessing strategy, where the SART updates follow the order in which the projections were acquired, induces a smearing artefact in the reconstructions. This smearing artefact is a remnant of the first back projections in the SART scheme, which uniformly distribute the projection errors along straight rays in the initially empty volume. The problem with this uniform redistribution is that the delineation of the object's support gets lost, and can only be restored by updating the volume through an orthogonal projection. Indeed, as for ART, the orthogonality of the updates is an important prerequisite to the fast convergence of SART. To artificially enforce this orthogonality, the projection access order can be guided through a '*Weighted Distance Scheme*' (WDS), which updates the volume with the projection situated at  $90^\circ$  from the weighted average of the angular positions already taken up in the updating sequence [32]. WDS produces more accurate reconstructions in situations where only a limited number of projections are available. However, for a large number of projections, simpler access schemes, such as the '*Random Access Scheme*' (RAS), produce CT reconstructions of a quality similar to WDS (see Figure 3.10). Again, there is an interesting parallel to be drawn with other iterative numerical schemes, such as CG and STP. Moreover, random access SART can be seen as a form of stochastic gradient descent (SGD) [33].

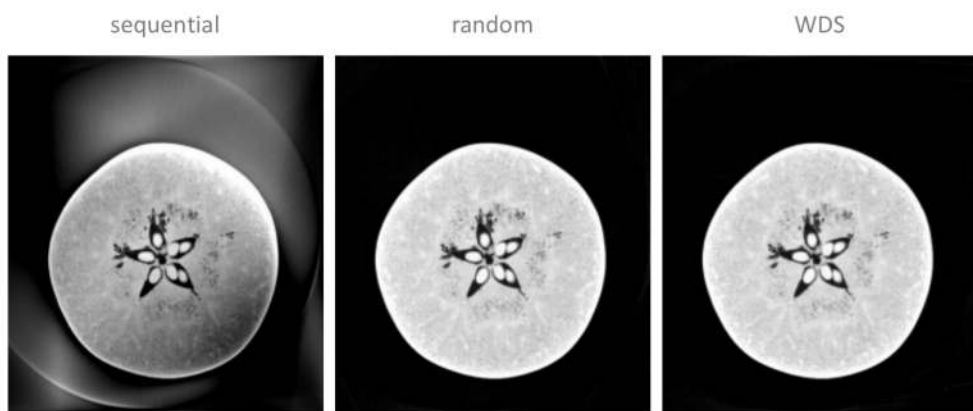


*Figure 3.10: Effect of the projection access pattern on SART based CT reconstructions. The results for this 500 projection reconstruction of an apple's cross section are nearly indistinguishable when a WDS or random access schemes is used. The sequential scheme on the other hand, clearly produces an unwanted smearing artefact.*

### 3.2.3 A GPU accelerated SART implementation

The efforts, in this work, pertaining to iterative CT reconstruction are almost solely based on the SART approach. The advantages of SART, notably:

- its fast convergence, often reached after only one pass over all of the projections in the CT dataset, and
- its leniency towards a GPU accelerated implementation,

have been thoroughly corroborated in the dissertation work conducted by one of the author's predecessors [6]. Some details on the practical implementation of SART will be revisited in the following sections, with the pretence of providing a research oriented and development friendly iterative CT reconstruction tool, written in a hybrid Python-CUDA code [34]. First, some strategic approximations to the update term in (3.19) are introduced to simplify and speed up its calculation. Many of the design choices made here, originally based on [6], are in fact common in the literature on iterative CT reconstruction, see e.g. [35]. Also, in the introduction to this chapter, it was mentioned that the upsurge in iterative CT reconstruction research is partly attributed to increasingly performing computational hardware, in particular GPU technology. Indeed, GPU acceleration is a crucial aspect to the implementation of iterative CT algorithms, to the extent that any respectable iterative reconstruction tool should preferably be GPU implemented [36–38].

#### Fast projections & back projection

The update rule in (3.19) can be broken down into a three step sequence, with:

1. a '*projection step*' to obtain a simulated estimate for the data,

$$\hat{p}_j = \sum_{l=0}^L t_{jl} \cdot \mu_l^{(k)} \quad (3.20)$$

2. a '*correction step*' calculating a length weighted and relaxed version of the projection error,

$$c_j = \lambda \frac{p_j - \hat{p}_j}{T_j} = \lambda \frac{q_j}{T_j} \quad (3.21)$$

3. and a '*back projection step*' which redistributes the previously calculated correction term across the volume

$$\vec{\mu}_m^{(k+1)} = \vec{\mu}_m^{(k)} + \sum_{j \in OS} c_j \cdot \frac{t_{jm}}{\sum_{j \in OS} t_{jm}} \quad (3.22)$$

The projection and back projection steps are particularly tedious because they involve the calculation of the ray-voxel intersection weights  $t_{ji}$ . While it was previously established that storing these weights is not an option, calculating them is also not a straight forward task. Luckily not all of the weights are always relevant since the projection and back projection steps are sparse in nature, and depending on how the interaction between the rays and the voxel elements is modelled only a very few to none of the weights need to be calculated explicitly. Here, the projections are simulated through a ‘*pixel driven sampling*’ approach, by tracing the rays connecting the source to the pixel centres. The line integrals on these rays are approximated through an equidistant sampling of the  $\mu$ -values following Joseph’s method [39], such that (cfr. (2.11))

$$\hat{p}_j \approx \Delta t \sum_{l=0}^L \mu(\vec{x}_l). \quad (3.23)$$

in which  $\vec{x}_l$  follows (2.12). In Joseph’s method the sampling interval ( $\Delta t$ ) is determined by the voxel grid spacing along the axis which is most parallel to the ray being sampled. If, for instance, the most parallel axis is the grid’s  $x$ -axis (as depicted in Figure 3.11),  $\Delta t$  will be given by

$$\Delta t = \frac{\Delta x}{S \cos \alpha} \quad (3.24)$$

where  $\alpha$  is the angle between the ray and the  $x$ -axis, and  $S$  represents a tunable oversampling factor (in most cases  $S \geq 1$ ). Through the sampling approaches, described by (3.23), the problem of finding the intersection weights is redefined as an interpolation problem of finding the  $\mu$ -values at the  $\vec{x}_l$ -positions. Coincidentally, these interpolation operations can be easily accelerated by storing the volume in GPU textures, which provide very fast trilinear and nearest neighbours interpolations, through efficient caching schemes [40]. The voxel basis which builds up the volume is determined by the interpolation scheme, i.e. a 3D hat and cubic indicator function for trilinear and nearest neighbours interpolations, respectively, and is no longer relevant for the calculation of the intersection weights when an equidistant sampling strategy is considered in the projection step.

Other sampling techniques implicitly assume that the voxels have a predetermined shape, e.g. Siddon’s and Köhler’s method [41, 42] for cubic voxels, and that the extent of this shape can intersect more rays emanating from the finite pixel area than just the one connected to the centre of a pixel (Figure 3.12). When the intersection weights are explicitly calculated based on an overlap between a voxel’s shape and a single ray or the ray bundle gathered on the finite extent of a pixel’s area, a so-called ‘*pixel driven splatting*’ technique arises.

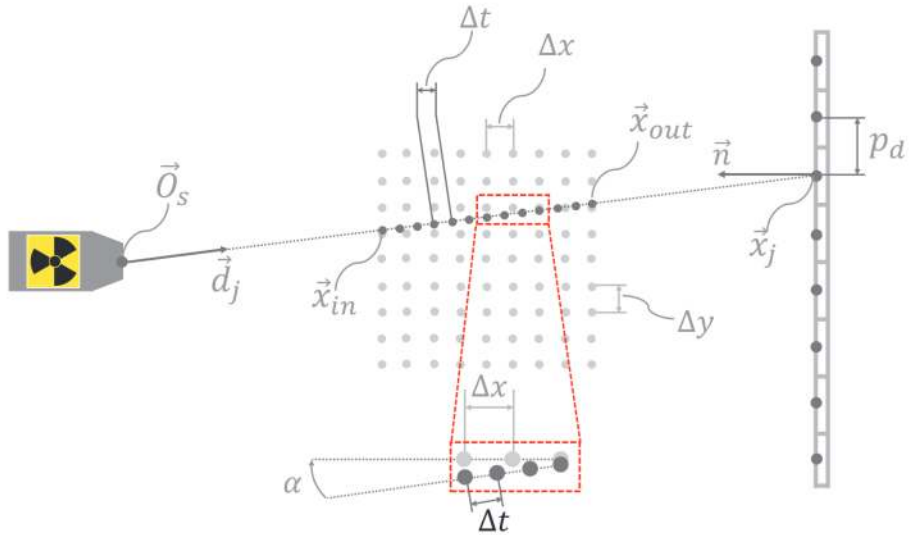


Figure 3.11: Joseph's method for an equidistant sample of  $\mu$ -values on a ray (cfr. Figure 2.19). The rays are sampled at equidistant multiples of  $\Delta t$ , which are determined by the grid spacing ( $\Delta x$ ) along the most parallel axis, following (3.24) with  $S = 1.5$ .

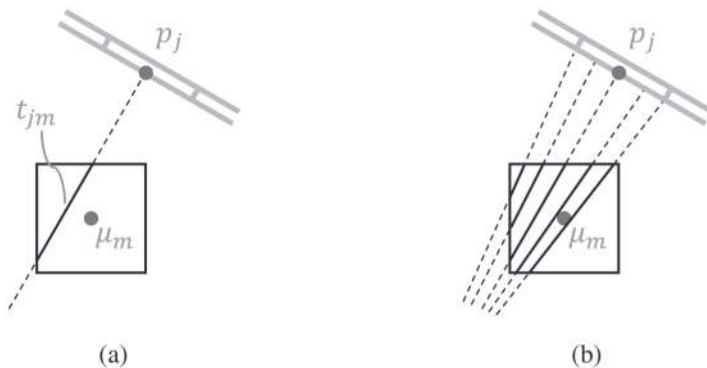


Figure 3.12: Calculating intersection weights through pixel based splatting on a cubic voxel. (a) The intersection weight  $t_{jm}$  is determined by a single ray connected to the centre of pixel  $p_j$ ; (b) The intersection weight is averaged over multiple intersections between voxel  $m$  and a ray bundle connected to equidistantly spaced points within the finite area of  $p_j$  (based on [6]).

A similar terminology, i.e. ‘voxel driven splatting’, is used when a projection is calculated by accumulating the footprints of all of the voxels on the detector plane, often taking more exotic voxel shapes into account, such as spherical Kaiser-Bessel basis functions [43, 44]. The voxel and pixel driven splatting approaches can even be combined in a distance driven approach [45], where the projection weights are calculated as an overlap between the voxel and pixel footprints projected on a dedicated plane. As shown in [6], the more advanced splatting techniques only marginally improve the quality of a reconstructed CT image, while taking a sig-

nificantly longer time to compute and taking up more CPU memory as compared to the sampling based techniques. This is why, as mentioned before, the simulated projections are calculated through a pixel driven sampling technique in this work’s implementation of SART.

A fast implementation for the back projection step can be obtained, by putting forward a plausible estimate for the subset averaged back projection weights in (3.22)

$$\hat{t}_{jm} = \frac{t_{jm}}{\sum_{j \in OS} t_{jm}}. \quad (3.25)$$

It can be argued that within each projection there is approximately one pixel ray that intersects voxel  $m$ , say  $j = j_p$ , such that  $t_{jm} \sim \delta_{jj_p}$ . This implies that the sum in the denominator of (3.25) contains only a limited number of entries, i.e. about one per projection. Given the number of projections per subset  $N_{p,OS}$ , the subset averaged intersection weights can thus be approximated by

$$\tilde{t}_m \approx \frac{1}{N_{p,OS}} \sum_{j \in OS} t_{jm} \delta_{jj_p}$$

such that

$$\hat{t}_{jm} \approx \frac{t_{jm}}{N_{p,OS} \tilde{t}_m}$$

Furthermore, if  $t_{jm}$  is non-zero its most likely value is precisely  $\tilde{t}_m$ , leading to

$$\hat{t}_{jm} \approx \frac{1}{N_{p,OS}} \quad (3.26)$$

which reflects the plausible assumption that each projection equally contributes to the back projection in a certain voxel. With (3.26) the update rule (3.22) simplifies to

$$\vec{\mu}_m^{(k+1)} = \vec{\mu}_m^{(k)} + \frac{1}{N_{p,OS}} \sum_{\vec{x}_s \in OS} c(\vec{x}_m, \vec{O}_s) \quad (3.27)$$

In this update formula, the back projection value  $c(\vec{x}_m, \vec{O}_s)$  is obtained through an interpolation of the correction term (3.21) at the intersection between the detector plane and the line connecting one of the source positions  $\vec{O}_s$ , contained within the ordered subset of selected projections, to the current voxel position  $\vec{x}_m$ . In other words, the back projection values are the result of a ‘voxel driven sampling’ in the detector plane. Again the correction terms can be stored in GPU texture memory, providing implicit bilinear and nearest neighbours interpolation schemes.

In summary, fast projection and back projection calculations can be achieved by respectively using pixel driven and voxel driven sampling strategies. More importantly, to further accelerate the reconstruction process, these sampling techniques can be readily implemented on GPUs by using their interpolation friendly texture memory.

### 3.2.4 Handling large CT reconstruction volumes

A drawback to the SART is that all of the voxel values are indirectly correlated through the system matrix, and that it is impossible to reconstructed a single voxel on its own, contrary to the analytical reconstruction techniques. As a result, the entire 3D volume needs to be stored in GPU memory for the projections and back projections to be correctly computed. If this volume does not fit into the GPU RAM, techniques to relax or redistribute the storage requirements have to be considered.

#### Multi GPU

When multiple GPUs are available, the volume can be evenly split up among these individual devices (see Figure 3.13), which then independently calculate the forward projection of their respective sub-volumes. The projection results are subsequently gathered on the host device into a single correction image, which is redistributed to all of the GPUs before they are back projected into each GPU's local sub-volume. The final reconstruction is obtained by reassembling the sub-volumes into one volume on the host device. The obvious disadvantage of a multi GPU implementation is that it requires multiple GPUs, and while their combined RAM could cover the needs for most CT reconstructions, there is still a limit to the available memory. More importantly, messages passed across their interconnection bus in order to synchronise the state of the correction images, are likely to form a bottleneck in the SART iterations.

#### Multiresolution reconstruction

To structurally overcome the GPU memory limitations, De Witte *et al.* have devised a '*multiresolution reconstruction*' scheme which can be run on a single GPU [46]. In this scheme, a high resolution sub-volume, with densely spaced voxels covering a small portion of the entire volume, is embedded within a larger low resolution representation of the entire volume with a relatively low amount of voxels (Figure 3.14). The idea is that both of these volumes can be stored in a single GPU, which first performs a reconstruction of the CT data onto the coarse representation of the volume. This coarse reconstruction can then serve as approxima-

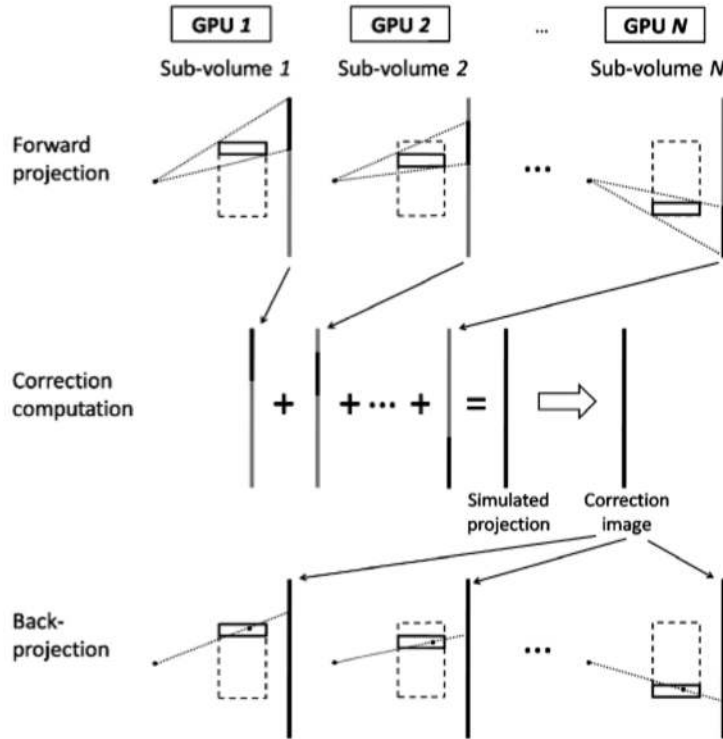


Figure 3.13: Multi GPU implementation of an iterative CT reconstruction scheme. Using multiple GPUs large volumes can be reconstructed with iterative techniques, while in the mean time reducing the reconstruction times (courtesy of Yoni De Witte [6]).

tion to the  $\mu$ -distribution which surrounds the high resolution sub-volume, leading to more accurate simulations and updates for the latter. The problem with this approach is that it is approximative in nature, since the simulated projections are mainly calculated from a coarse low resolution version of the entire volume. This discrepancy can be minimised by repeating the sub-volume reconstruction until the entire volume is covered in an overlapping manner, and possibly revisiting certain sub-region multiple times, but can never be entirely eliminated.

### Chunk swapping

On a single GPU the projections and back projections for a large volume could also be calculated exactly by sequentially swapping chunks of the entire volume between the CPU and GPU memory. Unfortunately, these copying operations are dreadfully slow, and as such introduce an unacceptable overhead in the OS iterations. However, a GPU does not necessarily need to remain idle in terms of computing during the time memory buffers are copied back and forward between the CPU and GPU. Indeed, there is a mechanism which allows a GPU to asynchronously perform computing and copying tasks at the same time, handled by

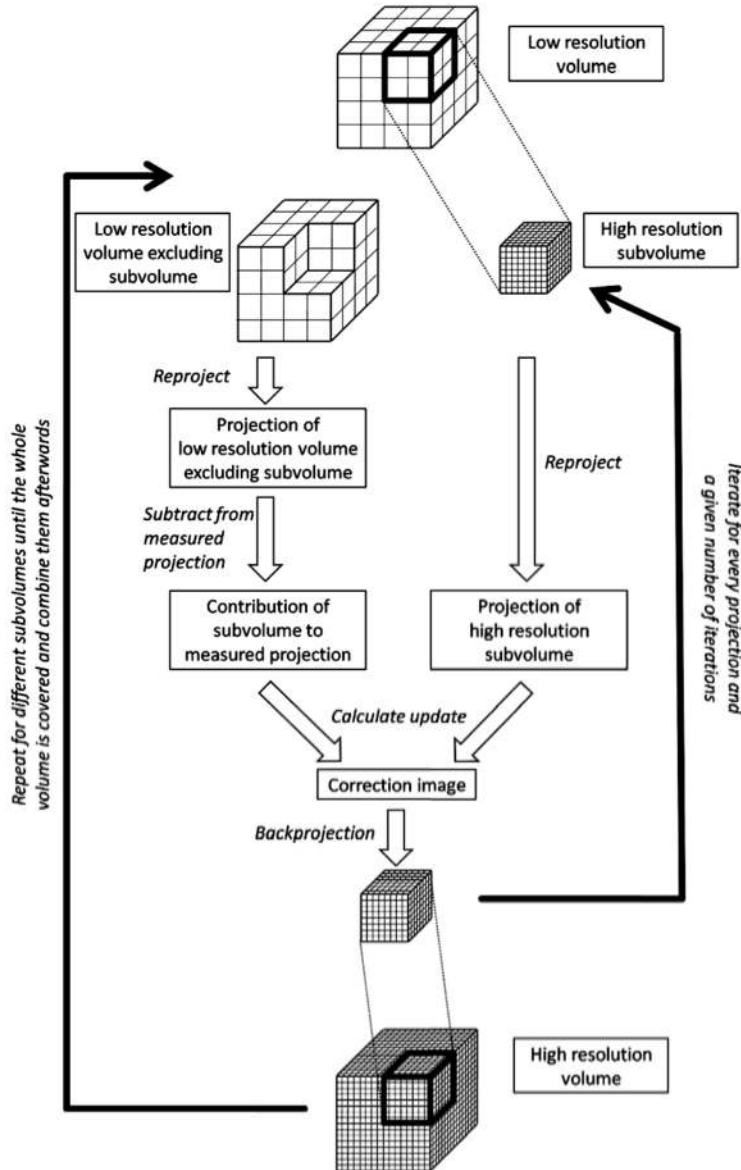


Figure 3.14: A multi resolution framework to reconstruct large CT volumes on a single GPU. High resolution sub-volumes, with densely spaced voxels, are embedded within a larger low resolution representation of the entire volume (courtesy of Yoni De Witte [6]).

their ‘compute and copy engines’, respectively [47]. The idea of the approach developed in this work is to increase the ‘arithmetic intensity’ of the chunk swapping technique, which is a technical formulation for hiding the swapping overhead by simultaneously performing computations. To this end, at least two buffers, dubbed ‘buffer 1’ and ‘buffer 2’, have to be allocated in GPU memory, which can each hold an equally large chunk of the volume, and take up the opposing roles of either being a compute or copy buffer (see Figure 3.15). While a projection or back projection operation is performed on buffer 1, the CPU copies data to or from buffer 2. When both of these tasks are finished, the buffers exchange their com-

puting and copying roles, such that the chunk in buffer 2 can be projected or back projected, while the next chunk is exchanged between the CPU and GPU in buffer 1. In the ideal case, as illustrated for the projection case in Figure 3.15(a), the copy operations take about the same time as for a complete subset of projections to be simulated, reducing the copying overhead to the time it takes for one chunk to be transferred to the GPU. In contrast, the back projection queue in Figure 3.15(b) does not ideally hide the copying tasks through computing, leaving the GPU idle during a large part of the copy operations. The copying tasks in the back projection case take longer, because these computations alter the contents of the loaded buffers, which thus need to be saved back to the CPU before their contents are overwritten with the data of the next chunk. In other words, in the back projection step the copy operations are effectively doubled. The extra copying overhead can be overcome by increasing the computational load, e.g. by gathering a higher number of projections in each subset, assuming this higher number of projections can be stored on the GPU next to the copy and compute buffers. Through a numerical experiment, the graphs in Figure 3.16 illustrate how in a multi chunk approach, with a large subset size, the projections and back projections can asymptotically reach the same speed as their single volume counter parts, for which the entire volume is preloaded beforehand. The graphs compare the time it takes for a single projection or back projection to be computed in the single volume case ( $\tau_{single}$ ), with the timings for a two chunk case ( $\tau_{chunked}$ ), by setting out their ratios, i.e.

$$\text{relative speed [-]} = \frac{\tau_{single}}{\tau_{chunked}}$$

The computations were performed on the phantom volume described in section 2.5, which was discretised to a voxelised grid of 508 by 532 by 543 in width, height and depth, respectively. Clearly, the chunking approach can not beat the single volume case, but as more and more projections are taken up in a subset, the copying overhead time gets filled up through computations, such that the time spent per projection in a subset effectively decreases. Increasing the number of chunks does not affect the computational speeds, since all of the involved operations, i.e. copying, projecting and back projecting, approximately scale linearly with the size of a chunk. This implies that the ratio between copying and computation time remains approximately constant, whatever the chunk size might be. To conclude, the chunk swapping approach is particularly interesting for OS reconstructions with large subset sizes (e.g. SIRT). Typically however, these large subset reconstructions require a higher amount of iterations, as compared to SART, which only needs about one or two passes through the whole projection dataset. Thus, for large CT volume reconstructions, there is an optimal subset size, which minimises the chunk swapping overhead, while converging in an acceptable number of iterations.

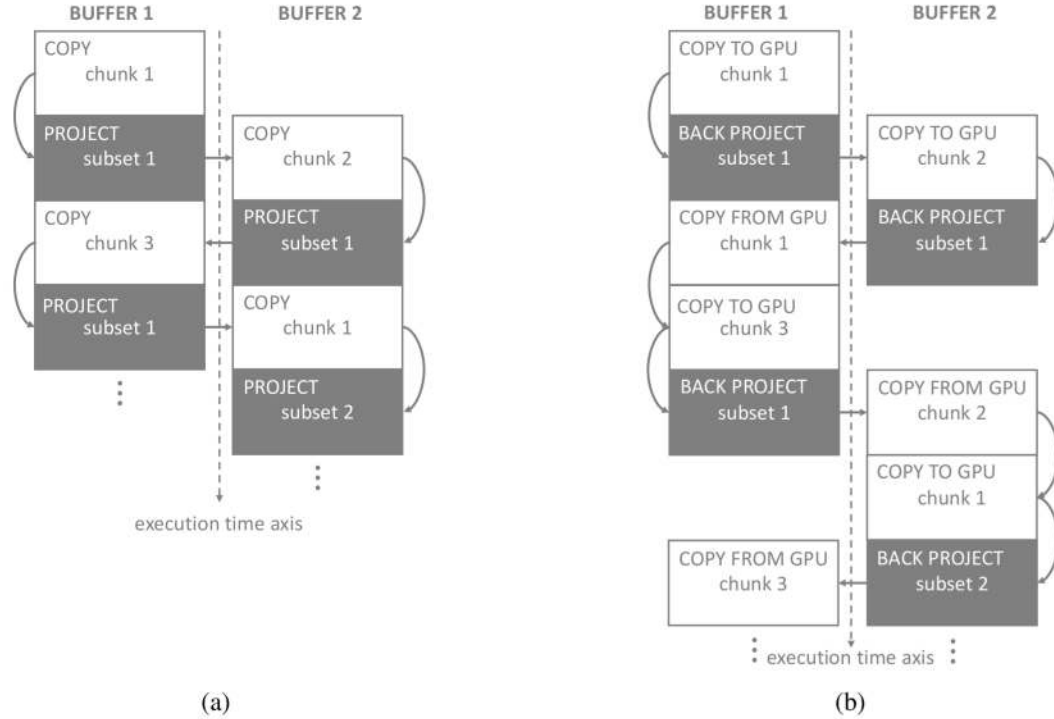


*Figure 3.15: Copy and compute queues to handle large volume iterative CT reconstructions through chunk swapping. (a) The projection computation only need to hide one copy operations to increase the arithmetic intensity. (b) Since the back projection alters the contents of a buffer, an extra copy operation is necessary to save the results back to the CPU. The non-dashed arrows in this figure indicate how the task queues for both of the buffers are filled up.*

### 3.2.5 A Python-CUDA iterative CT reconstruction tool

As a part of this work an iterative reconstruction tool was developed, which can perform OS reconstructions of CT data acquired along arbitrary source trajectories. The tool's interface is implemented in Python, while the bulk of the heavy reconstructive calculations are offloaded to a GPU with the help of the open source Python module 'PyCUDA' [34]. Key features of this module are the seamless integration of a GPU memory class with CPU based Python Numpy arrays [48], and more importantly its ability to compile Python string templates of C code '*Just In Time*' (JIT) to be loaded on and executed by a GPU. With this last feature, lower level C code can thus be formatted through higher level Python instructions. A concept called '*metaprogramming*', which together with the Numpy array integration extends the ease of coding in Python towards developing code for a GPU. An added advantage of the tight Python-CUDA integrations is the vast repository of freely available Python modules, notably SimpleITK [49, 50] and scikit-image [51], which can aid in the pre- and post-processing of CT datasets.

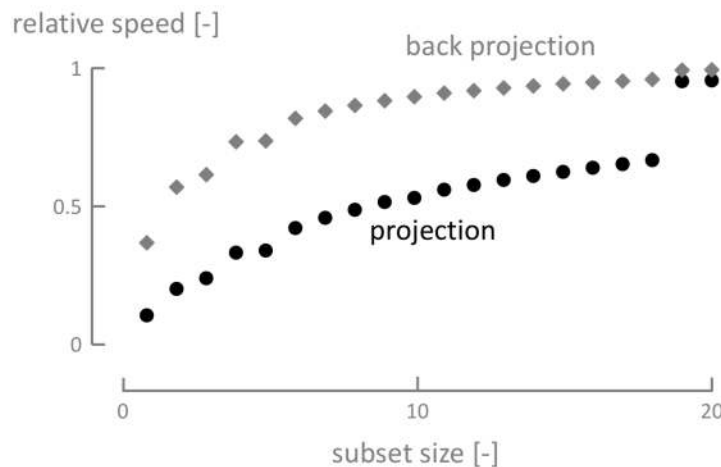


Figure 3.16: Speed of the chunk swapping technique as a function of the subset size. As the number of projections in a subset increases, the chunked projection and back projection sequences (using 2 chunks) asymptotically reach the speeds of their single volume counterparts. For reference, the absolute speeds of the projection and back projection operations in the single volume case were 3.08 ms and 44.03 ms, on the workstation specified in appendix A.

Apart from building a fast and flexible reconstruction tool, the main goal was to enable the reconstruction of CT data acquired in arbitrary geometrical configurations, other than simple circular cone beam acquisitions. The reconstruction tool attaches a geometrical configuration or ‘view’ to each radiograph in a CT dataset, based on the parametrisations discussed throughout section 2.4. The ability to reconstruct these arbitrary trajectories is an indispensable prerequisite to the feasibility study performed on in-line CT in chapter 4, and also in handling more common trajectories through iterative reconstruction, e.g. a helix (see section 3.2.6).

In summary, the notable features of the iterative reconstruction tool are:

- the ability to perform GPU based reconstructions with all types of OS schemes, going from SART to SIRT and all of the in between,
- based on CT data acquired in arbitrary geometrical configurations, with
- methods to easily define the geometrical views for all of the projections as parametrised throughout section 2.4, and
- a careful mapping between these geometrical views and GPU data buffers, with a future outlook to handling multi-source and poly-energetic CT reconstructions,
- a flexible and development friendly implementation through the metaprogramming and JIT paradigms, with PyCUDA [34],

- a fast pixel driven ray sampling and voxel driven back projection through GPU texture interpolation, with
- the capability of reconstructing large CT volumes, not limited by the GPU's memory, by using the chunk swapping approach discussed in section 3.2.4,
- techniques to handle ROI reconstructions and acquisitions, through a virtual geometrical extension of the CT volume [6], and an aperture weighting of the CT projections [52, 53],
- and finally, built-in functions to perform non-rigid registration of 3D volumes with spline based [54], demons [55, 56] and phase based wavelet techniques [57] (see also chapter 5).

There is also a great variety of CT reconstruction tools available in literature. Even more so, most of them are open source and provide highly efficient GPU or distributed CPU implementations. A non-exhaustive overview on a selected number of these toolboxes is given in table 3.1. UGCT also has a long running track record of developing CT reconstruction code with the first versions of 'Octopus' dating back to 1999. Nowadays, Octopus is further developed and distributed by one UGCT's spin-offs 'InsideMatters' ([www.insidematters.eu](http://www.insidematters.eu)). Octopus does not however allow the reconstruction of CT data coming from arbitrary geometries, and it being a production code with a tight integration to a user interface, makes it difficult to rapid prototype novel and flexible reconstruction approaches. This is why in this work the choice was made to reimplement the iterative reconstruction component in the PyCUDA JIT framework, to accommodate arbitrary CT geometries, but more importantly to obtain a more developer friendly implementation, that is resilient to a constant adaptation, typical for a research environment.

### 3.2.6 An example: iterative helical CT reconstruction

This section illustrates the capabilities of the OS reconstruction tool through the challenging example of iterative helical CT. As mentioned before, a drawback to iterative techniques is the fact the whole CT volume needs to be stored in memory, and for helical CT in particular this volume can become very large due to the sample's long vertical extent, making it an ideal testing case for the chunk swapping technique discussed in section 3.2.4. Moreover, the helical trajectory forms a convenient stepping stone towards reconstructing more general alternative trajectories with iterative techniques, while still providing a analytical alternative (e.g. Katsevich) for validation purposes.

The dataset presented here was acquired as one of many helical CT scans performed by Van den Bulcke *et al.* from the Ghent University laboratory for

*Table 3.1: Overview on a selected number of existing CT reconstruction tools.*

Name	Literature	GPU	Multi CPU	Iterative	Analytical	Core language	Interfacing language	JIT
ASTRA	[58–60]	CUDA	OpenMP	•	•	C/C++	Python,Matlab	
PyHST2	[61]	CUDA	MPI	•	•	C	Python	
RTK	[62]	CUDA,OpenCL		•	•	C/C++	Python,C++	
TIGRE	[63]	CUDA		•	•	C	Matlab	
Cph CT	[64]	CUDA,OpenCL		•	•	PyCUDA,C	Python	•
this work	-	CUDA		•	•	PyCUDA,C	Python	

Wood Science, to measure tree-ring features as key elements in dendrochronological studies [65]. Typically, the tree drill cores used in this study have a high aspect ratio shape with a long vertical extent of up to 15 cm, which explains the need for a helical scan to obtain a respectable voxel pitch. The helical scan, performed according to the settings in table 3.2, took approximately 70 minutes to complete, and resulted in both iterative and analytical reconstructions on a 912 by 912 by 4500 grid with a voxel pitch of  $\pm 35 \mu\text{m}$ . For the iterative reconstruction, this grid size leads to a staggering 14 GB of GPU storage requirement, markedly higher than the 6 GB mounted on an NVIDIA GeForce Titan GTX (see appendix A), one of the highest capacity GPUs available at the time this work was performed. A chunk swapping approach is thus necessary, and following the argument with respect to the graph Figure 3.16 that the ratio between copying and computation time is a constant (depending on the work station's specifications) the number of projections in each ordered subset can be set to 20. However, larger subset sizes tend to smooth out the volume updates, such that a higher number of iterations is required to clearly resolve fine structures in the reconstructions. As a compromise, the subset size was set to 6, since for higher subset sizes the performance gain through asynchronous chunk swapping is only marginal. With this subset size a single iteration, looping over all 5398 projections in the dataset, took approximately two hours. As a convergence measure, the central slice's histogram based entropy<sup>3</sup> is monitored up until the point where its relative iteration-to-iteration change drops below 0.1 percent. This leads to a total of 10 iterations, and thus 8997 subset updates over the course approximately 20 hours. This might seem slow, but it should be noted that during each of the 8 second subset update, a 14 GB volume is projected and back projected 6 times, which is a respectable timing for a single GPU iterative approach on a volume of this size. This aside, the analytical Katsevich algorithm [6, 21] vastly outperforms the OS technique in terms of speed, by realising a excellent quality reconstruction (see Figure 3.17) of the entire volume, in less than 30 min.

Although the analytical approach is clearly superior here, this case demonstrates the capability of the OS technique to handle alternative trajectories and the very large volumes, which tend to arise in day to day  $\mu\text{CT}$  applications. The iterative techniques will specifically have their merits, in particular for smaller datasets, when a more elaborate forward model or a priori information on the imaged object is incorporated in the reconstruction process.

---

<sup>3</sup>Chosen here for its simplicity, the histogram based entropy is only one of many metrics to quantify the sharpness of an image [66].

*Table 3.2: Scan settings of the helical tree-ring analysis dataset.*

Tube	Hamamatsu L9181			
	Tube voltage	( $V_t$ )	70	kV
	Tube power	( $P_t$ )	9	W
Detector	Varian PaxScan 2520			
	Exposure time	( $t_{exp}$ )	700	ms
	Detector size	(W,H)	(912,602)	-
	Binned pixel size	( $p_d$ )	254	μm
	Binning	(-)	2 by 2	-
Geometry	Helical cone beam			
	Source Detector Distance	(SDD)	440.0	mm
	Source Object Distance	(SOD)	62.7	mm
	Helical Pitch	( $z_p$ )	34	mm
	Number of projections	( $N_p$ )	5398	-
	Source per turn	(SPT)	1000	-
Reconstruction	Ordered Subsets			
	Voxel pitch	( $p_v$ )	35	μm
	Voxel grid	(W,H,D)	(912,912,4500)	-
	Iterations	(-)	10	-
	Subset size	(-)	6	-
	Relaxation	( $\lambda$ )	0.5	-

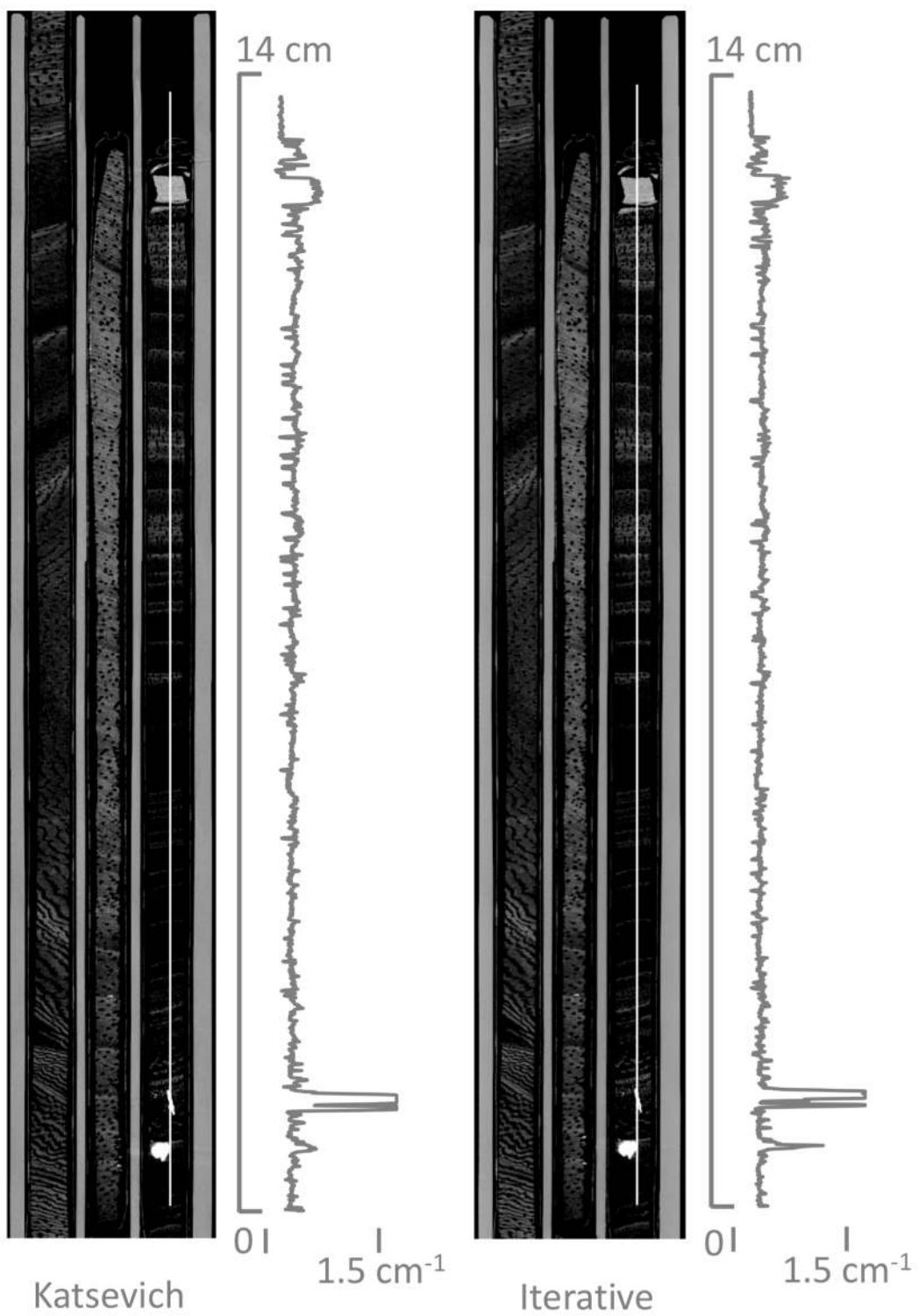


Figure 3.17: Analytical (left) and iterative (right) reconstructions of a helical CT acquisition, imaging a set of tree drilling cores. While the quality of these coronal slices is comparable for both reconstruction techniques, the iterative reconstruction took a significantly longer time to complete.

### 3.3 An outlook to more advanced iterative algorithms

The forward model in iterative reconstruction algorithms is an explicit part of the iterative loop, it can thus be readily replaced by a more extended version. These extended forward models can be veered towards a better representation of the underlying X-ray physics [2], such as the poly- energetic model described throughout section 2.3 and in literature [67, 68], or the noisy Poisson nature of the X-ray photons, included through likelihood expectation maximization [69, 70]. Additionally, extra information on the precise constitution of the imaged object or the way it evolves through time can be included in the algorithm. To put this in a general framework, the CT reconstruction problem is best interpreted through the ‘*Bayes Probability Theorem*’,

$$\mathcal{P}(\vec{\mu}|\vec{p}) = \frac{\mathcal{P}(\vec{p}|\vec{\mu})\mathcal{P}(\vec{\mu})}{\mathcal{P}(\vec{p})} \quad (3.28)$$

where the denominator, also known as the ‘*evidence*’ for a particular data set  $\vec{p}$ , serves as a constant normalization factor, such that

$$\mathcal{P}(\vec{\mu}|\vec{p}) \sim \mathcal{P}(\vec{p}|\vec{\mu})\mathcal{P}(\vec{\mu}) \quad (3.29)$$

This expression states that the ‘*a posteriori belief in  $\vec{\mu}$* ’ is proportional to the product of respectively ‘ $\vec{p}$ ’s likelihood’ and the ‘*a priori knowledge about  $\vec{\mu}$* ’. As an example, a solution for  $\vec{\mu}$  can be found by assuming that both the measurements, encapsulated by the likelihood, and the a priori knowledge on the  $\mu$ -values are independently and normally distributed

$$\mathcal{P}(\vec{\mu}|\vec{p}) \sim \exp\left(-\frac{\gamma_p}{2} \sum_j (p_j - T_{jl}\mu_l)^2\right) \exp\left(-\frac{\gamma_\mu}{2} \sum_l \mu_l^2\right)$$

Taking the negative logarithm of this expression brings about a more familiar representation of the reconstruction problem in the form of a cost function, hiding the possible solution for  $\vec{\mu}$  at its minima

$$\vec{\mu}^* = \arg \min_{\vec{\mu}} \left( \sum_j (p_j - T_{jl}\mu_l)^2 + \alpha \sum_l \mu_l^2 \right), \quad (3.30)$$

Equation (3.30) represents a so-called Tikhonov regularised least squares solution to the CT problem [71]. The regularization parameter  $\alpha = \frac{\gamma_\mu}{\gamma_p}$  reflects the credibility of the a priori information w.r.t. the data, and prevents excessively large  $\mu$ -values in the final reconstruction. While the Tikhonov regularisation is a simple and comprehensive example to illustrate the transition from a probabilistic to a cost function interpretation, it is not a popular form of a priori knowledge in CT

reconstructions. A more prevalent example is that of ‘*Prior Image Constrained Compressed Sensing*’ (PICCS) [72], which combines information on the initial state of a reconstruction volume, e.g. obtained through a preliminary FBP reconstruction, with the concept of ‘*Total Variation Minimization*’ (TV) [73]. The latter places the CT reconstruction problem in the ‘*Compressed Sensing*’ framework [74], which aims at a reduction of the problem’s complexity by promoting a sparse representation of the reconstruction volume, or a transformed version of it. In the case of TV, the regularization term enforces small spatial derivatives with an  $L_1$ -norm ( $\|\cdot\|_1$ ),

$$\vec{\mu}^* = \arg \min_{\vec{\mu}} \left( \|\vec{p} - \mathbf{T}\vec{\mu}\|^2 + \alpha \|\nabla_{\vec{x}}\vec{\mu}\|_1^2 \right),$$

leading to a smooth nearly piecewise reconstruction for  $\vec{\mu}$ . In TV, the gradient operator acts as a so-called sparsifying transform, reducing the number of unknowns in the problem. Other transforms expand  $\vec{\mu}$  in an alternative basis of e.g. wavelets [75] or an overcomplete dictionary of image patches, which are carefully chosen to represent recognisable feature in the final reconstructions [76, 77]. Most of these techniques are developed in a medical context and show very promising results for reconstruction with a small number of projections and thus low X-ray doses. The regularization terms do however introduce an extra complication in the optimization procedure, but can be handled with ‘*iterative shrinkage thresholding*’ [78, 79] or ‘*splitting*’ algorithms [80, 81], with an evident surplus in computation.

In this work, reconstruction regularization, or in the broader sense, the inclusion of a priori information is primarily studied in the context of dynamic processes, which alter the  $\mu$ -distribution during the course of a CT acquisition. To improve the reconstruction of these dynamic processes, the considered a priori information attempts to model the temporal evolution of the  $\mu$ -distribution, caused by the dynamic processes. The precise nature of this a priori information is often based on a simple understanding of processes taking place, e.g. distinguishing a fixed from a time evolving phase. However, the difficulty resides in the ability to cast this information into a mathematical formulation (cfr. TV) which models the interaction between the dynamics of the process and the imaged quantity, here the X-ray attenuation coefficient. This concept is nicely illustrated by Myers *et al.* [82, 83], where the a priori information is meant to model fluid displacements in a fixed matrix of porous rock. In chapter 5, a dynamic non-rigid deformation of a sample’s micro-structure is considered, and an estimate of this local deformation serves as a priori knowledge to compensate for motion blurring upon its integration in a SART reconstruction algorithm.

## 3.4 Conclusion: analytic or iterative?

First of all, it should be noted that the iterative and algebraic algorithms are mathematically not that different from each other. Both techniques sequentially update the volume through the back projection of a derivative, resembling a gradient descent direction in the former case, and the result of a Ram-Lak filter in the latter (cfr. equation (3.8)). Moreover, there are hybrid reconstruction schemes which mimic the behaviour of the algebraic techniques in an FBP setting through carefully designed filters [35]. The differences between both techniques are however more compelling.

For one, the example in section 3.2.6 clearly demonstrates that analytical reconstruction techniques are difficult to beat in terms of reconstruction speed, at least when very large volumes are considered. However, the analytic reconstruction algorithms reduce the radiographic projection process to the mathematical concept of a Radon transform acting on the scalar  $\mu$ -distribution. This Radon transform, which is essentially a collection of line or plane integrals, can thus be seen as the forward model for the projection process, and any physical process deviating from this integral formalism is likely to cause imaging artefacts in the analytical reconstructions. Furthermore, apart from pre-processing the projection data or post-processing the resulting reconstruction volumes, there are no direct mechanisms to incorporate an other forward model or any other information on the imaged sample into the analytical algorithms. Coincidentally, this is where iterative algorithms excel, by allowing improved versions of the forward model to be incorporated in the iterative loop, or by including a priori information for regularization purposes (see section 3.3). The choice between both techniques is thus reduced to a choice between speed and extensibility, which is generally dictated by the application.

In this work, the reconstructions are almost exclusively performed in an iterative way, with a view toward the non-standard trajectory, considered for the in-line CT study (chapter 4), and the inclusion of local, non-rigid deformation into a motion corrected SART algorithm (chapter 5).

## References

- [1] G N Hounsfield. *Computerized transverse axial scanning (tomography): Part 1. Description of system.* The British Journal of Radiology, 46(552):1016–1022, 1973.
- [2] J Nuyts, B De Man, J A Fessler, W Zbijewski, and F J Beekman. *Modelling the physics in the iterative reconstruction for transmission computed tomography.* Physics in medicine and biology, 58(12), 2013.
- [3] A M Cormack. *Representation of a Function by Its Line Integrals, with Some Radiological Applications.* Journal of Applied Physics, 34(9), 1963.
- [4] A M Cormack. *Representation of a Function by Its Line Integrals, with Some Radiological Applications. II.* Journal of Applied Physics, 35(10), 1964.
- [5] A Kak and M Slaney. *Principles of Computerized Tomographic Imaging.* Society for Industrial and Applied Mathematics, 2001.
- [6] Yoni De Witte. *Improved and practically feasible reconstruction methods for high resolution X-ray Tomography.* PhD thesis, Ghent University, 2010.
- [7] P Grangeat. *Mathematical framework of cone beam 3D reconstruction via the first derivative of the Radon transform,* 1991.
- [8] J Kim, S Jung, J Moon, and G Cho. *Industrial gamma-ray tomographic scan method for large scale industrial plants.* Nuclear Instruments and Methods in Physics Research Section A: Accelerators, Spectrometers, Detectors and Associated Equipment, 640(1):139–150, 2011.
- [9] T Rodet, F Noo, and M Defrise. *The cone-beam algorithm of Feldkamp, Davis, and Kress preserves oblique line integrals.* Medical Physics, 31(7):10–14, 2004.
- [10] L a Feldkamp, L C Davis, and J W Kress. *Practical cone-beam algorithm.* Journal of the Optical Society of America A, 1(6):612, 1984.
- [11] D L Parker. *Optimal short scan convolution reconstruction for fan beam CT.* Medical Physics, 9(2):254–257, 1982.
- [12] H Turbell and P E Danielsson. *Helical cone-beam tomography.* International Journal of Imaging Systems and Technology, 11(1):91–100, 2000.
- [13] F Noo, M Defrise, and R Clack. *Direct reconstruction of cone-beam data acquired with a vertex path containing a circle.* IEEE Transactions on Image Processing, 7(6):854–867, 1998.

- [14] P E Danielsson, P Edholm, J Eriksson, and M Magnusson Seger. *Towards exact reconstruction for helical cone-beam scanning of long objects. A new detector arrangement and a new completeness condition.* In D W Townsend and P E Kinahan, editors, Proc. 1997 Meeting on Fully 3D Image Reconstruction in Radiology and Nuclear Medicine (Pittsburgh, PA), pages 141–144, 1997.
- [15] K C Tam, S Samarasakera, and F Sauer. *Exact cone beam CT with a spiral scan.* Physics in Medicine and Biology, 43(4):1015, 1998.
- [16] A J Wunderlich. *The Katsevich Inversion Formula for Cone-Beam Computed Tomography.* Department of Mathematics, MS, 2006.
- [17] F Noo, J Pack, and D Heuscher. *Exact helical reconstruction using native cone-beam geometries.* Physics in Medicine and Biology, 48(23):3787, 2003.
- [18] H Turbell. *Cone-beam reconstruction using filtered backprojection.* PhD thesis, Linköping University, 2001.
- [19] H Kudo, T Rodet, F Noo, and M Defrise. *Exact and approximate algorithms for helical cone-beam CT.* Physics in Medicine and Biology, 49(13):2913, 2004.
- [20] A Katsevich. *Improved exact FBP algorithm for spiral CT.* Adv. Appl. Math., pages 32–681, 2004.
- [21] A Katsevich. *A general scheme for constructing inversion algorithms for cone beam CT.* International Journal of Mathematics and Mathematical Sciences, 2003(21):1305–1321, 2003.
- [22] H Yu and G Wang. *Studies on implementation of the Katsevich algorithm for spiral cone-beam CT.* Journal of X-ray Science and Technology, 12:97–116, 2004.
- [23] M Beister, D Kolditz, and W A Kalender. *Iterative reconstruction methods in X-ray CT.* Physica medica, 28(2):94–108, apr 2012.
- [24] S Kaczmarz. *Angenäherte Auflösung von systemen linearer gleichungen.* Bulletin International de l'Academie Polonaise des Sciences et des Lettres, 35:355–357, 1937.
- [25] V P Il'in. *On the Kaczmarz iterative method and its generalizations.* Journal of Applied and Industrial Mathematics, 2(3):357–366, 2008.
- [26] G L Zeng and G T Gullberg. *Unmatched projector/backprojector pairs in an iterative reconstruction algorithm.* IEEE Transactions on Medical Imaging, 19(5):548–555, 2000.

- [27] X-L Xu. *Iterative algebraic reconstruction algorithms for emission computed tomography: A unified framework and its application to positron emission tomography*. Medical Physics, 20(6):1675, 1993.
- [28] C Kamphuis and F J Beekman. *Accelerated iterative transmission CT reconstruction using an ordered subsets convex algorithm*. IEEE transactions on medical imaging, 17(6):1101–1105, 1998.
- [29] F J Beekman and C Kamphuis. *Ordered subset reconstruction for x-ray CT*. Physics in medicine and biology, 46(7):1835–1844, 2001.
- [30] A H Andersen and A C Kak. *Simultaneous Algebraic Reconstruction Technique (SART): A Superior Implementation of the Art Algorithm*. Ultrasonic Imaging, 6(1):81–94, jan 1984.
- [31] P Gilbert. *Iterative methods for the three-dimensional reconstruction of an object from projections*. Journal of Theoretical Biology, 36(1):105–117, 1972.
- [32] K Mueller, R Yagel, and J F Cornhill. *The weighted-distance scheme: a globally optimizing projection ordering method for ART*. IEEE Transactions on Medical Imaging, 16(2):223–230, apr 1997.
- [33] S Ruder. *An overview of gradient descent optimization algorithm*. <http://sebastianruder.com/optimizing-gradient-descent/>.
- [34] A Klöckner, N Pinto, Y Lee, B Catanzaro, P Ivanov, and A Fasih. *PyCUDA and PyOpenCL: A scripting-based approach to GPU run-time code generation*. Parallel Computing, 38(3):157–174, mar 2012.
- [35] K J Batenburg and L Plantagie. *Fast approximation of algebraic reconstruction methods for tomography*. IEEE transactions on image processing : a publication of the IEEE Signal Processing Society, 21(8):3648–58, aug 2012.
- [36] D Castaño Díez, H Mueller, and A S Frangakis. *Implementation and performance evaluation of reconstruction algorithms on graphics processors*. Journal of Structural Biology, 157(1):288–295, 2007.
- [37] W J Palenstijn, K J Batenburg, and J Sijbers. *Performance improvements for iterative electron tomography reconstruction using graphics processing units (GPUs)*. Journal of Structural Biology, 176(2):250–253, 2011.
- [38] L A Flores, V Vidal, P Mayo, F Rodenas, and G Verdú. *Parallel CT image reconstruction based on GPUs*. Radiation Physics and Chemistry, 95:247–250, 2014.

- [39] P M Joseph. *An Improved Algorithm for Reprojecting Rays through Pixel Images*. IEEE transactions on medical imaging, 1(3):192–196, 1982.
- [40] NVIDIA. *Cuda C Programming Guide*, 2015.
- [41] R L Siddon. *Fast calculation of the exact radiological path for a three-dimensional CT array*. Medical physics, 12(2):252–255, 1984.
- [42] T Kohler, H Turbell, and M Grass. *Efficient forward projection through discrete data sets using tri-linear interpolation*. In Nuclear Science Symposium Conference Record, 2000 IEEE, volume 2, pages 15/113–15/115 vol.2, 2000.
- [43] R M Lewitt. *Alternatives to voxels for image representation in iterative reconstruction algorithms*. Physics in medicine and biology, 37(3):705–16, 1992.
- [44] A Ziegler, T Köhler, T Nielsen, and R Proksa. *Efficient projection and backprojection scheme for spherically symmetric basis functions in divergent beam geometry*. Medical physics, 33(12):4653–4663, 2006.
- [45] B De Man and S Basu. *Distance-driven projection and backprojection in three dimensions*. Physics in medicine and biology, 49(11):2463–2475, 2004.
- [46] Y De Witte, J Vlassenbroeck, and L Van Hoorebeke. *A multiresolution approach to iterative reconstruction algorithms in X-ray computed tomography*. IEEE Transactions on Image Processing, 19(9):2419–2427, 2010.
- [47] J Sanders, E Kandrot, F Breu, S Guggenbichler, and J Wollmann. *CUDA by Example: An Introduction to General-Purpose GPU Programming*. Addison-Wesley Professional, 1st edition, 2010.
- [48] S Van Der Walt, S C Colbert, and G Varoquaux. *The NumPy array: A structure for efficient numerical computation*. Computing in Science and Engineering, 13(2):22–30, 2011.
- [49] B C Lowekamp, D T Chen, L Ibáñez, and D Blezek. *The Design of SimpleITK*. Frontiers in neuroinformatics, 7(December):45, 2013.
- [50] T S Yoo, Michael J Ackerman, W E Lorensen, W Schroeder, V Chalana, S Aylward, D Metaxas, and R Whitaker. *Engineering and Algorithm Design for an Image Processing API: A Technical Report on ITK - the Insight Toolkit*. Studies in Health Technology and Informatics, 85:586–592, 2002.
- [51] S van der Walt, J L Schönberger, J Nunez-Iglesias, F Boulogne, Joshua D Warner, N Yager, E Gouillart, and T Yu. *scikit-image: image processing in Python*. PeerJ, 2:e453, 2014.

- [52] P Koken and M Grass. *Aperture weighted cardiac reconstruction for cone-beam CT*. Physics in medicine and biology, 51(14):3433–3448, 2006.
- [53] A Ziegler, T Nielsen, and M Grass. *Iterative reconstruction of a region of interest for transmission tomography*. Medical physics, 35(4):1317–1327, mar 2008.
- [54] S Klein, M Staring, K Murphy, M A Viergever, and J P W Pluim. *Elastix: A toolbox for intensity-based medical image registration*. IEEE Transactions on Medical Imaging, 29(1):196–205, 2010.
- [55] J P Thirion. *Image matching as a diffusion process: an analogy with Maxwell’s demons*. Medical image analysis, 2(3):243–260, 1998.
- [56] T Vercauteren, X Pennec, A Perchant, and N Ayache. *Non-parametric Diffeomorphic Image Registration with the Demons Algorithm*. Medical image computing and computer-assisted intervention, 10(Pt 2):319–326, 2007.
- [57] H Chen and N Kingsbury. *Efficient registration of nonrigid 3-D bodies*. IEEE transactions on image processing : a publication of the IEEE Signal Processing Society, 21(1):262–72, jan 2012.
- [58] W van Aarle, W J Palenstijn, J De Beenhouwer, T Altantzis, S Bals, K J Batenburg, and J Sijbers. *The ASTRA Toolbox: A platform for advanced algorithm development in electron tomography*. Ultramicroscopy, 157:35–47, 2015.
- [59] W van Aarle, W J Palenstijn, J Cant, E Janssens, F Bleichrodt, A Dabravolski, J De Beenhouwer, K J Batenburg, and J Sijbers. *Fast and Flexible X-ray Tomography Using the ASTRA Toolbox*. Optics Express, 24(22):25129–25147, 2016.
- [60] W J Palenstijn, J Bédorf, J Sijbers, and K J Batenburg. *A distributed ASTRA toolbox*. Advanced Structural and Chemical Imaging, 2(1):19, 2016.
- [61] A Mirone, E Brun, E Gouillart, P Tafforeau, and J Kieffer. *The PyHST2 hybrid distributed code for high speed tomographic reconstruction with iterative reconstruction and a priori knowledge capabilities*. Nuclear Instruments and Methods in Physics Research, Section B: Beam Interactions with Materials and Atoms, 324:41–48, 2014.
- [62] S Rit, M Vila Oliva, S Brousmiche, R Labarbe, D Sarrut, and G C Sharp. *The Reconstruction Toolkit (RTK), an open-source cone-beam CT reconstruction toolkit based on the Insight Toolkit (ITK)*. Journal of Physics: Conference Series, 489:012079, 2014.

- [63] A Biguri, M Dosanjh, S Hancock, and M Soleimani. *TIGRE: a MATLAB-GPU toolbox for CBCT image reconstruction*. Biomedical Physics & Engineering Express, 2(5):055010, 2016.
- [64] J Bardino, M Rehr, and B Vinter. *Cph CT toolbox: CT reconstruction for education, research and industrial applications*. Proceedings - 15th International Symposium on Symbolic and Numeric Algorithms for Scientific Computing, SYNASC 2013, pages 311–320, 2014.
- [65] J Van den Bulcke, E L G Wernersson, M Dierick, D Van Loo, B Masschaele, L Brabant, M N Boone, L Van Hoorebeke, K Haneca, A Brun, C L Luengo Hendriks, and J Van Acker. *3D tree-ring analysis using helical X-ray tomography*. Dendrochronologia, 32(1):39–46, 2014.
- [66] R Ferzli and L J Karam. *A no-reference objective image sharpness metric based on the notion of Just Noticeable Blur (JNB)*. IEEE Transactions on Image Processing, 18(4):717–728, apr 2009.
- [67] B De Man, J Nuyts, P Dupont, G Marchal, and P Suetens. *An iterative maximum-likelihood polychromatic algorithm for CT*. IEEE transactions on medical imaging, 20(10):999–1008, 2001.
- [68] I A Elbakri and J A Fessier. *Segmentation-free statistical image reconstruction for polyenergetic X-ray computed tomography*. Proceedings - International Symposium on Biomedical Imaging, 2002-January(2):828–831, 2002.
- [69] K Lange and R Carson. *EM Reconstruction Algorithms for Emission and Transmission Tomography*. Journal of Computer Assisted Tomography, 8(2):306–316, 1984.
- [70] K Lange, M Bahn, and R Little. *A Theoretical Study of Some Maximum Likelihood Algorithms for Emission and Transmission Tomography*. IEEE Transactions on Medical Imaging, 6(2):106–114, 1987.
- [71] E L Piccolomini and F Zama. *The conjugate gradient regularization method in Computed Tomography problems*. Applied Mathematics and Computation, 102:87–99, 1999.
- [72] G-H Chen, J Tang, and S Leng. *Prior image constrained compressed sensing (PICCS): a method to accurately reconstruct dynamic CT images from highly undersampled projection data sets*. Medical physics, 35(2):660–663, 2008.
- [73] E Y Sidky and X Pan. *Image reconstruction in circular cone-beam computed tomography by constrained, total-variation minimization*. Physics in medicine and biology, 53(17):4777–4807, 2008.

- [74] D L Donoho. *Compressed sensing*. IEEE Transactions on Information Theory, 52(4):1289–1306, apr 2006.
- [75] B Vandeghinste, B Goossens, R Van Holen, C Vanhove, A Pizurica, S Vandenbergh, and S Staelens. *Iterative CT reconstruction using shearlet-based regularization*. IEEE Transactions on Nuclear Science, 60(5):3305–3317, 2013.
- [76] A Mirone, E Brun, and P Coan. *A dictionary learning approach with overlap for the low dose computed tomography reconstruction and its vectorial application to differential phase tomography*. PLoS ONE, 9(12):1–18, 2014.
- [77] Q Xu, H Yu, X Mou, L Zhang, J Hsieh, and G Wang. *Low-dose X-ray CT reconstruction via dictionary learning*. IEEE transactions on medical imaging, 31(9):1682–97, 2012.
- [78] I Daubechies. *An iterative thresholding algorithm for linear inverse problems with a sparsity constraint*. Communications on Pure and Applied Mathematics, LVII:1413–1457, 2004.
- [79] A Beck and M Teboulle. *A Fast Iterative Shrinkage-Thresholding Algorithm*. SIAM Journal on Imaging Sciences, 2(1):183–202, 2009.
- [80] T Goldstein and S Osher. *The split Bregman method for L1-regularized problems*. SIAM Journal on Imaging Sciences, 2(2):323–343, 2009.
- [81] H Raguet, J Fadili, and G Peyr. *Generalized Forward-Backward Splitting*. SIAM Journal on Imaging Sciences, 6(3):1199–1226, 2013.
- [82] G R Myers, A M Kingston, T K Varslot, M L Turner, and A P Sheppard. *Dynamic tomography with a priori information*. Applied optics, 50(20):3685–3690, 2011.
- [83] G R Myers, M Geleta, A M Kingston, B Recur, A P Sheppard, B Hooper, K K W Siu, and A Fouras. *Bayesian approach to time-resolved tomography*. Phys. Med. Phys. J. R. Soc. Interface, 38(15):2975–2985, 2015.



# 4

## Simulation and mock up validation of an alternative in-line CT geometry

As a solution to in-line non-destructive quality inspection in a high throughput production environment, this chapter presents a simple alternative CT geometry, referred to as the '*conveyor belt geometry*'. On this conveyor belt, the scanned object performs a rotational movement, while it translates in between a stationary X-ray source on one side and a fixed large flat panel detector on the other side. In section 4.2, this geometry is discussed in detail, showing that it is theoretically possible to perform a complete angular sampling of the points in an object's central plane, and a limited expression of the cone beam artefact in the vertical direction, as the projections are likely to be acquired at low magnifications and small cone beam angles. In section 4.3, the geometric design constraints, distilled throughout the theoretical discussion, form the basis for a simulation and mock-up study to compare different configurations of the conveyor belt setup, using the realistic Elstar apple phantom from section 2.5. The focus here is the CT acquisition, with a particular emphasis on acquiring sufficient photon statistics and accurate spatial sampling to guarantee qualitative reconstructions with a standard SART reconstruction technique. The quality of the 3D reconstructions is quantified through the Spectral Signal-to-Noise-Ratio (SSNR), introduced in section 4.4.1, and set out against the expected throughput for the configuration at hand. With the resulting methodology, which combines the work on radiography simulation (section 2.3) and iterative CT reconstruction (section 3.2), the trade-off between quality and throughput can be quantified, establishing the feasibility of performing in-line

CT inspections with the conveyor belt geometry, and providing general guidelines for its design.

The details on this study can also be found in the peer reviewed publication [1], which forms the basis for the contents of this chapter.

## 4.1 Introduction: from 2D to 3D

X-ray transmission imaging has become a valuable tool in many industrial branches to ensure the quality of a product through non-destructive evaluation. One way to image a product's interior is through simple 2D radiographic projection. Unfortunately, all of the scanned object's 3D features in a radiograph are superimposed onto one single 2D image, making it difficult to distinguish internal defects that are shaded by other features on the same line of sight. Nevertheless, radiographs are a fast way of imaging the interior of a product in-line and have been used as such in a wide variety of application fields, going from weld and crack inspections on metallic parts, to soldering inspection in electronics and contaminant detection in food products [2–6].

A full 3D visualization of an object's interior provided by X-ray CT can prove to be successful in applications where 2D radiographs are incapable of detecting defects. The CT imaging process itself is however a time consuming task, which might compromise the desired throughput in a production line. In other words, the image acquisition should be as fast as possible, while preserving enough image quality to ensure defect detectability. This can be attained by lowering the X-ray detector's exposure time, or by acquiring a fewer number projections, at the cost of a low Signal-to-Noise Ratio (SNR), and possibly an inaccurate reconstruction of the interesting features in the interior of the scanned object. For the food industry in particular, some defects, such as browning disorders in fruit, inherently show low contrast with respect to their surroundings and are often very small, consequently requiring a high contrast and high resolution image to be visible [7]. The trade-off between a high acquisition speed and a high contrast and resolution image is one of the main reasons why 3D X-ray CT has not yet touched ground as an inspection tool in food industry. The required throughputs can indeed be very high, e.g. the current quality inspection and grading systems that sort apples need to process anywhere between 3 to 10 apples per second [8]. These fast systems are often based and hyperspectral contour visualisation and classification of external defects, i.e. they do not provide information about a product's interior. Nevertheless, to be up to par with the throughput of these traditional inspection methods, a conveyor belt CT system should be able to attain a respectable throughput of

approximately 5 samples per second, depending on the targeted image quality.

On the other hand, CT is already used in-line or rather at-line in some industrial branches, primarily as a metrology tool for inspecting the tolerances on manufactured parts, and is also increasingly being used for the detection of explosives and other potential hazardous items by airport security. Most of these systems can either be categorised as batch delivery or pick-and-place systems [9, 10], where the samples are scanned one by one as shown in the example of Figure 4.1(a) [11]. In other systems, a continuous throughput can be realised by using a helical scanning approach, similar to medical CT equipment, see also Figure 4.1(b) [12, 13]. Helical scanning geometries offer a complete angular sampling of the entire object, but are often complex in their implementation. Hence, being a simpler and possibly low maintenance concept, the conveyor belt geometry presented below is put forward as a possible competitor to the helical approach. However, the need for moving parts can be completely set aside in a notable new development where the rotating gantry is replaced by a series of stationary sources and detectors, that are placed on a ring around the conveyor belt [14, 15]. There is even a commercially available system, that implements this approach (see Figure 4.1), for airport security applications, reaching a throughput of 0.5 luggage bags per second at a resolution of approximately 1 mm.

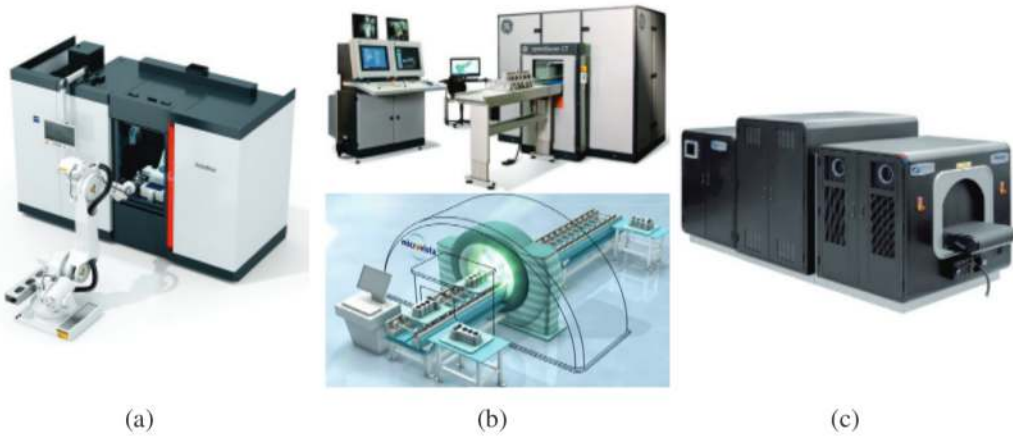


*Figure 4.1: Several commercially available in-line CT solutions. (a) The pick-and-place Volumax system of Zeiss [11], (b) The GE speedscan and the micro-vista helical gantry systems [12, 13], and (c) the Rapiscan RTT system with an electronically fired source ring and detector ring [15, 16].*

While the focus here is on CT acquisition, the imaging process (section 2.1) does not stop there. First of all, a valid 3D inspection and defect detection requires the 2D radiographic projections to be reconstructed into a 3D volume. Secondly, the 3D volumes have to be analysed to extract the relevant information about pos-

sible defects. The reconstruction and imaging analysis encompass a computational effort, which has to be addressed with the right computing power and clever algorithms. Improvements in these downstream imaging steps can however be very application dependent, which does not fit into the general study on the performance of the conveyor belt geometry. On the other hand, these improvements might greatly relax the demands on acquisition, e.g. by significantly lowering the amount of projections and X-ray dose, and thus the SNR, needed for a good reconstruction of an object's interior [17–19]. In this work the acquisition is handled separately, with a particular emphasis on acquiring sufficient photon statistics and accurate spatial sampling to guarantee qualitative reconstructions with a standard SART reconstruction technique.

## 4.2 The conveyor belt CT acquisition

### 4.2.1 Geometry

#### Geometrical constraints for an exact conveyor belt acquisition

In figure 4.2 a schematic top view of the conveyor belt setup is shown. An X-ray source point is kept at a fixed distance (Source Detector Distance, SDD) from a large flat panel detector. The sample itself performs a translation from the left to the right at a fixed distance from the source (Source Object Distance, SOD), parallel to the central row of the detector and in the plane containing both this central detector row and the source point. While travelling a horizontal distance ( $H$ ), the sample also performs a rotational movement as a supplement to the inherent change in parallax related to the translational movement. This is most efficiently realised with a counter clockwise rotation as viewed from the top.

The angle for this rotation has to be chosen such that every point in the sample is intersected by a source ray over an angular range of at least  $180^\circ$ , i.e. following the Tuy-Smith condition [20] introduced in section 2.1.2. Rephrasing the intuitive formulation from section 3.1.2 on helical CT, the Tuy-Smith condition requires that relative to any given point in the object the source traces out a trajectory in space which does not intersect the given point and for which the trajectory's end points are collinear with this given point. The resulting trajectory will henceforth be referred to as '*complete*'. For a conveyor belt geometry, the rotation angle forming a complete trajectory can be found by considering the object at its central position between the source and the detector, i.e. halfway its translation where the central ray cuts the Region Of Interest (ROI) into two symmetric halves (see figure 4.2). For now, the ROI is considered to be circular, but as shown in figure 4.5 its shape can be extended.

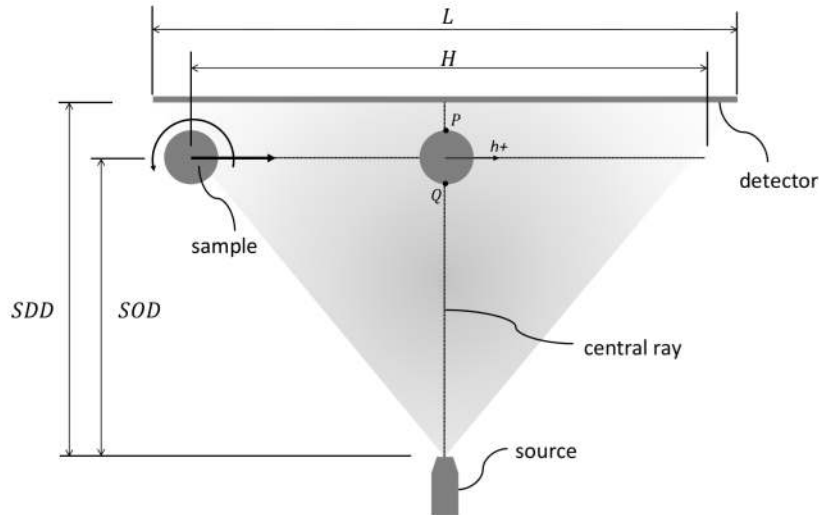


Figure 4.2: Schematic top view of the conveyor belt geometry. The sample combines a rotation and a translation over a distance  $H$  at a fixed distance from the detector, ODD. The source is kept stationary at a distance SDD from the detector.

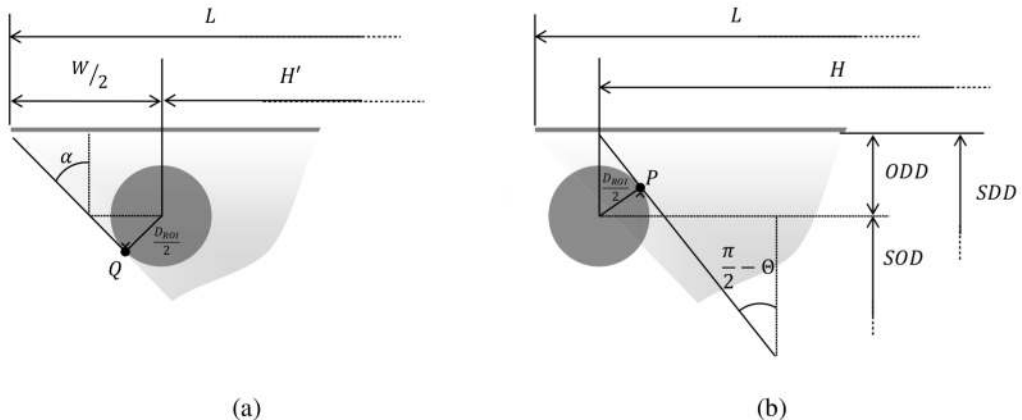


Figure 4.3: Conditions leading to a complete conveyor belt trajectory. (a) Condition 1: In point  $Q$ , the ROI is tangent to the outer ray, which connects the source point to the detector edge. (b) Condition 2: The ROI has a tangent source ray in point  $P$ .

Any conclusion regarding the covered angular range for a point in the right half of this ROI w.r.t. its movement on the left side of the source is equivalent to the symmetric case for a point in the left half w.r.t. its movement on the right side of the source. Furthermore, it can be shown (see figure 4.5) that the points on the intersection between the outer rim on the ROI and the central ray, indicated by  $P$  and  $Q$  in figures 4.2 and 4.3, will cover the smallest angular range of all points within the ROI. The fact that these points have to be sampled from at least  $180^\circ$  puts forward two conditions connecting the a priori chosen geometrical parameters, in most practical cases the detector length ( $L$ ), the Object Detector Distance (ODD), the ROI diameter ( $D_{ROI}$ ) and the source's half opening angle ( $\alpha$ ), to the a

priori unknown parameters, i.e. the SOD, SDD, the detector run-out ( $W$ ) and the half rotation angle ( $\Theta$ ) as defined by figure 4.3:

1. While moving backward from its central position, the point  $Q$  will be the first point to be projected out of the detector field. At this outer position the source rays should have covered at least  $90^\circ$  around point  $Q$ . This condition occurs when the ROI is tangent to the outer ray in  $Q$  as depicted in figure 4.3(a) and relates  $\alpha$  to  $W$ ,  $D_s$  and the ODD:

$$\frac{D_{ROI}}{\cos(\alpha)} = W - 2 \text{ ODD} \tan(\alpha) \quad (4.1)$$

The opening angle itself is given by

$$\frac{L}{2 \text{ SDD}} = \tan(\alpha) \quad (4.2)$$

2. To complete the trajectory for point  $P$  there has to be a source ray tangent to the ROI in  $P$  (see figure 4.3(b)). With  $\pi/2 - \Theta$  being the angle between this ray and the central source ray, the following condition holds:

$$H = \frac{1}{\sin(\Theta)} (2 \text{ SOD} \cos(\Theta) + D_{ROI}) \quad (4.3)$$

Keeping in mind that

$$\text{SDD} = \text{SOD} + \text{ODD} \quad (4.4)$$

and using equation 4.2, equation 4.1 can be reformulated as

$$H' = L - W = \frac{1}{\sin(\Theta')} (2 \text{ SOD} \cos(\Theta') - D_{ROI}) \quad (4.5)$$

with  $\alpha = \pi/2 - \Theta'$ . Finally, equations 4.1 to 4.5 can be combined to form the following set

$$\text{SDD} = \frac{L}{2 \tan(\alpha)} \quad (4.6)$$

$$\text{SOD} = \text{SDD} - \text{ODD} \quad (4.7)$$

$$\frac{\Theta'}{\Theta} = \frac{\sin(\Theta)}{\sin(\Theta')} \cdot \frac{2 \text{ SOD} \cos(\Theta') - D_{ROI}}{2 \text{ SOD} \cos(\Theta) + D_{ROI}} \quad (4.8)$$

where we have implicitly assumed that

$$\frac{\Theta'}{\Theta} = \frac{H'}{H} \quad (4.9)$$

which means that the rotation angle is uniformly distributed over the translation and as such evolves linearly with it. In general, when considering a counter clockwise rotation, the rotation angle can follow any continuous mapping along the

horizontal travel abiding to the restrictions discussed in next paragraph.

Using equations 4.6 to 4.8, the SDD, SOD and  $\Theta$  can be calculated, given  $L$ ,  $\alpha$ , ODD and  $D_{ROI}$ , which fixes the entire conveyor belt geometry. In figure 4.4, the trajectories for the points  $P$  and  $Q$  are plotted for a situation in which all of the geometrical parameters comply to equations 4.6 to 4.8, with  $L = 966\text{ mm}$ ,  $\alpha = 40^\circ$ , ODD = 75 mm and  $D_{ROI} = 90\text{ mm}$  (corresponding to  $H = 800\text{ mm}$ ). The angular ranges for each point in a rectangular region containing the ROI where calculated for this specific situation in figure 4.5(a). The contour containing the points which cover at least  $180^\circ$ , is indicated by a thick black line. Theoretically, all the points within this contour can be reconstructed exactly, in particular the points from the circular ROI considered in this study. From figure 4.5(b), which plots the angular range along the dashed line in figure 4.5(a), it can be seen that the points  $P$  and  $Q$  do indeed cover an angular range of  $180^\circ$ , while the other points on the ROI circumference cover a larger range.

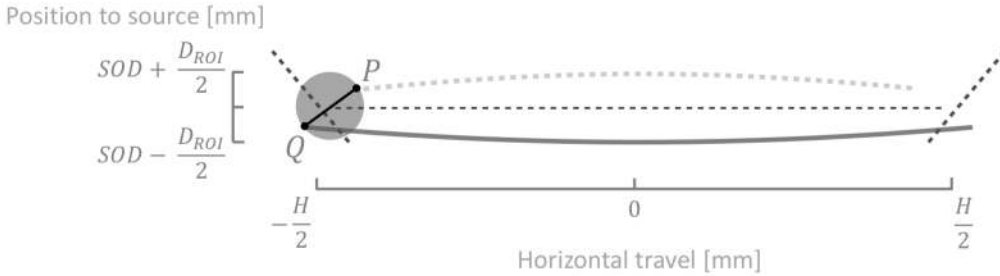


Figure 4.4: Trajectories of the points  $P$  and  $Q$  throughout their conveyor belt movement.

The ROI is drawn at the start of the acquisition, i.e. at the moment condition 2 for a complete trajectory holds. It should be noted that the object is only mildly rotated, i.e.  $111^\circ$  for the specific case depicted here, with  $L = 966\text{ mm}$ ,  $\alpha = 40^\circ$ , ODD = 75 mm and  $D_{ROI} = 90\text{ mm}$ .

In principle, only the ODD and  $D_{ROI}$  are known a priori, since the sample should be contained within the ROI and should not hit the detector plane. Hence, given the sample's diameter  $D_s$ , the following must hold

$$D_{ROI} \geq D_s$$

$$\text{ODD} \geq \frac{D_s}{2}$$

$L$  and  $\alpha$  have to be chosen but in practice will be dictated by a certain demand in throughput (see section 4.2.2) and technical limitations such as the detector size and source's collimator opening. Moreover, the fixed nature of either one ( $L$  or  $\alpha$ ) can be interchanged for a specific choice of SDD or SOD, as long as equation 4.6 to 4.8 are fulfilled.

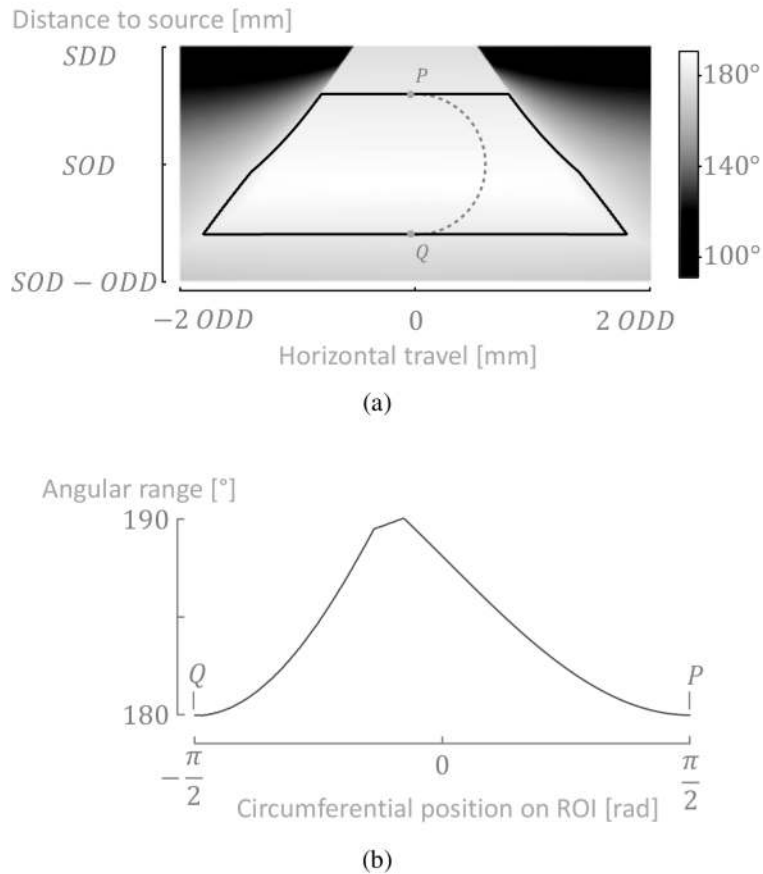


Figure 4.5: (a) The angular range covered by the points in a rectangular region containing the ROI. The thick black contour contains all of the points which cover at least  $180^\circ$ , including the ROI studied here; (b) By following the ROI circumference (dashed line in (a)) it can be seen that the points P and Q do indeed cover an angular range of  $180^\circ$ , while the other points cover a larger range. (cfr. figure 4.4;  $L = 966 \text{ mm}$ ,  $\alpha = 40^\circ$ ,  $ODD = 75 \text{ mm}$  and  $D_{ROI} = 90 \text{ mm}$ ).

### Generalised conveyor belt like trajectories

When considering a counter-clockwise rotation, the rotation angle ( $\theta$ ) can follow any continuous mapping ( $g$ ) along the horizontal travel coordinate( $h$ ), which can be expressed as follows

$$g : h \rightarrow \theta \quad h \in \left[ -\frac{H_{out}}{2}, \frac{H_{out}}{2} \right]$$

Subject to

$$\left| g \left( \pm \frac{H'}{2} \right) \right| \geq \Theta' \quad \text{and} \quad \left| g \left( \pm \frac{H_{out}}{2} \right) \right| \geq \Theta'$$

with

$$H_{out} = H' + \frac{2 D_{ROI}}{\cos(\alpha)}$$

representing the distance between the extremal position of the sample, where its ROI is just outside of the detector's field of view, tangent to the extremal source rays. In words, the conditions on the function  $g$  state that there should be at least one ray tangent to the ROI for  $P$  and  $Q$  on both the left and the right side of the central ray. This opens up a wide range of possible trajectories and embodiments for a conveyor belt geometry. The one focused upon in this work follows equation 4.9, where both the acquisition and the rotation are initiated at position  $h = -H/2$  as in figure 4.3(b). In a similar implementation the acquisition could be started together with the translation at  $h = -H_{out}/2$ , while the rotation would only start at  $h = -H'/2$ , eventually performing an identical rotation of  $2\Theta'$  between  $-H'/2$  and  $H'/2$ . These trajectories can be realised in practice by attaching a sample tray to a pinion, which in turn grabs into a linear rack gear, producing a simultaneous rotation around the pinion's axis and a linear translation parallel to the rack. It is clear that all of the conveyor belt like trajectories introduce an additional translational movement with respect to the traditional circular cone beam acquisitions. To that end, it is important to note that the projections of some points in the sample, more than others, may be subject to motion blurring when they are shifted by more than one detector pixel during the exposure time. Hence, an important question to be investigated in future work, is whether the generalised conveyor belt like trajectories offer a better reconstruction quality and most importantly whether they might provide larger reconstruction regions (cfr. figure 4.5(a)) while causing less motion blurring overall.

### 4.2.2 Throughput

At first glance there seems to be no apparent reason to choose a large horizontal travel  $H$ , specifically because this requires a larger and thus more expensive detector. Moreover, the average X-ray flux ( $I_{av}$ ) seen by the sample will quickly drop off for higher  $H$  according to

$$I_{av} = I_{ref} \cdot \frac{\text{SDD}_{ref}^2}{\text{SDD}^2} \cdot f(x) \quad (4.10)$$

given

$$f(x) = \frac{\arctan(x)}{x} \quad \text{for } x = \frac{H}{2 \text{SOD}},$$

where  $I_{ref}$  is the X-ray flux on the central ray measured at a reference distance  $\text{SDD}_{ref}$  from the X-ray source. Indeed, looking at figure 4.2, the distance between the source point and any given point on the central detector row can be written as a function of the travel position ( $h$ )

$$R(h) = \sqrt{\text{SDD}^2 + h^2}$$

As the X-ray intensity decreases quadratically with an increasing distance from the source point

$$I(h) = I_{ref} \frac{\text{SDD}_{ref}^2}{R(h)^2},$$

the average intensity can be calculated by solving the following integral

$$I_{av} = I_{ref} \cdot \text{SDD}_{ref}^2 \cdot \int_{-HM/2}^{HM/2} dh / R(h)^2$$

for a magnification  $M = \text{SDD}/\text{SOD}$ . Following equations 4.6 to 4.8, a larger  $H$  will lead to an on average less favourable SNR performance, primarily because of the quadratic intensity decrease caused by an increasing SDD, while  $f(x)$  remains practically constant. Hence, in order to maintain a constant SNR, the reference flux ( $I_{ref}$ ) has to be increased, for example by increasing the tube power. A larger  $H$  can however be advantageous considering more samples can be scanned simultaneously with a larger detector field. In the limiting case of a parallel beam ( $\text{SDD} \rightarrow \infty$ ) the projections of subsequent samples will not overlap, and the number of samples which can be scanned simultaneously ( $N_s$ ) is given by

$$N_s = \frac{L}{D_{ROI}}$$

However, for a real case, the cone beam can produce overlapping projections at the edges of the sample's translation path when the distance between two subsequent samples is too small. The minimal distance between the samples can be derived from figure 4.3(b), which depicts the start of a new acquisition. Here, the tangent ray in point  $P$  delineates the edge of a sample's projection on the detector, and dictates how close a preceding sample (not depicted in figure 4.3(b)) can be to the new sample. In other words, the tangent through  $P$  forms a mutual tangent between the ROI's of subsequent samples at the start of a new acquisition. The minimal distance between these samples is

$$\Delta_{min} = \frac{D_{ROI}}{\sin(\Theta)},$$

and thus for the number of samples which can be imaged simultaneously the following holds

$$N_s = \frac{H}{D_{ROI}} \cdot \sin(\Theta)$$

The effective throughput ( $T_{eff}$ ), as in the number of samples which can be scanned per second, for the conveyor belt setup is then given by

$$T_{eff} = \frac{N_s}{N_p \cdot t_{exp}} \left[ \frac{\text{samples}}{\text{sec}} \right] \quad (4.11)$$

with  $N_p$  the number of projections acquired during the scan at an exposure time of  $t_{exp}$  seconds for a single projection.

### 4.2.3 Detector & X-ray tube settings

Apart from the geometrical aspects, a good detector and X-ray tube are also essential to qualitative CT acquisition. Although their properties have to be tuned to the application at hand, there are some general guidelines which can be followed in the case of a conveyor belt setup, making it possible to extrapolate the methods discussed here to similar setups and other types of samples. First of all, it should be noted that the conveyor belt setup is meant to be operated in a so called '*focal spot demagnification*' regime, meaning that the ODD is typically smaller than the SOD. The advantages of demagnification are that:

1. the span of the cone beam is larger closer to the detector, and as such more product samples can be imaged simultaneously.
2. the X-ray spot size will be demagnified by a factor  $M_s = \text{ODD}/\text{SOD}$ , which allows for larger spot sizes ( $p_s$ ) than the detector pixel size ( $p_d$ ). As a consequence, a higher tube power can be set, and the heat generated in the tube's focal spot can be dissipated across a larger area.

Unfortunately, a demagnification of the focal spot also implies that there will barely be any object magnification ( $M_o$ ) and that the voxel size of the 3D CT reconstruction ( $p_v$ ) will be more or less equal and be limited to the detector's pixel pitch, according to (cfr. equation (2.5))

$$p_v = \frac{1}{M_o} p_d + \frac{M_s}{M_o} p_s \quad (4.12)$$

where  $p_s \leq p_d/M_s$ , i.e. the demagnified spot size should be smaller than the detector pixel size. Hence, choosing a detector pixel size indirectly imposes an upper limit on the X-ray focal spot size, while the latter limits the power which can be deposited in the focal spot area. Typically, the target of an X-ray tube can safely dissipate a maximum of 1kW per mm of focal spot diameter, which leads to the following coincidental relation between the tube power ( $P_t$ ) and the detector pixel size

$$P_t [W] \leq \frac{p_d [\mu\text{m}]}{M_s}$$

The cases discussed in section 4.3.1 use a detector with a pixel pitch of 0.254 mm in a setting where the X-ray focal spot is demagnified by a factor of at most  $M_s = 0.23$ , which implies a maximal focal spot size of approximately 1.1 mm, and subsequently a maximum tube power of about 1.1 kW. This tube power is quite large, in the sense that the dynamic range of most detectors will be clipped well before reaching this limit, even at very low exposure times. As it is implicitly assumed that the detector is read out as fast as possible in order to reach a high throughput (cfr. equation 4.11), the tube power is actually determined by the detector's saturation limit rather than any geometrical restrictions on the focal spot

size.

The SNR in the resulting CT reconstruction can also be optimised by setting an optimal tube high voltage. Again this parameter is highly dependent on the type and size of the sample, but can be estimated by looking at the theoretical attenuation through a slab with a material thickness representative for the sample under study. The Elstar apple can be modelled as a 6 cm thick slab of soft-tissue with a density of  $0.84 \text{ g/cm}^3$  (see section 2.5). The theoretical transmission through this slab can be calculated across several energy bins covering the complete X-ray tube spectrum, followed by a back projection of the attenuating mass and its associated error into a voxel element [21, 22]. The expected SNR, expressed in  $\text{dB}$  (see (2.34)), can finally be set out as a function of the X-ray tube's high voltage for a fixed tube output power, which clearly shows a maximum at 120 kV (figure 4.6).

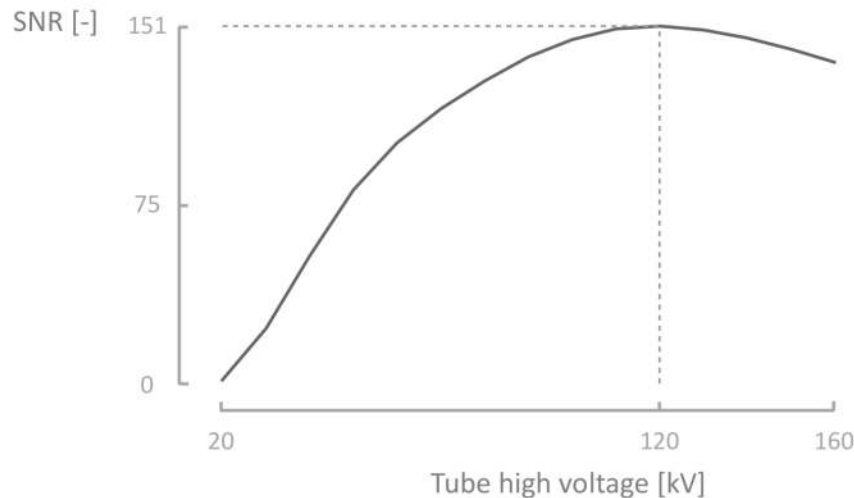


Figure 4.6: The estimated SNR on the calculated attenuation value of a 6 cm slab of soft tissue as a function of the X-ray tube's high voltage. A maximum for the SNR can be found at 120 kV, which subsequently serves as an optimal tube voltage for this sample at a given tube power.

## 4.3 A simulated & hardware mock up conveyor belt

### 4.3.1 Real life & simulated acquisitions

As mentioned in paragraph 4.2.1, a conveyor belt geometry is completely fixed with a specific choice for  $L$ ,  $\alpha$ , ODD and  $D_{ROI}$ . In most practical cases only the detector length  $L$  or more specifically the travel  $H$  will vary, since ODD and  $D_{ROI}$  are determined by the sample diameter  $D_s$  and  $\alpha$  will be limited by the source collimator opening or by a sensible limit posed upon the detector run-out  $W$ . Hence, in the following we consider  $H$  to be the only variable geometrical

parameter, while the other parameters will be either fixed at a certain value or calculated through equations 4.6 to 4.8. Given a fixed exposure time ( $t_{exp}$ ), the number of projections ( $N_p$ ) then completely defines a conveyor belt acquisition, which together with  $H$  leaves two independent variables for the characterization of the image quality produced by a conveyor belt setup. Although the problem of characterizing the image quality for conveyor belt scans is now reduced to sweeping a two dimensional ( $H, N_p$ ) parameter space, it is still difficult to do this in a real life setup, as several other parameters indirectly vary with  $H$  through equation 4.6 to 4.8. Nonetheless, an effort has been made to build a flexible mock-up, which can mimic a conveyor belt acquisition for a broad range of ( $H, N_p$ )-pairs.

To this end, UGCT's Medusa system (section 2.2.3) was equipped with an add-on module (figure 4.7) containing a flat panel detector (Varian Medical Systems GmbH, Willich, Germany) and an extra rotation stage (PI miCos GmbH, Freiburger, Germany). The detector and the rotation stage are fixed w.r.t. each other such that the distance between the detector surface and the rotation axis remains constant, i.e. ODD = 84.5 mm. The add-on module is mounted on a translation stage which is normally used to select one of the detectors from the setup, and to align its central row with the X-ray source and the original rotation axis of the setup. The combined movement of the translation stage and the rotation stage makes it possible to mimic conveyor belt trajectories with a travel limited to the translation stage's spindle length ( $H_{max} = 556$  mm). The translation stage in turn is mounted on another motorised stage which can set the SDD. The three axes of motion allow for practically any conveyor belt acquisition. However, some geometrical parameters are implicitly fixed, such as the detector run-out ( $W$ ) which is given here by the detector width, the ROI diameter set to the maximal diameter of the sample ( $D_s$ ) and subsequently the half opening angle ( $\alpha$ ), by taking into account equation 4.1. The opening angle is well within the limits of the setup, as here an uncollimated transmission type X-ray source (Feinfocus FXE160.51, X-RAY WorX GmbH, Garbsen, Germany) was used, which radiates quasi-uniformly from its source point. An overview of the geometrical parameters and their fixed nature is given in table 4.1. In order to minimise the drying and the build-up of browning disorders in the apple sample, all of the scans were performed on the same day, including the high resolution scan, which was used to construct the digital phantom.

Following table 4.2, a series of conveyor belt scans was acquired with the mock-up conveyor belt. Using the radiography simulator, discussed in section 2.3 [21], these scans were also simulated, opening the possibility to produce data beyond the travel limits set by the mock-up's design. Each of the setups, listed in table 4.2, was executed five times for a varying number of projections, going from

*Table 4.1: Overview of the geometrical parameters of the conveyor belt mock-up. Only the horizontal travel ( $H$ ) is varied independently, while the source detector distance (SDD) and the rotation angle ( $\Theta$ ) are calculated from equations 4.6 to 4.8. The other parameters are fixed by design.*

		Fixed?	Value \ Range		
horizontal travel	( $H$ )	no	-278	...	278 mm
source detector distance	(SDD)	no	200	...	1300 mm
rotation angle	( $\Theta$ )	no	no restrictions $^{\circ}$		
ROI diameter	( $D_{ROI}$ )	yes	65 mm		
object detector distance	(ODD)	yes	84.5 mm		
detector run-out	( $W$ )	yes	145.5 mm		
half opening angle	( $\alpha$ )	yes	24 $^{\circ}$		
binned pixel size	( $p_d$ )	yes	254 $\mu\text{m}$		

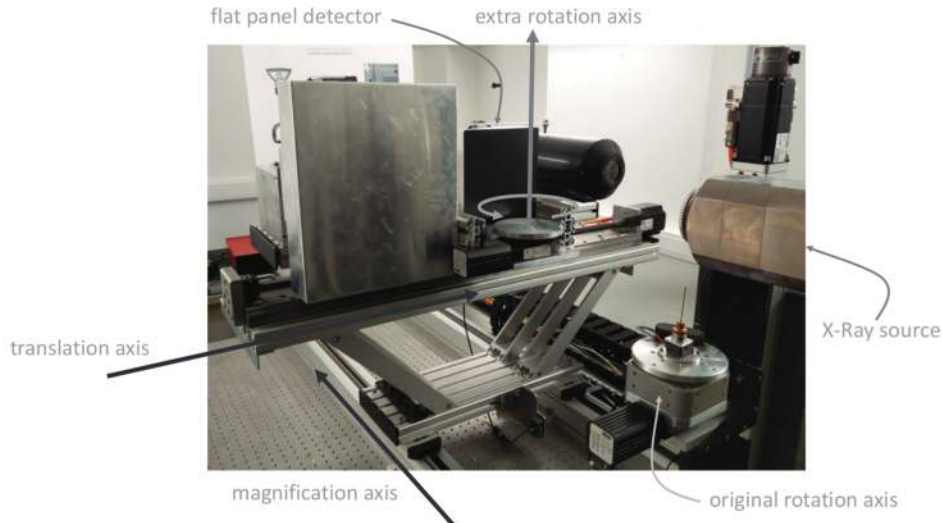


*Figure 4.7: UGCT's Medusa system (section 2.2.3) was equipped with an extra detector and a co-moving rotary stage. The module containing this detector and rotary stage is mounted on a translation axis, which is normally used to align one of several detectors on this setup with the X-ray source. The translation stage in turn is mounted on another axis which sets the SDD.*

100 to 500 in steps of 100, leading to 20 scans acquired with the mock-up and 35 simulated scans in total.

Regarding table 4.2 it should be noted that the detector illumination ( $t_{exp} \cdot P_t$ ) is varied in order to completely fill up the detector's dynamic range as to compensate for the quadratic drop in the X-ray flux with the increasing SDD. In the mock-up setup, this was achieved by altering the exposure time ( $t_{exp}$ ), because the transmission X-ray tube used in the setup had a limited output power, here set to 4 W. This power limitation is not an issue for industrial, directional tubes, which can reach up in the order of 1 kW in tube power. So in a practical setup, rather

*Table 4.2: Overview of the scans performed with the mock-up and the simulated scans. The travel ( $H$ ) is varied while the SDD,  $L$  and  $\Theta$  are calculated through equations 4.6 to 4.8. The detector illumination is expressed as a product of the exposure time and the tube power. The tube high voltage was set to 120kV.*

Simulated scans	Mock-up scans	$H$ [mm]	$L$ [mm]	SDD [mm]	$\Theta$ [ $^\circ$ ]	$t_{exp} \cdot P_t$ [Ws]
v	v	200	318.7	361.5	153.0	0.800
v	v	300	416.4	472.4	146.7	1.368
v	v	400	515.2	584.4	143.3	2.092
v	v	500	614.4	697.0	141.2	2.976
v		600	713.9	809.9	139.9	4.016
v		700	813.5	922.9	138.8	5.216
v		800	913.2	1036.0	138.0	6.568

than the detector's exposure time, the power would be adjusted towards filling up the dynamic range of the detector.

### 4.3.2 Comparing the simulations to the mock-up data

#### Projections

In figure 4.8, three projections of the sample, moving along its conveyor belt trajectory, are superimposed on what would be the full field of view of a stationary detector of length  $L = 319\text{ mm}$ , corresponding to a travel of  $H = 200\text{ mm}$ . Based on a visual comparison, a good agreement was found between the mock-up scans and the simulated scans, while some small differences can clearly be seen on the line profiles for transmission and the local SNR, following a horizontal line through the centre of the middle projection (indicated in figure 4.8). These small differences can to a large extent be explained by a slight misalignment between the digital phantom and the real sample. Most importantly, the SNR, calculated of over ten voxel wide moving window, is very similar in both cases, which is crucial with respect to evaluating the quality of the CT reconstructions.

#### Reconstructions

For standard circular cone beam and helical cone beam acquisitions the reconstruction can be performed through fast analytical reconstruction algorithms like the FDK [23] and Katsevich [24] algorithms (section 3.1.2). An essential prerequisite to the FDK algorithm is that the projections are sampled in an equiangular fashion on a circular trajectory, which is not the case for the conveyor belt setup. By remapping the ray paths into an equiangular sequence, and by applying appropriate back projection weights, the FDK algorithm can still be used to perform a recon-

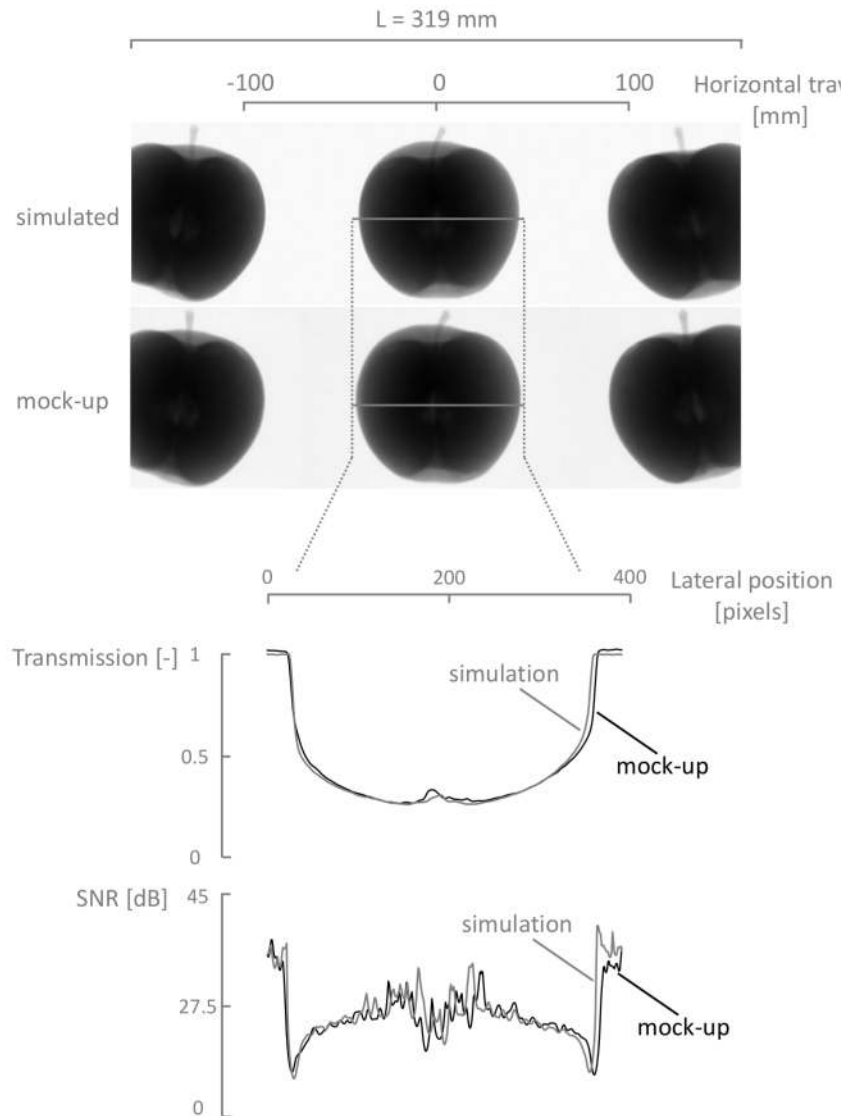


*Figure 4.8: Comparison between three projections acquired with the mock-up conveyor belt and their simulated counterparts (top). The projections are shown from left to right as they would be acquired on a stationary detector with a span  $L$ , here  $L = 319 \text{ mm}$  for  $H = 200 \text{ mm}$ . Although the overall agreement is good, some small differences, which can be attributed to slight misalignments between the digital phantom and the real apple, are visible on line profiles for the transmission and the local SNR (bottom).*

struction of a conveyor belt acquisition. To avoid these remapping and reweighting steps, the data from the uncommon conveyor belt geometry are reconstructed with the simultaneous algebraic reconstruction technique (SART) [25] (section 3.2.3). The SART reconstructions were performed with the Python-C tool, which uses PyCUDA [26] to off-load the computationally demanding tasks to a GPU, offering a tremendous decrease in reconstruction times (section 3.2.5).

The reconstructions are performed on a grid of 545 slices containing 570 by

570 cubical voxels with a volume of  $128^3 \mu\text{m}^3$  each, of which the central slice is shown in figure 4.9 for  $H = 200 \text{ mm}$ . Visually the simulated and mock-up reconstructions proved to be very similar, although the simulated scans appear to be slightly sharper. This can also be seen in the histograms, where some of the features are smoothed out in the mock-up reconstructions. Most importantly, the overall sharpness improves as the number of projections ( $N_p$ ) is increased. This effect can be leveraged when setting a larger travel ( $H$ ), which allows for more projections to be acquired at a similar throughput, and for smaller features to be visualised. This gain in sharpness is barely visible to the naked eye, and is therefore not conveyed through figure 4.9, though it can be quantified through the Spectral Signal-to-Noise Ratio (see section 4.4.1). On the other hand, there is loss in sharpness as  $H$  increases, at a fixed number of projections. This is primarily caused by a decrease in the geometrical magnification for larger SDD's at a constant ODD, next to a slight drop in the factor  $f(x)$  in equation 4.10, which is not compensated for by setting a higher illumination.

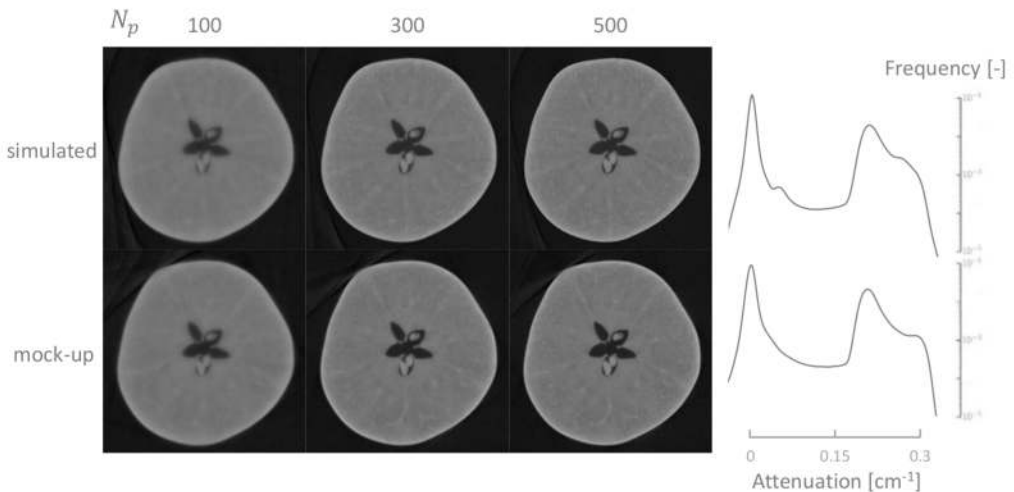


*Figure 4.9: Reconstruction for the central slice in the Elstar apple based on the simulated (top) and the mock-up projections (bottom) for a varying number of projections ( $N_p$ ) and  $H = 200 \text{ mm}$ . The simulated scans seem to be sharper, and as expected the sharpness increases significantly with  $N_p$ . The histograms for the  $N_p = 500$  case (right) are very similar, apart from a small streaking artefact in the mock-up reconstructions. This is probably caused by a misalignment in the reconstruction geometry, which is difficult to pinpoint at this stage, but could be eliminated by an automated trajectory calibration.*

## 4.4 Reconstruction quality & throughput

### 4.4.1 Spectral resolution metrics

The spatial resolution of a reconstruction forms an absolute lower bound on the smallest features that can be detected through CT. The voxel pitch, given by (2.5), is however not always a fair reflection of the apparent resolution, which is also affected by noise and the filtering effects of the reconstruction process. To determine a reliable estimate for the apparent resolution, the SNR concept can be extended towards the frequency domain, leading to so-called spectral resolution metrics. The idea of these metrics is to identify the highest spatial frequency that can marginally be discerned from the noisy background. In other words, they identify the frequency for which the SNR drops below a certain visibility threshold. Here, this frequency, or more specifically its inverse, which sets a lower bound on the detectable feature size, serves as a measure for the quality of a CT reconstruction. In the context of this work, two spectral resolution metrics have been studied: (1) the Spectral Signal-to-Noise Ratio (SSNR), and (2) Fourier Shell Correlation (FSC).

#### The Spectral Signal-to-Noise Ratio (SSNR)

For the SSNR [27, 28] the 3D Fourier transforms of two distinct volumes are calculated, i.e. a reconstruction of the projections taken from a sample, and a reconstruction based on projections containing only noise. To obtain these noise-only reconstructions, the noise component in the projections has to be estimated. This can be done by considering a Gaussian error propagation on the ray sums (cfr. equation (2.6))

$$p = -\ln \left( \frac{U}{U_0} \right) = -\ln(u)$$

where the measurements  $U$  and  $U_0$ , expressed in ADUs, are distributed normally in the high photon count limit of a Poisson distribution (equation 2.18). The variance on  $U$  and  $U_0$  is thus proportional to the number of detected photons

$$N_0 \approx \beta^2 \cdot \sigma_{U_0}^2 \quad (4.13a)$$

$$n_o \cdot N \approx \beta^2 \cdot \sigma_U^2 \quad (4.13b)$$

where  $\beta$  represents the number of photons needed to fill up one ADU-level, and  $n_o$  the number of open beam images acquired for each data frame (here  $n_o = 5$ ). The factor  $\beta$  can be estimated from the simulated radiographs, after a proper tuning of the gain factor  $\kappa$  (see equation 2.16) which matches the simulations to the real data (here  $\beta = 2.5$ ). In a next step, the error on  $p$  can be approximated through a first order expansion under the Gaussian propagation assumption

$$\sigma_p^2 \approx \left( \frac{\partial p}{\partial u} \right)_{u=1}^2 \sigma_u^2 \quad (4.14a)$$

$$\approx \frac{\sigma_u^2}{u^2} \quad (4.14b)$$

$$\approx \frac{\sigma_{U_0}^2}{U_0^2} + \frac{\sigma_U^2}{U^2} \quad (4.14c)$$

By combining (4.13) and (4.14), it follows that

$$\sigma_p^2 \approx \left( \frac{\alpha}{u} + 1 \right) \cdot \frac{1}{\beta U_0} \quad (4.15)$$

With (4.15), the variance  $\sigma_p^2$  can be estimated for each pixel individually by approximating  $u$  and  $U_0$  through low pass filtered versions of the normalised projections and the open beam images, respectively. Here, a 50 pixel wide Gaussian blur is applied to the normalised projections and open beam images, in order to eliminate their inherent shot noise through a spatial smoothing.

Subsequently, the power of the 3D Fourier signals is averaged out over a series of spherical shells centred on the zero frequency. This essentially reduces a 3D signal to a 1D signal representing the power spectra, denoted by  $F_d(f_R)$  for the data reconstruction and by  $F_n(f_R)$  for the noise-only reconstruction (Figure 4.10).

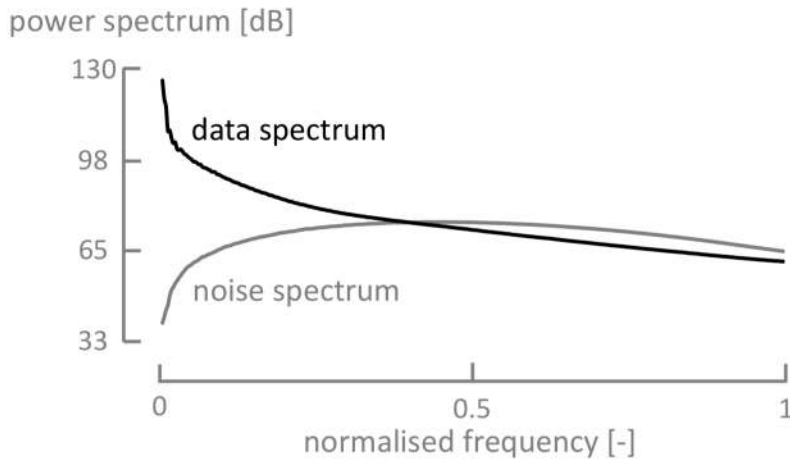
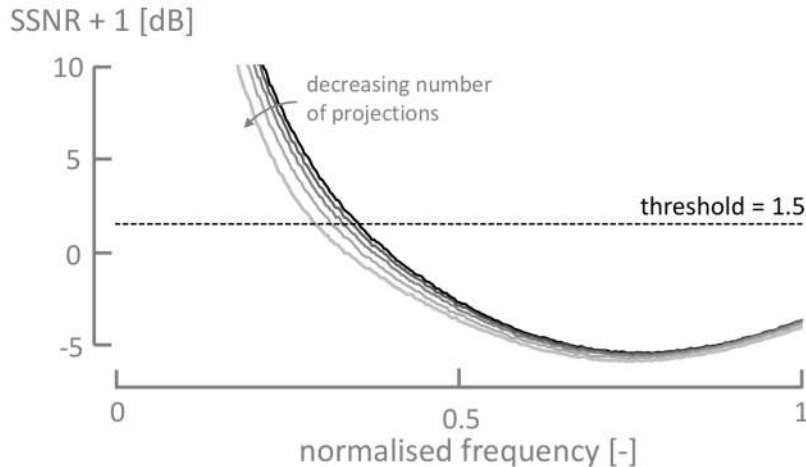


Figure 4.10: Radial power spectra for the noise only and data reconstructions of a mock up data set ( $H = 200\text{mm}$  and  $N_p = 500$ ). The radial frequency associated to the spherical shells in the Fourier domain are normalised w.r.t. the Nyquist frequency, i.e.  $f_{max} = 1/(2 p_v)$ . The power spectra are expressed in dB relative to the unit power.

Given the noise and data power spectra, the SSNR can be calculated as follows

$$\text{SSNR}(f_R) = \max \left( \frac{F_d(f_R)}{F_n(f_R)} - 1, 0 \right) \quad (4.16)$$

where  $f_R$  is the frequency radius of the spherical shells. A cut-off can then be set on the resulting SSNR-curve, representing the minimal Signal-to-Noise Ratio ( $\text{SNR}_{\min}$ ) necessary for a frequency component to be distinguishable from its noisy background (Figure 4.11). It should be noted that following this definition of the SSNR, the SNR is implicitly defined as the ratio of the square mean value to the variance of a signal ( $\text{SNR} = \mu^2/\sigma^2$ ).



*Figure 4.11: The Spectral Signal-to-Noise Ratio (SSNR) of a volume reconstructed with a varying number of projections. As the number of projections decreases, going from 500 to 100 in steps of 100, so does the maximal frequency cut off at the threshold. This graph depicts an SSNR offset by one in dB, i.e.  $10^{-10} \log(\text{SSNR} + 1)$ .*

Here, the SNR threshold is defined by

$$2 \log(1 + \text{SNR}_{\min}) = 0.5$$

assuring that the average information content of a voxel in Fourier space is at least  $1/2$  bit [29, 30]. The frequency at which the SSNR-curve reaches the cut-off  $\text{SNR}_{\min}$  can be interpreted as the maximal frequency ( $f_{\max}$ ) which is adequately represented by the reconstructed volume, and hence its inverse ( $f_{\max}^{-1}$ ) serves as a resolution measure indicating the minimal feature sizes visible on the reconstruction. Figure 4.11 illustrates how  $f_{\max}$  shifts downward with subsequent degradation of the apparent resolution when a lower number projections is taken up in the reconstruction process.

A drawback to the SSNR method is obviously the fact that the noise-only projections have to be estimated through a noise model. As seen on Figure 4.10, this might lead to a slight overestimation of the noise component. These anomalies are caught by the SSNR definition by throwing out the negative values in the high frequency range, where the noise component is expected to take over. The proper interpretation of this effect is to consider these high frequencies as being

pure noise, or at least to be indistinguishable from it, in the light of the noise model introduced throughout this section.

### Fourier Shell Correlation (FSC)

As an alternative to the SSNR, a correlation can be drawn between the reconstruction of the data and a reference volume in the Fourier domain. Whereas the SSNR requires a noise model to generate the noise-only reconstructions, the problem in FSC is shifted towards finding an appropriate reference volume. A popular choice is to split the projections from a data set into two non-overlapping sets, indexed  $d1$  and  $d2$ , containing an equal amount of projections, i.e. the so-called ‘*half-data split*’. A shell correlation for the Fourier transforms of the resulting reconstructions, denoted by  $F_{d1}(\vec{\xi})$  and  $F_{d2}(\vec{\xi})$ , is then calculated as follows [29]

$$FSC(f_R) = \frac{\sum_{\vec{\xi}_i \in f_R} F_{d1}(\vec{\xi}_i) \cdot F_{d2}^*(\vec{\xi}_i)}{\sqrt{\sum_{\vec{\xi}_i \in f_R} F_{d1}^2(\vec{\xi}_i) \cdot \sum_{\vec{\xi}_i \in f_R} F_{d2}^2(\vec{\xi}_i)}}, \quad (4.17)$$

where the sums accumulate all of the values at discrete frequency positions  $\vec{\xi}_i$  within a spherical shell of diameter  $f_R$  and a predetermined thickness  $\Delta f$ , and  $*$  implies complex conjugation. Again, the underlying idea is that the correlation quantified by the FSC will drop below a certain threshold at the maximal frequency  $f_{max}$  which reflects the effective resolution of the reconstructed volume. The threshold curve in Figure 4.12 is linked to the SNR, following van Heel *et al.* [29],

$$FSC_t(f_R) = \frac{2\sqrt{\text{SNR}_{min}} + \text{SNR}_{min}\sqrt{n(f_R)} + 1}{2\sqrt{\text{SNR}_{min}} + (\text{SNR}_{min} + 1)\sqrt{n(f_R)}} \quad (4.18)$$

This threshold is a function of  $f_R$  through the number of frequency voxels  $n(f_R)$  contained within the shell at this diameter, and is determined by the minimally required  $\text{SNR}_{min}$ . Which threshold to use on these FSC curves is however still a matter of debate [29], contrary to the SSNR where the threshold is just  $\text{SNR}_{min}$  itself. This clear cut interpretation makes the SSNR the preferred measure for quantifying the image quality throughout section 4.4.2, despite its noise estimation step. The SSNR is also a slightly more conservative measure when comparing the Figures 4.11 and 4.12. It can also be shown that the expectation values for the SSNR and FSC are linked to each other by [27, 31]

$$\text{SSNR} = 2 \frac{\text{FSC}}{1 - \text{FSC}},$$

which stipulates their equivalence. The main reason, however, to set aside the FSC in favour of the SSNR, is that the FSC is a somewhat more computa-

ally demanding task, requiring the GPU memory to hold up to eight arrays of the reconstruction volume's size.

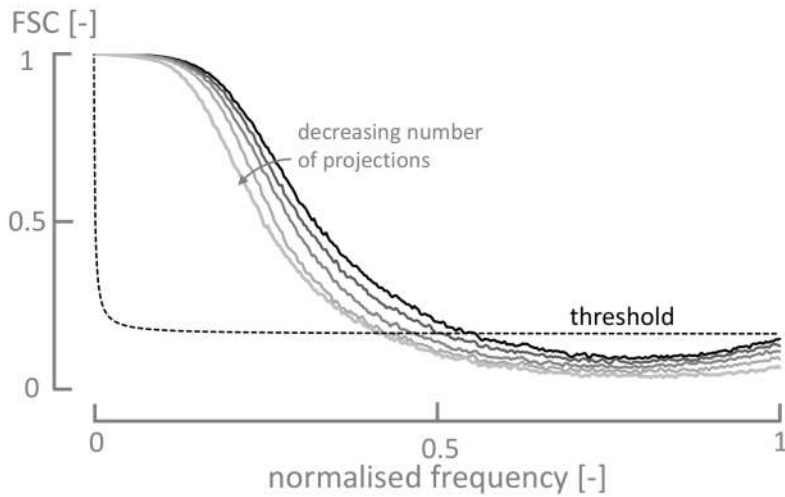


*Figure 4.12: Fourier shell correlation curves (FSC) of a volume reconstructed with a varying number of projections. The dashed curve represents the threshold according to (4.18). Again the cut-off frequency decreases as the number of projections decreases from 500 to 100 in steps of 100.*

#### 4.4.2 Image quality as a function of throughput

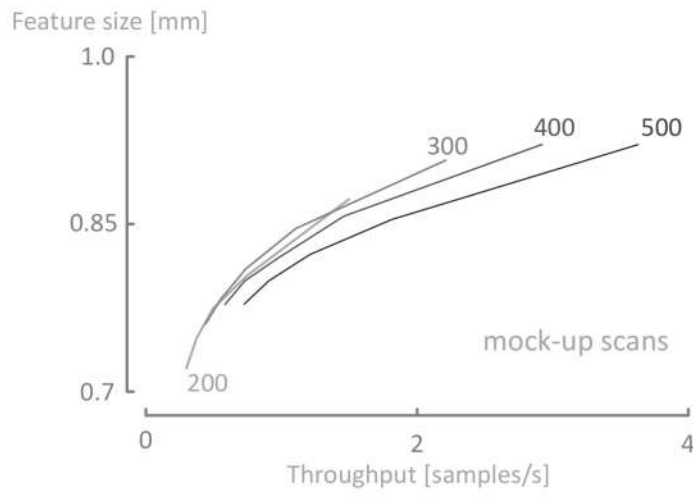
In the previous section, the SSNR was introduced as a means to quantify the smallest detectable features in the reconstruction of a conveyor belt acquisition. It is particularly interesting to look at this minimal feature size in terms of the throughput realised by the conveyor belt system, calculated according to equation 4.11 for a given exposure time of 20 ms per projection<sup>1</sup>. Looking at figure 4.13, it is clear that the image quality produced by the mock up is not as good as for the simulated scans, in the sense that the simulated scans might be overestimating quality. Nevertheless, the general trends as a function of the horizontal travel and the number of projections are reproduced in both the simulated and the mock up case, apart from one anomaly occurring at a horizontal travel of 200 mm in the mock up data. As the number of projections increases the detectable feature size significantly decreases, with the drawback of longer acquisition times and thus a lower throughput. This drop in throughput can be countered by increasing the horizontal travel, causing the curves to slowly shift towards higher throughputs, such that smaller features can only be detected in a fast way by using larger setups.

The minimal feature size calculated through the SSNR is up to seven times larger than the voxel size (here 128  $\mu\text{m}$ ) of the reconstruction grid, which under-

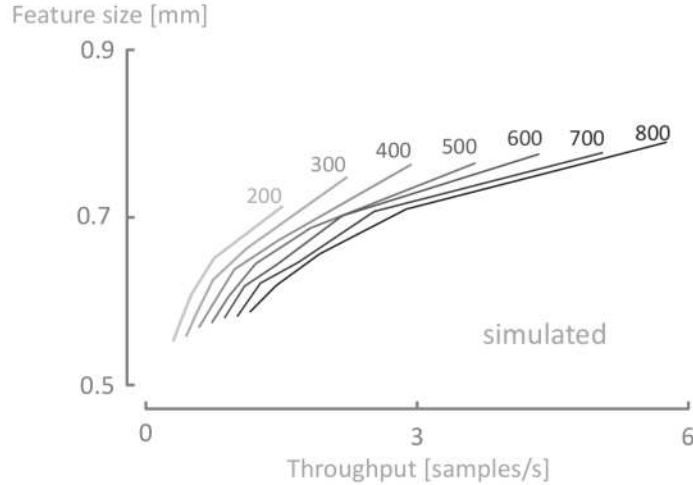
---

<sup>1</sup>Corresponding to the minimal exposure time of the mock up's detector (Varian Medical Systems GmbH, Willich, Germany).

lines the fact that the voxel size is not a fair reflection of the apparent resolution. The double of the voxel size ( $256 \mu\text{m}$ ) does however constitute an absolute minimum to the spatial resolution, theoretically attained for  $N_p \rightarrow \infty$ . It should also be noted that the voxel size of  $128 \mu\text{m}$  is deliberately chosen to be smaller than the detector's pixel pitch  $p_d = 254 \mu\text{m}$ . Through this choice, the lower limit on the resolution estimates calculated according to equation 4.16 is primarily governed by  $N_p$  rather than the voxel size itself. In retrospect, based on the lowest resolution values in figure 4.13(b), setting the reconstruction grid's voxel size ( $p_v$ ) to approximately  $250 \mu\text{m}$  would have been an optimal choice towards minimizing the voxel count and avoiding the voxel pitch's influence on the resolution estimate.



(a)



(b)

*Figure 4.13: The detectable feature sizes as a function of the throughput for the mock up scans (a) and the simulated scans (b). Each curve represents a different travel as indicated next to the curve in ‘mm’. The number of projections increases from 100 to 500 following each curve from right to left, showing a clear trend towards smaller feature sizes for slower scanning regimes.*

## 4.5 Towards a simulation based design

An analysis, such as the one outlined in this work, can be performed purely on a simulation basis, but care needs to be taken in drawing conclusions as the mismatch between the simulations and the mock up case in figure 4.13 points out. Several sources of uncertainties are not accounted for in the simulations, and can to a large part explain the loss in resolution encountered in the real data. In order of importance:

- Sample movement and small calibration errors in the real life sample trajectories can cause excessive blurring in the resulting reconstructions. Hence, when a conveyor belt system is commissioned, a careful mechanical calibration of the sample trajectories and/or an algorithmic strategy to compensate for positioning errors during reconstruction, will be necessary.
- Systematic downward offsets with respect to the tube power setpoint can cause an illumination shortage, and subsequently a lower SNR. Together with the aforementioned point, the author believes this might partly explain the shift of the  $H = 200 \text{ mm}$  curve with respect to the other curves on figure 4.13 in the mock up case.
- Photon scattering caused by the sample itself, which is particularly a problem for small ODDs where the scattering footprint forms a smeared out halo like structure around the projection of the sample (cfr. section 2.3.3).
- Cross talk between the detector pixels caused by an oblique entrance of X-rays might impose a practical limit upon the cone angle and the detector length, next to a degradation of resolution.
- Finally, the detector's point spread function might also cause the resolution to degrade.

As mentioned before, a slight improvement in image quality can be achieved while maintaining a similar throughput by increasing the horizontal travel, or vice versa a higher throughput can be achieved for the same image quality. There are however other ways, next to larger travels, to increase throughput, e.g. by introducing multiple inspection stations in parallel, or even better, by considering the fact that several samples might simultaneously fit into the reconstruction region depicted on figure 4.5(a). As such, the shape of this reconstruction region and the way it is filled up by the sample is equally important in the design phase. For instance, the ROI diameter might deliberately be chosen larger than the sample such that the reconstruction region can indeed contain several samples at once. The shape of the reconstruction region can also be tailored by introducing a whole series of alternative conveyor belt like trajectories through a generalisation of the mapping between the rotational and the translational movement.

## 4.6 Conclusion

In this chapter it was shown that under certain mathematical constraints the combination of a translational and rotational sample movement can produce a series of radiographs from which a theoretically exact CT reconstruction can be obtained,

leaving small cone beam artefacts for off-centre slices aside. Within the boundaries of these mathematical constraints a methodology to evaluate the design of a conveyor belt system was developed, which may serve as a tool to tailor and optimise the design of the system toward a specific type of sample, i.e. other than the Elstar apple and its phantom presented in section 2.5. As an end result to the design exercise, plots can be generated, which visualise the trade-off between a quality measure, here the minimal feature sizes that need to be detected, and how fast they have to be imaged. The throughput of a conveyor system which is a function of the size of the system and the duration of an acquisition, expressed in terms of the horizontal travel and the number of projections, can thus be optimised with respect to this quality measure.

Regarding Figure 4.13, generated here for the Elstar apple sample in both a simulated and mock up environment, it can be concluded that the throughput for this particular case tends to a realistic, practically usable range of up to 5 samples per second. In general, also valid for other types of samples, the analysis performed here indicates that larger setups can achieve a higher throughput at the same level of image quality. Furthermore, other ways to improve throughput remain to be investigated in future work, primarily the tailoring of the reconstruction region's shape by looking at alternative conveyor belt like sample trajectories. In conclusion, the concept of a conveyor belt acquisition geometry is shown to be a viable solution to in-line non-destructive testing with 3D X-ray CT in a continuous high throughput environment.

## References

- [1] T De Schryver, J Dhaene, M Dierick, M N Boone, E Janssens, J Sijbers, M van Dael, P Verboven, B Nicolai, and L Van Hoorebeke. *In-line NDT with X-ray CT combining sample rotation and translation.* NDT & E International, 84:89–98, 2016.
- [2] R P Haff and N Toyofuku. *X-ray detection of defects and contaminants in the food industry.* Sensing and Instrumentation for Food Quality and Safety, 2(4):262–273, jun 2008.
- [3] R Hanke, T Fuchs, and N Uhlmann. *X-ray based methods for non-destructive testing and material characterization.* Nuclear Instruments and Methods in Physics Research Section A: Accelerators, Spectrometers, Detectors and Associated Equipment, 591(1):14–18, jun 2008.
- [4] N Kotwaliwale, K Singh, A Kalne, S N Jha, N Seth, and A Kar. *X-ray imaging methods for internal quality evaluation of agricultural produce.* Journal of food science and technology, 51(1):1–15, jan 2014.
- [5] Y Zou, D Du, B Chang, L Ji, and J Pan. *Automatic weld defect detection method based on Kalman filtering for real-time radiographic inspection of spiral pipe.* NDT & E International, 72:1–9, jun 2015.
- [6] J Xu, T Liu, and X M Yin. *Automatic X-ray crack inspection for aircraft wing fastener holes.* 2nd International Symposium on NDT in Aerospace, pages 1–8, 2010.
- [7] E Herremans, A Melado-Herreros, T Defraeye, B Verlinden, M Hertog, P Verboven, J Val, M E Fernández-Valle, E Bongaers, P Estrade, M Wevers, P Barreiro, and B M Nicolaï. *Comparison of X-ray CT and MRI of watercore disorder of different apple cultivars.* Postharvest Biology and Technology, 87:42–50, jan 2014.
- [8] M S Kim, Y R Chen, B K Cho, K Chao, C C Yang, A M Lefcourt, and D Chan. *Hyperspectral reflectance and fluorescence line-scan imaging for online defect and fecal contamination inspection of apples.* Sensing and Instrumentation for Food Quality and Safety, 1:151–159, 2007.
- [9] N Kondo. *Robotization in fruit grading system.* Sensing and Instrumentation for Food Quality and Safety, 3(1):81–87, 2009.
- [10] L De Chiffre, S Carmignato, J-P Kruth, R Schmitt, and A Weckenmann. *Industrial applications of computed tomography.* CIRP Annals - Manufacturing Technology, 63(2):655–677, 2014.

- [11] Zeiss. *Inline process control with industrial computed tomography.* <https://www.zeiss.com/metrology/products/systems/process-control-and-inspection/volumax.html>.
- [12] O Brunke, F Hansen, I Stuke, and F Butz. *A new Concept for High-Speed atline and inlineCT for up to 100% Mass Production Process Control.* Proceedings 18th World Conference on Non-Destructive Testing, pages 16–20, 2012.
- [13] Micro Vista. *Inline CT: 100 % examination of components in line with series production.* <http://www.microvista.de/en/inline-ct/>.
- [14] W M a Thompson, W R B a Lionheart, E J b Morton, M b Cunningham, and R D b Luggar. *High speed imaging of dynamic processes with a switched source x-ray CT system.* Measurement Science and Technology, 26(5):1–11, 2015.
- [15] J M Warnett, V Titarenko, E Kiraci, A Attridge, W R B Lionheart, P J Withers, and M A Williams. *Towards in-process x-ray CT for dimensional metrology.* Measurement Science and Technology, 27(3):035401, 2015.
- [16] Rapiscan Systems. *The next generation technology for hold baggage screening.* [http://www.rapiscansystems.com/en/products/hbs/rapiscan\\_rtt](http://www.rapiscansystems.com/en/products/hbs/rapiscan_rtt).
- [17] D Matenine, Y Goussard, and P Després. *GPU-accelerated regularized iterative reconstruction for few-view cone beam CT.* Medical physics, 42(4):1505–17, apr 2015.
- [18] E Y Sidky, C M Kao, and X Pan. *Accurate image reconstruction from few-views and limited-angle data in divergent-beam CT.* Journal of X-ray Science and Technology, 14(2):119–139, 2006.
- [19] L Flores, V Vidal, and G Verdú. *Iterative Reconstruction from Few-view Projections.* Procedia Computer Science, 51:703–712, 2015.
- [20] B D Smith. *Image reconstruction from cone-beam projections: necessary and sufficient conditions and reconstruction methods.* IEEE transactions on medical imaging, 4(1):14–25, jan 1985.
- [21] J Dhaene, E Pauwels, T De Schryver, A De Muynck, Manuel Dierick, and L Van Hoorebeke. *A realistic projection simulator for laboratory based X-ray micro-CT.* Nuclear Instruments and Methods in Physics Research Section B: Beam Interactions with Materials and Atoms, 342:170–178, jan 2015.

- [22] D A Chesler, S J Riederer, and N J Pelc. *Noise due to photon counting statistics in computed X-ray tomography*. Journal of computer assisted tomography, 1(1):64–74, 1977.
- [23] L a Feldkamp, L C Davis, and J W Kress. *Practical cone-beam algorithm*. Journal of the Optical Society of America A, 1(6):612, 1984.
- [24] A Katsevich. *Improved exact FBP algorithm for spiral CT*. Adv. Appl. Math, pages 32–681, 2004.
- [25] A H Andersen and A C Kak. *Simultaneous Algebraic Reconstruction Technique (SART): A Superior Implementation of the Art Algorithm*. Ultrasonic Imaging, 6(1):81–94, jan 1984.
- [26] A Klöckner, N Pinto, Y Lee, B Catanzaro, P Ivanov, and A Fasih. *PyCUDA and PyOpenCL: A scripting-based approach to GPU run-time code generation*. Parallel Computing, 38(3):157–174, mar 2012.
- [27] P A Penczek. *Three-dimensional spectral signal-to-noise ratio for a class of reconstruction algorithms*. Journal of Structural Biology, 138(1-2):34–46, apr 2002.
- [28] M Unser, C O S Sorzano, P Thévenaz, S Jonić, C El-Bez, S De Carlo, J F Conway, and B L Trus. *Spectral signal-to-noise ratio and resolution assessment of 3D reconstructions*. Journal of structural biology, 149(3):243–55, mar 2005.
- [29] M van Heel and M Schatz. *Fourier shell correlation threshold criteria*. Journal of structural biology, 151(3):250–62, sep 2005.
- [30] C E Shannon. *A mathematical theory of communication*. ACM SIGMOBILE Mobile Computing and Communications Review, 5(1):3, jan 2001.
- [31] H Y Liao and J Frank. *Definition and estimation of resolution in single-particle reconstructions*. Structure, 18(7):768–775, jul 2010.



# 5

## Imaging dynamic processes with CT

High-resolution X-ray Computed Tomography or micro-CT ( $\mu$ CT) has matured to the point where it is now possible to image dynamic processes within micro-structures in 3D with a sufficient temporal resolution to follow the micro-structural changes caused by these processes through time, i.e. in 4D. Especially synchrotron experiments, armed with the luxury of a high X-ray flux, have pushed the boundaries of the temporal resolution up to the 1 kHz range, at spatial resolutions down to 3  $\mu$ m [1]. An exhaustive survey on the achievements in literature, regarding temporal and spatial resolutions, can be found in [2, 3], from which it should be noted that high temporal and spatial resolution CT imaging is becoming tractable at lab-based CT facilities as well [4, 5]. The obvious advantage of lab-based set-ups is their compactness, and the ability to rotate the X-ray source and detector instead of the sample, as in the gantry based EMCT scanner described by section 2.2.2, which allows the sample to be attached to peripheral measuring or in-situ conditioning equipment. On the other hand, the X-ray fluxes produced by micro-focused lab sources are much lower than those available at synchrotron and medical sources. The available flux is an important quantity, as it puts up an inherent, physical lower bound on the process time constants that can be resolved with a 4D-CT acquisition. Indeed, in the extreme cases of very fast 4D scanning, at low detector exposure times and number of projections, the acquired photon statistics might be insufficient to extract a usable CT signal form the shot noise background, while scanning at a slower rate to gather more photon statistics, can cause excessive temporal blurring, due to the sample's time evolving attenuation distribution. If this is the case, this simply means that, given its available flux, the imaging

device or protocol is incapable of resolving the time constants of the underlying process, with an acceptable amount of noise or temporal blurring. But, even if the X-ray CT device is perfectly capable of producing a relatively noise free acquisition at the desired temporal resolution, a slower scanning protocol might be desirable to suppress the massive amount of data produced during a 4D acquisition. In other words, tolerating a small amount of temporal blurring is not just compelling through physical limitations, i.e. shot noise, but also through other limitations, particularly the data rates.

This chapter addresses the scenarios, where at first glance a certain degree of temporal blurring seems to be inevitable. In general, temporal blurring can be caused by any change in the attenuation distribution following a dynamic process within the sample, e.g. stress induced internal deformations, temperature related phase changes, fluid transport in rock's micro-pores etc. To effectively reduce or eliminate the temporal blurring effects, and indirectly boost the temporal frequencies of CT imaging, *à priori* information on the underlying dynamic processes can be incorporated in the CT reconstruction algorithm. In this chapter, a dynamic non-rigid deformation of a sample's micro-structure is considered, for which temporal blurring is henceforth referred to as '*motion blurring*'. In section 5.2, some algorithms are discussed to estimate this deformation under the form of a dense displacement field, which can be incorporated in the projection and back projections steps of an iterative reconstruction algorithm, as described in section 5.3. How this eliminates the motion blurring effects, is illustrated through a series of applications in section 5.4, primarily based on deformation processed that can, to certain extent, be controlled with the in-situ devices, discussed in section 5.1.

## 5.1 In-situ process control

There is an ongoing effort at the UGCT to develop, acquire and implement add-on modules to accurately control the conditions a sample is scanned in, i.e. temperature, pressure, humidity, flow, compression, etc.. First of all, these modules can provide a stabilised environment by minimizing the micro-structural changes that could be caused by an improper conditioning of the sample. But more importantly, the ability to accurately control the dynamics related to a changing environment opens a broad range of applications in dynamic or 4D  $\mu$ CT. Various add-on modules are available at the UGCT of which two in particular are relevant to the applications discussed in the section 5.4 of this chapter, i.e. for (1) setting a sample's temperature, and (2) applying a unilateral extension or compression to a sample, during a CT scan.

### 5.1.1 Temperature control

#### Design constraints

As outlined in [6], a compact heating/cooling stage was developed, with the goal of studying temperature related micro-structural changes in a sample, in both a static and dynamic regime, within the  $-20^{\circ}C$  to  $50^{\circ}C$  temperature range. This compact, low cost in-situ module was made to fit samples of approximately 1 cm in diameter, with a density ranging from  $0.5 \text{ g/cm}^3$  or lower for soft organic samples, such as food and wood, up to  $2.5 \text{ g/cm}^3$  for dense structures, e.g. rock samples. With these constraints on the sample size and density, the material choices and geometry are tailored towards high voltages of at least 60 to 100 kV, resulting in a polychromatic X-ray beam spectrum with an average energy of approximately 30 keV.

#### Materials & Geometry

To realise a compact design, and reach the low temperature of  $-20^{\circ}C$ , a ‘*thermo-electric Peltier element*’ (TEC) was chosen to actively cool the sample. An added advantage of TECs is that by varying their supply voltage, different degrees of cooling or heating can be obtained, by including them into a feedback loop with a temperature sensor. The feedback loop and its accompanying electronics are described in detail later in the next section.

Using thermal grease one end of a highly conductive aluminum extension rod, with a thermal conductivity of  $237 \text{ W/(m} \cdot \text{K)}$  [7], is attached to the TEC’s cold surface, with the goal of elevating the actively cooled sample volume to within the X-ray setup’s field of view. This essentially transfers the TEC’s cold surface temperature to the other end of the aluminum rod, which is topped off with a highly conductive, hollow cap that homogenises the temperature distribution over the actively cooled volume (Figure 5.1(a)). In particular, the temperature gradient between the top and the bottom of the actively cooled volume should be as small as possible, leading to a specific choice for the material and the wall thickness of the conductive cap, which is governed by a trade-off between the need for a high thermal conductivity and low X-ray attenuation properties. To investigate these trade-offs, the temperature distributions in the cooling stage were simulated using QuickField (Svendborg, Denmark), resulting contour plots similar to the one in Figure 5.1(a). Two cap materials, with complementary properties on thermal conductivity and X-ray attenuation (see table 5.1), were investigated. The cap material can then be chosen depending on the application it is used for, because essentially it serves as an X-ray beam hardening filter. While dense and highly attenuating samples can be imaged in the cooling stage using the aluminum cap, light and translucent samples can be imaged with the graphite cap, keeping in mind that

cooling performance will be less in the latter case. To further optimise the heat transfer from the actively cooled volume on the tip of the rod to the TEC surface, the rod needs to be insulated. Contrary to the rod's material, the thermal conductivity of the insulating material needs to be as low as possible, hence a polyurethane foam ( $W/(m \cdot K)$ ) is used.

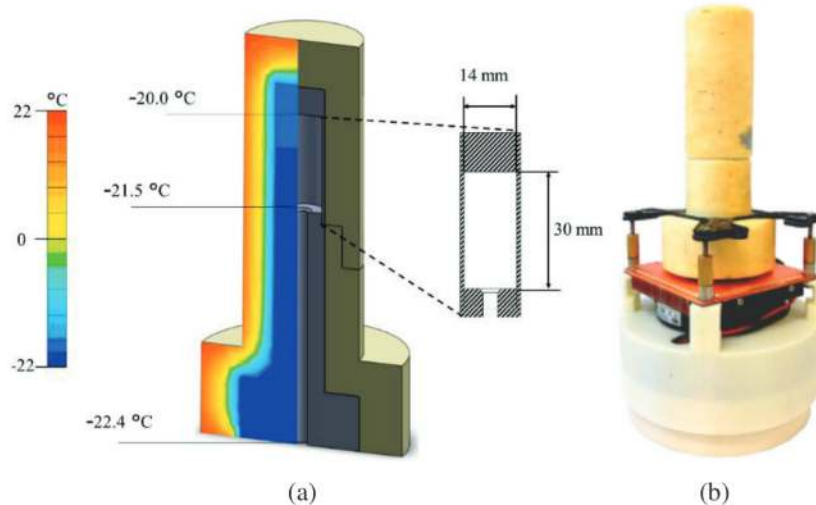


*Figure 5.1: UGCT's home made cooling stage. (a) A longitudinal cross-section through the aluminum extension rod, its polyurethane insulation and the graphite cap containing the sample volume, with a simulated temperature contour overlay. Based on the simulation the temperature difference between the top and the bottom of the actively cooled sample volume is approximately 1.5°C. In this simulation the TEC was modelled as a surface with its temperature fixed at -22.4°C. (b) The cooling stage in its assembled state, measuring approximately 24 cm from top to bottom and 13 cm in diameter.*

*Table 5.1: Thermal conductivity and X-ray mass attenuation properties of aluminum (Al) and graphite (C). The attenuation, being energy dependent, is listed at 30keV [8, 9]. Both materials are complementary in their use as a cap material.*

	Thermal Conductivity [ $W/(m \cdot K)$ ]	X-ray Mass Attenuation at 30keV [ $cm^2/g$ ]
Aluminum	237	1.13
Graphite	96	0.26

The simulation using a graphite cap (Figure 5.1(a)) indicates that the desired temperature of  $-20^\circ C$  at the top of the cooled region is already attained, when the cold side of the TEC reaches approximately  $-22.4^\circ C$ . Moreover, there is only a small temperature difference of approximately  $1.5K$  between the top and the bottom of the cap. Reaching the a temperature of  $-22.4^\circ C$  is not a problem for a TEC

if the heat dissipated at its hot side is adequately drained off to the surroundings. This can be done with standard CPU coolers, which are rated by their thermal resistance between their hot side and the surroundings. The one used in this cooling stage has a minimum thermal resistance of  $0.24 \text{ K/W}$ , depending on the fan's rotary speed, which proved to be sufficient to reach the minimum temperature of  $-20^\circ\text{C}$ . A drawback in using these CPU coolers is the fact that their fans can induce vibrations, which are unwanted in a  $\mu\text{CT}$  imaging setup. This practically limits the image resolution, that can be obtained with the add-on module, to twice the principal vibration amplitude. This amplitude has not been thoroughly investigated, but is expected to be well below  $9 \mu\text{m}$  since no degradation of the quality of scans at this resolution has been observed after switching on the fan. In its completely assembled state the cooling stage measures approximately 24 cm from top to bottom and 13 cm in diameter (see Figure 5.1(b)). The bottom part was 3D printed, serving as a mount for the CPU cooler, and holding the stage controller electronics.

## Electronics

The temperature in the sample volume is controlled by a custom-made carrier board (see Figure 5.2), which can measure up to four different temperature signals through TTF-103 thermistors. These temperature signals are interpreted by a PID controller embedded on an Arduino<sup>TM</sup> Nano micro-controller [10]. Based on the temperature measurement, the PID regulates an H-bridge module, which sets the voltage for the TEC. The H-bridge can also invert the polarization of the TEC supply voltage, so that the sample volume can be heated as well. This maximum heating temperature is determined by the thermistor's series resistor, which sets the clipping value for the Arduino's ADC. So, while higher temperatures can be reached, their measurements will be clipped, unless a larger series resistor for the TTF-103 is chosen. This can however drastically deteriorate the measuring accuracies for the lower temperature range. With a  $10 \text{ k}\Omega$  series resistor, the 1 kbit ADC can measure temperatures up to  $50^\circ\text{C}$ , and an accuracy of  $0.22 \text{ K/ADU}$  at  $-20^\circ\text{C}$ .

The stage electronics transmit the temperature measurements wirelessly (through RF) to a USB module, which can be attached to a PC. A user can then read out the current temperature, and set the desired temperature and PID parameters through a custom LabVIEW interface. Furthermore, the LabVIEW interface seamlessly integrates into UGCT's scanner control software [11], making it possible to completely automate the combined cooling and  $\mu\text{CT}$  experiment. An advantage of the wireless communication is that the power supply cable is the only wire externally connected to the stage. A battery could be used, but most batteries do not last an entire experiment, considering that the current drawn by the TEC can go up 6 A.

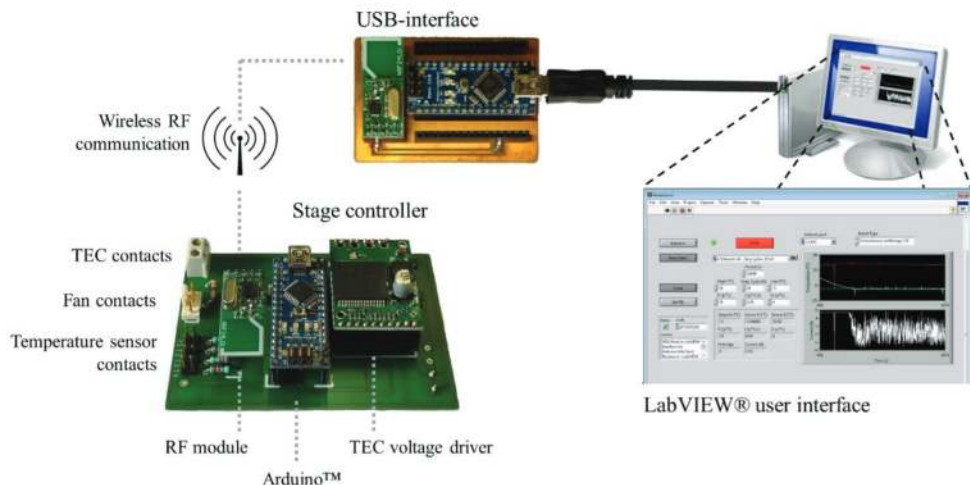


*Figure 5.2: Cooling stage electronics and control interface. The stage controller, encased in the 3D printed CPU cooler mount (Figure 5.1(b)), communicates wirelessly with its USB counterpart, which is attached to a PC. Users can measure and set the cooling stage temperature through a LabVIEW based interface.*

For the moment, any commodity AC to DC adaptor, which can deliver up to 6A at 15V, can be used with the cooling stage.

### Application range

The cooling stage has been used to facilitate several applications, categorised by a rising degree in dynamism, going from sample immobilization, over time-lapse evolution studies to fully dynamically evolving, temperature dependent processes.

In Figure 5.3(a), a sagittal slice through a CT reconstruction of puff paste frozen to  $-20^{\circ}\text{C}$  is shown. Yeasted, laminated dough products progressively start leavening when they are left at room temperature, consequently changing their internal structure and making it difficult to image their interior with a long, high quality and motion artefact free  $\mu\text{CT}$  acquisition. Freezing the puff paste during the scan solves this problem. When on the other hand yeasted doughs are heated to their preferred leavening temperature, the process is accelerated and becomes an ideal case study to test out new developments in 4D-CT research (see section 5.4.4).

Of special interest are the applications where the freezing process alters the micro-structural properties of a sample. Figure 5.3(b) shows a sagittal slice through a frozen (also  $-20^{\circ}\text{C}$ ) ice cream mock up mixture. By adding a contrast agent, the ice crystals are clearly delineated, making it possible to investigate their formation as a function of mixture composition, and the number of freeze-thaw cycles the mixture is exposed to [12]. Freeze-thaw cycling also has a marked effect on crack

initiation and propagation in rocks, where the crystallization-induced stress fractures the material, forming new pathways for water to penetrate deeper into the rock's pore space [13].

In a final application, the dynamics of a crystallization process were captured by using the cooling stage in UGCT's Environmental CT-scanner (EMCT) (2.2.2). Figure 5.3(c) shows one time-frame out of a 4D rendering, capturing the crystallization process of a highly concentrated sodium sulfate ( $\text{Na}_2\text{SO}_4$ ) solution cooling down from  $10^\circ\text{C}$  to  $-5^\circ\text{C}$  [14].

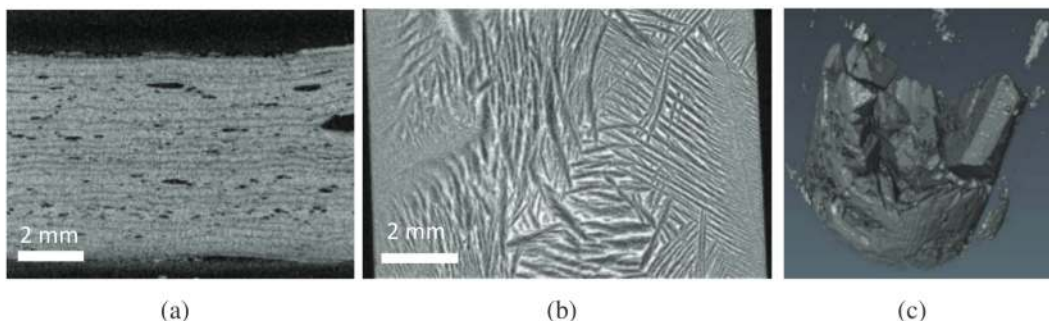


*Figure 5.3: Examples of some applications with the cooling stage. (a) Sagittal slice through a frozen ( $-20^\circ\text{C}$ ) puff paste sample with a clear visualization of its layered structure. (b) Ice crystal formation in an ice cream mock up mixture containing a contrast agent at  $-20^\circ\text{C}$  (sagittal slice). (c) A snapshot from a 4D rendering of the  $\text{Na}_2\text{SO}_4$  crystallization process in a cylindrical capillary of 9 mm in diameter, cooling from  $10^\circ\text{C}$  to  $-5^\circ\text{C}$ .*

### 5.1.2 Tensile & compression stage

A second add-on module, central to this work, is the CT5000-TEC stage (*Deben UK Ltd.*, Suffolk), which can unilaterally apply loads of up to 5 kN in both a tensile and compressive direction (Figure 5.4). The CT5000 stage, acquired by the '*Pore-scale Processes in Geomaterials Research group (PProGRess)*', was specifically customised by Deben to fit the UGCT scanners. With it, as a first key application, the PProGRess team is able to perform Unconfined Compressive Strength (UCS) tests on geomaterials, and is able to simultaneously visualise the internal structural disintegration of the loaded geomaterials in 3D, through in-situ  $\mu\text{CT}$  imaging.

The CT5000's claws can also be heated or cooled within a range of  $-20^\circ\text{C}$  up to  $160^\circ\text{C}$ , again through the use of TEC elements, although in a less uniform way. An object can thus be compressed or extended up to 10 mm or up to the maximal load

of the installed load cell (500N, 1 kN, 2 kN or 5 kN)<sup>1</sup>, which ever of these limits is reached first, while at the same being subjected to a form of temperature control. In a typical compression or extension experiment, a prescribed load or displacement is set, which is then attained by moving the bottom yaw or compression plate in the vertical direction at a fixed speed (0.1, 0.2, 0.5, 0.7 or 1 mm/min), while the top yaw remains stationary. In other words, an object can undergo a controlled in-situ deformation, which is additionally characterised by an accurate load-displacement curve acquired through the Deben Microtest software. An example of such a curve, setting out the load applied during the compression of an aluminum foam cube ( $1.5^3 \text{ cm}^3$ ), is depicted Figure 5.4(b) (see also section 5.4.3).

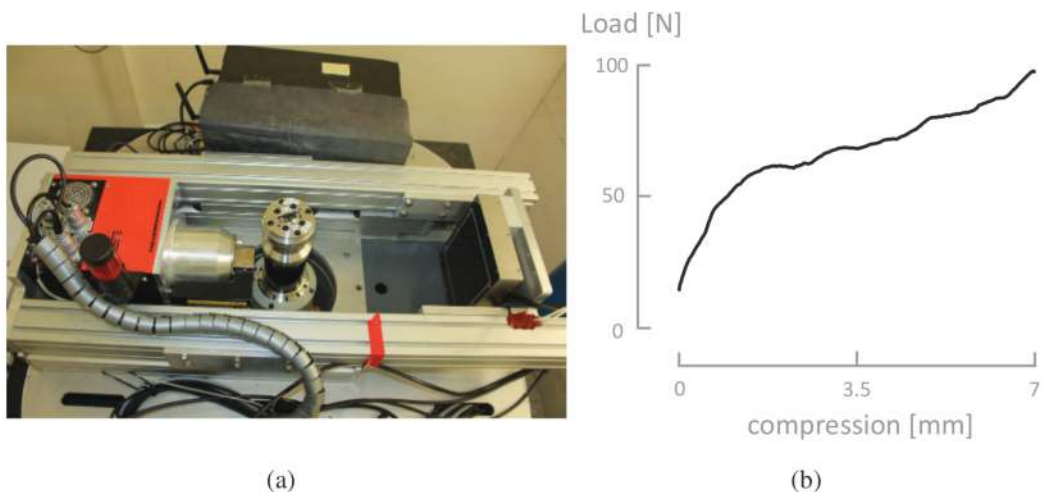


Figure 5.4: (a) The Deben CT5000-TEC stage installed on the EMCT. With this combination long running dynamic compression or extension experiments can be conducted, since the stage's wiring can not be caught up in any rotational movement. (b) Example of a load-displacement curve for the compression of an aluminum foam cube ( $1.5^3 \text{ cm}^3$ ; Picture of CT5000 courtesy of Jeroen Van Stappen).

## 5.2 Tracking 3D deformation with CT

### 5.2.1 Registration of 3D images

#### Free form deformation (FFD)

Before introducing the concept of registration, it is important to note that the final goal here is to determine how objects, and in particular their internal structures, move or more generally deform through space. From a mathematical perspective, a 3D deformation can be described by a mapping

<sup>1</sup>When small loads are expected, a lower capacity cell with a higher accuracy can be used.

$$\mathcal{M} : \Omega_f \rightarrow \Omega_m \quad (5.1)$$

which transforms the points  $\vec{x}_f$  of a ‘fixed’ (initial) region in 3D space ( $\Omega_f$ ) to a ‘moving’ (deformed) state  $\Omega_m$ , containing the points  $\vec{x}_m$ , such that

$$\mathcal{M}(\vec{x}_f) = \vec{x}_m = \vec{x}_f + \vec{u}(\vec{x}_f) \quad (5.2)$$

In other words, the deformation is defined by  $\vec{u}(\vec{x}_f)$ , known as a ‘dense displacement field’ or ‘Motion Vector Field’ (MVF), which describes how points move through space (Figure 5.5). In section 2.4, a particular type of deformation was already introduced through the parametrisation of an acquisition geometry, namely ‘affine deformation’, given by

$$\vec{x}_m = \mathbf{A} \cdot \vec{x}_f + \vec{O}_t,$$

which leads to an MVF

$$\vec{u}(\vec{x}_f) = (\mathbf{A} - \mathbf{I}) \cdot \vec{x}_f + \vec{O}_t, \quad (5.3)$$

where  $\mathbf{I}$  represents the identity transform. The affine transform is able to capture rigid deformations, i.e. rotations and translations, as well as non-rigid deformations in the form of scaling and shear. More importantly, (5.3) is a ‘global’ parametrisation of  $\vec{u}(\vec{x}_f)$ , in the sense that changing any of the components in  $\mathbf{A}$  or  $\vec{O}_t$  will affect the MVF over its entire support.

Apart from affine deformations, this chapter will mainly address the more general notion of a ‘Free Form Deformation’ (FFD), which implies a local and non-rigid deformation of an object, and as such requires a ‘local’ parametrisation of  $\vec{u}$ . For example, if  $\vec{u}$  would be set out on a regularly spaced grid of positions  $\vec{x}_m$ , similar to the grid of a 3D reconstruction volume, the most extreme case of FFD defines a different  $\vec{u}(\vec{x}_m)$  in each voxel position. The neighbouring field vectors may even not be correlated. In reality however, deformations will always be correlated locally through a certain extent of space, and with a view to registration it is important to capture this correlation through a minimal amount of parameters. This is why in the context of registration, the brute-force deformation parametrisation, where each voxel position has its own  $\vec{u}$ , is actually referred to as ‘non-parametric’.

## Registration

During the registration of two images, a spatial transformation that optimises the similarity between these images is estimated. This similarity can be defined in

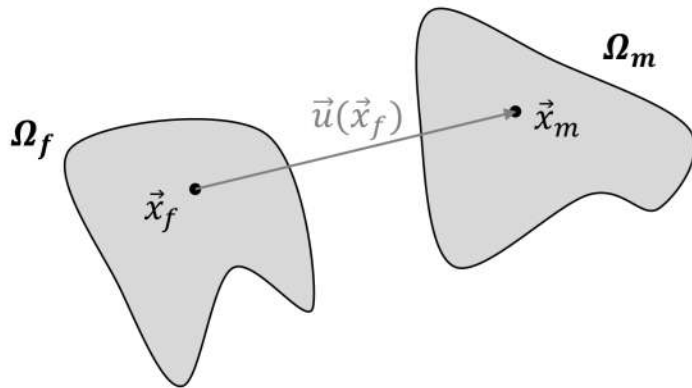


Figure 5.5: General formulation of deformation as a mapping that can be represented by a ‘Motion Vector Field’ (MVF)  $\vec{u}(\vec{x}_f)$ .

several ways, but a plausible though rigorous approach in the context of registering CT attenuation images, is to instate the ‘*constancy of brightness*’

$$\mu(\vec{x}_m, \tau_m) = \mu(\vec{x}_f + \vec{u}(\vec{x}_f, \tau_f), \tau_f). \quad (5.4)$$

In this equation, the images are implicitly linked to distinct instances in time ( $\tau_f$  and  $\tau_m$ ), which underlines the fact that in the following a time evolving deformation field ( $\vec{u}(\vec{x}_f, \tau_f)$ ) is to be inferred from the time evolving attenuation distribution of an object. Although the general problem of registration extends across multiple imaging modalities (CT, MRI, PET, SPET, etc.), equation (5.4) also implies that the registered images originate from one single imaging modality, namely  $\mu$ CT in the case of this work.

The goal is thus to find an MVF that deforms one of the images such that it matches or in the ideal case is equal to the other image. When these images are represented by 3D volumes, image registration is sometimes referred to as ‘*Digital Volume Correlation*’ (DVC), which according to the author is a somewhat confusing terminology, that might imply the image’s similarity is always quantified through a correlation metric. The chosen similarity metric can greatly affect the outcome of any registration method, as one of its key elements.

Following [15], the crucial elements of a registration method are gathered in the flow chart of Figure 5.6. As outlined above, the inputs are two distinct images, referred to as a fixed ( $\mu_f$ ) and a time evolved or moving image ( $\mu_m$ ), where the explicit time stamp notation has been replaced with an appropriate indexation. A first important observation is that most registration methods adopt a ‘*hierarchical strategy*’, which represents the images in multi-resolution pyramids, going from a coarse to a fine scale through dyadic decimation and smoothing. At each level ‘ $k$ ’ of these pyramids,  $\mu_f$  is sampled in a series of points  $\vec{x}_s$ , while  $\mu_m$  is interpolated

in the same points, though in their moved state  $\mathcal{M}(\vec{x}_s; \vec{w}^{(k)})$ , following the mapping  $\mathcal{M}$  defined by the vector of parameters  $\vec{w}^{(k)}$ . The resulting image samples are then combined in a metric ( $\mathcal{C}$ ), which at its optimum<sup>2</sup> yields a new estimate for the parameter vector.

$$\vec{w}^{(k+1)} = \arg \min_{\vec{w}} \mathcal{C} [\mu_f(\vec{x}_s), \mu_m(\mathcal{M}(\vec{x}_s; \vec{w}))]. \quad (5.5)$$

This optimum can be found as a direct solution to (5.5), or as in most cases through an iterative optimisation algorithm. The new parameters are passed on to the next pyramid level as an estimate for the finer scale displacements, which are thus at the mercy of good coarse scale estimates.

Nevertheless, the coarse scale estimates are crucial in tackling the '*aperture problem*', and avoiding '*temporal aliasing*' in the deformation fields [16]. The aperture problem states that through a limited aperture on a moving image only the components of motion perpendicular to the edges, i.e. in the direction of the image gradient, can be accurately inferred. In practice, this means that the aperture and thus the scale on which the displacements are inferred, needs to be large enough such that it contains an adequate amount of texture for robust and correct displacement estimation. Temporal aliasing, on the other hand, occurs when the deformations tend to be larger than the scales on which they are estimated. By eliminating the large scale deformation, through a coarse scale estimation, temporal aliasing can be avoided at the smaller scales.

In summary, the essential components of any registration algorithm are:

1. the metric used to quantify the similarity between the fixed and moving images,
2. the choice on how the MVF is parametrised, and
3. the strategy used to find an optimal set for the deformation parameters.

Hence, in an attempt to classify the different registration methods, the type of the metric can be considered, which can either be based on image intensity, e.g. the mean square difference [17], normalised cross correlation [18] and mutual information [19, 20], or on motion constraints, e.g. optical flow [16] (see sections 5.2.2 and 5.2.3). Moreover, the metric can be evaluated and optimised over the entire image, or over smaller sub-regions across the image, for which the displacements are then estimated individually. This brings about a classification that underlines either a global or local nature of the registration problem [21, 22]. This global or local character is also partly determined by the deformation model, which may capture the deformation across multiple voxels in a smooth and continuous way,

---

<sup>2</sup>Minimum or maximum depending on how the metric is defined

e.g. with b-splines (see section 5.2.4), or may define a motion vector for each voxel individually, leading to the respective parametric and non-parametric classifications. So, in order of importance, a registration method can be:

- quantified through an intensity or constraint based metric,
- evaluated on a global or local (sub-region) scale,
- parametric or non-parametric.

In the following sections 5.2.2 to 5.2.4, a global method with a b-spline parametrisation and two constraint based, local methods, are discussed in more detail. These methods are used to estimate FFDs throughout the applications described in section 5.4.

## 5.2.2 Optical intensity flow

### Optical flow constraint

One the oldest concepts in registration is that of optical flow, which is firmly rooted in the assumption of brightness constancy. The optical flow constraint can be found by expanding the right hand side of (5.4) into a first order Taylor expansion, resulting in

$$0 = \mu(\vec{x} + \vec{u}, \tau + \delta\tau) - \mu(\vec{x}, \tau) \approx \mu_\tau(\vec{x}, \tau) \cdot \delta\tau + \vec{u}(\vec{x}, \tau)^T \cdot \nabla_{\vec{x}}\mu(\vec{x}, \tau) \quad (5.6)$$

with

$$\begin{aligned} \vec{u}(\vec{x}, \tau) &= \left[ \frac{\partial x}{\partial \tau}, \frac{\partial y}{\partial \tau}, \frac{\partial z}{\partial \tau} \right]^T = [u_x, u_y, u_z]^T \\ \nabla_{\vec{x}}\mu(\vec{x}, \tau) &= \left[ \frac{\partial \mu}{\partial x}, \frac{\partial \mu}{\partial y}, \frac{\partial \mu}{\partial z} \right]^T = [\mu_x, \mu_y, \mu_z]^T, \end{aligned}$$

and  $\mu_\tau = \partial\mu/\partial\tau$ . Without any loss in generality,  $\delta\tau$  may be set to one, keeping in mind that

$$\mu_\tau(\vec{x}, \tau) \cdot \delta\tau \approx \mu_f - \mu_m$$

is a measure for the difference between the fixed and moving images. Alternatively, equation (5.6) can also be found in the total derivative along a path of constant brightness,  $\mu(\vec{x}(\tau), \tau) = \text{constant}$ .

The problem with the optical flow constraint is that it provides only one equation to solve for three velocity components. Hence, to recover  $\vec{u}$ , the constraints in

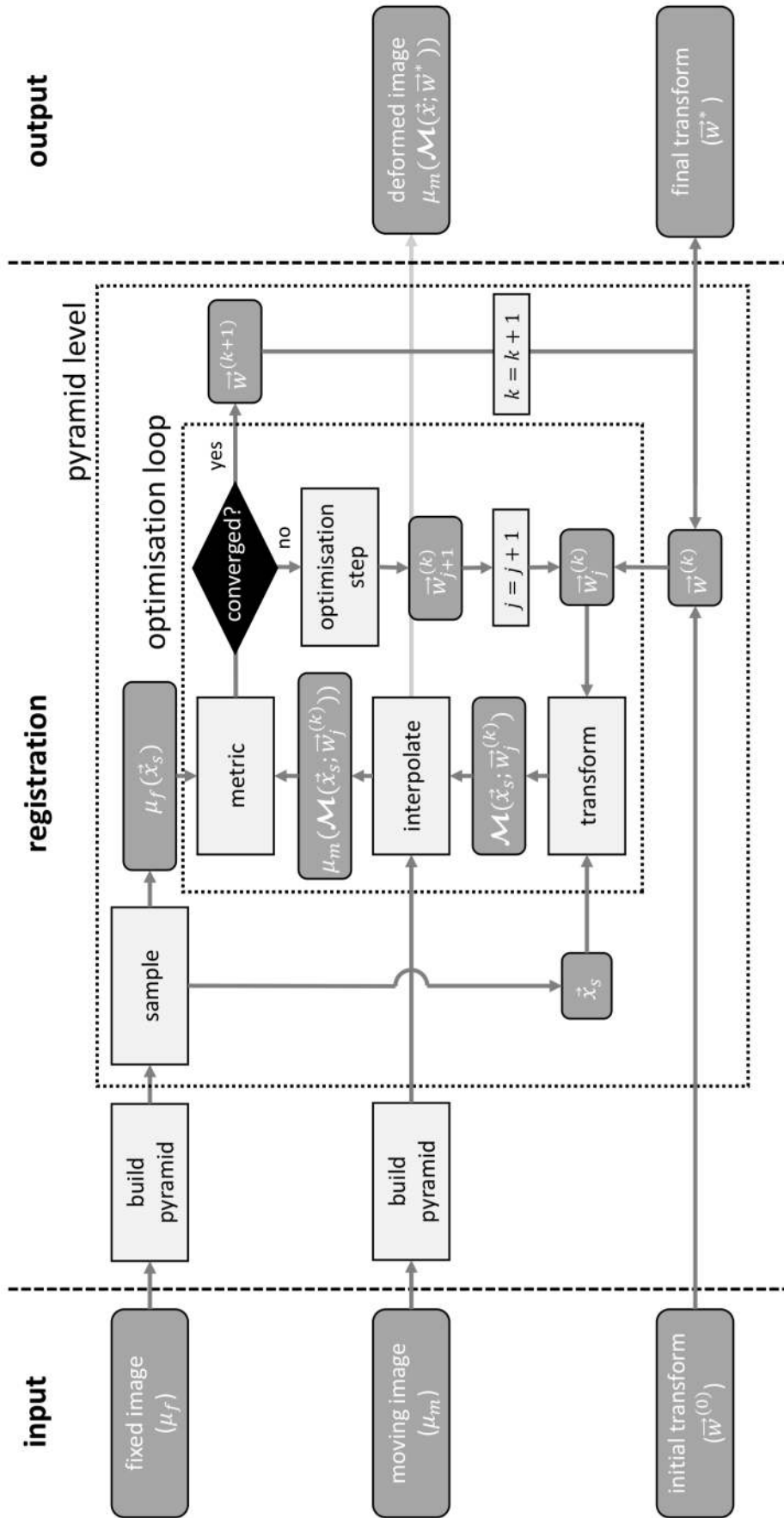


Figure 5.6: Image registration flow chart. A moving image  $\mu_m$  is deformed through a deformation model in such a way that its similarity to the fixed image, as quantified by the predefined metric, is optimal. The deformation model parameters, which optimise this metric, can be found as a direct solution to the extremum problem, or in most cases through an iterative optimisation algorithm. The optimisation process is executed at different scales, adopting a coarse-to-fine strategy in a multi-resolution pyramid (based on [15]).

neighbouring pixels can be combined in a least-squares sense by minimising their weighted sum

$$\mathcal{C}(\vec{u}) = \sum_{\vec{x}} g(\vec{x})^2 [\mu_\tau + \vec{u}^T \cdot \nabla_{\vec{x}} \mu]^2 \quad (5.7)$$

With (5.7) the displacement  $\vec{u}$ , or more generally its parametrisation, is assumed to be constant over the support of  $g(\vec{x})$ , whose local values serve as weights, reflecting how strongly the outcome of  $\vec{u}$ 's underlying motion models is influenced by a local constraint. A more convenient form of (5.7) arises by introducing the constraint vector

$$\vec{c} = g(\vec{x}) \cdot \begin{bmatrix} \nabla_{\vec{x}} \mu(\vec{x}) \\ \mu_\tau(\vec{x}) \end{bmatrix}, \quad (5.8)$$

and by extending the displacement vector to  $\vec{v} = [\vec{u}^T 1]^T$ , such that

$$\mathcal{C}(\vec{v}) = \sum_{\vec{x}} \vec{v}(\vec{x})^T \cdot [\vec{c}(\vec{x}) \ \vec{c}(\vec{x})^T] \cdot \vec{v}(\vec{x}) \quad (5.9)$$

This expression is invariant with respect to any linear parametrisation of  $\vec{v}$ , i.e.

$$\vec{v}(\vec{x}) = \mathbf{K}(\vec{x}) \cdot \vec{w}. \quad (5.10)$$

By plugging this general motion model into (5.9), the optical flow metric becomes

$$\begin{aligned} \mathcal{C}(\vec{w}) &= \vec{w}^T \sum_{\vec{x}} [\mathbf{K}(\vec{x})^T \ \vec{c}(\vec{x}) \ \vec{c}(\vec{x})^T \ \mathbf{K}(\vec{x})] \ \vec{w} \\ &= \vec{w}^T \tilde{\mathbf{Q}} \vec{w} \end{aligned} \quad (5.11)$$

for which a minimum can be found at

$$\vec{w} = \mathbf{Q}^{-1} \vec{q} \quad (5.12)$$

by setting  $\nabla_{\vec{w}} \mathcal{C} = 0$ , under the condition that  $\mathbf{Q}$  is full-rank. It can be shown that (see also [23])

$$\begin{aligned} \mathbf{Q} &= \sum_{\vec{x}} g \mathbf{K}^T \cdot \nabla_{\vec{x}} \mu^T \nabla_{\vec{x}} \mu \cdot \mathbf{K} \\ \vec{q} &= \sum_{\vec{x}} g \mathbf{K}^T \nabla_{\vec{x}} \mu^T \mu_\tau \\ q_0 &= \sum_{\vec{x}} g \mu_\tau^2, \end{aligned}$$

which represent the components of the structure matrix  $\tilde{\mathbf{Q}}$  introduced in (5.9)

$$\tilde{\mathbf{Q}} = \begin{bmatrix} \mathbf{Q} & \vec{q} \\ \vec{q} & q_0 \end{bmatrix}.$$

This structure matrix can be interpreted as a tensor that encodes preferential directions in the motion model's parameters space. If  $\mathbf{K} \equiv \mathbf{I}$ , this parameter space is nothing but the displacement vector space, resulting in a so-called non-parametric method, when respecting the terminology introduced in the previous section. More complicated deformation fields, can also be described through  $\mathbf{K}$ , e.g. an affine one, centred at  $\vec{x}_0$  [16]

$$\mathbf{K}(\vec{x}; \vec{x}_0) = [\mathbf{I} \ \mathbf{X}_0 \ \mathbf{X}_0 \ \mathbf{X}_0]$$

$$\mathbf{X}_0 = \begin{bmatrix} x - x_0 & 0 & 0 \\ 0 & y - y_0 & 0 \\ 0 & 0 & z - z_0 \end{bmatrix}$$

with a parameter vector that holds 12 entries,  $\vec{w} = [w_0, \dots, w_{11}]^T$ .  $\mathbf{K}$  can even represent a local B-spline model, but as more parameters are introduced,  $\mathbf{Q}$  may not be full-rank, unless more constraints are combined through a larger support of  $g$ . Unfortunately, as  $g$ 's support grows larger the displacement field's resolution degrades. To overcome this loss in resolution, extra regularisation terms, e.g. enforcing a certain degree of smoothness upon  $\vec{u}$ , can be added to (5.9) [24], or the optical flow constraint can be evaluated on derived image characteristics that might be more informative on a signals displacement, specifically the local phase (see section 5.2.3).

### Demons registration

Interestingly, it can be shown that the optical flow metric is equivalent to a Sum of Square Differences (SSD), as a direct result of the Taylor expansion in (5.6) that leads to the optical flow constraint. In the limit for small displacements  $\delta\vec{u}$ , it follows that

$$\text{SSD}(\delta\vec{u}) = \sum_{\vec{x}} g(\vec{x}) \|\mu(\vec{x} + \delta\vec{u}, \tau + \delta\tau) - \mu(\vec{x}, \tau)\|^2 \approx \mathcal{C}(\delta\vec{u}) \quad (5.13)$$

This particularly holds for iterative optimisation methods, which minimise the optical flow metric by gradually removing the motion from the moved images through small incremental estimates for the displacement  $\delta\vec{u}^{(k)}$ , known as the update field. As the metric converges to its optimum, the update field grows smaller and smaller until the fixed and moving images overlap. In finding a suitable update

field, it is interesting to note that the optical flow constraint defines a plane in the displacement vector space normal to  $\nabla_{\vec{x}}\mu$ , and at a distance  $\mu_\tau / \|\nabla_{\vec{x}}\mu\|$  from the origin. Similar to the Kaczmarz method (see section 3.2.2), the deformation field can thus be found by iteratively projecting the intermediate solutions between the planes corresponding to the constraints, with an update of the form

$$\delta\vec{u}^{(k)} = \frac{\mu_m(\vec{x} + \vec{u}^{(k-1)}) - \mu_f(\vec{x})}{\|\nabla_{\vec{x}}\mu\|^2} \nabla_{\vec{x}}\mu \quad (5.14)$$

where  $\vec{u}^{(k)} = \sum_k \delta\vec{u}^{(k)}$  adds up all of the update fields to form a final solution for  $\vec{u}$ . It was Thirion [25] that first proposed this update in his more general framework, using ‘*Maxwell’s demons*’ to register images. He also introduced an extra regularisation term to handle points with a vanishing gradient, leading to

$$\delta\vec{u}^{(k)} = \frac{\mu_m(\vec{x} + \vec{u}^{(k-1)}) - \mu_f(\vec{x})}{\|\nabla_{\vec{x}}\mu\|^2 + \alpha \cdot (\mu_m(\vec{x} + \vec{u}^{(k-1)}) - \mu_f(\vec{x}))^2} \nabla_{\vec{x}}\mu \quad (5.15)$$

The regularisation parameter  $\alpha$  limits the size of the update field, and while Thirion simply set  $\alpha$  to one, it may generally not even be scalar [26], i.e. a different value at each field location. Several demons registration algorithms evolved, as more complicated models for and feature of the motion fields were taken into account. For example, the SSD metric may be symmetrised

$$\begin{aligned} \text{SSD}^*(\delta\vec{u}) &= \sum_{\vec{x}} g(\vec{x}) \|\mu(\vec{x} + \delta\vec{u}, \tau + \delta\tau) - \mu(\vec{x}, \tau)\|^2 \\ &\quad + \sum_{\vec{x}} g(\vec{x}) \|\mu(\vec{x}, \tau + \delta\tau) - \mu(\vec{x} - \delta\vec{u}, \tau)\|^2 \end{aligned}$$

to enforce a ‘*Symmetric Demons Registration*’ update, yielding a consistent forward and backward deformation transform. Or, a diffeomorphic transform<sup>3</sup> can be obtained by looking at the problem as an optimisation over Lie groups of transforms, rather than a vector space of displacements [27, 28]. And finally, by applying a simple Gaussian smoothing on the update field or the total field, the eventual motion model can be forced to show a fluid like or elastic behaviour, respectively [26].

To conclude, algorithm 1 outlines the basic demons registration approach. A Python implementation of the demons algorithm and several of its variants, is available through the SimpleITK module [29–31]. Among others, the SimpleITK module was used to perform registration tasks in the applications discussed throughout 5.4 by employing ITK’s fast implementation of the symmetric demons algorithm [31].

---

<sup>3</sup>A smooth bijective mapping with a smooth inverse.

---

**Algorithm 1** Demons registration algorithm

---

- Set the initial displacement field for  $k = 0$ :  $\vec{u}^{(0)} = \vec{0}$
  - Do until (5.13) converges:
    1. Compute the update according to (5.15):  $\delta\vec{u}^{(k)}$
    2. Gaussian smoothing of the update field for a fluid like behaviour:
$$\delta\vec{u}^{(k)} \leftarrow \mathcal{G}_{\sigma_f} \star \delta\vec{u}^{(k)}$$
    3. Compose the transforms:  $\vec{u}^{(k+1)} \leftarrow \vec{u}^{(k)} + \delta\vec{u}^{(k)}$
    4. Gaussian smoothing of the total field for an elastic behaviour:
$$\vec{u}^{(k+1)} \leftarrow \mathcal{G}_{\sigma_e} \star \vec{u}^{(k+1)}$$
  - 5.  $k \leftarrow k + 1$
- 

### 5.2.3 Optical phase flow

#### The phase based constraint

In substituting the image's intensity for its phase  $\theta_d$ , such that the optical flow constraint becomes

$$\theta_{d,\tau} + \vec{u} \cdot \nabla_{\vec{x}} \theta_d = 0 \quad (5.16)$$

with  $\theta_{d,\tau} = \partial\theta_d/\partial\tau$ , it should first of all be noted that an image's phase is indeed a stable characteristic, in the sense that it does not wildly fluctuates as a result of small deformations. Especially in the vicinity of salient image features, which require a high coherence of the underlying frequency components, the phase has to be stable if a constructive interference is to build up these features [32]. Moreover, the phase is approximately linear over a relatively large spatial extent [16], making the optical phase flow constraint (5.16) particularly accurate. In the extreme case of a Fourier transform, this linearity holds across the entire image, such that a signal displacement is exactly proportional to a phase shift of the Fourier spectrum. Unfortunately, this property is of little practical interest to estimate local non-rigid deformations from one image to the next, as the locality of the image features is clearly lost under the Fourier transform. Hence, a more local analysis of phase needs to be conducted, which preferable also yields components in a limited band across frequency space, an ideal task for wavelets.

### The problem with wavelets

For a detailed description on wavelets and the discrete wavelet transform (DWT), the reader is referred to the appropriate literature [33–35]. The DWT was originally conceived, by among others Ingrid Daubechies, to facilitate a compact representation for the analysis of a signal in both the spatial and the frequency domain [36–38]. It can be implemented very efficiently by passing a signal through a cascade of filter banks, which splits a signal into a high frequency part, the ‘*wavelet coefficients*’, and a low frequency part, the ‘*scaling coefficients*’, while intermittently decimating the signal dyadically<sup>4</sup> at each level of the cascade. In Figure 5.7, two levels of such a cascade are depicted, indicating that the decomposition into wavelet and scaling coefficients is governed by the high and low pass filters,  $h_0$  and  $h_1$ , respectively. The original signal can also be exactly reconstructed from the wavelet and scaling coefficients by reversing the direction of the filter bank, and by replacing the filters by their synthesis counter parts ( $\tilde{h}_1$  and  $\tilde{h}_0$ ) [33]. However, since the reconstruction aspect is not relevant in the context of deformation estimation, it is not discussed any further. Important to note is that the DWT has two shortcomings, which are specifically problematic in the context of deformation estimation [33, 35]:

1. The DWT is ‘*shift variant*’.
2. The DWT has ‘*no directional selectivity*’.

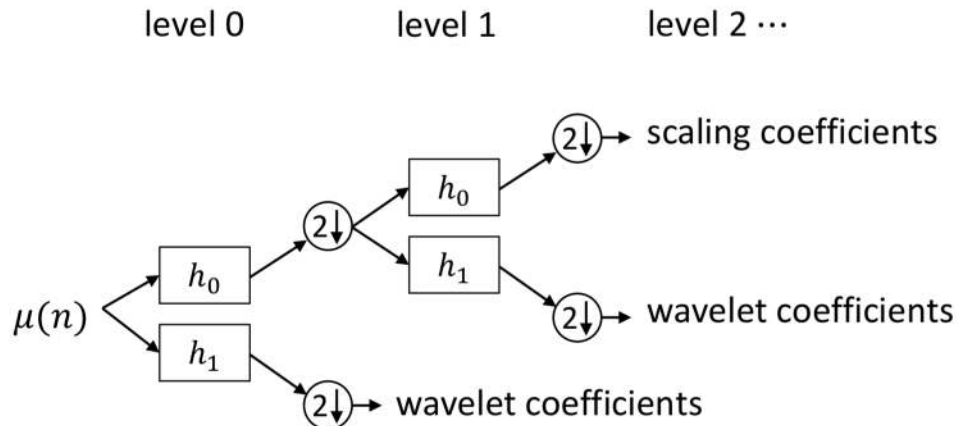


*Figure 5.7: A 1D wavelet analysis with a cascading filter bank. A 1D signal is split into high frequency and low frequency parts by passing it through high and low pass filters. The dyadically decimated results are called wavelet and scaling coefficients, respectively.*

*The scaling coefficients are passed on the next level in the filter bank.*

---

<sup>4</sup>By powers of two.

Indeed, the DWT coefficients of a shifted signal may differ significantly from those of the original signal. As a result, the signal's phase is not stable, nor is it linear. Ideally, the high and low pass filters ( $h_1$  and  $h_0$ ) should exactly split up the frequency domain into two equal halves. The accompanying block-like filter responses in the frequency domain will thus correspond to an infinite support of the spatial impulse response, which does not stroke with the philosophy of a wavelet analysis. Practically usable wavelet filters with a finite support will thus necessarily exhibit a slight overlap (Figure 5.8). It is precisely this overlap that causes the shift variance, since both the high and low frequency filter outputs are contaminated by components that do not belong to their respective bands after decimation, i.e. the decimated signals are distorted by aliasing terms.

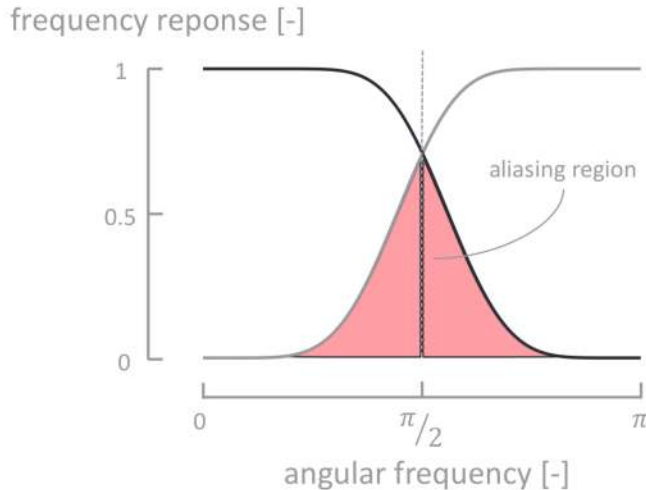


Figure 5.8: Aliasing region in the frequency responses of the db7 wavelet filters.

To illustrate the lack in directional selectivity, consider a 2D extension of a real DWT high pass filter, such as the one depicted in Figure 5.8. As the DWT allows it to act on the rows and columns of an image in a completely separable way, the composite frequency response arises through a tensor product of the individual row and column filter (see Figure 5.9). The resulting spectrum occupies the four corners of frequency space, which means this composite filter does not select a preferred direction in space. The link between directionality and the structure of the Fourier spectrum can be explained by looking at the opposite scenario of a basis function that can basically encode any desired direction, namely a plane wave with wave vector  $\vec{k}$

$$e^{j \vec{k} \cdot \vec{x}} = \cos(\vec{k} \cdot \vec{x}) + j \sin(\vec{k} \cdot \vec{x}). \quad (5.17)$$

Coincidentally, this is the Fourier transform's expansion basis, for which it was already established that a signal displacement expresses itself as a phase shift of

these plane waves. The most important observation to be made on the plane wave expression (5.17) is the one-sided build up of its spectrum, i.e. it only has non-zero components (in this case one) on one side of the plane with normal  $\vec{k}$ . It can be shown that any  $N$ -dimensional signal, which has non-zero frequency components at just one side of an  $(N + 1)$ -dimensional hyperplane dividing its frequency space, will predominantly fluctuate in the direction normal to this hyperplane [39]. These types of signal are so-called ‘*analytical signals*’, for which the real and imaginary parts form a Hilbert transform pair. As an added perk, the projections of a signal on a basis of analytical signals is also shift invariant. In other words, the problems of the DWT’s shift variance and poor directional selectivity, are solved in defining a complex analytical basis of wavelets and scaling functions.

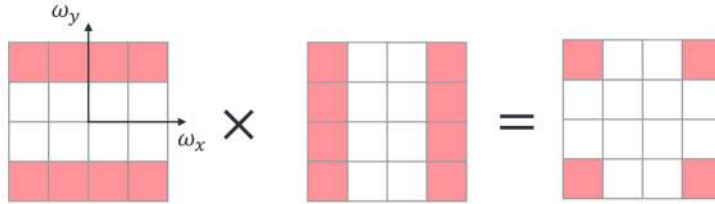


Figure 5.9: Artistic impression of a 2D-DWT high pass filter spectrum’s amplitude. The four cornered spectrum does not encode a clear preference for any direction.

### The Dual-Tree Complex Wavelet Transform (DT-CWT)

Again, the decomposition of a signal onto a complex analytical wavelet basis can be executed by a filter bank. However, this time the signal is simultaneously passed through two filter banks, the standard filter bank from Figure 5.7 and a dual filter bank, where the filters have been exchanged for half-sample delayed versions of  $h_1$  and  $h_0$  (see Figure 5.10)

$$g_0(n) = h_0(n - 0.5) \quad g_1(n) = h_1(n - 0.5). \quad (5.18)$$

It can be shown that the wavelets functions ( $\psi_h(n)$  and  $\psi_g(n)$ ) and scaling functions ( $\phi_h(n)$  and  $\phi_g(n)$ ) represented by both of these trees are indeed linked through a Hilbert transform [33]

$$\psi_g(n) = \mathcal{H}[\psi_h](n) \quad \phi_g(n) = \mathcal{H}[\phi_h](n)$$

which gives rise to the ‘*Dual-Tree Complex Wavelet Transform (DT-CWT)*’, with complex analytical wavelet and scaling functions of the form (in 1D)

$$\psi(n) = \psi_h(n) + j \psi_g(n) \quad \phi(n) = \phi_h(n) + j \phi_g(n) \quad (5.19)$$

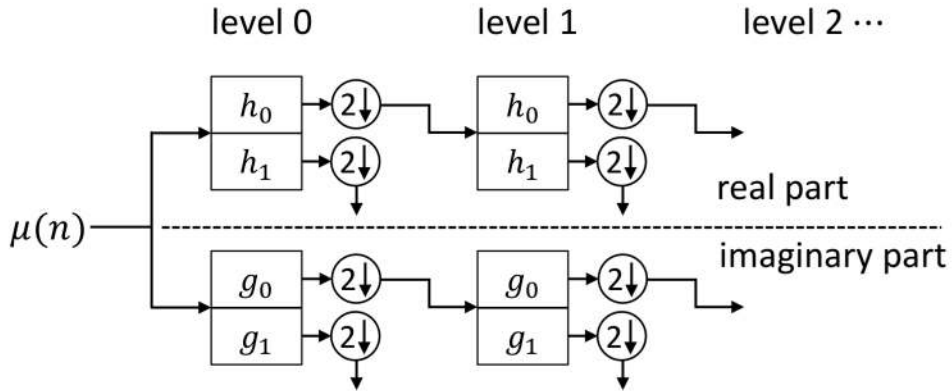


Figure 5.10: A 1D dual-tree complex wavelet transform filter bank. The individual trees respectively generate the real and imaginary parts of the complex wavelet and scaling coefficient.

In 2D, the tensor products of these complex wavelets inherently exhibit directionality, which again is best seen on the idealised impulse response spectra of Figure 5.11. The wavelet corresponding to the spectrum in this figure is given by

$$\psi(n_x, n_y) = \psi(n_x) \psi(n_y),$$

which is a tensor product of the complex wavelet function from (5.19). This wavelet can be labelled as '*HH*' (*High, High*), as both the rows and columns of the analysed imaged will be high pass filtered. Five other tensor products can be composed by also taking into account the low pass filter behaviour of the complex scaling wavelets, and by complex conjugation the wavelets in the Y-direction<sup>5</sup>, e.g. the *HL* (*High, Low*) band

$$\psi(n_x, n_y) = \psi(n_x) \phi(n_y)$$

This leads to six sub-bands in total, *HH, HL, LH, LH\**, *HL\** and *HH\**, which, looking at Figure 5.12, clearly encode different directions. This is not the case for the *LL*-variants, which why they are not considered here.

In 3D, the tensor products of complex wavelet and scaling functions are made up out of three factors, e.g.

$$\psi(n_x, n_y, n_z) = \psi(n_x) \psi(n_y) \psi(n_z),$$

representing the *HHH* sub-band wavelet. Each factor may represent a high or low pass filtering operation with the wavelet or scaling functions, or their conjugate forms, leading to the following 28 sub-bands

---

<sup>5</sup>Complex conjugation in the X-direction does not yield any extra components, since the input signal is a real image.

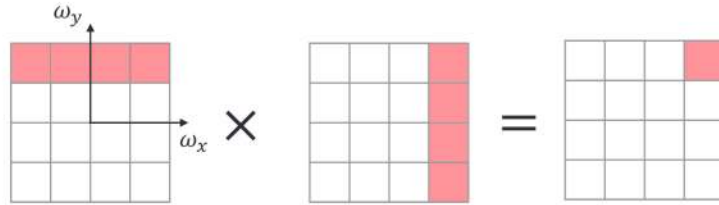


Figure 5.11: Idealised spectrum from one of the six bands of 2D DT-CWT. By composing the X- and Y- analytic high pass band, only the top right corner in the idealised spectrum shows non-zero values. The accompanying wavelet will be directed towards  $45^\circ$ .

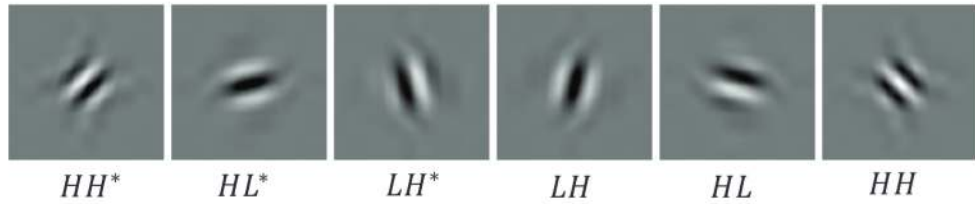


Figure 5.12: Real part of the six complex wavelet bands of DT-CWT. These images clearly show the directionality of the wavelets.

$$\begin{array}{ccccccc}
 HHH & HHL & HLH & HLL & LHH & LHL & LLH \\
 HH^*H & HH^*L & HL^*H & HL^*L & LH^*H & LH^*L & LL^*H \\
 HHH^* & HHL^* & HLH^* & HLL^* & LHH^* & LHL^* & LLH^* \\
 HH^*H^* & HH^*L^* & HL^*H^* & HL^*L^* & LH^*H^* & LH^*L^* & LL^*H^*
 \end{array}$$

Again, each of these sub-bands filters out a certain direction in the 3D input image. In other words, the analysis performed by the 3D DT-CWT unveils which directions are predominantly expressed through the image's features, and this on a local basis.

A particularly interesting feature of the DT-CWT is that all of the resulting wavelet subbands can be stored without taxing an excessively redundant amount of memory. This is a direct result of decimation and thus the fact that the DT-CWT remains (approximately) shift invariant and keeps its directional sensitivity across different scales. The redundancy factor, as in the number of times the original data needs to be stored, is only  $2^d$  for  $d$ -dimensional signals, whereas the undecimated DWT, which can also be made shift invariant, is memory redundant by a much larger factor of  $\log_2 N$ , where  $N$  is a typical number of data entries in one of the dimensions [33, 35].

### Back to the phase constraint

Since each of the 28 sub-bands, coming out of a 3D DT-CWT analysis, carries its own phase information, 28 phase constraints of the form (5.16) can be composed. So, instead of aggregating the constraints across a certain spatial extent, follow-

ing equation (5.7), the phase constraints can be combined locally to solve motion models with up to 28 parameters. Moreover, both strategies can be combined to boost the robustness of the displacement estimation, according to the following metric (cfr. (5.7)) [40]

$$\mathcal{C}(\vec{v}) = \sum_{\vec{x}} \vec{v}(\vec{x})^T \cdot \left[ \sum_{d=1}^{28} \vec{c}_d(\vec{x}) \vec{c}_d(\vec{x})^T \right] \cdot \vec{v}(\vec{x}) \quad (5.20)$$

where the constraint vector is given by

$$\vec{c}_d = g_d(\vec{x}) \cdot \begin{bmatrix} \nabla_{\vec{x}} \theta_d(\vec{x}) \\ \theta_{d,\tau}(\vec{x}) \end{bmatrix} \quad (5.21)$$

with an index  $d$  that refers to the individual sub-bands. Alternatively, the phase constraints can be gathered in a single matrix

$$\mathbf{C} = [\vec{c}_1 \vec{c}_2 \cdots \vec{c}_{28}],$$

leading to the following metric (cfr. (5.11))

$$\mathcal{C}(\vec{v}) = \vec{w}^T \cdot \mathbf{K}^T \mathbf{C} \mathbf{C}^T \mathbf{K} \cdot \vec{w},$$

by adopting the parametrisation given in (5.10). Again, the solution can be found through equation (5.12), with a slightly different structure tensor

$$\begin{aligned} \mathbf{Q} &= \sum_{\vec{x}} \mathbf{K}(\vec{x})^T \cdot \sum_{d=1}^{28} [g_d(\vec{x}) \nabla_{\vec{x}} \theta_d(\vec{x})^T \nabla_{\vec{x}} \theta_d(\vec{x})] \cdot \mathbf{K}(\vec{x}) \\ \vec{q} &= \sum_{\vec{x}} \mathbf{K}(\vec{x})^T \cdot \sum_{d=1}^{28} [g_d(\vec{x}) \nabla_{\vec{x}} \theta_d(\vec{x})^T \theta_{d,\tau}(\vec{x})]. \end{aligned}$$

Following Chen *et al.* [40], a 3D version of the phase based registration approach was developed as an extension to an already existing 2D implementation of the algorithm, available through an open source Python module [41]. The extension makes it possible to track local non-rigid deformations in 3D by producing a dense displacement field that maps each voxel in a reference volume to its position in the deformed volume. In summary, the phase based optical flow approach, combined with a DT-CWT analysis, has some appealing properties that makes it a viable and robust candidate for local non-rigid deformation estimation:

- An image's phase can be linear over a relatively large extent of space, making the constraint (5.16) even more accurate for phase than in the intensity based context.

- The DT-CWT provides a built-in directional analysis, leading to 28 directional sub-bands. Up to 28 motion model parameters can be estimated, by combining their phase constraints locally, instead of aggregating constraints spatially, as in the intensity based approach.
- A hierarchical scheme for the estimation of deformation naturally arises, since the DT-CWT analysis inherently decomposes the image into a multi-resolution pyramid.

### 5.2.4 B-spline registration

Both of the constrained based techniques, outlined in the previous sections, produce a local result for the displacement vector or the parameters of the motion model describing this displacement. However, alternative parametrisations, following equation (5.10), were not considered in the implementations of the constrained based techniques, that were used throughout the applications in section 5.4. In other words, as they were exploited in this work, the constrained based optical flow registrations are of the local, non-parametric kind.

As a third, parametric and global registration technique, the B-splines registration approach was also explored. In this approach, the entire displacement field is described as a linear combination of B-splines, set out on a regularly spaced grid of control points. In 1D, the one and only displacement component can thus be approximated by

$$u(x) = \sum_{n_x=1}^{N_x} w(n_x) \mathcal{B}_{n_x,k}(x) \quad (5.22)$$

where  $k$  indicates the B-spline's order<sup>6</sup>,  $N_x$  fixes the number of control points, and the  $w$ -values form a set of parameters that fix the motion model. The cubic B-spline functions ( $k = 3$ ) on a 1D control grid of 11 points uniformly spaced throughout the unit interval, are set out in Figure 5.13. In 3D, the linear expansion basis is constructed out of B-spline tensor products, which are now used to approximate three displacement components, leading to

---

<sup>6</sup>Here, the order equals the degree of the polynomials composing the B-spline function. Confusingly, in literature the order sometimes refers to the degree plus one.

$$u_x(\vec{x}) = \sum_{n_x, n_y, n_z=1}^{N_x, N_y, N_z} w_x(n_x, n_y, n_z) \mathcal{B}_{n_x, k}(x) \mathcal{B}_{n_y, k}(y) \mathcal{B}_{n_z, k}(z) \quad (5.23a)$$

$$u_y(\vec{x}) = \sum_{n_x, n_y, n_z=1}^{N_x, N_y, N_z} w_y(n_x, n_y, n_z) \mathcal{B}_{n_x, k}(x) \mathcal{B}_{n_y, k}(y) \mathcal{B}_{n_z, k}(z) \quad (5.23b)$$

$$u_z(\vec{x}) = \sum_{n_x, n_y, n_z=1}^{N_x, N_y, N_z} w_z(n_x, n_y, n_z) \mathcal{B}_{n_x, k}(x) \mathcal{B}_{n_y, k}(y) \mathcal{B}_{n_z, k}(z) \quad (5.23c)$$

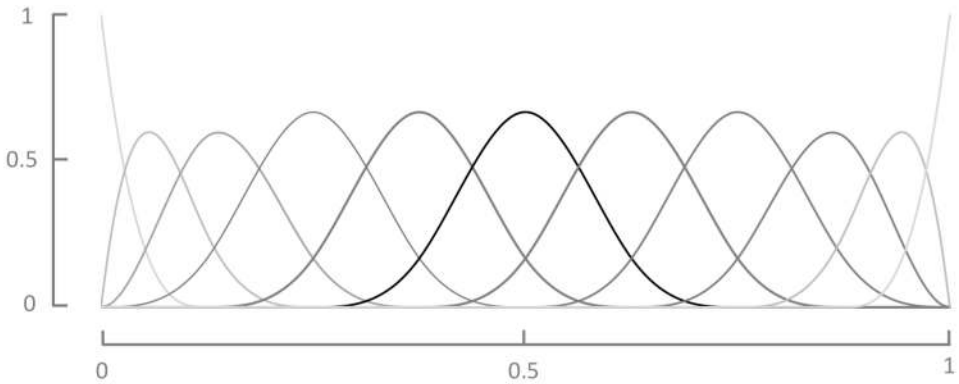


Figure 5.13: 1D cubic B-splines on an 11 point control grid.

The displacement vector field is thus described by a parameter vector field  $\vec{w} = [w_x, w_y, w_z]$ . In this work, the parameter vector was optimised according to scheme outlined in Figure 5.6, through the implementation provided by the ‘elastix’ toolbox [15], which is also exposed to Python through the SimpleElastix module [42]. The elastix B-spline registration procedure was configured to optimise a ‘Normalised Cross Correlation (NCC) metric

$$\text{NCC}(\vec{w}) = \frac{\sum_{\vec{x}} \mu_m(\vec{x} + \vec{u}(\vec{w})) \mu_f(\vec{x})}{\sqrt{\sum_{\vec{x}} \mu_m(\vec{x} + \vec{u})^2 \sum_{\vec{x}} \mu_f(\vec{x})^2}} \quad (5.24)$$

with an ‘Adaptive Stochastic Gradient Descent (ASGD) optimiser [43], and this on a 3D grid of control points that is decimated by a factor of eight in every direction with respect to the original image grid.

## 5.3 Motion corrected iterative reconstruction

### 5.3.1 Recap - The SART algorithm

In 4D X-ray CT imaging a delicate balance must be maintained between motion blurring artefacts, arising when on the one hand a dynamic process is imaged at

an insufficient temporal resolution, and on the other hand a low SNR, as a result of acquiring an insufficient number of photons during fast imaging. When considering non-rigidly deforming samples, both the motion blurring and low SNR can be alleviated by integrating an estimate of the deformation into the CT reconstruction algorithm. Although, the Simultaneous Algebraic Reconstruction Technique (SART) or rather its generalised Ordered Subset version has been thoroughly discussed in section 3.2, it is revisited here with the prospect of incorporating a free form deformation into its projection and back projection steps.

In doing so, it is important to build up a time scale for the projections used in a reconstruction. If  $\tau_0$  represents the instant in time at which the first projection ( $P_0$ ) in a CT data set is acquired, the other projections are expected at the time steps  $\tau_s$ , given by

$$\tau_s = \tau_0 + s t_{exp}, \quad s \in [0 \dots N_S[,$$

if an exposure time  $t_{exp}$  is set. However, a valid CT reconstruction does not necessarily require all of the  $N_S$  projections ( $P_s$ ) contained within the CT dataset ( $S$ )

$$S = \{P_s : s \in [0 \dots N_S]\}.$$

For example, a dynamic acquisition might consist out of multiple rotations, such that several subsets of the entire dataset may provide a sufficient sampling to calculate an ‘accurate’ CT reconstruction of the imaged object. The term ‘accurate’ is however relative in considering the dynamic nature of such an experiment, in which the underlying  $\mu$ -distribution is in fact time dependent. Each reconstruction thus reflects a certain temporal state of the object, which is uniquely determined by the subset of the projections ( $R$ ) used for this reconstruction

$$R = \{P_r : r \subset s\}$$

such that  $R \subset S$ . Whether the reconstruction accurately represents the underlying state, i.e. with little to no motion blurring, depends on how much the object deforms during the acquisition of all the projections in  $R$ . If this deformation is negligible, it makes sense to attach a time stamp

$$\tau_R = \frac{1}{N_R} \sum_{P_r \in R} \tau_r$$

to the reconstruction, which is then supposed to accurately reflect the underlying ground truth  $\mu$ -distribution. The object is assumed to be stationary in the time it takes to acquire  $R$ , i.e. ‘local time stationarity’ is assumed [44].

To reconstruct the time instant  $\tau_R$ , the SART algorithm implements a sequence of three steps, that iteratively loop (in a random fashion) over all the projections in  $R$  (see algorithm 2). In a first step, a simulated version of the currently handled projection  $P_r$  is calculated by tracing out a line integral through an intermediate estimate of the  $\mu$ -distribution. At iteration  $k$ , this amounts to (cfr. equation (3.23))

$$\hat{P}_{r,j}^{(k)} = \Delta t_j \sum_{l=0}^L \mu^{(k)}(\vec{x}_{jl}) \quad (5.25)$$

where, following Joseph's approach [45], the  $L$  points  $\vec{x}_{jl}$  are equidistantly sampled with an interval  $\Delta t_j$  on the ray that connects the source point  $\vec{O}_s$  to detector pixel  $j$  (see equation (2.12)). In the second step, the error with respect to the real measurement  $P_{r,j}$  is calculated and weighted by a factor containing the relaxation  $\lambda$ , a weight  $w_r^c$  reflecting the contribution of projection  $P_r$  to the current time step  $\tau_R$ , an aperture function  $w_j^a$  to reduce artefacts inherent to region of interest reconstructions [46], and the intersection length between the ray  $j$  and the voxel volume.

$$C_{r,j}^{(k)} = \left( P_{r,j} - \hat{P}_{r,j}^{(k)} \right) \cdot \frac{w_r^c w_j^a}{L \Delta t_j} \quad (5.26)$$

Finally, during the back projection step, the  $\mu$ -value in each voxel is updated by interpolating the correction term  $C_r^{(k)}$  at the intersection between the detector plane and the line connecting the source positions  $\vec{O}_s$  to the voxel's position  $\vec{x}_m$ . The resulting interpolation value is then added to the previous estimate for the  $\mu$ -distribution

$$\mu^{(k+1)}(\vec{x}_m) = \mu^{(k)}(\vec{x}_m) + C^{(k)}(\vec{O}_s, \vec{x}_m). \quad (5.27)$$

### 5.3.2 Motion corrected SART

The goal is now to go beyond the local time stationarity assumption, and adapt algorithm 2 in a way that it accounts for FFDs (cfr. [46, 47]). It is assumed that these FFDs can be described by dense displacement fields  $\vec{u}_{rR}(\vec{x})$ , known beforehand or more specifically estimated through one of the FFD registration techniques described in the previous section. Important here is the indexation ' $rR$ ', which indicates that the  $\vec{u}_{rR}$  describes the displacement of an object as it deforms from its state at time instant  $\tau_r$ , when the projection  $P_r$  is acquired, to the state represented in the reconstruction, at the averaged time stamp of the entire subset  $\tau_R$ . Given this definition, algorithm 3 can be composed, which clearly only differs from algorithm 2 in its projection and back projection steps.

**Algorithm 2** The standard SART algorithm

---

- Set the initial  $\mu$ -distribution for  $k = 0$ :  $\mu^{(0)} = 0$
- Randomly permute  $R$
- For all  $P_r \in R$  do:
  1. Project according to (5.25):

$$\hat{P}_{r,j}^{(k)} = \Delta t_j \sum_{l=0}^L \mu^{(k)}(\vec{x}_{jl})$$

2. Correct according to (5.26):

$$C_{r,j}^{(k)} = \left( P_{r,j} - \hat{P}_{r,j}^{(k)} \right) \cdot \frac{w_r^c w_j^a}{L \Delta t_j}$$

3. Back project according to (5.27):

$$\mu^{(k+1)}(\vec{x}_m) = \mu^{(k)}(\vec{x}_m) + C^{(k)}(\vec{O}_s, \vec{x}_m)$$


---

To calculate the correction term at  $\tau_r$ , the volume at this time instant has to be projected. The reconstruction volume however, represent the deformed state at  $\tau_R$ , in which the points that ought to be projected are now situated at the downstream side of the displacement field, hence the plus sign in the deformation transform for the projection step. In the back projection step, a minus sign needs to be adopted, since the correction term now pertains to a time step at which the voxel position were situated at the upstream side of the displacement field.

Algorithm 3, also gives some hints on how the motion correction can be efficiently implemented. In first, brute force approach, the deformation transform could be executed across the entire intermediate reconstruction volume. In handling a projection  $P_r$ , the reconstruction volume is thus reverted to its state at that time. After the back projection, the volume is then deformed back to the reconstruction time stamp  $\tau_R$ . This amounts to a twofold resampling of the entire volume, which for one, is a computationally demanding task, especially because it needs to be executed during each SART iteration, but foremost, might also induce an interpolation error to be carried and accumulated across the many SART iterations. In this work, a somewhat more lightweight implementation is considered, that uses a non-parametric displacement vector field as an overlay to the reconstruction volume. The major advantage of this approach is that the three displacement vector components ( $u_x$ ,  $u_y$  and  $u_z$ ) can be stored in texture memory. Using

**Algorithm 3** The motion corrected SART algorithm

- Set the initial  $\mu$ -distribution for  $k = 0$ :  $\mu^{(0)} = 0$
- Randomly permute  $R$
- For all  $P_r \in R$  do:
  1. Project the volume's state at  $\tau_r$ :

$$\hat{P}_{r,j}^{(k)} = \Delta t_j \sum_{l=0}^L \mu^{(k)}(\vec{x}_{jl} + \vec{u}_{rR}(\vec{x}_{jl}))$$

- 2. Correct according to (5.26):

$$C_{r,j}^{(k)} = \left( P_{r,j} - \hat{P}_{r,j}^{(k)} \right) \cdot \frac{w_r^c w_j^a}{L \Delta t_j}$$

- 3. Back project to volume's state at  $\tau_R$ :

$$\mu^{(k+1)}(\vec{x}_m) = \mu^{(k)}(\vec{x}_m) + C^{(k)}(\vec{O}_s, \vec{x}_m - \vec{u}_{rR}(\vec{x}_m))$$

the texture's built in trilinear interpolation capabilities, a displacement vector can be sampled, which is then used to redefine the position at which the  $\mu$ -volume is sampled. While this approach introduces virtually no overhead <sup>7</sup> with respect to the original SART implementation, there are some limitation to be considered:

- The approach requires more memory, as now three extra volumes need to be stored in GPU RAM. However, the displacement vector volumes do not have to be represented at the same resolution level as the  $\mu$ -volume. A down-sampling can be carried out, of course at the cost of some loss in the displacement field's accuracy.
- The parametrisation of the registration technique used to estimate the displacement vectors is lost. This does not mean that the registration procedure itself will not benefit from a more advanced parametric motion model. In the SART iterations, the vector field will simply not be sampled according to this motion model. A B-spline sampling model could be implemented on the GPU, but then the advantages of using textures will have to be sacrificed.
- The technique falls or stands with a good model for the displacement field's evolution through time.

<sup>7</sup>Three texture memory fetches and three addition.

Indeed, this last remark is crucial, but since a registration procedure, between a fixed image at time  $\tau_f$  and a moving image at  $\tau_m$ , only yields a single displacement field, without any information on its temporal information, not a lot of choices are left for the parametrisation of its temporal behaviour. As demonstrated in section 5.4, the simple linear evolution of a displacement field

$$\vec{u}_{rR}(\vec{x}) = \vec{u}_{mf}(\vec{x}) \frac{\tau_r - \tau_R}{\tau_m - \tau_f}, \quad (5.28)$$

adopted in this work, already proved to be a good and useful approximation. More complicated models, such as piece wise linear or higher order ones, can be constructed by considering extra reference volumes in between  $\tau_f$  and  $\tau_m$ . The potentially high number of parameters in these models will however lead to an even higher demand in GPU RAM and sampling overhead, which is why only (5.28) is considered in the following.

## 5.4 Applications

### 5.4.1 Registration in µCT applications

In X-ray µCT literature, registration of 3D local non-rigid deformation has particularly gained interest as a way to visualise full-field strain maps in a wide variety of materials. Ever since Bay *et al.* introduced 3D registration as a means to study deformations in trabecular bone [48], it has been widely used, in combination with µCT, in this biomechanical context [21, 22, 49–52], but also in other material disciplines like wood [53], aluminium foam [54–56], gypsum [57], soil [58], sand packings [59] and composites [60].

Clearly, deformation registration is no stranger to X-ray µCT, while its motion corrective potential is not that widely studied in the context of µCT. To the author's knowledge, motion corrected reconstruction, using dense displacement maps, has as of recently mainly been covered in literature on medical CT applications [47, 61, 62]. In a notable development at the University of Antwerp, Van Nieuwenhove *et al.* have implemented a very similar motion correction scheme, which slightly differs from the approach presented in algorithm 3 in its parametrisation of the MVF during the motion correction step [63, 64]. Van Nieuwenhove *et al.* uphold the higher order B-Spline parametrisation to sample the MVF in the warping procedures, which despite being a more accurate approach may cause an unnecessary computational overhead in the motion corrected projection and back projection steps. In this work, the native linear GPU texture interpolation is used, which only amounts to a first order B-spline, though much faster, interpolation. Hence, it should be interesting to assess this trade-off between speed and com-

plexity in future work.

In the following sections, the registration approaches discussed throughout section 5.2, and the motion correction framework of section 5.3, are tested on three applications, either rooted in the day to day activities of the UGCT, in its goal to spread  $\mu$ CT across multiple research disciplines, or as a particular case study in the context of the TomFood project (see chapter 1). The application on aluminium foams, described in section 5.4.3, was also presented at the iCT 2017 conference with an accompanying proceeding [65].

### 5.4.2 Rigid registration of a moving tree stem

The Laboratory of Plant Ecology at the UGent Department of Applied Ecology and Environmental Biology collaborates with the UGCT to image tree stems, through X-ray  $\mu$ CT imaging, in an effort to visualise their internal water transport structures. In drought periods, these transport structures might lose water conducting function. The cavitated, water drained vessels show up on CT scans as air filled cylindrical structures, with diameters down to and below the ten micron range.

For the experiment presented here, a researcher of the Laboratory of Plant Ecology set up a young beech tree for CT acquisitions with the EMCT system (see section 2.2.2). This gantry based system allowed peripheral equipment to be attached, such as tensiometers, sapflow sensors or microphones to audibly detect cavitation events [66]. To visualise the cavitated vessels, the magnification was set as high as possible, reaching a voxel pitch of  $\pm 6.7 \mu\text{m}$ . Moreover, to also discern the water filled vessels from the wood tissue matrix, a long imaging protocol was adopted to ensure a high contrast and SNR. The details of the initial single turn protocol, are summarised in table 5.2.

The problem with this  $30 \text{ min}$  single rotation protocol is that the tree could move significantly during the acquisition, leading to motion blurring artefacts in the reconstruction. Even when only the data for a short scan angular range ( $180^\circ + 2\gamma$ ) is reconstructed (Figure 5.14), the motion blurring artefact is not completely eliminated. More importantly, the resulting SNR is too low for the water filled vessels to be distinguished from the wood matrix. Hence, a new protocol had to be devised, in order to circumvent both the motion blurring and low SNR problem.

In the new protocol, three  $10 \text{ min}$  rotations were performed, measuring 1200 projections each. As such, a similar amount of image statistics was acquired,

*Table 5.2: Imaging parameters for circular cone beam scans of a beech tree, using one or several rotations.*

		Single rotation	Multiple rotations	
Tube	Hamamatsu L9181			
	Tube voltage	( $V_t$ )	60	kV
	Tube power	( $P_t$ )	5	W
Detector	Xineos1313			
	Exposure time	( $t_{exp}$ )	300	100 ms
	Detector size	(W,H)	(1316,1312)	-
	Binned pixel size	( $p_d$ )	100	μm
Geometry	Circular cone beam			
	Source Detector Distance	(SDD)	367.0	mm
	Source Object Distance	(SOD)	24.6	mm
	Number of projections	( $N_p$ )	2000	6000 -
	Number of rotations	( $N_r$ )	1	3 -
Reconstruction	FDK			
	Voxel pitch	( $p_v$ )	6.7	μm
	Voxel grid	(W,H,D)	(450,510,1101)	-

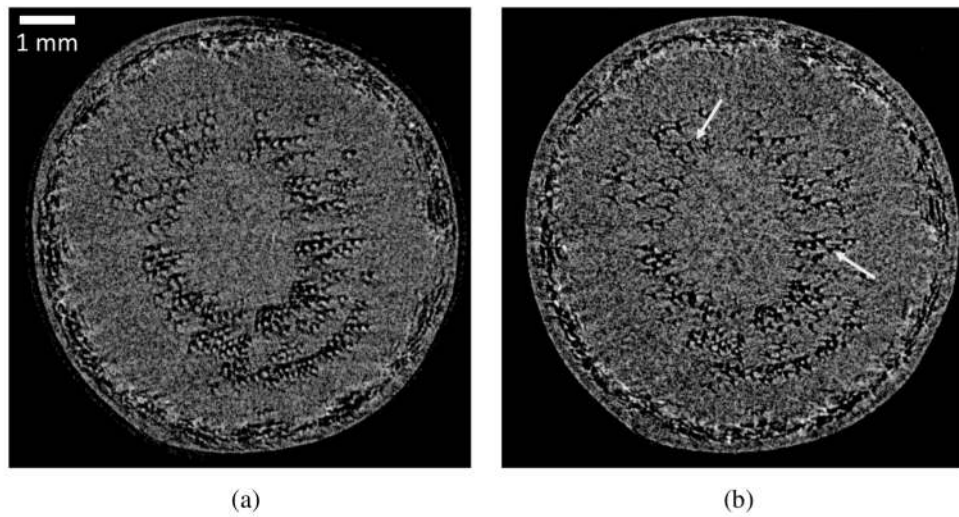


*Figure 5.14: Reconstructions of single rotation circular scan of a beech. The scanning time proved to be too long for the tree to stay still, which resulted in clear motion blurring artefacts in (a) the reconstruction of the entire dataset, and (b) as indicated by the arrows some residual motion blurring artefact in the short scan reconstruction. Their respective SNRs are 11.2dB and 9.2dB. In reporting these SNR values it is important to note that no special reconstruction filters were used other than the Ram-Lak filter.*

while keeping the individual rotations short enough to avoid unmanageable motion blurring artefacts in the reconstructions. In other words, during one rotation

it is assumed that the beech stem remains stationary. During the entire acquisition however, the beech stem moves significantly, which is clear when all of the single rotation reconstructions are simply averaged in an attempt to restore the SNR of the full acquisition (Figure 5.15(a)). To eliminate the motion blurring artefact, the SimpleElastix toolbox [42] was used to rigidly register all of the short scan reconstructions to the same point in time, before taking their average (Figure 5.15(c)). Specifically, an intermediate average reconstruction was rigidly transformed to match the next in a series of six consecutive short scan reconstructions, before taking the latter up into the average.

While very simple, this approach also proves to be very effective in solving motion blurring, to the extent it is caused by a rigid displacement of the object. The next application extends this deblurring to local non-rigid deformation. In any case, with this multi rotation protocol, the UGCT has a new technique at its disposal to tackle motion blurring without having to resort to fast low SNR acquisitions.

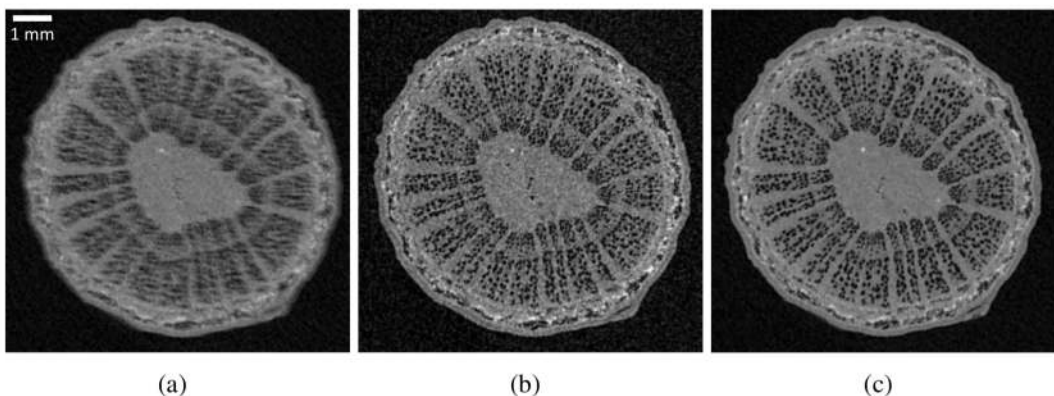


*Figure 5.15: Motion corrected reconstructions of a multi rotation acquisition by using rigid registration before averaging. (a) The reconstruction of a multi rotation scan is rendered useless due to motion blurring artefacts, if the individual reconstructions are simply averaged. (b) The individual reconstruction (first short scan) shows no motion blurring, at the cost of a low SNR (5.8 dB). (c) By registering the individual reconstructions before averaging, the SNR could be restored (6.9 dB), while avoiding motion blurring. The SNR for (a) is 10 dB, which is higher than in (c) due to the blurring effects of motion.*

### 5.4.3 In-situ compression of aluminium foams

#### Aluminium foam

For the second application, the Deben compression stage (section 5.1.2) was installed on the EMCT system to compress aluminium foams at a controllable strain rate. The deformation of aluminium foams has been studied before with X-ray  $\mu$ CT in literature [55, 56]. Besides its use as an advanced engineering mate-

rial [54], due to its low weight and load bearing capacity, it has also been brought forward as a surrogate model for bone, which has a similar micro structure, though a rather brittle mechanical behaviour as opposed to the ductile nature of aluminium [67, 68]. The precise properties of aluminium foams strongly depend on the way it is manufactured, leading to a wide variety in structures of an open- or closed-cell type, and with various aluminium strut thicknesses and air pore volumes [69]. The foam used here, shown in its uncompressed state in Figure 5.16(a), was provided by the Applied thermodynamics and heat transfer group at the UGent Department of Flow, Heat and Combustion mechanics, that studies these foams in their capacity to efficiently transfer heat [70]. With the goal of optimising this heat transfer the foams are manufactured to have high surface area to volume ratio, resulting in fairly thin aluminium struts ( $\pm 200 \mu\text{m}$ ). As such, these type of foams are not specifically designed to support large compressive loads. Hence, while it is not particularly relevant to look at their compressive behaviour, this behaviour is still fairly predictable<sup>8</sup>, making these foams an ideal candidate to benchmark the registration approaches presented above.

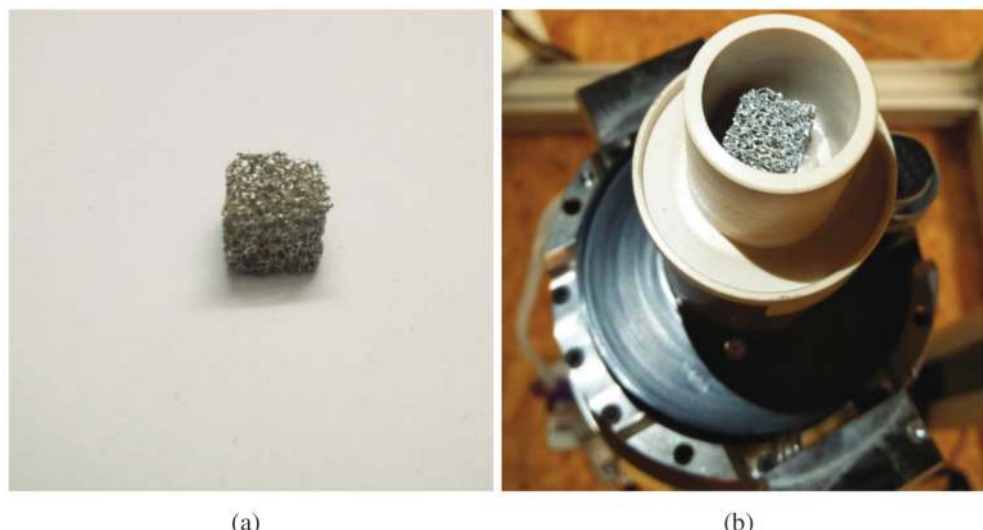


*Figure 5.16: An aluminium foam (a) in its uncompressed state, and (b) how it is placed on the bottom plate of the Deben compression stage.*

### Dynamic in-situ compression

A cubical aluminium foam sample, with a side length of  $\pm 1.5 \text{ cm}$ , was placed in a cylindrical PEEK<sup>9</sup> container, which is attached to the bottom (moving) plate of the Deben compression cell (see Figure 5.16(b)). A piston, attached to the top

<sup>8</sup>They tend to deform in a smooth plastic way, with a small amount of discrete motion events, such as buckling or brittle strut breaking.

<sup>9</sup>Polyetheretherketone

(stationary) plate, inserts itself into the PEEK container, as the bottom part moves upward, thus effectuating a compressive action upon the aluminium foam cube. At the onset of this compression, a CT acquisition (see table 5.3) was initiated, to dynamically image the foam's 3D deformation at a compression rate of 0.5 mm/min. During the 14 min acquisition, 60 gantry rotations measuring 700 projections each, were completed, which amounts to a total compression of  $\pm 8$  mm or  $\pm 133 \mu\text{m}$  per rotation. Each of the rotations in this 34 GB dataset, can be reconstructed separately, showing a relatively low degree motion blurring. Due to the inherent contrast of the aluminium foam structure with respect to its air-filled background (Figure 5.17), the low SNR of 14 sec rotations was not an issue.

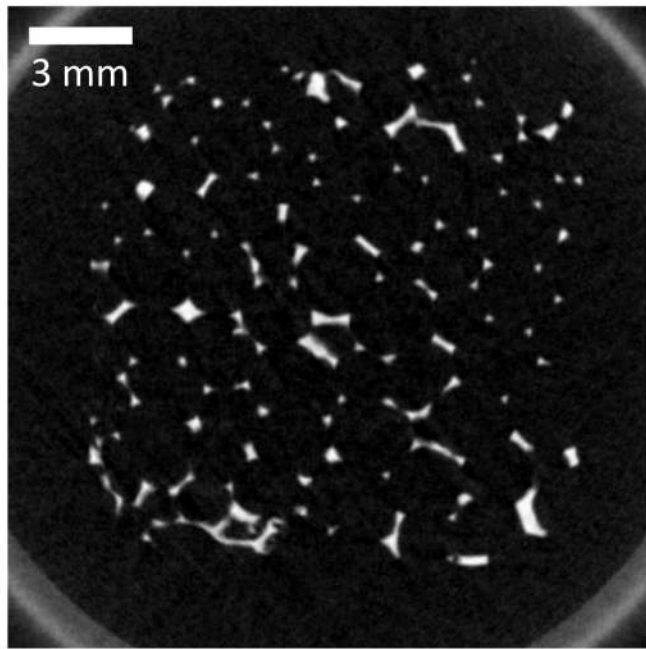


*Figure 5.17: Reconstruction of the first rotation in a dynamic acquisition of an in-situ aluminium foam compression.*

### Comparing registration algorithms

The data produced by this dynamic acquisition (table 5.3), presents an ideal opportunity to benchmark the registration algorithms of section 5.2. The most straightforward way to analyse the precision of these algorithms, is to measure how well the deformation field, produced by the registration, maps a fixed image onto the moving image. The '*Root Mean Square Error*' (RMSE)

$$\text{RMSE}(\mu_m, \mu_f^*) = \sqrt{\frac{1}{N_x N_y N_z} \sum_{n_x, n_y, n_z=1}^{N_x, N_y, N_z} ||\mu_f^*(n_x, n_y, n_z) - \mu_m(n_x, n_y, n_z)||^2} \quad (5.29)$$

which averages the SSD (cfr. (5.13)) between the transformed fixed image

$$\mu_f^*(n_x, n_y, n_z) = \mu_f(n_x + u_x(n_x), n_y + u_y(n_y), n_z + u_z(n_z))$$

and the moving image ( $\mu_m$ ), over the entire voxel grid ( $N_x, N_y, N_z$ ), before taking its square root, and the ‘Normalised Cross Correlation’ (NCC) (cfr. (5.24)), are combined in the following definition for a registration algorithm’s score ( $\chi_s$ )

$$\chi_s(n_v) = \frac{\chi_{\text{ncc}}(n_v) + \nu \chi_{\text{rmse}}(n_v)}{\chi_{\text{ncc}}(0) + \nu \chi_{\text{rmse}}(0)} - 1 \quad (5.30\text{a})$$

$$\chi_{\text{ncc}}(n_v) = \frac{\text{NCC}(\mu_m, \mu_f^*)}{\text{NCC}(\mu_m, \mu_f)} \quad (5.30\text{b})$$

$$\chi_{\text{rmse}}(n_v) = \frac{1 - \text{RMSE}(\mu_m, \mu_f^*)}{1 - \text{RMSE}(\mu_m, \mu_f)} \quad (5.30\text{c})$$

In this equation, the factor  $\nu$  scales the RMSE-component of  $\chi_s$  to lay within the same range as the NCC-component. By progressively registering the first rotation’s reconstruction to the reconstruction of a rotation further down the line, a set

*Table 5.3: Settings for the dynamic acquisition of an in-situ compression of aluminium foam.*

Tube	Hamamatsu L9181			
Tube voltage	( $V_t$ )	90	kV	
Tube power	( $P_t$ )	19.8	W	
Detector	Xineos1313			
Exposure time	( $t_{exp}$ )	20	ms	
Detector size	(W,H)	(658,656)	-	
Binnend pixel size	( $p_d$ )	200	μm	
Binning	(-)	2 by 2	-	
Geometry	Circular cone beam			
Source Detector Distance	(SDD)	367.02	mm	
Source Object Distance	(SOD)	73.4	mm	
Number of projections	( $N_p$ )	42000	-	
Number of rotations	( $N_r$ )	60	-	
Voxel pitch	( $p_v$ )	40	μm	
Reconstruction	SART			
Voxel grid	(W,H,D)	(512,512,512)	-	
SART iterations	(-)	1	-	
Relaxation	( $\lambda$ )	0.5	-	
In-situ apparatus	Deben CT5000-TEC			
Load cell	(-)	5	kN	
Compression rate	(-)	0.5	mm/min	

of scoring curves can be generated as a function of the separation between these two rotations (see Figure 5.18). This separation is reflected through  $n_v$ , which counts how many voxels (of  $40 \mu\text{m}$ ) the compression stage has moved, in between two consecutive rotations  $n_v = 3.3$  voxels.

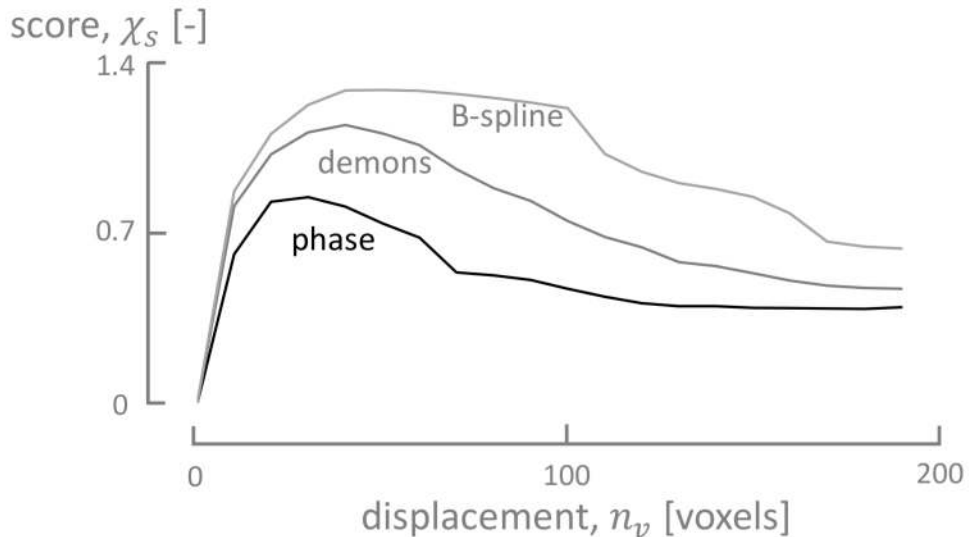
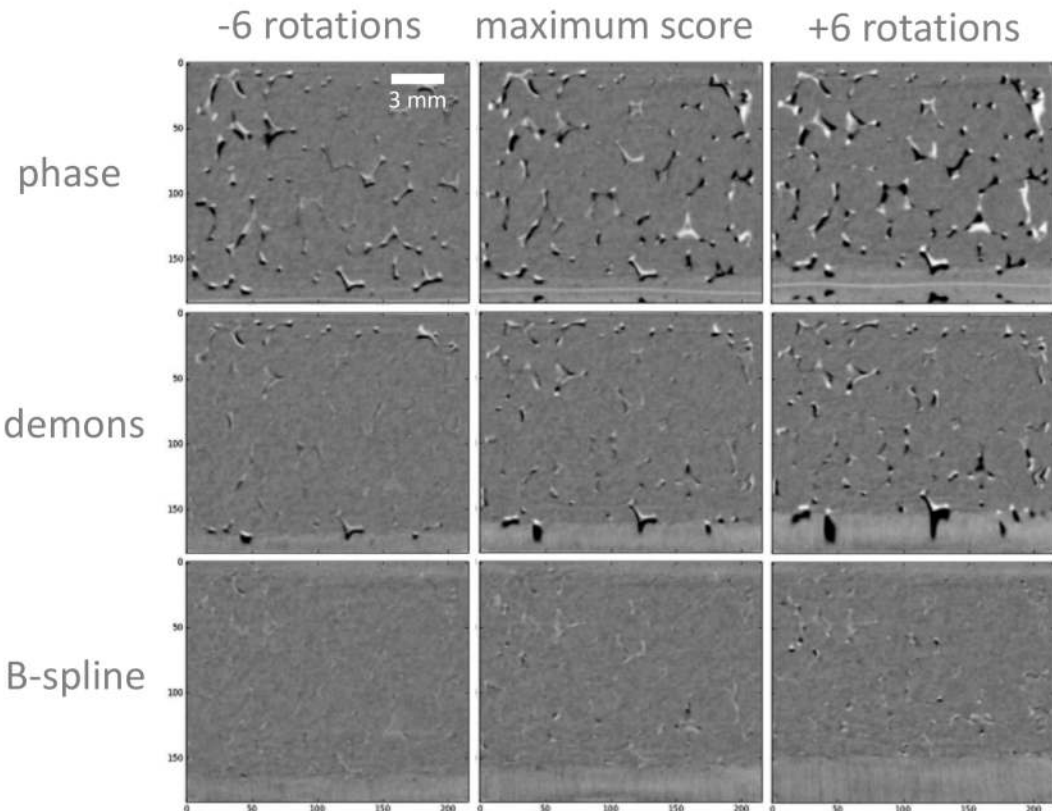


Figure 5.18: Scoring curves for Demons, phase flow and B-spline registration for the aluminium foam acquisition. The B-spline method performs best overall, providing qualitative registrations up to very high deformations as indicated by its flat maximum.

The pretence of equation (5.30) is to have an indication on how good the correspondence between the transformed fixed image and the moving image really is, i.e. if the registration technique effectively removes the mismatch between the original fixed image and the moving image, which is the case if  $\chi_s > 0$ . Notably, the curves in Figure 5.18 show a maximum, implying that the initial deformations are not large enough for the registrations to significantly boost (decrease) the NCC (RMSE), and that the algorithms completely lose track of deformations that are too large. The maximum should thus be interpreted as the optimal state of deformation at which the registration algorithms are most effective. More importantly, beyond the maximum the registration results are not to be trusted entirely. Indeed, while some regions of the images might be registered correctly, explaining the fact that  $\chi_s > 0$ , other regions might not be registered or even be distorted by the inferred deformation field. The registration results are also compared in Figure 5.19, by taking the difference between the moving images and the transformed fixed image at the maxima ( $n_{v,max}$ ) of the scoring curves, and six rotations before and after these maxima, i.e.  $n_{v,max} \pm 20$  voxels).

Purely based on the scores alone, the B-spline method is clearly superior to the others, providing qualitative registrations up to very a high deformation ( $n_v \approx$



*Figure 5.19: Difference between the moving images and the transformed fixed image at the maxima of the scoring curves, and six rotations before and after these maxima. The B-spline method clearly performs best.*

100 voxels) as indicated by its flat maximum. Moreover, the B-spline method is also very fast (56 sec per registration), despite the fact that it is inherently more complex, specifically in its higher order resampling steps. This speed is a direct result of the excellent rate at which a set of B-splines can approximate a function, i.e. it can accurately represent (smooth) functions with a relatively small amount of control grid points. The optical phase flow technique is notably slower than the other techniques (114 sec per registration), partly because the resampling operation are implemented in Python rather than C/C++ as is the case for the other two, and mainly because it calculates a Demons-like iteration update for each of its 28 sub-bands, thus making it roughly 28 times slower. The phase flow method also did not perform well on the finer scale pyramid levels, where the phase information is expected to lose its linearity [32]. If one of these finer scales is taken up in the pyramid schedule, it can distort the registration by causing a phase wrap that produces an inverted deformation field (see Figure 5.20). This is why a different registration pyramid schedule was set for the phase flow technique (see table B.1 in appendix B). While leaving out the fine scales significantly reduces the calculation time, it leaves the algorithm blind to small scale deformations. A similar sensitivity to the registration schedule could be expected from the Demons, which not is

pronounced in this aluminium foam case, but was determining for the registration results in leavening dough example of section 5.4.4, to the extent that both optical flow techniques had difficulties in producing a valid registration result. Intuitively, the registration schedules should be tuned to bridge the gap between the resolution scale of the deformation and the scale of the moving features. And ideally, both of these scales should populate the same spatial frequency range.

Due to its explicit sensitivity to the registration schedule, the author does not recommend using the phase flow technique, despite its elegant though rigorous mathematical background. The Demons method is a worthy alternative to the B-spline method, particularly due to its short calculation time (38 sec per registration), although this depends on how fine the scales in the registration schedule have been for a successful registration. Moreover, in this work, only non-parametric motion models are considered the implementation of algorithm 3 anyway. To conclude, the B-spline method is unmistakably the best choice for most registration problems, specifically when the underlying deformation is smooth, which for most naturally occurring deformation is a good assumption.

### **Reconstructing an arbitrary set of projections**

Having proven its worth as an effective registration method, the B-spline technique is now used to estimate a displacement vector field between the first reconstruction of the aluminium foam acquisition, i.e. the fixed image, and the reconstruction corresponding to the B-spline scoring curve's maximum (see Figure 5.18), i.e. the moving image. By following the motion corrective scheme discussed in section 5.3.2, several strategies can be devised to reconstruct the time instances within and even outside of the range bounded by the fixed and moving frames. Let  $\tau_f$  and  $\tau_m$  denote the time stamps linked to these respective frames, then any time instant  $\tau_R \in [\tau_f, \tau_m]$  can be reconstructed by selecting a random set  $R$  of projections in between these two time instances, which at least provides a sufficient angular sampling. Since the exposure time is constant throughout the entire experiment, the time scale may be expressed in terms of projections indices, with  $\tau_f = 350$  and  $\tau_m = 10850$ . Three scenarios are now considered to reconstruct the time instance  $\tau_c = 5600$ , at the centre of the interval:

- case 1:  $\tau_c$  is reconstructed with the 700 projections from its enclosing rotation, which is the standard approach.
- case 2:  $\tau_c$  is reconstructed using 700 projections, equidistantly sampled across the interval  $[\tau_f, \tau_m]$ .
- case 3:  $\tau_c$  is reconstructed using 2800 projections, which is the equivalent of four complete rotations, though again equidistantly spread out across the

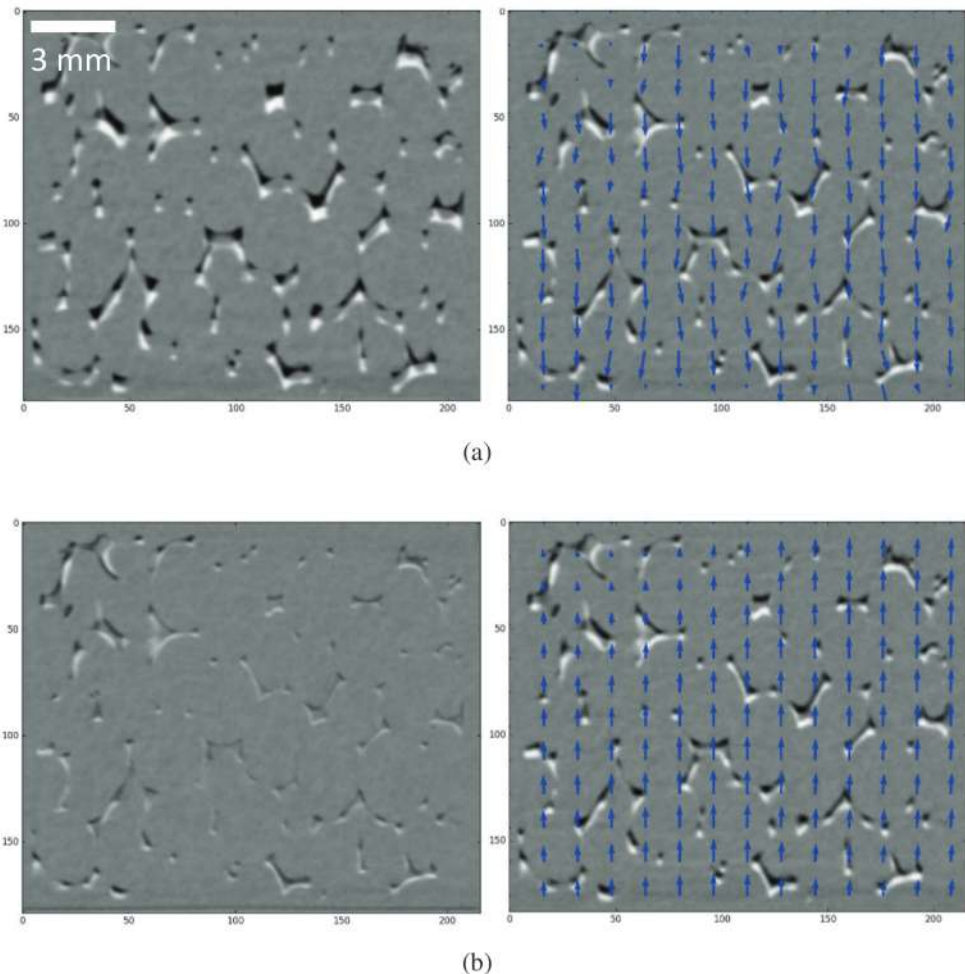


*Figure 5.20: (a) An inverted deformation field caused by a phase wrap in the fine scale levels of the phase flow registration pyramid (pyramid schedule: 5,4,3,2). (b) Leaving out these fine scale yields a valid registration (pyramid schedule: 5,4). The vertical reconstruction slices on the left reflect the registration results as a difference between the first rotation and the third one. On the right these same rotations are depicted in their original (unregistered) state, with the inferred displacement vector field as an overlay.*

interval  $[\tau_f, \tau_m]$ .

An axial reconstruction slice for each of these three scenarios is shown in Figure 5.21, with and without engaging the motion correction scheme (algorithm 3). The vector field, used in this correction is set out on a  $256^3$  grid, which is decimated by a factor of two with respect to the original  $512^3$  reconstruction grid . By incorporating this vector field, the motion blurring artefacts can effectively be eliminated, which is very clear in the second and third reconstruction case, while in the first case there is practically no motion blurring to begin with. As an important note on case 3, it should be mentioned that the reconstruction is actually performed with an ordered subset approach, i.e. OS instead of SART with four projections in each subset. The OS approach is adopted here to avoid the inher-

ent instability of SART at an excessive amount of iterations. As such, due to this alternate OS approach, the improved SNR in case 3 can not solely be attributed to the incorporation of more projections. Finally, in comparing cases 2 and 3 to the first case, which may serve as a ground truth for reconstruction of  $\tau_c$ , there are some residual motion artefacts, which could not be eliminated through the motion corrected reconstructions.

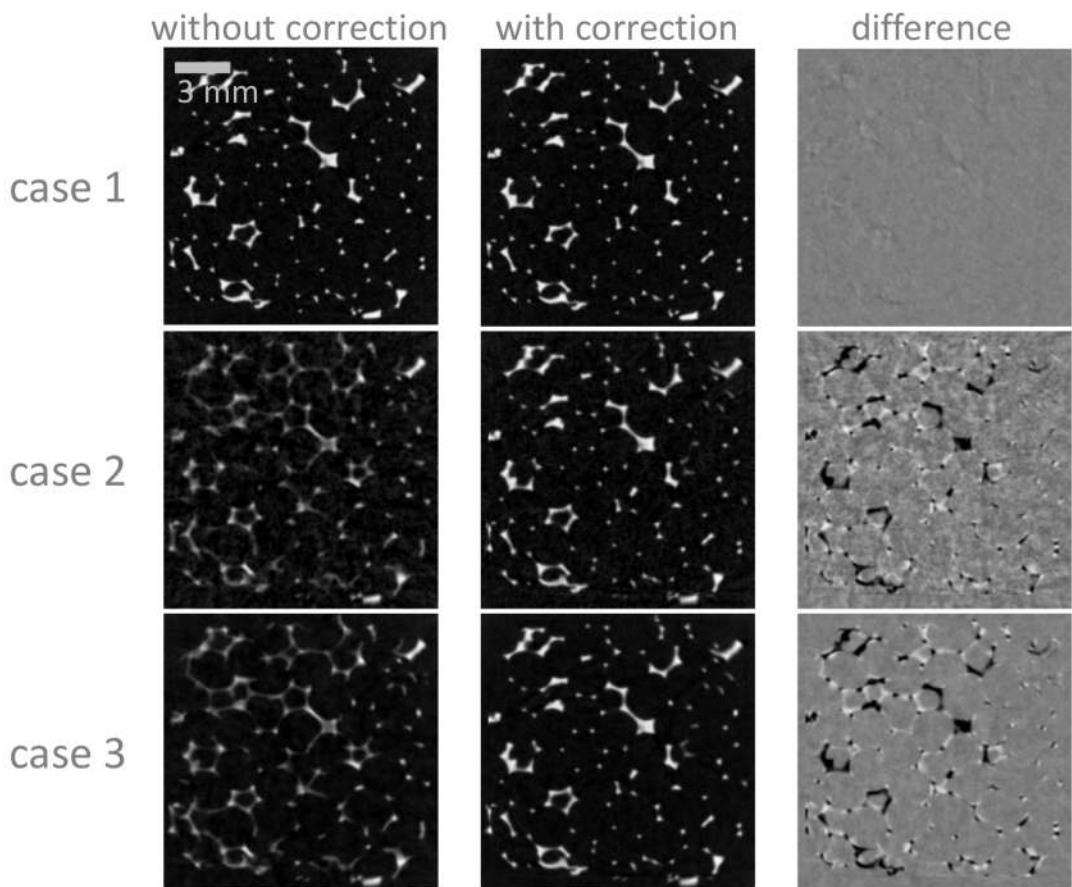


*Figure 5.21: Three cases showing the impact of a motion corrected reconstructions of compressed aluminium foam. From top to bottom: a standard single rotation reconstruction with 700 projections, a reconstruction with 700 projections spread over 14 rotations and a reconstruction with 2800 projections spread over 14 rotations.*

### Deblurring single rotation scans

For the multi-rotation dynamic acquisition above motion correction is not strictly necessary, as the individual rotations already provide a qualitative reconstruction. It is more interesting to test the motion correction scheme in a scenario where the acquisition is effectively too slow to capture the aluminium foam's deformation. To this end a second aluminium foam cube was compressed in the Deben stage at a rate of 0.1 mm/min, while imaging it with a standard, single rotation circular cone

beam scan (see table 5.4). In fact, three datasets were acquired, with an increasing exposure time while keeping the compression rate fixed, which resulted in scans of respectively 4, 8 and 16 minutes. The underlying deformation is thus perceived to be more dynamic, in the sense that the motion blurring artefacts will be more pronounced, as the scan duration increases.

*Table 5.4: Settings for three single rotation acquisition of an in-situ compression of aluminium foam. Only the scan duration is varied by setting different exposure times.*

Tube	Hamamatsu L9181			
	Tube voltage	( $V_t$ )	90	kV
	Tube power	( $P_t$ )	16	W
Detector	Xineos1313			
	Exposure time	( $t_{exp}$ )	(160,320,640)	ms
	Detector size	(W,H)	(658,656)	-
	Binned pixel size	( $p_d$ )	200	$\mu\text{m}$
	Binning	(-)	2 by 2	-
Geometry	Circular cone beam			
	Source Detector Distance	(SDD)	367.02	mm
	Source Object Distance	(SOD)	71.4	mm
	Number of projections	( $N_p$ )	1500	-
	Number of rotations	( $N_r$ )	1	-
	Voxel pitch	( $p_v$ )	39	$\mu\text{m}$
Reconstruction	SART			
	Voxel grid	(W,H,D)	(512,512,512)	-
	SART iterations	(-)	1	-
	Relaxation	( $\lambda$ )	0.5	-
In-situ apparatus	Deben CT5000-TEC			
	Load cell	(-)	1	kN
	Compression rate	(-)	0.1	mm/min

Similar to the beech tree example (section 5.4.2), the goal is now to estimate a deformation field by strategically defining sub-acquisitions in the acquired datasets, that reflect at least two different states of motion of the aluminium foam cube. The logical choice is to assign the fixed and moving frames to the reconstructions of the two short scans, that are separated furthest in time within the bounds of the full rotation, i.e. the angular ranges  $[0, 180^\circ + 2\gamma]$  and  $[180^\circ - 2\gamma, 360^\circ]$ . The maximum compression reached in the 16 min scan, is approximately the same as the compression reached up to the maximum of the B-spline scoring curve in the previous experiment, i.e. 1.6 mm versus 1.75 mm respectively. The 16 min acquisition is thus already situated at the limits of deformation that can be registered with the B-spline technique. Moreover, the fixed and moving images, how they are

defined here, are expected to also show a certain degree of motion blurring, which may hinder the registration step.

In Figure 5.22, a vertical slice for the motion blurred reconstructions of the 4, 8 and 16 minute acquisitions are compared to their motion corrected versions, where the deformation vector field between the short scan sub-acquisitions is incorporated into the reconstructions. Most of the motion blurring artefacts are eliminated, even in the relatively long 16 min scans. However, new artefacts are introduced in the reconstruction of the 16 min acquisition, as the bottom plate of the compression stage enters the registration window. The discrepancy between this large displacing feature, and the implicit assumption of zero displacement at the registration window boundaries, leads to a form of temporal aliasing. In general, most registration techniques fail on the image boundaries, especially when matter enters or exits through them. Indeed, to explain the unexpected loss or gain in image intensity and features, boundary sources and sinks should be incorporated into the registration models, a future development that fits into the discussion of section 5.5.

A logical next step, is to iterate the motion correction approach to gradually eliminate the motion artefacts in the short scan sub-acquisitions. It is plausible to assume that in doing so, better estimates for the deformation vector field can be found at each iteration. However, the deformation vector field did not significantly change from iteration to iteration, implying that its solution is stuck in a flat optimum. As a result, the image quality also did not improve significantly by performing multiple iterations. On the contrary, the aliasing artefacts introduced through a motion correction of the 16 min scan seemed to amplified, and persisted throughout further iterations (Figure 5.23). Intuitively, the flat nature of the deformation field optimum can be explained by considering that the short scan reconstructions are corrected by deformation vector fields, whose estimates are based on these same reconstructions. In the light of consistency, it is logical that more iterations will not produce widely different deformation vector fields, or at least vector fields that will further promote the motion correction. A future, potential improvement may be found in higher order temporal parametrisations of the vector field, i.e. other than (5.28), by taking into account multiple time instances through a short scan window that slides across the entire acquisition.

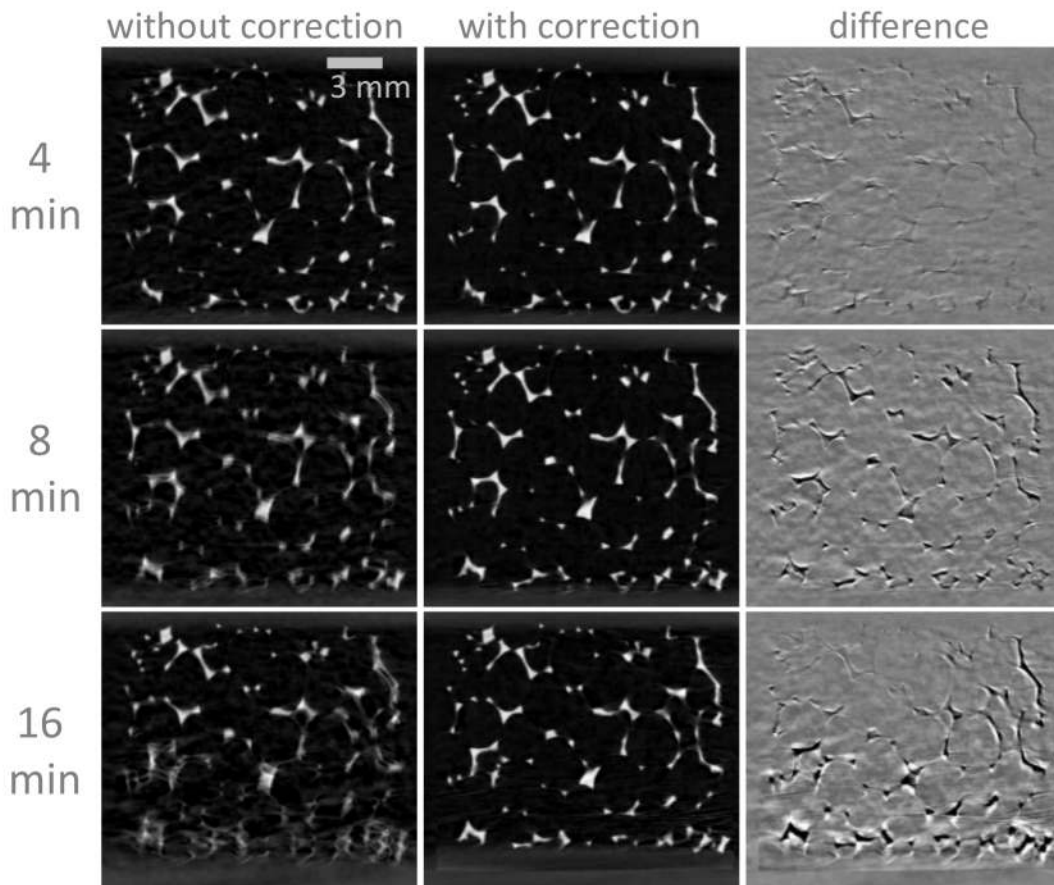


*Figure 5.22: Motion corrected reconstruction of a single rotation acquisition by registering the short scan sub-acquisitions. Most of the motion blurring effects are eliminated, although an aliasing artefact arises for the 16 min acquisition. This can be attributed to the bottom plate of the compression stage that gradually enters the registration window. Most registration techniques can not handle this sudden introduction of extra image features.*

#### 5.4.4 In-situ leavening of dough

##### Dynamic in-situ leavening

In the context of the TomFood project, the UGCT collaborated with KULeuven's Lab4Food in setting up dynamic CT acquisitions to image the internal micro structure of bread dough, while it is leavening. The Lab4Food is interested in how this micro structure is correlated to a tasting panel's perception of food products, that were based on slight variations of a standard recipe or ways of preparing them. Indeed, the micro structure might be changed by these variations, and X-ray  $\mu$ CT is a powerful tool towards understanding how the dynamics of a preparation process lead to a certain micro structure. For example, the bubble formation, during a bread dough's leavening process, can have a significant impact on the bread's quality.

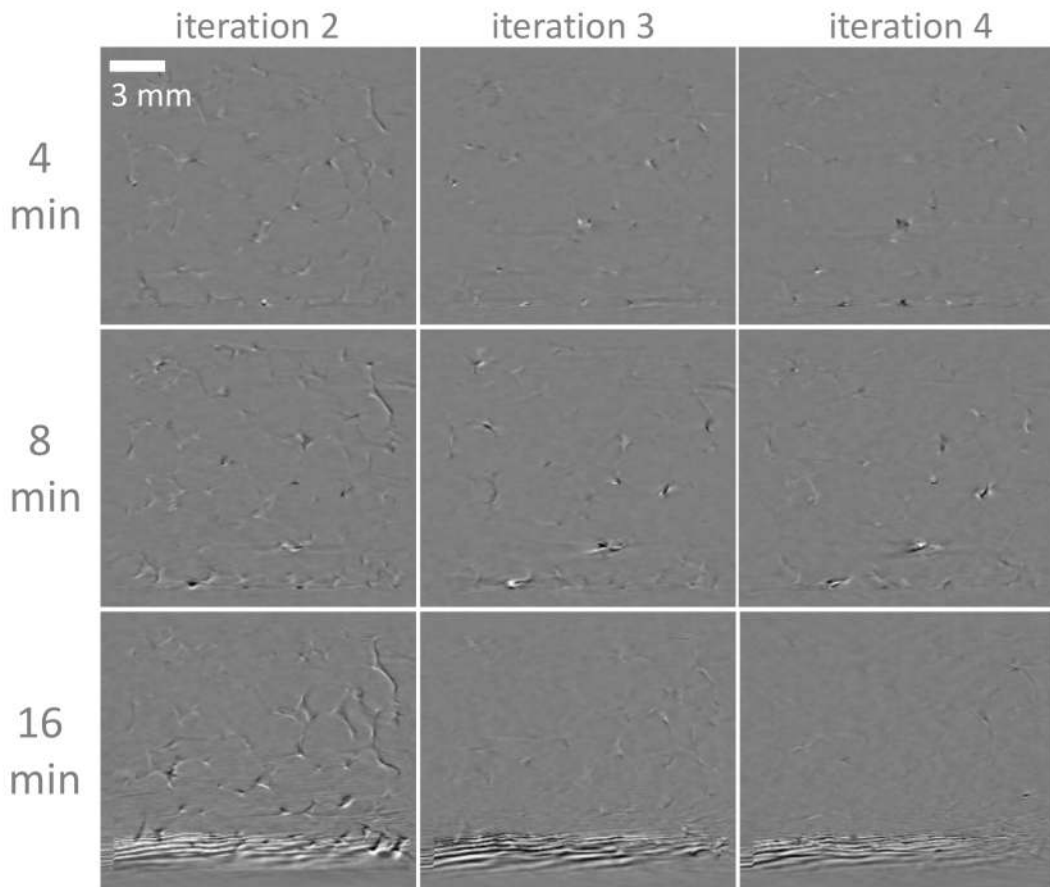


*Figure 5.23: Multiple iterations in a motion corrected reconstruction of a single rotation acquisition. These images show the incremental differences between the results of the current and the previous iterations. By performing multiple rotation the image quality is not significantly improved. Moreover, the temporal aliasing artefacts in the 16 min acquisition are amplified persistently throughout several iterations.*

To investigate this bubble formation, a piece of bread dough was kept at an ideal leavening temperature of 30°C, ready to be imaged according to the protocol presented in table 5.5. As depicted in Figure 5.24, the temperature control stage from section 5.1.1 was modified to hold and heat a bread dough recipient of a representable size. A vertical slice through the last rotation's reconstruction (Figure 5.25) shows no motion blurring, though contrary to the aluminium foam example, the low SNR of the fast 24 second rotations has a recognisable impact on the image quality.

### Comparing registration algorithms

As for the aluminium case, a scoring curves can be generated for the dough acquisition (see Figure 5.26). Again, the B-spline method produces the best results, and

is in fact the only method capable of doing this in a robust way. Both, the Demons and phase flow method can produce a valid deformation field at the finest scales of the registration pyramid schedule. However, the problem is that at these small feature scales only small scale deformations can be tracked effectively, which explains the rapid performance breakdown of the Demons and phase flow methods. The parameters used for the three registration methods are given in table B.2 of appendix B. It also important to note that the scoring curves are set out as a function of time, more precisely the rotation index, since there is no ground truth indication on the overall deformation. The deformation could be estimated from the registration results themselves, but this would only be consistent if the registrations are successful across the entire duration of the acquisition, which is not the case.

In comparing the registrations scores for the leavening dough with the ones of the aluminium foam, it is clear that the former is a more challenging case. This might not be surprising since the dough's deformation is dominated by displacements of small scale features, not much larger than several tens of voxels. Moreover, during the course of the process new features are introduced under the form of bubbles that bloat up to a clearly visible size from actually being invisible at

*Table 5.5: Settings for a dynamic acquisition with in-situ temperature control of a bread dough sample.*

Tube	Hamamatsu L9181			
	Tube voltage	( $V_t$ )	90	kV
	Tube power	( $P_t$ )	27	W
Detector	Xineos1313			
	Exposure time	( $t_{exp}$ )	30	ms
	Detector size	(W,H)	(658,656)	-
	Binned pixel size	( $p_d$ )	200	μm
	Binning	(-)	2 by 2	-
Geometry	Circular cone beam			
	Source Detector Distance	(SDD)	367.02	mm
	Source Object Distance	(SOD)	76.6	mm
	Number of projections	( $N_p$ )	60000	-
	Number of rotations	( $N_r$ )	75	-
	Voxel pitch	( $p_v$ )	41.7	μm
Reconstruction	SART			
	Voxel grid	(W,H,D)	(640,640,640)	-
	SART iterations	(-)	1	-
	Relaxation	( $\lambda$ )	0.5	-
In-situ apparatus	Homemade temperature control stage			
	Temperature	(-)	30	°

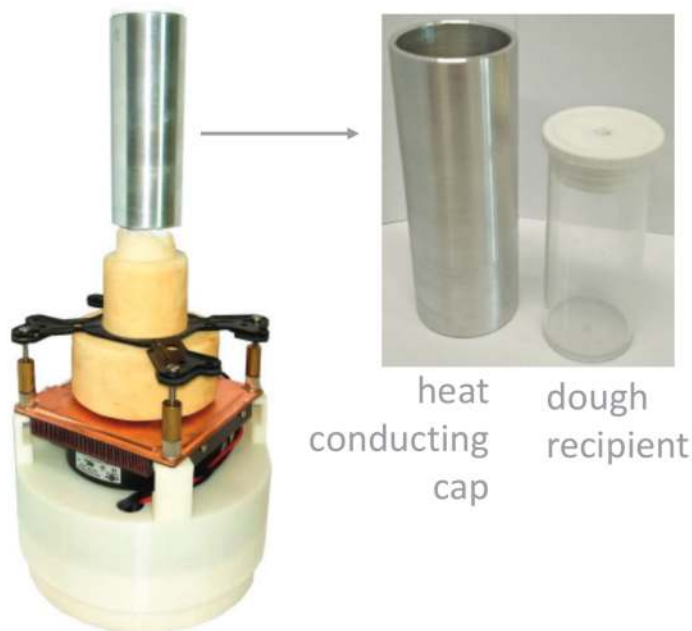


*Figure 5.24: Modification to the temperature control stage, which allows it to heat up dough samples. A dough recipient can be inserted into a heat conductive cap, ensuring a uniform temperature distribution, in this case 30 °C*

the onset of the experiment. Only the B-spline method proved to be robust against this sudden introduction or in this case loss of image intensity. It can however not explain the newly generated (bubble) features (see Figure 5.27), and in fact no registration algorithm purely based on modelling the deformation vector field, which does not include sink or source terms, could.

### Reconstructing an arbitrary set of projections

In the dough leavening case, the B-spline method is able to produce consistent deformation fields up to the 24th rotation, corresponding to an average and maximum displacement magnitude of approximately 287  $\mu\text{m}$  and 1435  $\mu\text{m}$ , respectively . Given the time instances linked to the first and 24th rotation, i.e.  $\tau_f = 400$  and  $\tau_m = 19600$  , the same three reconstruction cases as for the aluminium foam case, are now considered for the reconstruction of time instant  $\tau_c = 10000$ :

- case 1:  $\tau_c$  is reconstructed with the 800 projections from its enclosing rotation, which is the standard approach.
- case 2:  $\tau_c$  is reconstructed using 800 projections, equidistantly sampled across the interval  $[\tau_f, \tau_m]$ .
- case 3:  $\tau_c$  is reconstructed using 3200 projections, which is the equivalent

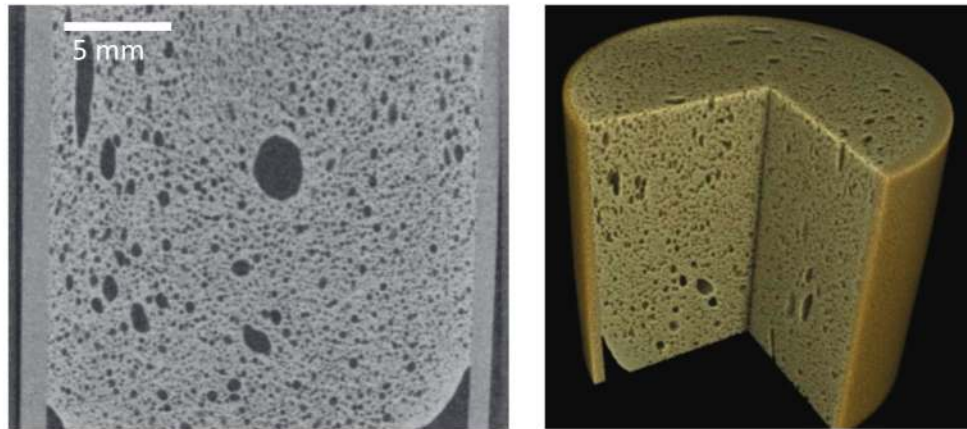


Figure 5.25: Reconstruction of the last rotation in the in-situ dough leavening acquisition, represented in a vertical slice (left) and a 3D rendering (right).

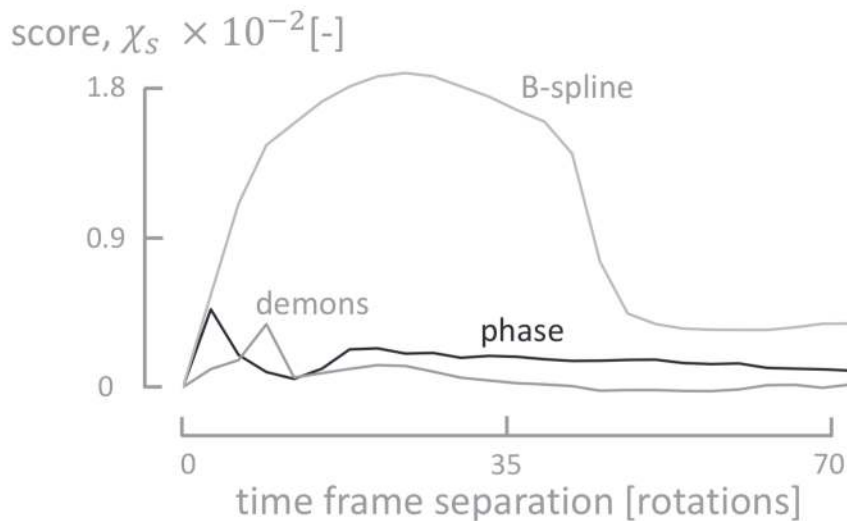
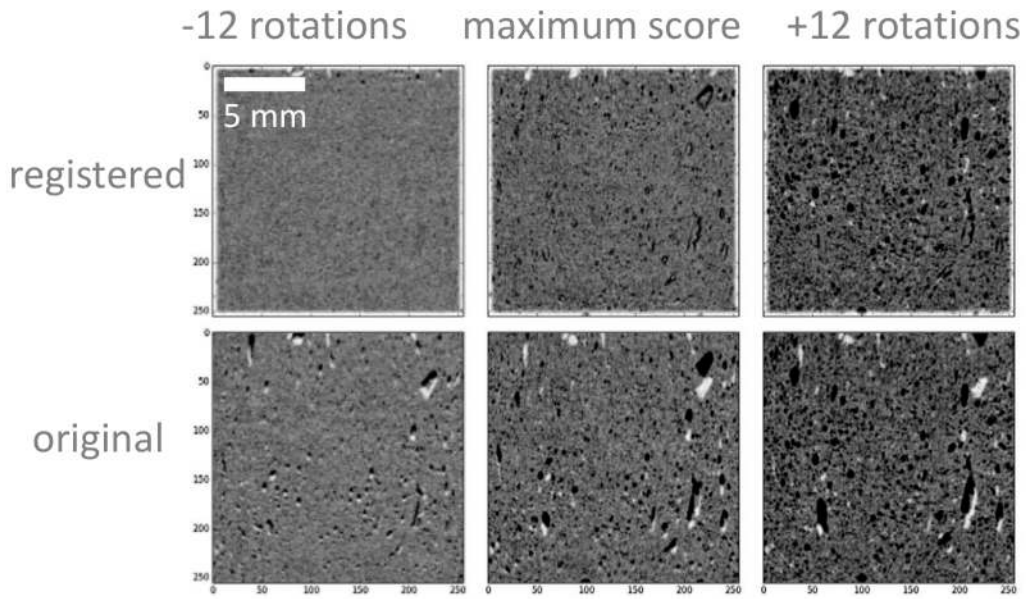


Figure 5.26: Scoring curves for Demons, phase flow and B-spline registration for the leavening dough acquisition. Only the B-spline method yields consistent and robust deformation fields up to high deformations.

of four complete rotations, though again equidistantly spread out across the interval  $[\tau_f, \tau_m]$ .

The deformation field used in these three cases does not cover the entire reconstruction volume. As a result, the motion correction is only active on sub-volume, as shown on the vertical dough reconstruction slices gathered in Figure 5.28. Again, the motion blurring artefacts are significantly reduced in the second and third case. As in the aluminium foam example, case two and three are difficult to compare in terms of SNR, since the SART algorithm intrinsically amplifies high frequency components at each volume update. To compare these cases in a fair way, case two was also reconstructed by looping its 800 projections four times over, instead of the single sweep leading the results in Figure 5.28. By thus ap-



*Figure 5.27: Difference between the moving images and the transformed fixed image at the maximum of the B-spline scoring curve, and twelve rotations before and after the maximum. The B-spline method can robustly estimate a deformation field, even when bubbles are formed during the leavening processes. The bottom row represents the same difference, but with an untransformed fixed image.*

plying the same amount of updates in both cases, it can be seen that case three does indeed provide a better SNR, i.e. 16.4 dB versus 14.6 dB in case two (see Figure 5.29). However, to optimally benefit from the motion correction, it is better to adopt an ordered subset approach, providing a more robust and monotonic convergence.

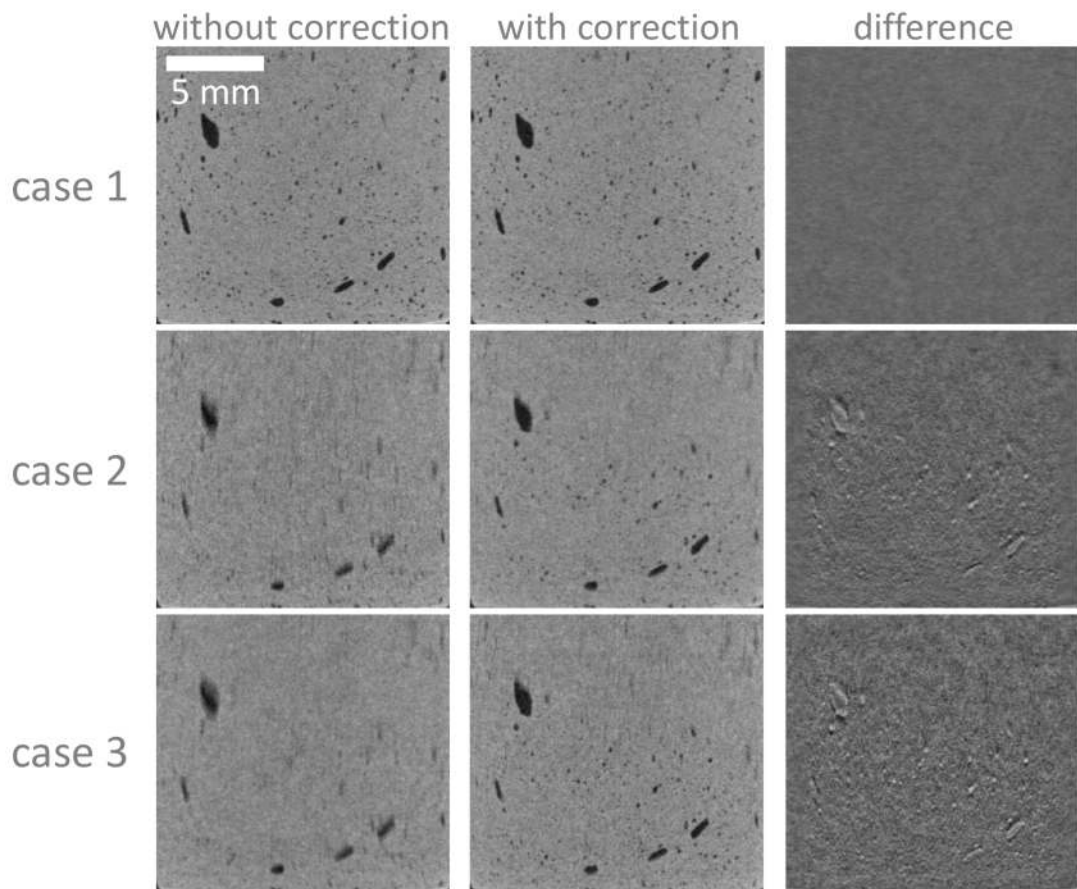


Figure 5.28: Three cases showing the impact of a motion corrected reconstructions of a leavening dough. From top to bottom: a standard single rotation reconstruction with 800 projections, a reconstruction with 800 projections spread over 34 rotations and a reconstruction with 3200 projections spread over 34 rotations.

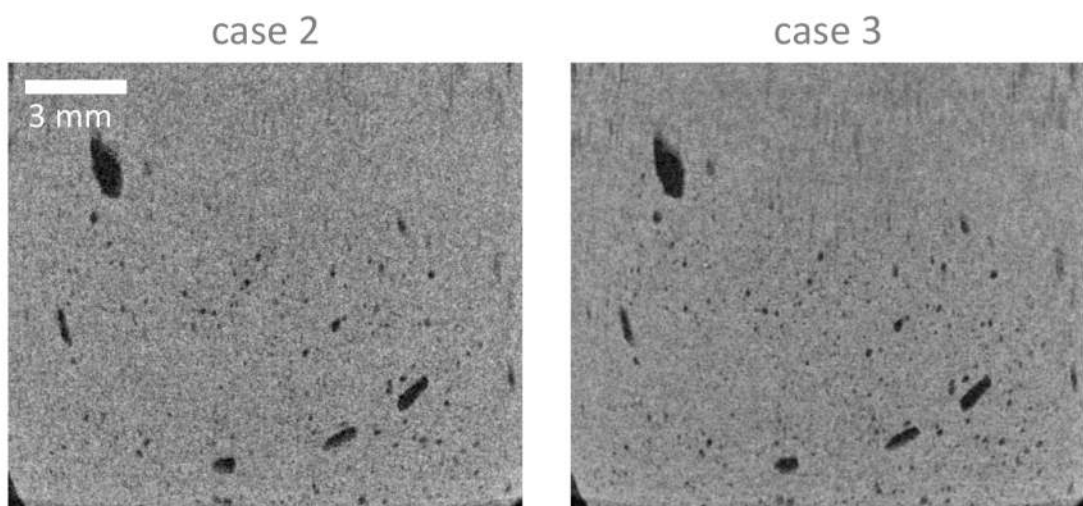


Figure 5.29: Motion corrected leavening dough reconstructions of cases two and three with an equal amount of volume updates. It is clear that in case three the SNR is improved by combining the image statistics of multiple rotations.

## 5.5 An outlook to in-situ 3D characterisation of micro structured materials

Next to their motion corrective potential, registration techniques also show a great potential towards the analysis of a sample's material characteristics. Indeed, a strain tensor can be mapped across an entire sample through a proper differentiation of the deformation vector field. For example, when the strains are small enough, Cauchy's strain tensor can be considered, as given by

$$\begin{aligned}\epsilon_{ij} &= \frac{1}{2} (u_{i,j} + u_{j,i}) \\ &= \begin{bmatrix} \frac{\partial}{\partial x} u_x & \frac{1}{2} \left( \frac{\partial}{\partial y} u_x + \frac{\partial}{\partial x} u_y \right) & \frac{1}{2} \left( \frac{\partial}{\partial z} u_x + \frac{\partial}{\partial x} u_z \right) \\ \frac{1}{2} \left( \frac{\partial}{\partial x} u_y + \frac{\partial}{\partial y} u_x \right) & \frac{\partial}{\partial y} u_y & \frac{1}{2} \left( \frac{\partial}{\partial z} u_y + \frac{\partial}{\partial y} u_z \right) \\ \frac{1}{2} \left( \frac{\partial}{\partial x} u_z + \frac{\partial}{\partial z} u_x \right) & \frac{1}{2} \left( \frac{\partial}{\partial y} u_z + \frac{\partial}{\partial z} u_y \right) & \frac{\partial}{\partial z} u_z \end{bmatrix},\end{aligned}\quad (5.31)$$

where in the first line the Einstein notation is adopted. This is how local, non-rigid registration was initially exploited in the context of µCT, as apparent from the literature introduced in section 5.4.1. By going one step further, a stress field can be deduced, e.g by adopting a linear elastic and isotropic material model [71]

$$\sigma_{ij} = \frac{E}{1+\nu} \left( \frac{\nu}{1-2\nu} \epsilon_{kk} \delta_{ij} + \epsilon_{ij} \right) \quad (5.32)$$

where  $E$  and  $\nu$  respectively denote '*Young's modulus*' and '*Poisson's ratio*'. By fixing these parameters a stress tensor field, and specifically its scalar invariants can be visualised, like the '*von Mises stress*' depicted in Figure 5.30. In order to produce this figure, a simple linear relation between the material parameters and the X-ray attenuation coefficient is considered

$$E(\mu) = E_{max} \frac{\mu}{\mu_{max}} \quad (5.33)$$

$$\nu(\mu) = \nu_{max} \frac{\mu}{\mu_{max}} \quad (5.34)$$

reflecting the intuitive notion that a stiffer and less compressible material will also appear denser on an X-ray CT image. For the aluminium foam in Figure 5.30,  $E_{max}$  and  $\nu_{max}$  were set to 69 GPa and 0.3, respectively [72]. But, as the constitutive behaviour proposed by (5.33) and (5.34) are in no way validated, the von Mises stresses in Figure 5.30 have been normalised to their maximal values, making the exact values for  $E_{max}$  and  $\nu_{max}$  irrelevant. In other words, for the moment only qualitative conclusions can be drawn from Figure 5.30, like the fact that stresses tend to build up at interfaces, which are in contact with the compression

plates.

In a next step, the compression process can be simulated, e.g. with the finite element method (FEM), in order to cross validate the deformation inferred through X-ray CT images. To set up such a FEM-model, first of all the structures in its computational domain have to be meshed, cfr. Figure 5.31. While the completion of this aluminium foam FEM-model with accurate material models and boundary conditions is still an ongoing effort, it is important at this point to recognise the potential synergy between these kind of advanced process models and the dynamic CT images that can visualise them. On the one hand, the deformation fields obtained through CT registration can be used to pinpoint the material parameters, leading to a consistent FEM-model deformation field, while on the other hand the FEM-model's deformation fields can also serve as an initial estimate in the registration procedure itself. The deformation field and the material parameters can thus be subjected to an iterative optimisation, which loops between a deformation estimation step and a FEM-model parameter estimation step. This last step opens up a new prospect to CT imaging, possibly in combination with other modalities, towards shifting the focus from a simple reconstruction of attenuation values, to characterising mechanical material properties. The framework presented here is set out for a mechanical deformation, but it can also be built around other physical processes, to the extent that the aspects pertaining to their modelling can be linked

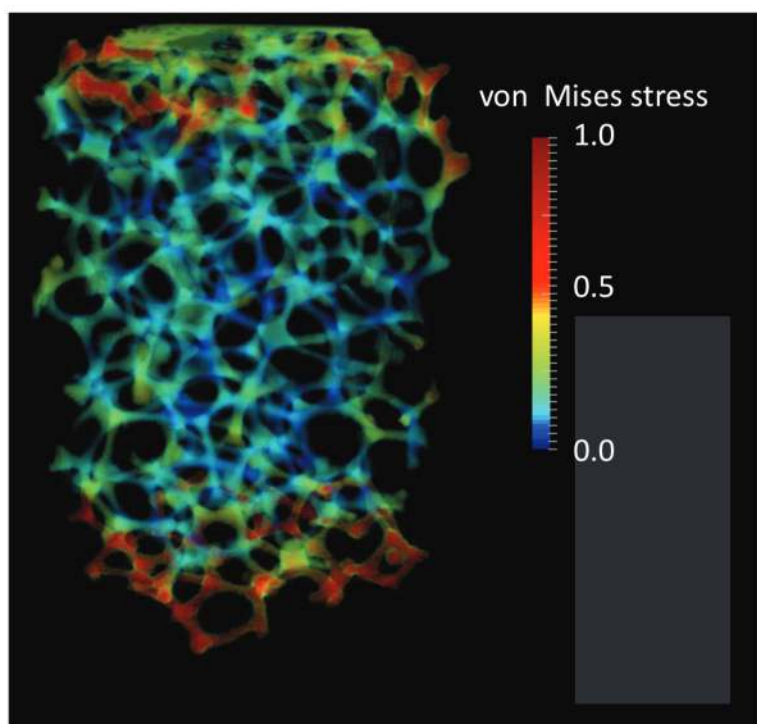
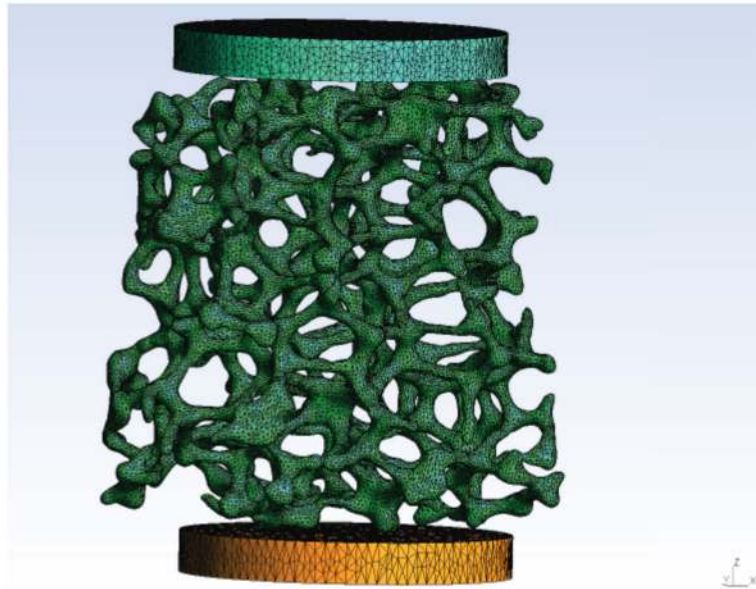


Figure 5.30: von Mises stress distribution in a compressed aluminium foam. Stresses tend to build up at the compression plate interfaces.

to image properties or changes therein. Equations (5.33) and (5.34) are specific examples of such a link, under the form of a constitutive relation between the imaged quantity and the material model parameters, which effectively reduces the number of parameters in the model.



*Figure 5.31: Example of a tetrahedral finite element mesh of an aluminium foam.*

## 5.6 Conclusion

In this chapter, a dynamic evolution of a sample's attenuation distribution during a CT acquisition, is considered, and while many processes can initiate this evolution in time, the focus is put here on local and non-rigid mechanical deformations. When left unchecked, these deformations cause motion blurring artefacts in the resulting CT reconstructions, which in first instance can be reduced by performing faster CT scans. However, faster scanning also produces an abundant amount of data, and only helps to the extent that a deformation process's speed does not exceed a scanner's mechanical limitations, on e.g. the gantry's rotation speed; or, more importantly, in so far the fast acquisitions do not lead to an inadequate CT image SNR, as a result of physical limitations on the lab-based source's X-ray flux. Particularly in these borderline scenarios, motion blurring can not be avoided, unless a motion corrected reconstruction is applied. This chapter presents a motion corrected version of the SART reconstruction algorithm through an alteration of its projection and back projection steps, which involves a virtual, local and non-rigid displacement of the ray sampling points and back projection points, respectively.

Three popular registration strategies to estimate these local, non-rigid defor-

mations, namely the Demons, optical phase flow and B-spline approaches, were discussed and evaluated on CT acquisition of dynamic deformation processes, that to some extent can be controlled with in-situ devices. In both the aluminium foam compression and dough leavening cases, the B-spline method proved to be the best and most robust option to estimate deformation fields, across a wide range of feature scales, and is thus the preferred method to generate the deformation fields, used in the motion corrected SART approach. As demonstrated through several cases, motion corrected SART can effectively eliminate motion blurring artefacts up to very large deformations, even with a simple time linear scaling of the motion vector fields ((5.28)). The motion correction also proved to be successful when the sub-acquisitions, that are used as a basis for the registration are also affected by motion blurring, e.g. short scan portions of a full rotation scan. With this prospect new CT protocols can be devised, that can tolerate a significant degree of sample motion, as long as this motion can be estimated from at least two strategically chosen sub-acquisitions.

Finally, the most promising aspect of performing local, non-rigid registration on acquisitions of a dynamic in-situ controllable deformation, can be found in its combination with an in-depth modelling of the deformation itself, e.g. through finite element models. By doing this, X-ray  $\mu$ CT could be elevated from a simple attenuation imaging technique, to a way of characterising a sample's material properties at a micro-structure level. Moreover, this paradigm of combining modelling and imaging is not limited to mechanical deformation and  $\mu$ CT imaging, as long as the results of a process model and its relevant parameters can be correlated to the values, structures and derived features visualised with the imaging technique.

## References

- [1] S M Walker, D A Schwyn, R Mokso, M Wicklein, T Müller, M Doube, M Stampanoni, H G Krapp, and G K Taylor. *In Vivo Time-Resolved Microtomography Reveals the Mechanics of the Blowfly Flight Motor*. PLoS Biology, 12(3):e1001823, mar 2014.
- [2] E Maire and P J Withers. *Quantitative X-ray tomography*. International Materials Reviews, 59(1):1–43, 2014.
- [3] T Bultreys, M A Boone, M N Boone, T De Schryver, B Masschaele, L Van Hoorebeke, and V Cnudde. *Fast laboratory-based micro-computed tomography for pore-scale research: Illustrative experiments and perspectives on the future*. Advances in Water Resources, i:1–11, 2015.
- [4] M Dierick, D Van Loo, B Masschaele, J Van den Bulcke, J Van Acker, V Cnudde, and L Van Hoorebeke. *Recent micro-CT scanner developments at UGCT*. Nuclear Instruments and Methods in Physics Research Section B: Beam Interactions with Materials and Atoms, 324:35–40, 2014.
- [5] T Bultreys, M A Boone, M N Boone, T De Schryver, B Masschaele, D Van Loo, L Van Hoorebeke, and V Cnudde. *Real-time visualization of Haines jumps in sandstone with laboratory-based microcomputed tomography*. Water Resources Research, 51(10):8668–8676, 2015.
- [6] T De Schryver, M A Boone, T De Kock, B Duquenne, M Christaki, B Masschaele, M Dierick, M N Boone, and L Van Hoorebeke. *A compact low cost cooling stage for lab based X-ray micro-CT setups*. AIP Conference Proceedings, 1696:0–5, 2016.
- [7] R W Powell, Cho Yen Ho, and Peter Edward Liley. *Thermal conductivity of selected materials*. Technical report, DTIC Document, 1966.
- [8] M J Berger, J H Hubbell, S M Seltzer, J Chang, J S Coursey, R Sukumar, D S Zucker, and K Olsen. *XCOM: Photon Cross Section Database (version 1.5)*. <http://physics.nist.gov/xcom>, 2010.
- [9] R G Sheppard, D M Mathes, and Bray D J. *Thermal Conductivity*, pages 13.1–13.2. Poco Graphite, Inc., Decatur, TX, 2015.
- [10] Arduino. <https://www.arduino.cc/>.
- [11] M Dierick, D Van Loo, B Masschaele, M N Boone, and L Van Hoorebeke. *A LabVIEW® based generic CT scanner control software platform*. JOURNAL OF X-RAY SCIENCE AND TECHNOLOGY, 18(4):451–461, 2010.

- [12] B Duquenne, B Vergauwen, C Capdepon, M A Boone, T De Schryver, L Van Hoorebeke, S Van Weyenberg, P Stevens, and J De Block. *Stabilising frozen dairy mousses by low molecular weight gelatin peptides.* Food Hydrocolloids, 60:317–323, 2016.
- [13] T De Kock, M A Boone, T De Schryver, J Van Stappen, H Derluyn, B Masschaele, G De Schutter, and V Cnudde. *A pore-scale study of fracture dynamics in rock using X-ray micro-CT under ambient freeze-thaw cycling.* Environmental Science & Technology, 49(5):2867–2874, 2015.
- [14] H Derluyn, M A Boone, M N Boone, T De Schryver, B Masschaele, T De Kock, and V Cnudde. *Visualization and characterization of 3D crystal growth.* In CrysPoM IV : the 4th international workshop on crystallization in porous media, page 28, 2014.
- [15] S Klein, M Staring, K Murphy, M A Viergever, and J P W Pluim. *Elastix: A toolbox for intensity-based medical image registration.* IEEE Transactions on Medical Imaging, 29(1):196–205, 2010.
- [16] D Fleet and Y Weiss. *Optical Flow Estimation.* Mathematical models for Computer Vision: The Handbook, pages 239–257, 2005.
- [17] P Thévenaz, U E Ruttmann, and M Unser. *A Pyramid Approach to Subpixel Registration Based on Intensity.* IEEE Transactions on Image Processing, 7(1):27–41, 1998.
- [18] G P Penney, J Weese, J a Little, P Desmedt, D L Hill, and D J Hawkes. *A comparison of similarity measures for use in 2-D/3-D medical image registration.* IEEE transactions on medical imaging, 17(4):586–595, 1998.
- [19] P Thévenaz, M Unser, and P Thevenaz. *Optimization of mutual information for multiresolution image registration.* IEEE Transactions on Image Processing, 9(12):2083–2099, 2000.
- [20] J P W Pluim, J B a Maintz, and M Viergever. *Mutual information based registration of medical images: a survey.* IEEE Transactions on medical imaging, XX(Y):1–21, 2003.
- [21] K Madi, G Tozzi, Q H Zhang, J Tong, A Cossey, A Au, D Hollis, and F Hild. *Computation of full-field displacements in a scaffold implant using digital volume correlation and finite element analysis.* Medical engineering & physics, 35(9):1298–312, sep 2013.
- [22] M Palanca, G Tozzi, L Cristofolini, M Viceconti, and E Dall'Ara. *Three-Dimensional Local Measurements of Bone Strain and Displacement: Comparison of Three Digital Volume Correlation Approaches.* Journal of Biomechanical Engineering, 137(7):71006, jul 2015.

- [23] G Farneback. *Very high accuracy velocity estimation using orientation tensors, parametric motion, and simultaneous segmentation of the motion field.* In Proceedings Eighth IEEE International Conference on Computer Vision. ICCV 2001, volume 1, pages 171–177 vol.1, 2001.
- [24] J L Barron, D J Fleet, and S S Beauchemin. *Performance of optical flow techniques.* International Journal of Computer Vision, 12(1):43–77, 1994.
- [25] J P Thirion. *Image matching as a diffusion process: an analogy with Maxwell's demons.* Medical image analysis, 2(3):243–260, 1998.
- [26] X Pennec, P Cachier, and N Ayache. *Understanding the Demon's Algorithm: 3D non-rigid registration by gradient descent.* International Conference on Medical Image Computing And Computer-Assisted Intervention (MICCAI), 1679:597–605, 1999.
- [27] T Vercauteren, X Pennec, A Perchant, and N Ayache. *Symmetric Log-Domain Diffeomorphic Registration: A Demons-Based Approach*, pages 754–761. Springer Berlin Heidelberg, Berlin, Heidelberg, 2008.
- [28] F Dru, P Fillard, and T Vercauteren. *An ITK Implementation of the Symmetric Log-Domain Diffeomorphic Demons Algorithm.* Insight Journal, pages 1–10, 2010.
- [29] T S Yoo, Michael J Ackerman, W E Lorensen, W Schroeder, V Chalana, S Aylward, D Metaxas, and R Whitaker. *Engineering and Algorithm Design for an Image Processing API: A Technical Report on ITK - the Insight Toolkit.* Studies in Health Technology and Informatics, 85:586–592, 2002.
- [30] B C Loweckamp, D T Chen, L Ibáñez, and D Blezek. *The Design of SimpleITK.* Frontiers in neuroinformatics, 7(December):45, 2013.
- [31] T Vercauteren, X Pennec, A Perchant, and N Ayache. *Non-parametric Diffeomorphic Image Registration with the Demons Algorithm.* Medical image computing and computer-assisted intervention, 10(Pt 2):319–326, 2007.
- [32] D J Fleet and A D Jepson. *Stability of phase information.* IEEE Transactions on Pattern Analysis and Machine Intelligence, 15(12):1253–1268, 1993.
- [33] I W Selesnick, R G Baraniuk, and N C Kingsbury. *The dual-tree complex wavelet transform.* IEEE Signal Processing Magazine, 22(6):123–151, nov 2005.
- [34] Bart Goossens. *Multiresolution image models and estimation techniques.* PhD thesis, Ghent University, 2010.

- [35] Jan Aelterman. *Multiresolution models in image restoration and reconstruction with medical and other applications*. PhD thesis, Ghent University, 2014.
- [36] A Grossmann and J Morlet. *Decomposition of Hardy Functions into Square Integrable Wavelets of Constant Shape*. SIAM Journal on Mathematical Analysis, 15(4):723–736, jul 1984.
- [37] I Daubechies. *The wavelet transform, time-frequency localization and signal analysis*. Information Theory, IEEE Transactions on, 36(5):961–1005, 1990.
- [38] I Daubechies. *Orthonormal Bases of Compactly Supported Wavelets II. Variations on a Theme*. SIAM Journal on Mathematical Analysis, 24(2):499–519, 1993.
- [39] M Hemmendorff, M T Andersson, T Kronander, and H Knutsson. *Phase-based multidimensional volume registration*. IEEE transactions on medical imaging, 21(12):1536–43, dec 2002.
- [40] H Chen and N Kingsbury. *Efficient registration of nonrigid 3-D bodies*. IEEE transactions on image processing : a publication of the IEEE Signal Processing Society, 21(1):262–72, jan 2012.
- [41] R Wareham, S Forshaw, and T Roberts. *dtcwt: a Python Dual Tree Complex Wavelet Transform Library*. Zenodo, 2016.
- [42] K Marstal, F Berendsen, M Staring, and S Klein. *SimpleElastix : A user-friendly , multi-lingual library for medical image registration*. International Workshop on Biomedical Image Registration (WBIR), 2016.
- [43] Stefan Klein, Josien P W Pluim, Marius Staring, and Max A. Viergever. *Adaptive stochastic gradient descent optimisation for image registration*. International Journal of Computer Vision, 81(3):227–239, 2009.
- [44] S Bonnet, A Koenig, S Roux, P Hugonnard, R Guillemaud, and P Grangeat. *Dynamic X-ray computed tomography*. Proceedings of the IEEE, 91(10):1574–1587, 2003.
- [45] P M Joseph. *An Improved Algorithm for Reprojecting Rays through Pixel Images*. IEEE transactions on medical imaging, 1(3):192–196, 1982.
- [46] A a Isola, M Grass, and W J Niessen. *Fully automatic nonrigid registration-based local motion estimation for motion-corrected iterative cardiac CT reconstruction*. Medical physics, 37(3):1093–1109, 2010.

- [47] A A Isola, A Ziegler, T Koehler, W J Niessen, and M Grass. *Motion-compensated iterative cone-beam CT image reconstruction with adapted blobs as basis functions*. Physics in Medicine and Biology, 53(23):6777–6797, dec 2008.
- [48] B K Bay, T S Smith, D P Fyhrie, and M Saad. *Digital volume correlation: three-dimensional strain mapping using X-ray tomography*. Experimental mechanics, 39(3):217–226, 1999.
- [49] L Liu and E F Morgan. *Accuracy and precision of digital volume correlation in quantifying displacements and strains in trabecular bone*. Journal of Biomechanics, 40(15):3516–3520, 2007.
- [50] G Kerckhofs, S Van Bael, M Moesen, and F Maes. *Novel micro-CT based local strain mapping tool to characterize the failure modes of bone tissue engineering scaffolds*. In Skyscan User Meeting, pages 43–45, Skyscan N.V., Kontich, Belgium, 2009.
- [51] I Jandejsek, O Jirousek, and D Vavrik. *Precise strain measurement in complex materials using digital volumetric correlation and time lapse micro-CT data*. Procedia Engineering, 10:1730–1735, 2011.
- [52] B C Roberts, E Perilli, and K J Reynolds. *Application of the digital volume correlation technique for the measurement of displacement and strain fields in bone: A literature review*. Journal of Biomechanics, 47(5):923–934, 2014.
- [53] F Forsberg, R Mooser, M Arnold, E Hack, and P Wyss. *3D micro-scale deformations of wood in bending: Synchrotron radiation  $\mu$ CT data analyzed with digital volume correlation*. Journal of Structural Biology, 164(3):255–262, 2008.
- [54] T Ohgaki, H Toda, M Kobayashi, K Uesugi, T Kobayashi, M Niinomi, T Akahori, K Makii, and Y Aruga. *In-situ high-resolution X-ray CT observation of compressive and damage behaviour of aluminium foams by local tomography technique*. Advanced Engineering Materials, 8(6):473–475, 2006.
- [55] T S Smith, B K Bay, and M M Rashid. *Digital Volume Correlation Including Rotational Degrees of Freedom during Minimization*. Experimental Mechanics, 42(3):272–278, 2002.
- [56] E Verhulp, B Van Rietbergen, and R Huiskes. *A three-dimensional digital image correlation technique for strain measurements in microstructures*. Journal of Biomechanics, 37(9):1313–1320, 2004.

- [57] A Bouterf, S Roux, F Hild, J Adrien, E Maire, and S Meille. *Digital volume correlation applied to X-ray tomography images from spherical indentation tests on lightweight gypsum*. Strain, 50(5):444–453, 2014.
- [58] S Schlueter, F Leuther, S Vogler, and H-J Vogel. *X-ray microtomography analysis of soil structure deformation caused by centrifugation*. Solid Earth Discussions, 7(4):2807–2831, 2015.
- [59] S A Hall, M Bornert, J Desrues, Y Pannier, N Lenoir, G Viggiani, and P Bésuelle. *Discrete and continuum analysis of localised deformation in sand using X-ray  $\mu$ CT and volumetric digital image correlation*. Géotechnique, 60(5):315–322, may 2010.
- [60] A Van Ende, E Van de Casteele, M Depypere, J De Munck, X Li, F Maes, M Wevers, and B Van Meerbeek. *3D volumetric displacement and strain analysis of composite polymerization*. Dental materials : official publication of the Academy of Dental Materials, 31(4):453–61, apr 2015.
- [61] M Prümmer, L Wigström, J Hornegger, J Boese, G Lauritsch, N Strobel, and R Fahrig. *Cardiac C-arm CT: Efficient motion correction for 4D-FBP*. IEEE Nuclear Science Symposium Conference Record, 4:2620–2628, 2007.
- [62] C P V Christoffersen, D Hansen, P Poulsen, and T S Sorensen. *Registration-based reconstruction of four-dimensional cone beam computed tomography*. IEEE Transactions on Medical Imaging, 32(11):2064–2077, 2013.
- [63] G Van Eyndhoven, J Sijbers, and J Batenburg. *Combined motion estimation and reconstruction in tomography*. Lecture Notes in Computer Science, 7583 LNCS(PART 1):12–21, 2012.
- [64] V Van Nieuwenhove, J De Beenhouwer, J Vlassenbroeck, M Moesen, M Brennan, and J Sijbers. *Registration Based SIRT : A reconstruction algorithm for 4D CT*. In Industrial Computed Tomography Conference, Leuven, Belgium, 2017.
- [65] T DE Schryver, J Van Stappen, M A Boone, M N Boone, M Dierick, V Cnudde, and L Van Hoorebeke. *4D visualisation of in-situ aluminium foam compression with lab-based motion compensated X-ray micro-CT*. In Industrial Computed Tomography Conference, Leuven, Belgium, 2017.
- [66] L L Vergeynst, M Dierick, J A N Bogaerts, V Cnudde, and K Steppe. *Cavitation: A blessing in disguise? New method to establish vulnerability curves and assess hydraulic capacitance of woody tissues*. Tree Physiology, 35(4):400–409, 2015.

- [67] L J Gibson. *Biomechanics of cellular solids.* Journal of Biomechanics, 38(3):377–399, 2005.
- [68] B K Bay. *Methods and applications of digital volume correlation.* The Journal of Strain Analysis for Engineering Design, 43(8):745–760, 2008.
- [69] M F Ashby. *Metal foams : a design guide.* Butterworth-Heinemann, 2000.
- [70] S De Schampheleire, P De Jaeger, K De Kerpel, B Ameel, H Huisseune, and M De Paepe. *How to study thermal applications of open-cell metal foam: Experiments and computational fluid dynamics.* Materials, 9(2):1–27, 2016.
- [71] L D Landau, E M Lifshits, A M Kosevich, and L P Pitaevskii. *Theory of elasticity.* Butterworth-Heinemann, 1986.
- [72] The Engineering Toolbox. <http://www.engineeringtoolbox.com>.



# 6

## Conclusion & Outlook

As a reminder, the developments presented in this work all fit within the unifying premise of **fast CT imaging using non-standard geometries and protocols**, with the goal of

- bringing X-ray CT to an in-line setting as a non-destructive quality inspection tool, i.e. in-line CT, and
- improving the visualisation of dynamic processes, specifically pertaining to local and non-rigid structural changes of an imaged object, i.e. 4D-CT.

CT imaging in both of these applications does indeed have to be fast, in the former case because the in-line CT apparatus should be able to keep up with a high throughput conveyor belt, while in the latter case the 4D-CT acquisition's temporal resolution has to match the time constants of the dynamic deformation process. Also, in both applications the CT geometry is non-standard, either at the level of the sample's trajectory or its state of local, non-rigid deformation. The fundamental difference is that in the in-line CT case the non-standard character is introduced by design, through the so-called '*conveyor belt geometry*', while in the 4D-CT case it is an intrinsic consequence of the dynamic process.

The conveyor belt geometry was introduced as an alternative approach towards a feasible quality inspection with X-ray CT. A particular advantage of this geometry is that it can be readily plugged into an existing conveyor belt configuration. Moreover, it subjects the imaged sample to a trajectory, that produces Tuy-Smith

sufficient CT datasets and thus exact CT reconstructions. While theoretically sound, CT data had to be generated for the conveyor belt geometry in order to properly evaluate its performance in terms of throughput and image quality. This is why a first order model for radiography simulation was ported to a Graphical Processing Unit, with a specific focus on accurately capturing the polychromatic nature and noise characteristics of the radiography technique. Furthermore, a flexible description of the scanner component's geometric configuration made it possible to simulate CT acquisition in arbitrary geometries, such as the conveyor belt setup. In a next step, both these simulated acquisitions and real life data, obtained through mock-up realisation of the conveyor belt geometry, were reconstructed to form a 3D representation of the scanned object. For this to work, an ordered subset iterative reconstruction technique was coded in Python-CUDA tool, with the ability to reconstruct data coming from arbitrary CT geometries. By evaluating the quality of these reconstructions, by estimating their apparent resolution through Fourier shell correlation and the Spectral Signal to Noise Ratio, it could finally be concluded that in-line quality inspection with CT is indeed a feasible endeavour, although it needs to be mentioned that this study was conducted for one particular type of sample.

Looking at the broader picture, the combination of a simulated acquisition, a flexible reconstruction and a valid quantitative form of evaluation, forms a solid methodology towards the optimisation of throughput with respect to image quality for the conveyor belt geometry, though not limited thereto. This methodology on its own is not new, but there are some interesting prospects towards exploiting its parts and the synergy between them. For one, the spectral resolution metrics form a new and fair way to evaluate and replace the somewhat arbitrary voxel size as an indication for a reconstruction's resolution. They do this by measuring how strongly each frequency component in an image distinguishes itself from background noise, and as such determine which of the frequencies are relevant. This is a powerful notion that can be coupled back to the design of reconstruction filters (e.g. Figure 3.3). In other words, there is an interesting synergy between the reconstruction and evaluation components. Such a synergy also exists between the simulation and reconstruction components, particularly when iterative reconstruction algorithms are considered. The first order polychromatic model can for instance be introduced as an improved forward projection model in the iterative scheme, with the prospect of eliminating beamhardening artefacts, or more importantly, improving the reconstruction of multi-spectral datasets.

This tight integration of iterative reconstruction with better models was also demonstrated in the CT reconstruction of dynamically deforming objects. Out of three registration methods, the B-spline approach was identified as the most robust

and accurate way to estimate an object's deformation, based on two strategically chosen acquisitions, producing a valid reconstruction of the object. By incorporating the estimated deformation fields into the iterative reconstruction, motion blurring artefacts could effectively be eliminated in the applications discussed throughout chapter 5. This provides a new option towards avoiding motion blurring, other than simply scanning faster to the extent that this would be technically possible. As a result, a new type of CT protocol, which tolerates a certain degree of motion blurring, could be devised. Including the deformation fields is another example of how the iterative techniques can be augmented to provide better reconstructions. But in fact, an analytical technique, such as FDK, could also benefit from the deformation estimates by simply incorporating the motion fields in its back projection step.

A final interesting prospect is that the deformation fields can be used to study the material characteristics of the imaged object. Strain and even stress fields can be derived from them by adopting a proper material model. On the other hand, the dynamic process can be modelled, e.g. through finite element analysis. First of all, this provides an opportunity to cross validate the deformation fields obtained through imaging and modelling, but foremost the forced consistency between these fields implies that a valid material model with correctly set parameters is used. In other words, the images could be used to infer the material parameters, and vice versa the modelled deformation field could be plugged back into the image based deformation estimation. This is only an example of how a thorough modelling of dynamic processes, not necessarily limited to mechanical deformation, can be combined with 3D imaging, not necessarily limited to X-ray CT. As a future prospect, the tight integration of advanced numerical models for dynamic processes with 3D X-ray CT imaging should be investigated, with the potential of elevating X-ray CT from a simple visualisation of attenuation to a 3D dynamic material characterisation.



# A

## Machine specifications

All of the calculations in this work are performed on a workstation for which the specifications are outlined in table A.1.

*Table A.1: Workstation specifications.*

CPU	Intel Core i7 4770K	
	Base clock	3.5 Hz
	Cores	4
CPU RAM	Corsair CMZ32GX3M4X1600	
	Type	DDR3
	Capacity	32 GB
	Clock	1600 Hz
GPU	NVIDIA GeForce Titan GTX	
	Base clock	837 Hz
	Cores	2688
GPU RAM		
	Type	GDDR5
	Capacity	6144 MB
	Clock	1502 Hz



# B

## Registration parameters

The parameters used in the registration calculations throughout section 5.4 are listed below. Most of the parameters pertain to internal settings of the elastix and ITK modules, providing the registration implementations. The list below gives a brief explanation of the parameters, following the table's order:

- ‘*image size*’: dimensions of the two input images
- ‘*schedule*’: determines how the original image is dydically decimated in order to represent it in a multi-resolution pyramid.
- ‘*registration scale*’: determines on which scale of this pyramid the parameters of the deformation field are estimated, i.e. the control grid points in the case of a B-spline registration and the grid of displacement vectors in the case of Demons or optical phase flow.
- ‘*interpolation scale*’: determines on which scale the displacement field vectors are calculated.
- ‘*optimiser*’: used to iteratively find the optimal value for the parameters of the deformation field.
- ‘*learning rate*’: controls the convergence speed of the optimiser by (down)scaling the updates it provides, when set too large the algorithm may become unstable.
- ‘*iterations*’: number of iterations performed by the optimiser.

- ‘*spline transform order*’: order of the spline basis functions used in the B-spline deformation model.
- ‘*warp interpolation order*’: used to resample the images when applying one of the transforms.
- ‘*update field smoothing*’ : standard deviation of the Gaussian used to smooth the Demons update field, giving the deformation viscous character.
- ‘*total field smoothing*’: standard deviation of the Gaussian used to smooth the Demons total update field, giving the deformation elastic character.

*Table B.1: Registration parameters for calculating the aluminium foam registration scores.*

	Demons	Phase	B-spline
image size	(218,216,184)	(218,216,184)	(218,216,184)
schedule	(5,4,3,2)	(5,4)	(5,4,3,2)
registration scale	2	2	3
interpolation scale	2	2	2
optimiser	Gradient Descent	Gradient Descent	Stochastic Gradient Descent
learning rate	1.0	0.5	Adaptive
iterations	50	50	500
spline transform order	n/a	n/a	3
warp interpolation order	1	1	3
update field smoothing	2 voxels	2 voxels	n/a
total field smoothing	2 voxels	2 voxels	n/a

*Table B.2: Registration parameters for calculating the leavening dough registration scores.*

	Demons	Phase	B-spline
image size	(256,256,256)	(256,256,256)	(256,256,256)
schedule	(3,2)	(3,2)	(5,4,3,2)
registration scale	2	2	3
interpolation scale	2	2	2
optimiser	Gradient Descent	Gradient Descent	Stochastic Gradient Descent
learning rate	1.0	0.5	Adaptive
iterations	50	20	500
spline transform order	n/a	n/a	3
warp interpolation order	1	1	3
update field smoothing	2 voxels	2 voxels	n/a
total field smoothing	2 voxels	2 voxels	n/a



